

University of Warwick institutional repository: <http://go.warwick.ac.uk/wrap>

A Thesis Submitted for the Degree of PhD at the University of Warwick

<http://go.warwick.ac.uk/wrap/50791>

This thesis is made available online and is protected by original copyright.

Please scroll down to view the document itself.

Please refer to the repository record for this item for information to help you to cite it. Our policy information is available from the repository home page.

AN EXAFS STRUCTURAL STUDY OF THE PASSIVE FILMS FORMED ON

FE-CR ALLOYS

by

Michael C L Ward

A Thesis

presented to the University of Warwick

in partial fulfilment of the requirements

for entry to the degree of

Doctor of Philosophy

Department of Physics

November 1986

BEST COPY

AVAILABLE

Variable print quality

ABSTRACT

Comparatively little is known about the nature of the passive films formed upon the technologically important iron-chromium alloys. It is known however, that they are both very thin (50\AA) and possibly amorphous: as such they are difficult to characterize by conventional diffraction methods. To avoid the problems associated with the diffraction techniques, the EXAFS technique has been used to characterize the passive film.

Iron-chromium alloys containing up to 29% atomic chromium were passivated in 0.1M NaNO_2 , 0.05M K_2CrO_4 and 2.0M H_2SO_4 . X-ray absorption measurements were then made upon the passivated alloys, using both total electron yield and fluorescence yield to determine the X-ray absorption.

Analysis of the extended X-ray absorption fine structure has revealed that an increase in structural disorder of the passive film may be correlated with an increase in the chromium content of the alloy. It has been shown that chromium contained in the passive film is associated with the disorder in the film Fe-O and Fe-Fe bond lengths compatible with the known oxides and hydroxides of iron have been obtained, but the uncertainties in the bond length determination prevent any structure being put forward for the passive film.

CONTENTS

	Page No.
Abstract	(i)
Contents	(ii)
List of Illustrations - Tables	(vi)
- Figures	(vii)
Acknowledgements	(xi)
Declaration	(xii)
<u>CHAPTER 1 - INTRODUCTION</u>	1
1.1 Corrosion Studies	1
1.2 Fe-Cr Alloys	3
1.3 Thermodynamics and Corrosion	6
1.4 Wet and Dry Corrosion/Oxidation	7
1.5 The Electrochemical Nature of Corrosion	8
1.6 Passivation	11
1.7 The Pourbaix Diagram & Electrochemical Behaviour	13
1.8 Passivation and Corrosion Resistance of Fe-Cr Alloys	16
1.9 Review of the Passive Film on Fe-Cr Alloys	20
1.9.1 The Oxides of Iron	20
1.9.2 Previous Studies of the Passive Film Formed on Fe	23
1.9.3 Electron Configuration and Oxygen Adsorption	29
1.9.4 The Passive Film formed on Fe-Cr Alloys	31
1.10 Extended X-Ray Absorption Fine Structure	38
1.10.1 Previous EXAFS Studies of Passive Films	40
1.11 Summary	44
1.12 Thesis Plan	46

<u>CHAPTER 2 - EXAFS THEORY</u>	47
2.1 Introduction	47
2.2 The Experimental EXAFS Function	48
2.3 X-Ray Absorption	51
2.4 X-Ray Absorption Near Edge Structure	53
2.5 Extended X-ray Absorption Fine Structure	55
2.5.1 The Theoretical EXAFS Function	55
2.5.2 Electron Scattering	58
2.5.3 The Phase and Amplitude Functions	62
2.6 Interpretation of EXAFS Spectra	64
2.6.1 The Fourier Transform	64
2.6.2 Further Methods of EXAFS Analysis	66
2.6.3 Modelling	68
 <u>CHAPTER 3 - EXPERIMENTAL METHODS</u>	 70
3.1 Sample Preparation	70
3.1.1 Thermal Evaporation	71
3.1.2 Starting Material	72
3.1.3 Evaporation of Alloy Films	73
3.1.4 Alloy Film Characterisation	75
3.1.5 Sample Passivation	77
3.2 EXAFS Measurement	78
3.2.1 The Synchrotron Radiation Source	79
3.2.2 The Monochromator	82
3.2.3 Incident Flux Monitor	84
3.2.4 Fluorescence X-ray Detection	85
3.2.5 Electron Yield Detection System	86
3.3 Data Collection	88
3.4 Averaging and Calibration	89

<u>CHAPTER 4 - EXAFS ANALYSIS</u>	90
4.1 Introduction	90
4.2 Data Smoothing	91
4.3 Background Removed	92
4.3.1 Pre-edge Absorption, Approximation and Normalisation	92
4.3.2 Background Subtraction	93
4.3.3 Free Atom Absorption, Approximation and Removal	93
4.4 Conversion to Momentum Space and the E_0 Problem	96
4.5 Weighting and Data Truncation	98
4.6 Fourier Transformation	101
4.7 Model Compound Results	102
4.8 Errors due to the choice of E_0	104
4.9 Single Shell Analysis	105
4.10 Conclusion	107
 <u>CHAPTER 5 - RESULTS</u>	 108
5.1 Introduction	108
5.2 Nitrite Passivated Films	109
5.2.1 Total Electron Yield Results	109
5.2.2 Fluorescence Yield Results	112
5.2.3 Summary of the Nitrite Passivated Film Results	112
5.3 Chromate Passivated Films	114
5.3.1 Summary of the Chromate Passivated Film Results	118
5.4 H_2SO_4 Passivated Films	120
5.4.1 Introduction	120
5.4.2 Electrochemical Study	120
5.4.2.1 Electrochemical Results	121
5.4.2.2 Conclusion of Electrochemical Results	122
5.4.3 EXAFS Results	122

5.4.4	Summary of the H ₂ SO ₄ Passivation Studies	123
5.5	Summary of Results	125
 <u>CHAPTER 6 - CONCLUSION AND DISCUSSION</u>		 127
6.1	Introduction	127
6.2	EXAFS as a Probe of the Passive Film Structure	128
6.2.1	Conclusion - Fluorescence vs Electron Yield	129
6.3	EXAFS Analysis	130
6.3.1	Conclusion - EXAFS Analysis	131
6.4	The Nature of the Passive Film	132
6.4.1	Conclusion - The Nature of the Passive Film	135
6.5	Future Work	136
 <u>REFERENCES</u>		 137

LIST OF ILLUSTRATIONS

<u>Tables</u>	<u>Following Page</u>
1.1 The Free Energy of Formation of Several Oxides	6
2.1 The EXAFS Weighting Factors (after Teo and Lee) ⁽³⁹⁾	65
3.1 The Analysis of the Bulk Fe-Cr Alloys	72
4.1 The Bond Lengths and Correction Factors obtained from the model compounds	103
4.2 The Correction Factors and Errors by R.D.F and S.S.A.	106
4.3 Correction Factors used in this Study	107
5.1 Fe-O Bond Lengths of some Iron Compounds	111
5.2 Bond Lengths determined from Nitrite Passivated Alloys by Total Yield	112
5.3 Bond Lengths determined from Chromate Passivated Alloys by Total Yield	112
5.4 Correction Factors based upon the Reduced Data Range Scheme	116
5.5 Fe-O Bond Lengths determined from Chromate Passivated Samples	116
5.6 Analysis of the Bulk Alloys	121
5.7 Bond Lengths determined from H ₂ SO ₄ Passivated Samples	123

<u>Figures</u>	<u>Following Page</u>
1.1 The Electrochemical Nature of Corrosion	8
1.2 Polarisation of Electrolyte under Anodic Potential	11
1.3 The Pourbaix Diagram for Iron	11
1.4 The Simplified Pourbaix Diagram for Iron	13
1.5 The Simplified Pourbaix Diagram for Chromium	13
1.6 The Anodic Behaviour of Iron in H ₂ SO ₄	14
1.7 The Pourbaix Diagram for Fe-Cr Alloys	16
1.8 The Anodic and Cathodic Behaviours of Fe-Cr Alloys	17
1.9 The Oxides of Iron	20
1.10 The Structure of γ -FeOOH	22
1.11 The 'K' Edge X-ray Absorption Spectrum of Iron	38
1.12 Auger and Fluorescence Decay	39
2.1 The Components of an X-ray Absorption Edge	48
2.2 XANES and EXAFS	51
2.3 Photo-electron Scattering in X-ray Absorption	55
2.4 Mechanism of Electron Scattering	58
2.5 The Photo-electron Backscattering Factors of Iron and Oxygen (after Teo and Lee) ⁽³⁹⁾	62
3.1 Schematic of the Thermal Evaporation Apparatus	71
3.2 Arrangement of Glass and NaCl Substrates used during Alloy Deposition	73
3.3 Electron Micrograph and Diffraction Pattern of a Typical Fe-Cr Alloy Film	75
3.4 Schematic of the Apparatus used to Measure the X-ray Absorption of the Passivated Films	78
3.5 The Spectrum of the Daresbury S.R.S.	81
3.6 The Channel Cut Monochromator	82
3.7 The Use of Manganese X-ray Filters	85
3.8 The Electron Yield Detection Chamber	86
3.9 Bias Circuit for the Channeltron Electron Detector	86

4.1	The Raw Absorption X-ray Spectrum of a Nitrite Passivated Film	91
4.2	The Spline Smoothed X-ray absorption Spectrum of a Nitrite Passivated Film	91
4.3a)	Spline Smoothed X-ray Absorption Spectra for Fe and)	92
4.3b)	$\alpha\text{Fe}_2\text{O}_3$)	
4.4a)	Pre-edge Absorption Subtracted Spectra of Fe and)	93
4.4b)	$\alpha\text{Fe}_2\text{O}_3$)	
4.5	Cubic Polynomial Approximation to U_f	94
4.6a)	U_f Approximations for Fe and $\alpha\text{Fe}_2\text{O}_3$)	94
4.6b))	
4.7a)	The Normalised EXAFS of Fe and $\alpha\text{Fe}_2\text{O}_3$	95
4.7b)		
4.8a)	The Normalised EXAFS as a Function of 'k' of Fe and)	97
4.8b)	$\alpha\text{Fe}_2\text{O}_3$)	
4.9a)	$k^2X(k)$ for Fe and $\alpha\text{Fe}_2\text{O}_3$	98
4.9b)		
4.10a)	Truncated $k^2 X(k)$ for Fe and $\alpha\text{Fe}_2\text{O}_3$	99
4.10b)		
4.11a)	The R.D.F.'s of Fe and $\alpha\text{Fe}_2\text{O}_3$	101
4.11b)		
4.12a)	The X-ray Absorption Spectra of Cr and Cr_2O_3	102
4.12b)		
4.13a)	The R.D.F.'s of Cr and Cr_2O_3	102
4.13b)		
4.14	Variation of Fe-O Bond Length with E_o	104
5.1	Total Electron Yield Iron 'K' Edge Spectrum of a Nitrite Passivated Fe Film	109
5.2	Total Electron Yield Iron 'K' Edge Spectrum of a Nitrite Passivated Fe6Cr Alloy	109
5.3	Total Electron Yield Iron 'K' Edge Spectrum of a Nitrite Passivated Fe16Cr Alloy	109
5.4	Total Electron Yield Iron 'K' Edge Spectrum of a Nitrite Passivated Fe29Cr Alloy	109
5.5	Total Electron Yield Chromium 'K' Edge Spectrum of a Nitrite Passivated Fe16Cr Alloy	109
5.6	The R.D.F. of an Fe Film Passivated in Nitrite Measured by Total Yield	110

5.7	The R.D.F. of an Fe6Cr Alloy Passivated in Nitrite Measured by Total Yield	110
5.8	The R.D.F. of an Fe16Cr Alloy Passivated in Nitrite Measured by Total Yield	110
5.9	The R.D.F. of an Fe29Cr Alloy Passivated in Nitrite Measured by Total Yield	110
5.10	The R.D.F. on an Fe16Cr Alloy Passivated in Nitrite (Cr edge) Measured by Total Yield	110
5.11	The R.D.F. on an Fe16Cr Alloy Passivated in Nitrite (Cr edge) Measured by Total Yield	111
5.12	The R.D.F.'s of Alloys Containing 0, 6, 16 and 29% Atomic Chromium	112
5.13	The Total Electron Yield Iron 'K' Edge Spectrum of a Chromate Passivated Film	114
5.14	The R.D.F. of an Fe6Cr Chromate Passivated Film Measured by Total Yield	114
5.15	The R.D.F. of Iron under the Reduced Data Range Scheme	116
5.16	The R.D.F. of $\alpha\text{-Fe}_2\text{O}_3$ under the Reduced Data Range Scheme	116
5.17	The R.D.F. of an Iron Film Passivated in Chromate Measured by Total Yield	116
5.18	The R.D.F. of an Fe6Cr Alloy Film Passivated in Chromate Measured by Total Yield	116
5.19	The R.D.F. of an Fe6Cr Alloy Film Passivated in Chromate Measured by Total Yield	116
5.20	The R.D.F. of an Fe29Cr Alloy Film Passivated in Chromate Measured by Total Yield	116
5.21	The R.D.F. of an Iron Film Passivated in Chromate Measured by Fluorescence	116
5.22	The R.D.F. of an Fe6Cr Alloy Passivated in Chromate Measured by Fluorescence	116
5.23	The R.D.F. of an Fe16Cr Alloy Passivated in Chromate Measured by Fluorescence	116
5.24	The R.D.F. of an Fe29Cr Alloy Passivated in Chromate by Fluorescence	116
5.25	The R.D.F. of an Fe16Cr Alloy Passivated in Chromate (Cr edge)	118
5.26	The Anodic Behaviour of Fe in 2.0M H_2SO_4	121
5.27	" " " " Fe5Cr in 2.0M H_2SO_4 (ix)	121

5.28	The Anodic Behaviour of Fe10Cr in 2.0M H ₂ SO ₄	121
5.29	" " " " Fe15Cr " "	121
5.30	" " " " Fe20Cr " "	121
5.31	" " " " Fe25Cr " "	121
5.32	The R.D.F.'s of Alloys Containing 6,16 and 29% Atomic Chromium Passivated in H ₂ SO ₄	122
5.33	The R.D.F. of an Fe29Cr Alloy Passivated in H ₂ SO ₄ under the Reduced Data Range Scheme	122
6.1a)	The Model for the Passive Film on Fe-Cr Alloys	134
6.1b)		
6.1c)		

Acknowledgements

I should like to thank Professors P N Butcher, P W Macmillan and A J Forty in their capacity as Chairmen of the Physics Department during my time at Warwick for allowing me the use of the laboratory facilities. I am also grateful to S.E.R.C. and A.E.R.E. Harwell for providing my initial grant, and to British Steel for supplying the alloys used in this study.

Special thanks go to Professor A J Forty for his help, encouragement and patience during the preparation of this thesis.

To all those who have helped me to complete this study including my parents, Elaine, Tim, Pete, Dave, Andros and Sulah - my thanks.

Finally, I should like to thank Mrs M Hodgkiss for typing this thesis and displaying great patience and humour.

Declaration

This thesis contains an account of my independent research work performed in the Department of Physics at the University of Warwick between October 1981 and May 1985 under the general supervision of Professor A J Forty.

CHAPTER 1

1.1 Corrosion Studies

Traditionally the scientific study of corrosion has been justified by the huge burden which corrosion inflicts upon the industry. While this cost remains very high, there are today other more pressing environmental reasons for studying the corrosion process. The first of these is the general realization, that the earth's resources are finite. Thus natural resources, such as metallic ores, must be used prudently. If unacceptable levels of damage to the environment and the economy are to be avoided. The other and perhaps more important consideration is the use of many metallic components in the Chemical, Aviation and Nuclear industries, where failure of any component in these industries has adverse consequences for mankind and the environment alike.

The economic and environmental concerns can only be overcome when the ravages of corrosion have been brought under control. These in turn can only be contemplated when detailed models of the mechanisms of corrosion and corrosion resistance have been developed. In this context it is interesting to note that comparatively little is known about the detailed corrosion processes of the widely used and technologically important stainless steels. It is therefore the intention of this thesis to add to the overall level of understanding of the corrosion resistance of the stainless steels, so that the above concerns can be more fully met.

It is known that the corrosion rate of the iron-chromium alloy system is a function of the amount of chromium contained in the alloy. The interesting

feature of this alloy system is the significant fall in the rate of corrosion that is seen to occur when the atomic fraction of chromium exceeds 12%. It is this experimental observation that is discussed herein.

1.2 Iron-Chromium Alloys

The iron-chromium alloy system is of great interest to the corrosion scientist, for not only is the system of technological importance itself, but it forms the basis of stainless steels. Together with these stainless steels, the corrosion resistance of the iron chromium alloys is believed to be closely related to the phenomena of passivation. In this study the word passive will be defined in the following way: a metal or alloy is passive when it substantially resists corrosion in an environment where thermodynamically there is a large free energy decrease associated with its passage from the metallic state to the appropriate corrosion products.

While there have been several theories put forward to account for the passivation process, the one most widely held is that immediately the corrosion reaction starts, corrosion products begin to form. In the case of silver-gold alloys corroding in dilute nitric acid the reaction products are soluble and so they diffuse away from the reaction site, causing little hindrance to the corrosion reaction. However, in the corrosion of iron in concentrated nitric acid the corrosion products are not soluble, but form instead as a thin oxide layer upon the surface of the iron. This passive film serves to separate the iron from its environment thereby controlling the rate of further attack: the corrosion reaction stops, and the iron is said to be passive. A similar explanation is put forward to account for the corrosion resistance of stainless steels and iron-chromium alloys.

Why should certain alloys should be more easily passivated than others and why should some offer better corrosion resistance once they have been passivated? This work seeks to answer those questions.

The current thinking is that any variation in the passivation and corrosion behaviour of the alloys is not due to the differences in the alloys themselves, but to the structure and nature of the surface oxides which are formed.

We will attempt to gain a greater understanding of the passivation process by studying the structure of the passive film formed on a range of iron-chromium alloys containing up to atomic 30% chromium. This range was chosen because at the low chromium end of the range the alloys are difficult to passivate and corrodible, while the chromium-rich alloys are easily passivated and corrosion-resistant. Because previous studies have shown that the passive films tend to be very thin (50\AA) and non-crystalline under conditions expected to lead to good corrosion resistance, the new structural technique of EXAFS (Extended X-ray Absorption Fine Structure) has been used. This technique, unlike the more traditional methods of X-ray and electron diffraction, can deal easily with thin, non-crystalline films. Modification of the basic EXAFS technique offers the possibility of studying the film, without the need to remove it from the aqueous environment in which it was formed.

The iron-chromium alloy system was studied because of its technological importance and typical stainless steel corrosion behaviour; moreover, the improvement in corrosion resistance which follows the rise in the amount of chromium contained in the alloy is not accompanied by any structural phase transformations. A corrosion resistant iron-chromium alloy containing, say, 18% atomic chromium, is known to undergo a B.C.C. to F.C.C. phase transformation at 1000°C . This makes it unsuitable for applications where it is likely to be subjected to excessive temperature cycling. To avoid these problems 8% nickel may be added to the alloy to stabilise the F.C.C.

phase down to room temperature. However, in the presence of the nickel the increase in the chromium content leads to an increase in corrosion resistance, and to a phase transformation between the B.C.C. low chromium alloy and the high chromium F.C.C. structure. This complicates the study of the transition to corrosion resistant behaviour, therefore the simpler iron-chromium alloy system has been chosen for the study.

1.3 Thermodynamics and Corrosion

Most of the metals of importance occur naturally as ores, which are the stable chemical compounds of the metal in the chemical environment of the earth. It is not surprising, that once extracted from their respective ores the metals should display a marked tendency to react with the environment to re-form the original ore.

A measure of the likelihood that such a reaction will take place is given by the associated change in free energy. Table (1.1) lists the free energy of formation of the oxides of some common metals. Compare the change in free energy associated with the oxidation of one mole of sodium atoms and one mole of aluminium atoms: thermodynamics alone cannot be used to predict corrosion behaviour, since we should expect aluminium to be more readily oxidized than sodium. This does not imply that thermodynamics has no part to play in determining corrosive behaviour. As we shall see later, when thermodynamics is combined with the fact that wet corrosion is electrochemical in nature, Pourbaix diagrams are important in determining the conditions likely to lead to the establishment of passivity, but they cannot provide any information about how well the passivated alloy will resist further environmental attack.

Oxide	Free energy of formation @ 295K kJ/mol
Al_2O_3	-1582
Fe_2O_3	-741
Na_2O	-376
MgO	-596

Table (1.1) A comparison of the free energy of formation of several oxides.

1.4 Wet and Dry Corrosion/Oxidation

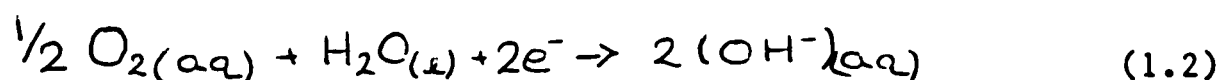
Before proceeding to describe more fully the basic principles of corrosion it should be pointed out that we are dealing here with a corrosion process that occurs in the presence of water. An alternative type of corrosion oxidation or tarnish that takes place in the absence of water, generally occurs at temperatures higher than the processes to be considered here, and leads to the formation of relatively thick ($\sim 5000\text{\AA}$) crystalline oxides. Unlike the films that are the concern of this work, these are easily studied by conventional diffraction methods. This has lead them to be well characterised and their growth mechanisms and corrosion properties are well understood. While the corrosion processes both wet and dry, rely upon the movement of atoms or ions through the surface oxide layer, the thick oxides formed at high temperatures under dry conditions have little to do with the corrosion resistance of thin passive films and will not be dealt with here.

1.5 The Electrochemical Nature of Corrosion

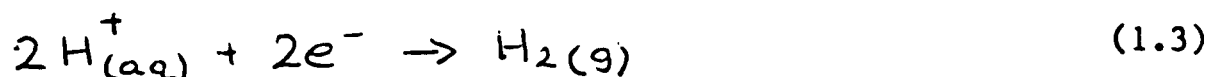
The electrochemical nature of the corrosion process is shown schematically in Fig. (1.1), which depicts the corrosion of iron by an aerated sodium chloride solution. This picture may be conveniently divided into two parts, the anodic half cell and the cathodic half cell. It is at the anodic half cell that active dissolution of the iron takes place, according to the reaction



The electrons travel through the metal as shown to the cathodic site where the reduction of dissolved oxygen takes place, by the following reaction



Since both of the corrosion products are soluble we can expect that the reaction will continue as long as there is sufficient dissolved oxygen to drive the cathodic half of the cell. In the case of acidic solutions we would expect the cathodic reaction to be the reduction of the hydroxonium ion.



When the two reaction products meet, insoluble iron (II) hydroxide is precipitated which is then further oxidised by dissolved oxygen to yellow FeOOH , rust.

In some cases, the corrosion product may totally enclose the anodic area and so limit the rate of attack. However, the poor mechanical properties of the

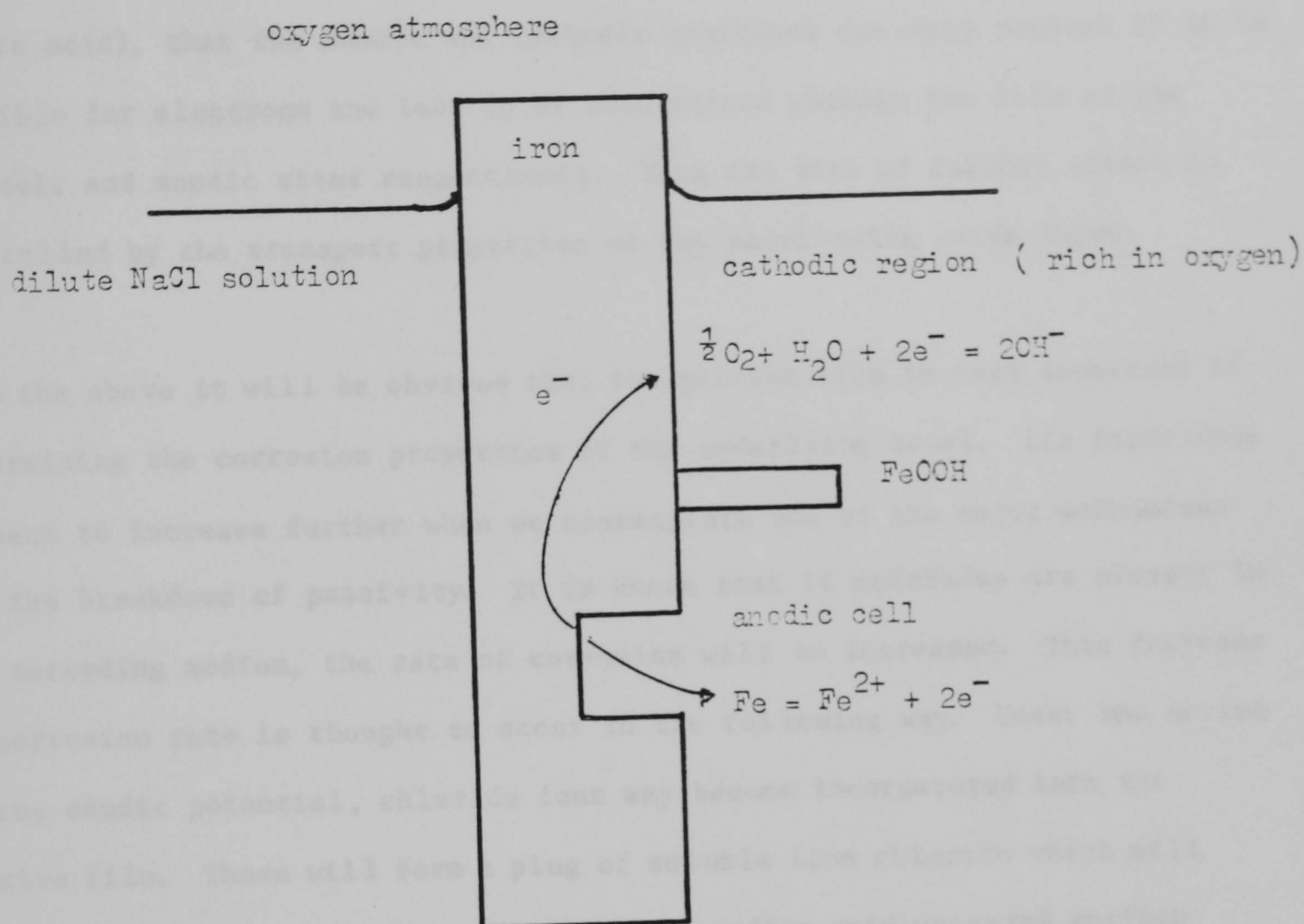


Figure (1.1). Schematic representation of the electrochemical nature of the corrosion of iron in dilute NaCl solution.

rust layer make it of little use for any major form of corrosion control. What is needed instead is some form of protective oxide.

In this case we see in the presence of a dense oxide layer formed upon the surface of, say, iron (as is the case when iron is passivated in concentrated nitric acid), that the anodic and cathodic reactions can only proceed if it is possible for electrons and ions to be transported through the film at the cathodic and anodic sites respectively. Thus the rate of further attack is controlled by the transport properties of the passivating oxide layer.

From the above it will be obvious that the passive film is very important in determining the corrosion properties of the underlying metal. Its importance is seen to increase further when we contemplate one of the major mechanisms for the breakdown of passivity. It is known that if chlorides are present in the corroding medium, the rate of corrosion will be increased. This increase in corrosion rate is thought to occur in the following way. Under the action of the anodic potential, chloride ions may become incorporated into the passive film. These will form a plug of soluble iron chloride which will dissolve to form a corrosion pit. The surrounding oxide-covered surface acting as a large area cathode drives a large anodic current through the corrosion pit so causing rapid corrosion. It is vital therefore that for good lasting resistance to so-called 'Pitting Corrosion' the passive film must be able to resist attack by chloride ions.

It might be thought either that in the presence of a break in the film, the rate of attack will be solely determined by the rate of arrival of dissolved oxygen atoms at the cathodic surface, or if the removal of the electrons were to take place via an external circuit that the rate of dissolution of an iron anode could be made as great as wished. This is not the case however, and as

we shall see, in the next section the same mechanism is responsible for limiting the rate of dissolution of metal, and the formation of the passive oxide and its repair.

1.6 Passivation

Under the influence of the cathodic reaction or some external circuit we can expect that the anodic dissolution of the iron from a gap in the protective oxide layer will be enhanced. This is not the only effect that the anodic voltage will have, it will also cause the alignment of the surrounding water molecules, as shown in Fig. (1.2). This dipole alignment, produced by the gradient of the anodic electric field, produces a potential barrier which the dissolving iron ions must pass over if the reaction is to continue. The barrier is shown schematically in Fig. (1.2). Only a certain fraction of the dissolving ions will have sufficient energy to surmount this barrier, so the rate of dissolution will be limited.

This current limiting causes a polarisation of the cell potential in the anodic direction which then makes the formation of oxide given by equation (1.4) thermodynamically possible.



Such a mechanism is responsible for the passivation of iron in sulphuric acid under anodic polarisation. While the reaction given by equation (1.1), the dissolution of iron, is still possible at the greater anodic potential, the reaction products of equation (1.4) (Fe_2O_3 in the case of iron passivated in H_2SO_4) form on the surface of the exposed iron and so prevent further active dissolution.

The electrochemical conditions required to produce such an effect may be conveniently summarised by means of a Pourbaix diagram: one for the iron/water system is reproduced in Fig. (1.3). As has already been stated

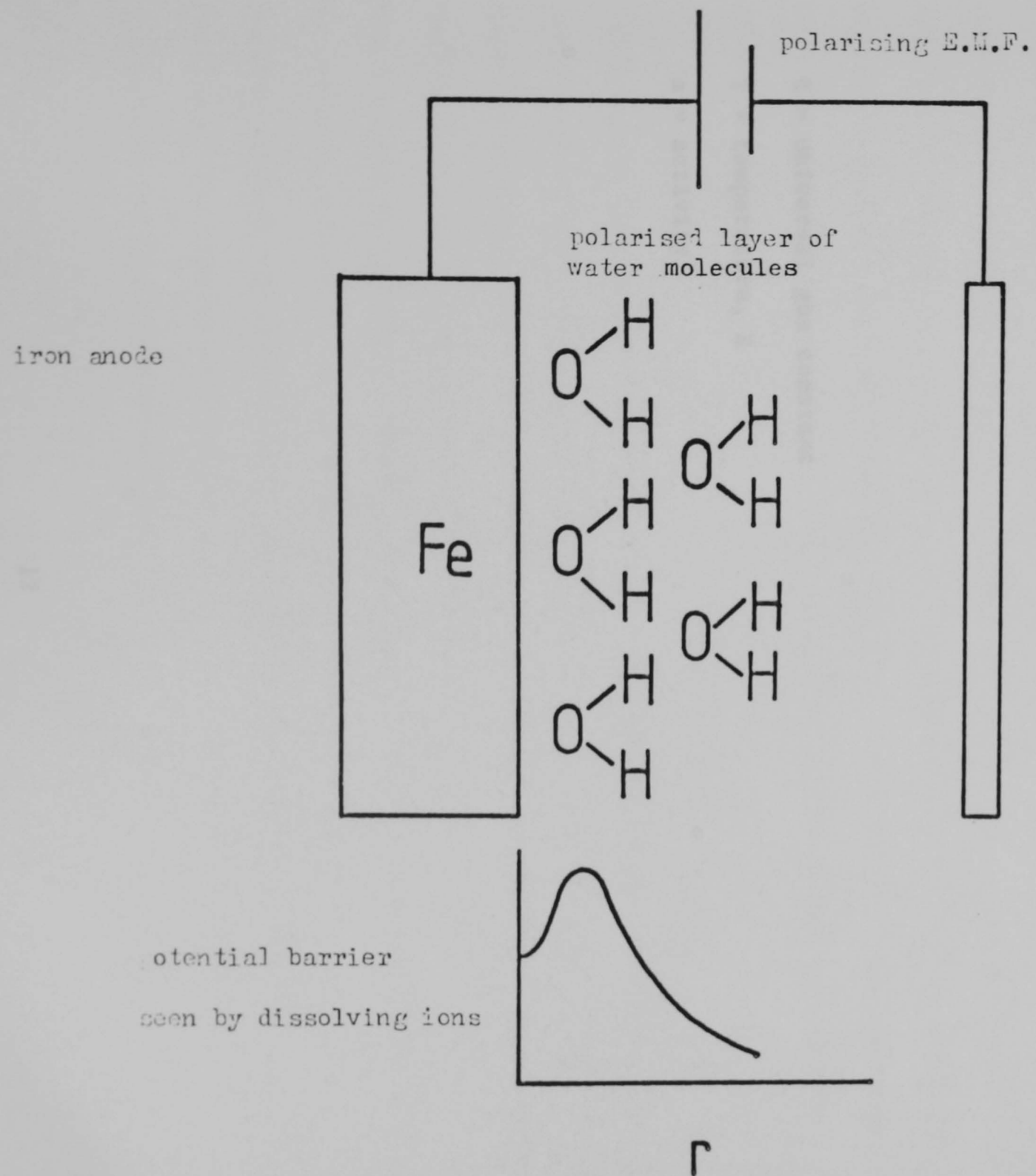


Figure (1.2). Polarisation of water molecules creates potential barrier for dissolving ions.

the change in free energy associated with a reaction may be taken as a measure of the possibility of such a reaction occurring. This is related to the potential at which the reaction will occur by equation (1.5).

$$\Delta G^{\circ} = -nFE^{\circ} \quad (1.5)$$

nF = electronic charge taking part in reaction

Variation of this potential with the concentration of the contents of the cell is given by the Nernst equation (1.6).

$$E = E^{\circ} + \frac{RT}{nF} \ln \left(\frac{a_{\text{oxidised states}}}{a_{\text{reduced states}}} \right) \quad (1.6)$$

R = universal gas constant

T = temperature, K

a = activity

1.7 The Pourbaix Diagram and Electrochemical Behaviour

The Pourbaix diagram is a graphical representation of the conditions of equilibrium for the various metal water reactions. The graph has pH and potential as its co-ordinates and each line on the graph represents the conditions of equilibrium of some reaction. Each region represents the conditions of stability of the various species taking part in the reaction. For example, the lines labelled 'A' in the iron-water system diagram of Fig. (1.3) represent the equilibrium potentials for the cell reaction of equation (1.1), plotted for various concentrations of Fe^{2+} ions. The lines labelled 'B' indicate the equilibrium conditions for the reactions of equation (1.4) and the shaded area represents the region of stability for hematite $\gamma\text{Fe}_2\text{O}_3$. As previously mentioned the active dissolution of iron is still possible in this region, but the passage of the Fe ion into solution is now hindered by the presence of the hematite layer. Thus it is possible to simplify the original diagram into three regions; immunity, passivity and corrosion. The boundaries have been defined somewhat arbitrarily for concentrations of soluble species of 10^{-6} molar.

The Pourbaix diagram makes no claim about how well the sample will be passivated or even that passivation will occur. All it indicates is that a reaction product will be stable under the conditions indicated. In the immune region it is not thermodynamically possible for the iron to dissolve and so the iron can be considered immune. Polarisation into this region is the basis of cathodic protection, while in the areas indicating corrosion only the soluble species are stable and so active corrosion must be expected to continue. The simplified diagrams for iron and chromium are reproduced in Figs. (1.4) and (1.5) respectively.

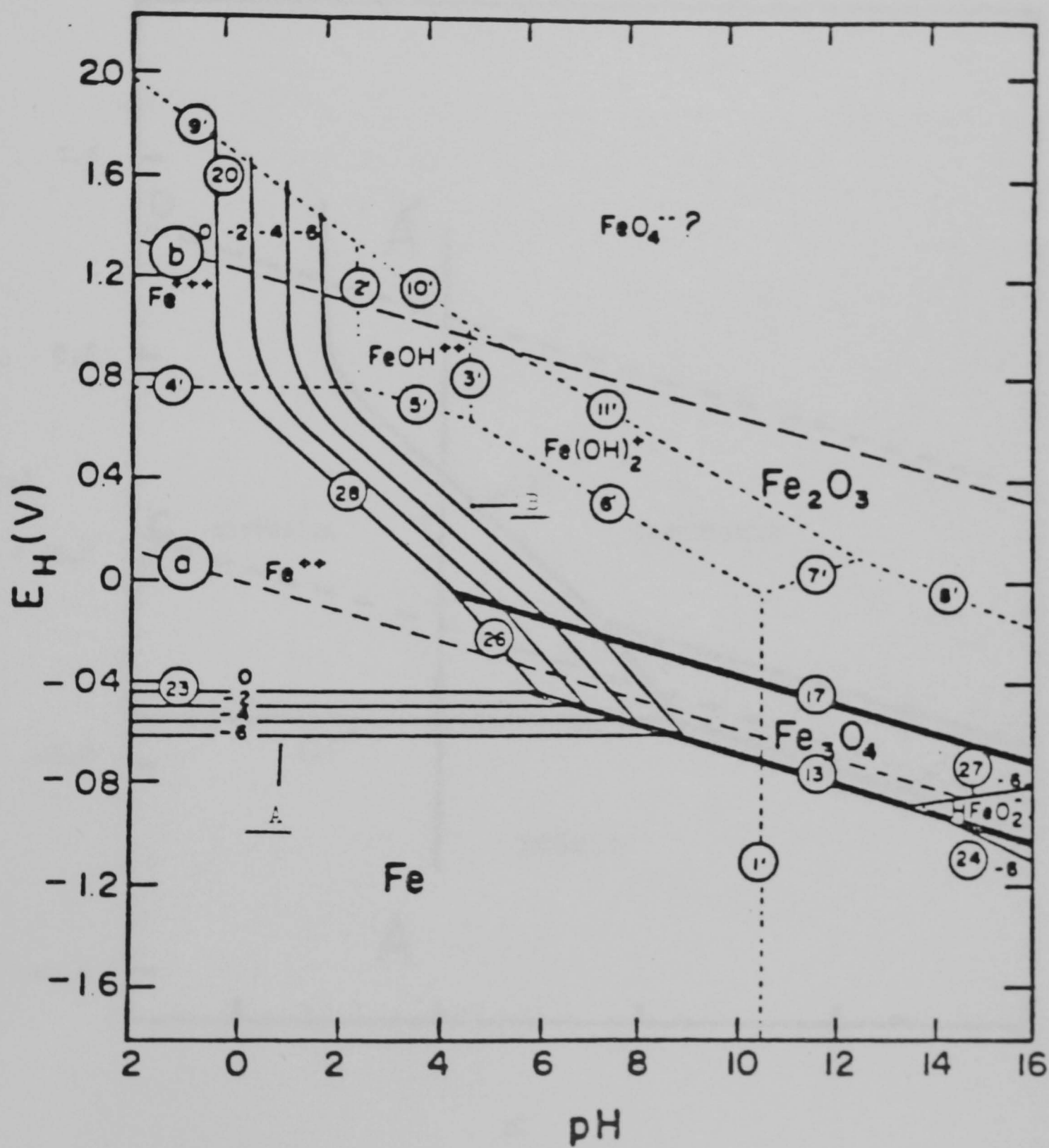
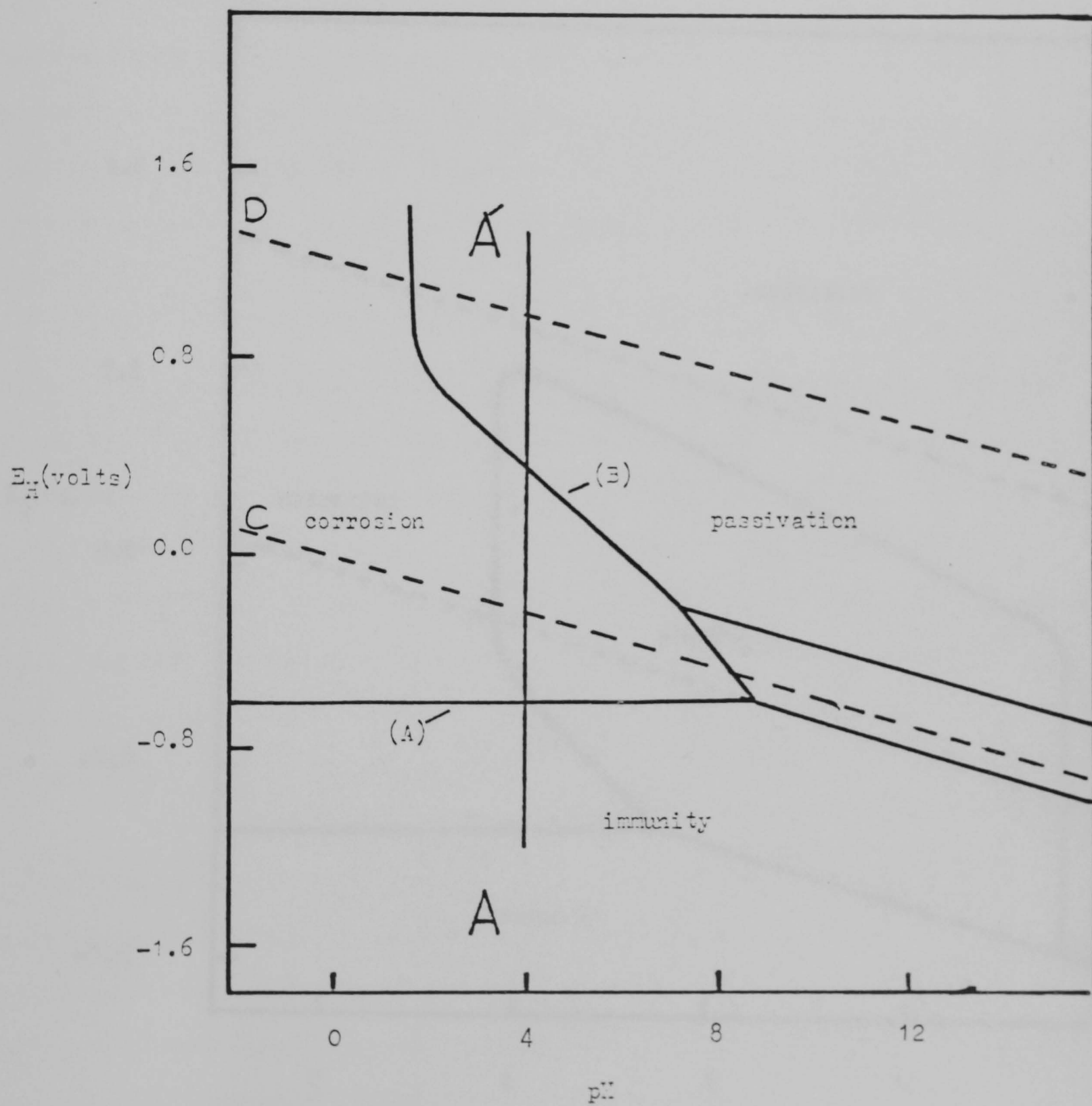
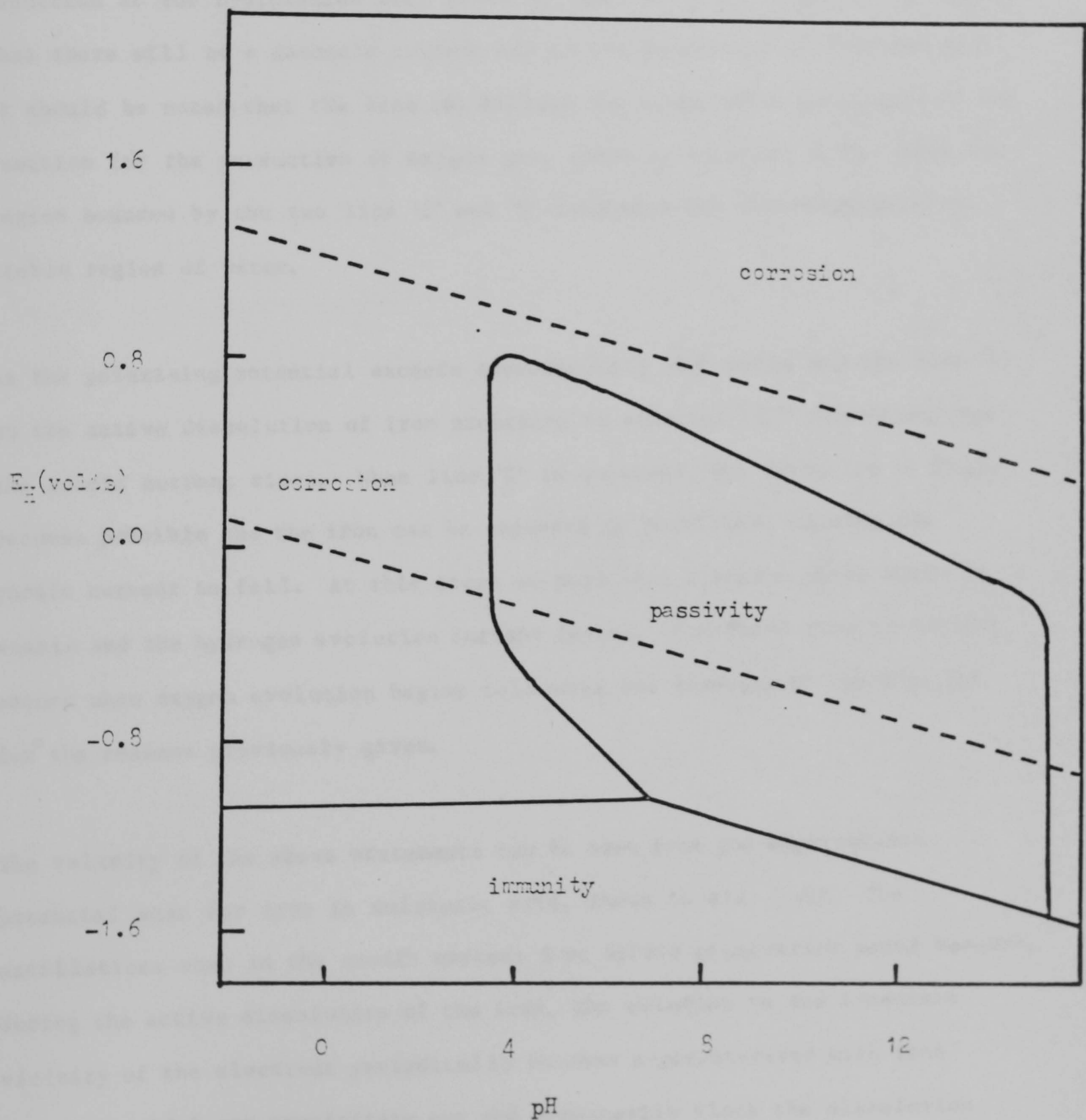


Figure (1.3). The Pourbaix diagram for the iron/water system at 25°C.

Figure(1.4). The simplified Pourbaix diagram for the iron/water system at 25°C, indicating the regions: passivity, corrosion and immunity.



Figure(1.5). The simplified Pourbaix diagram for the chromium/ water system at 25°C, indicating the regions of passivity, corrosion and immunity.



As a further example of the Pourbaix diagram it is interesting to consider what would happen to an iron electrode, sitting in a solution of pH4, if the immune region was polarised along the line (A-A') of the simplified Pourbaix diagram of Fig. (1.4). In the immune region, the iron is thermodynamically stable and so cannot be expected to contribute to any corrosion current. We are, however, below the line (C) representing the equilibrium potential of the reduction of the hydroxonium ion, given by equation (1.3). Thus we can expect that there will be a cathodic current due to the generation of hydrogen gas. It should be noted that the line (D) follows the equilibrium conditions of the reaction for the production of oxygen gas, shown by equation (1.2). Thus the region bounded by the two line 'C' and 'D' indicates the thermodynamically stable region of water.

As the polarising potential exceeds approximately -0.6 volts and the line 'A' so the active dissolution of iron according to equation (1.1) commences, and the anodic current rises. When line 'B' is exceeded, the formation of Fe_2O_3 becomes possible and the iron can be expected to passivate, causing the anodic current to fall. At this stage we pass into a region where water is stable and the hydrogen evolution current ceases. The final rise in current occurs when oxygen evolution begins following the crossing of the line (D), for the reasons previously given.

The validity of the above statements can be seen from the experimental potential scan for iron in sulphuric acid, shown in Fig. (1.6). The oscillations seen in the anodic current just before passivation occur because, during the active dissolution of the iron, the solution in the immediate vicinity of the electrode periodically becomes supersaturated with iron sulphate, which can precipitate out and momentarily block the dissolution process. The resulting drop in the concentration of iron ions due to their

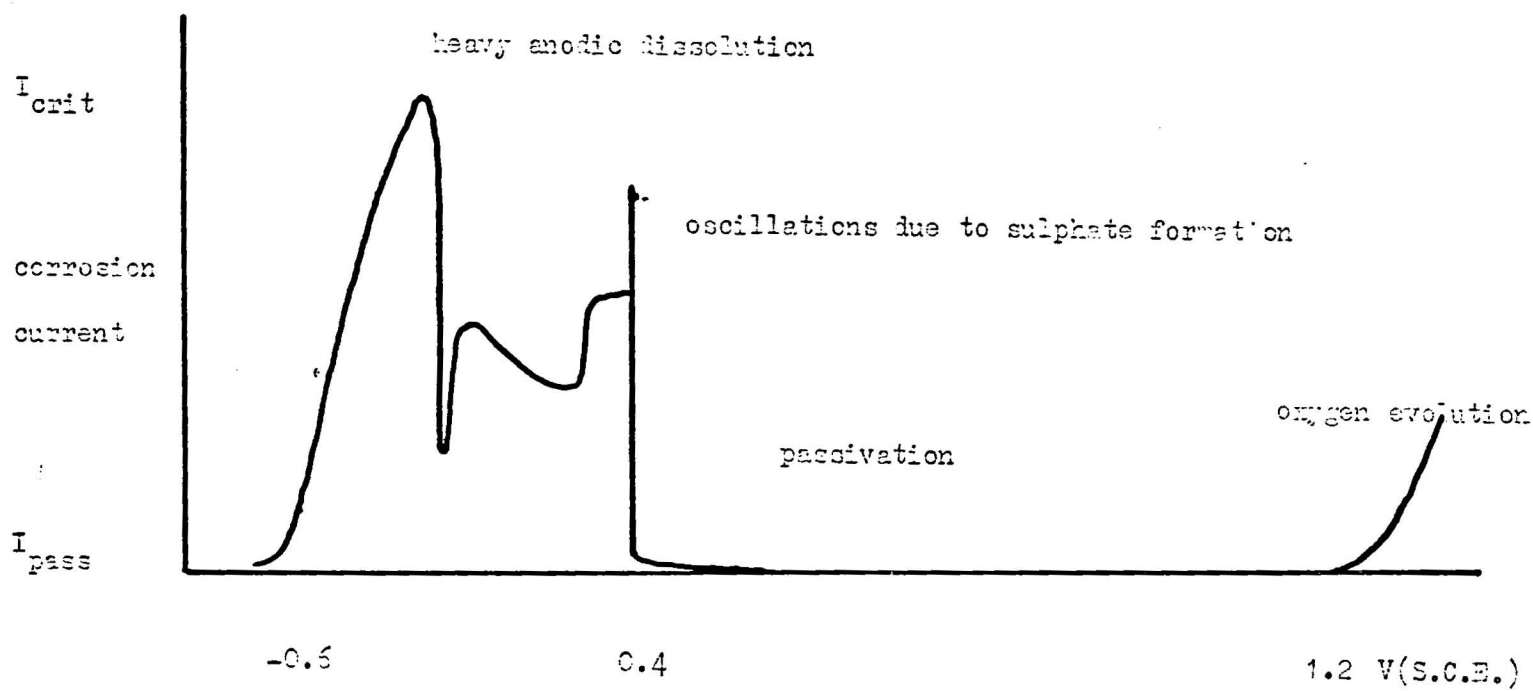


Figure (1.6). The anodic behaviour of Iron in H₂SO₄ (pH4).

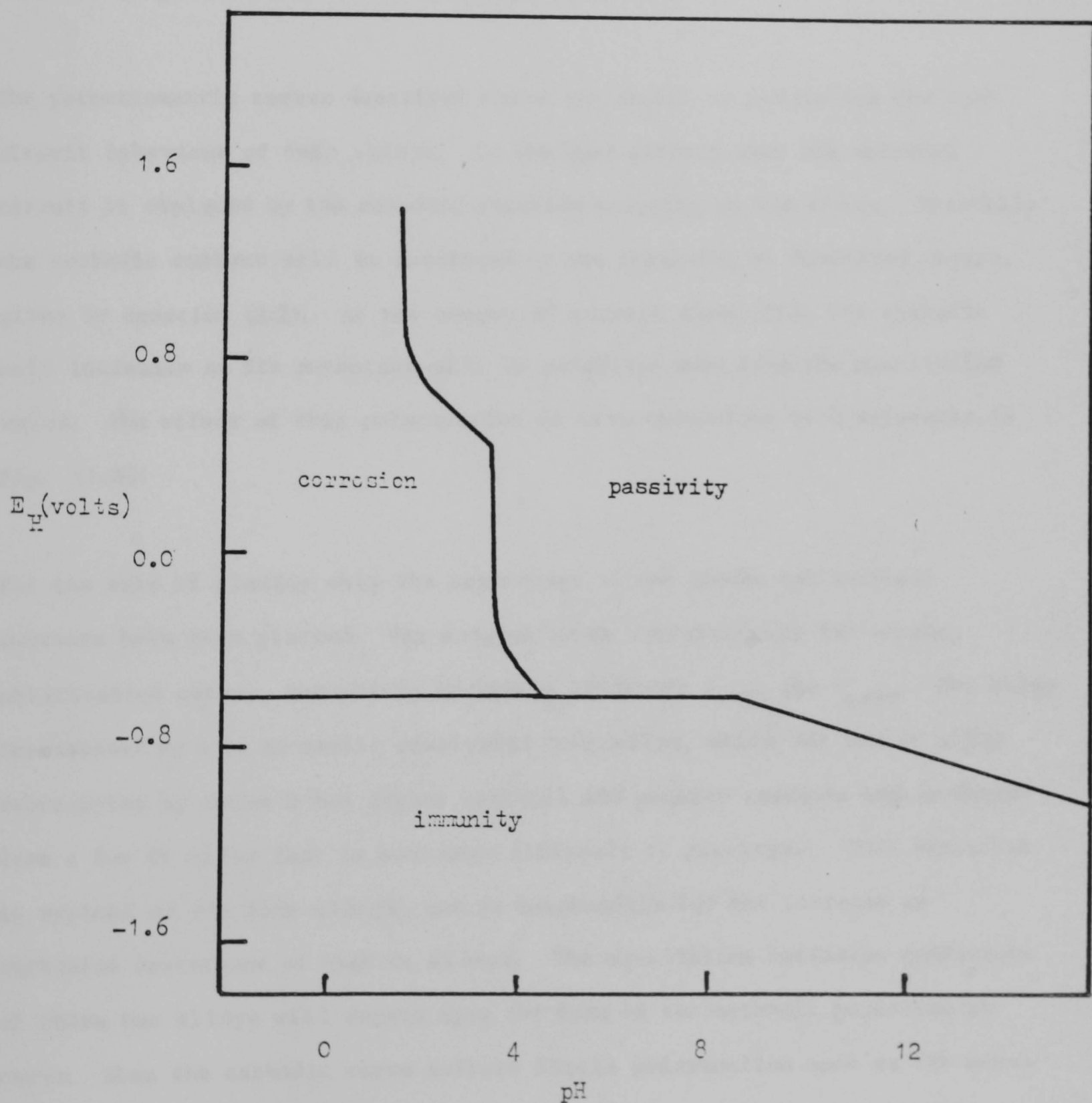
diffusion out into the bulk of the solution causes the iron sulphate to dissolve and the active dissolution to recommence. Thus iron sulphate may be considered an 'ineffective' passivating layer.

1.8 Passivation and Corrosion Resistance of Fe-Cr Alloys

From the above it is obvious that thermodynamics is capable of determining the conditions likely to provide passivity. It will also be obvious that the conditions for the passivity of an alloy may be obtained by superposing the regions of passivity derived for its constituents. Such a superposition for the iron-chromium system is shown in Fig. (1.7). The expansion of the passive region can be easily understood, for while one particular element may remain active, if the other is passive it can be assumed that the second element will form a protective layer upon the remaining alloy and so produce passivity. While for simplicity the above description has assumed that the passive films formed on iron and chromium are Fe_2O_3 and Cr_2O_3 it must be remembered that the Pourbaix diagram merely indicates the possibility that these oxides can form. It must also be borne in mind that any passive film is not likely to be grown under equilibrium conditions, and it is therefore highly unlikely that the film will consist solely of one of the stoichiometric oxides quoted above. Rather we should consider the passive films to be based upon the structure of these oxides. In the case of an alloy the passive film should also be considered to be a mixture of two metallic oxides. It is not unreasonable to assume that the film may possibly contain extra water, hydrogen and hydroxide groups. This may infer that the passive film has a complex structure, and as we shall see later this appears to be supported by other studies.

Thermodynamics is not able to determine the corrosion rate of the alloy, once it has been passivated. The corrosion rate may be seen to be directly related to the current flowing during the passive region of the data shown in Fig. (1.6). This current I_{pass} is due to the slow dissolution of the iron from the passive film by the mechanisms previously described.

Figure (1.7). Superposition of the simplified Pourbaix diagrams of iron and chromium, indicating the corrosion behaviour of iron-chromium alloys.

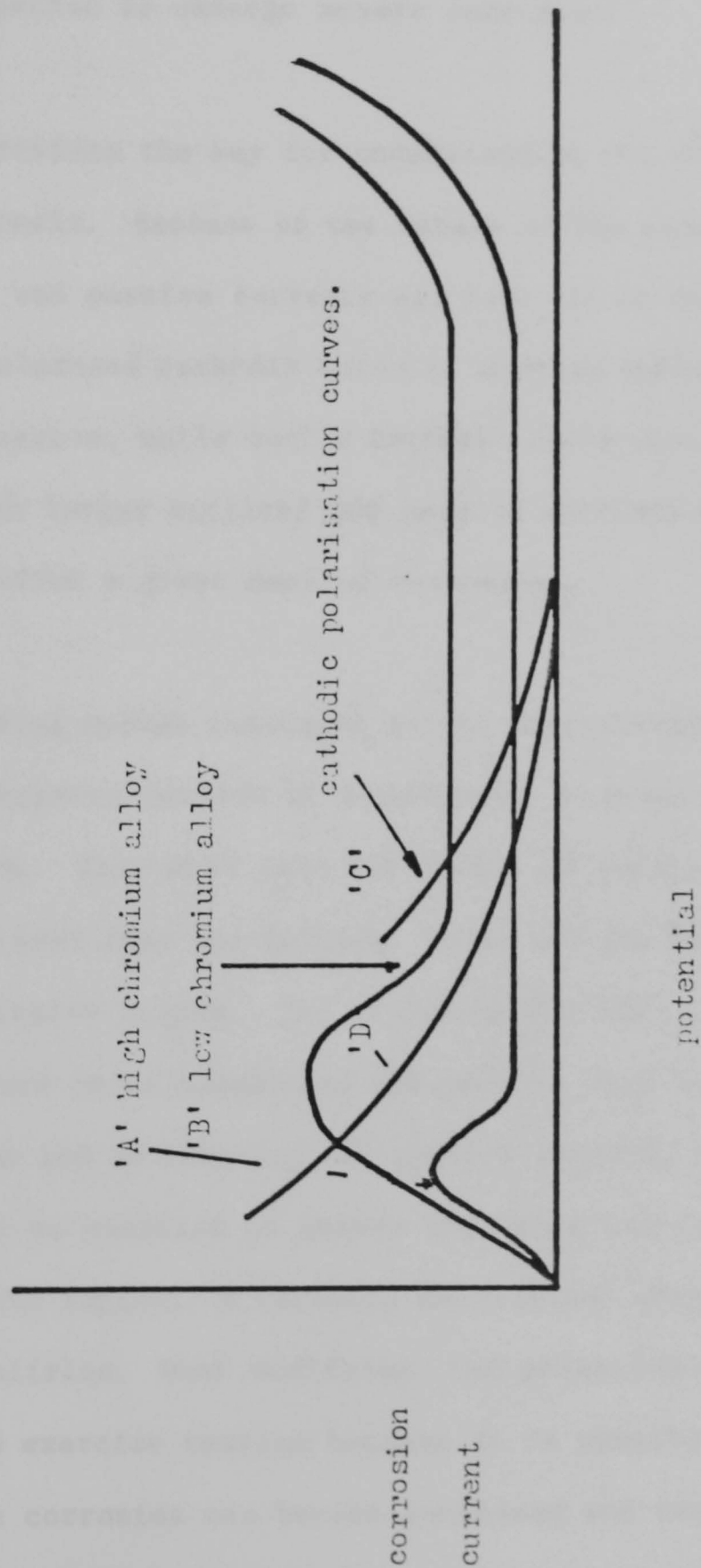


The ease with which passivation takes place is determined by the magnitude of the critical current I_{crit} of Fig. (1.6) - that must be raised to bring about passivation. The smaller this is the easier passivation will be. Thus when a break does occur in the passive film, the ease with which it is plugged by the passivation process is determined by I_{crit} . The smaller I_{crit} , so the smaller will be I_{pass} . I_{pass} is therefore seen to be a useful parameter with which to judge the effectiveness of a passive film.

The potentiometric curves described above are useful in predicting the open circuit behaviour of FeCr alloys. In the open circuit case the external circuit is replaced by the cathodic reaction occurring on the alloy. Typically the cathodic current will be generated by the reduction of dissolved oxygen, given in equation (1.2). As the amount of current drawn from the cathodic cell increases so its potential will be polarised away from the equilibrium value. The effect of this polarisation is best understood with reference to Fig. (1.8).

For the sake of clarity only the magnitudes of the anodic and cathodic currents have been plotted. The diagram shows schematically two anodic polarisation curves, for alloys of widely differing I_{crit} and I_{pass} . The alloy represented by A is an easily passivated FeCr alloy, while the low Cr alloy represented by curve B has higher critical and passive currents and is therefore a low Cr alloy that is much more difficult to passivate. This behaviour is typical of the FeCr alloys, and is responsible for the increase in corrosion resistance of high Cr alloys. The equilibrium corrosion conditions of these two alloys will depend upon the form of the cathodic polarisation curve. When the cathodic curve suffers little polarisation such as the curve labelled C then both anodic curves are intersected in the passive region. Since equilibrium occurs when the cathodic current equals the anodic current,

Figure(1.8). The effect of I_{pass} , I_{crit} and cathodic cell polarisation upon the corrosion behaviour of iron-chromium alloys.



both alloys are seen to be passive. However, it is clear that the low Cr alloy, B, suffers a much larger corrosion current and so can be expected to exhibit a much shorter working life. The second cathodic curve D is much more heavily polarised; while the Cr rich alloy A is passivated, the second low Cr alloy is now seen to have been brought into a region of active dissolution where it can be expected to undergo severe corrosion.

This diagram now provides the key for understanding the corrosion resistance of the stainless steels. Because of the nature of the passive film formed on them, the critical and passive currents are low. It is therefore possible for even the heavily polarised cathodic curve to provide sufficient current to render the alloy passive, while such a cathodic curve applied to an alloy associated with much larger critical and passive currents will be put into the active state and suffer a great deal of corrosion.

In a heavily corroding system indicated by the intersection of curves B and D, it is possible to improve matters by introducing an anodic inhibitor such as potassium chromate. That will have the effect of reducing the passive current to such a level that the cathodic curve and the new anodic curve intersect in the passive region. The mechanism for this reduction in corrosion is believed to be based upon the passive film being modified by the anodic inhibitor and so reducing the passive current. Alternatively, the cathodic curves may be modified to ensure that they intersect the anodic curves in the passive region. A cathodic depolariser often used for this purpose is sodium nitrite. When modifying the polarisation curves in this way one must always exercise caution because it is possible to engineer a situation where the corrosion can become localised and very intense, especially when insufficient cathodic depolariser has been employed.

We have now seen how the process of passivation occurs and how the presence of chromium in the alloy makes passivation possible even under small cathodic currents. However, the following questions remain unanswered:

- 1) why does the chromium reduce the passive current?
- 2) why once formed does the passive film on iron-chromium alloys resist the attack of chloride ions better than passive films formed on iron?

These questions can only be addressed when more is known about the nature of the passive film. We have now arrived at the situation, where we know how the mechanism of passivation takes place, and the conditions under which it may possibly occur. What we still do not know is why the presence of chromium in the alloy should reduce both I_{crit} and I_{pass} . In particular the cause of the sudden rise in corrosion resistance seen when the alloy composition exceeds 12% atomic chromium has still not been explained. Nor has the resistance towards chloride induced breakdown of the passive film been understood. To try and understand these observations it is necessary to understand the transport processes that prevail in the passive films. This can only be done when we have a detailed physical picture of the passive film; for this reason previous studies of the passive film structure will now be reviewed.

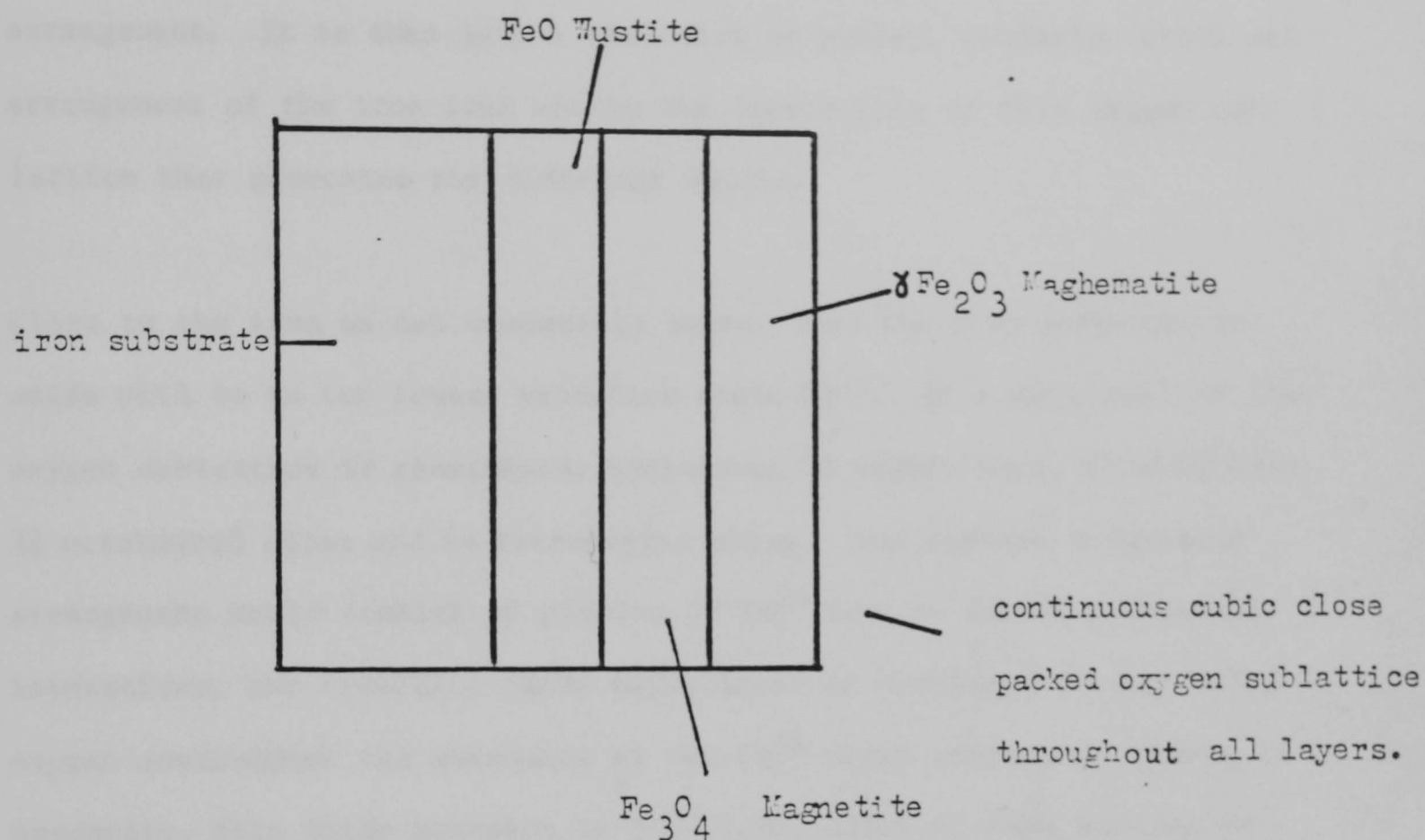
1.9 Review of the Passive Film on Fe-Cr Alloys

Before we review the previous studies that have been undertaken on the passive films formed on iron-chromium alloys, the apparently much simpler case of pure iron will be discussed. This approach may be justified because the effect upon corrosion resistance of the chromium is thought to occur by the chromium modifying in some way, the passive film that is formed on iron. Before this however the structure of some of the common iron oxides, formed by dry oxidation, will be described. This is relevant because as we shall see many of the structures put forward as candidates for the passive film are best described as thin layers of these well known 'bulk' oxides. We should note that any passive oxide can be expected to be much more complex, both chemically and structurally, than these simple stoichiometric oxides.

1.9.1 The Oxides of Iron

In describing the oxides of iron it is perhaps best to look at an idealised picture representing the oxides found on iron after its exposure to dry air at elevated temperatures. The expected oxide layer structure is shown in Fig. (1.9). There are two things that should be noted from this; the variable valency of iron leading to a great many oxides, and that while we have written the oxide formulae as stoichiometric, all of the oxides of iron are non-stoichiometric. This has great implications for the electronic and ionic conduction of the oxides, for in order to maintain electrical neutrality, defects must present themselves within the oxide and so aid any transport processes.

Figure(1.9). An idealised picture of the oxide structure found on air-oxidised iron.



Returning to the structure of the oxides, Fig. (1.9), shows that there is an increase in the oxidation state of the iron as the oxide-gas interface is approached. However, throughout this apparently quite complex range of structures one thing remains constant: the oxygen ion sub-lattice. For all three of these oxides it remains the same cubic close packed arrangement. It is then just a variation of number, oxidation state and arrangement of the iron ions within the interstices of this oxygen sub-lattice that generates the different oxides.

Close to the iron we can reasonably expect that the iron contained in oxide will be in its lowest oxidation state Fe^{2+} . If a unit cell of the oxygen sublattice is considered, containing 32 oxygen ions, it will have 32 octahedral sites and 64 tetrahedral sites. One obvious structural arrangement would consist of placing 32 Fe^{2+} ions in the 32 octahedral interstices, the resultant oxide being known as Wustite. Closer to the oxygen environment the abundance of the Fe^{3+} state increases. Known as Magnetite, this oxide contains 16 Fe^{3+} ions, eight of them sitting in octahedral sites, the remaining eight Fe^{3+} and sixteen Fe^{2+} sitting in the octahedral sites: the traditional inverse spinel structure. If the replacement of Fe^{2+} by Fe^{3+} is continued until no more Fe^{2+} remains, and the iron ions distributed over octahedral and tetrahedral sites, Maghematite results, with the inverse spinel structure.

Generally, the oxide Maghematite can be prepared by the careful oxidation of Magnetite; however, at 1300°C Magnetite will slowly transform into Hematite. While sharing the same chemical formula as Maghematite, Hematite is best considered as an hexagonal close packed array of oxygen

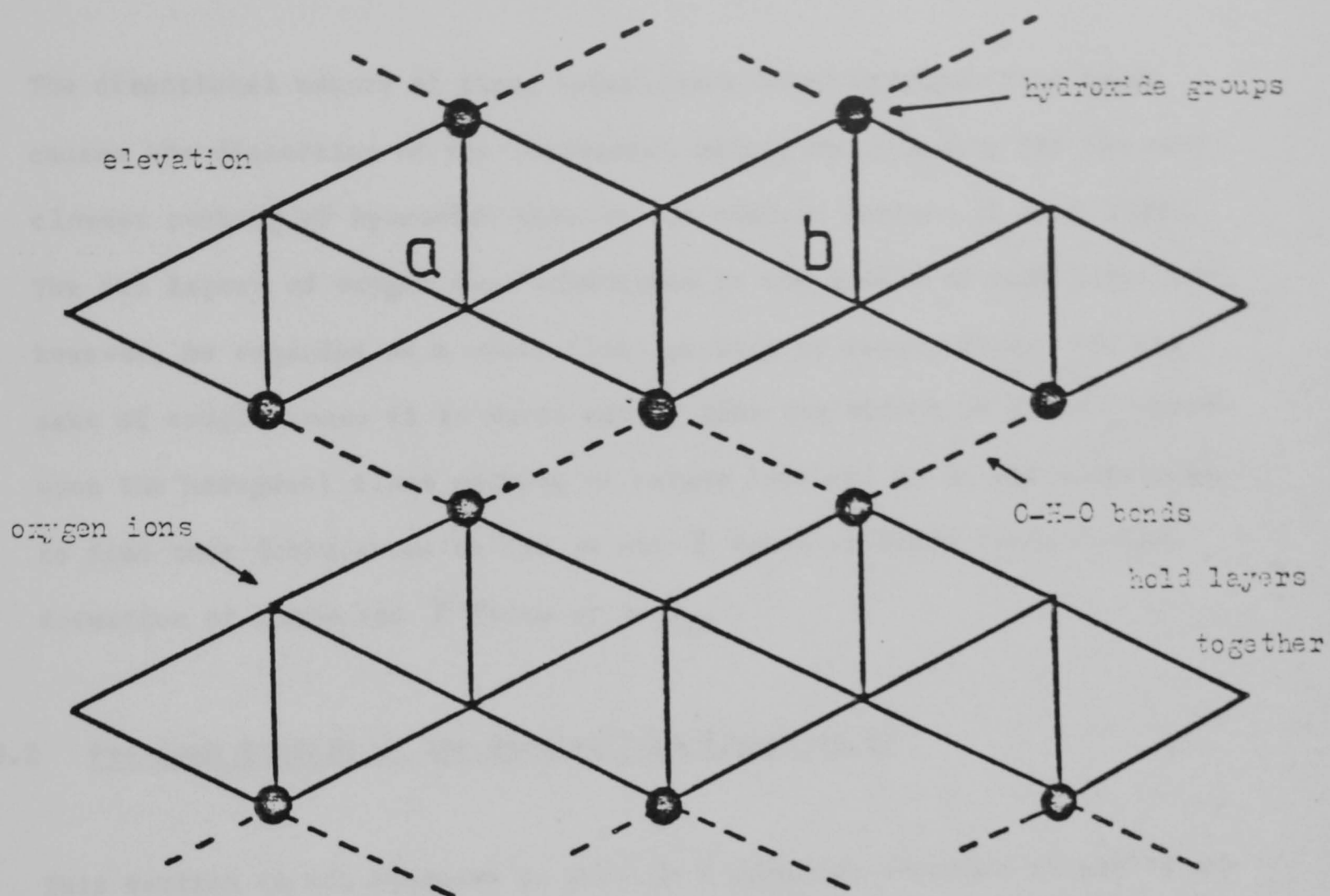
ions, with Fe^{3+} sitting in the octahedral sites: the Corundum structure.

The presence of the common oxygen sub-lattice in Wustite, Magnetite and Maghematite, allows the formation of solid solutions of all three oxides. Many of the reports of the passive film speak of mixtures of these oxides.

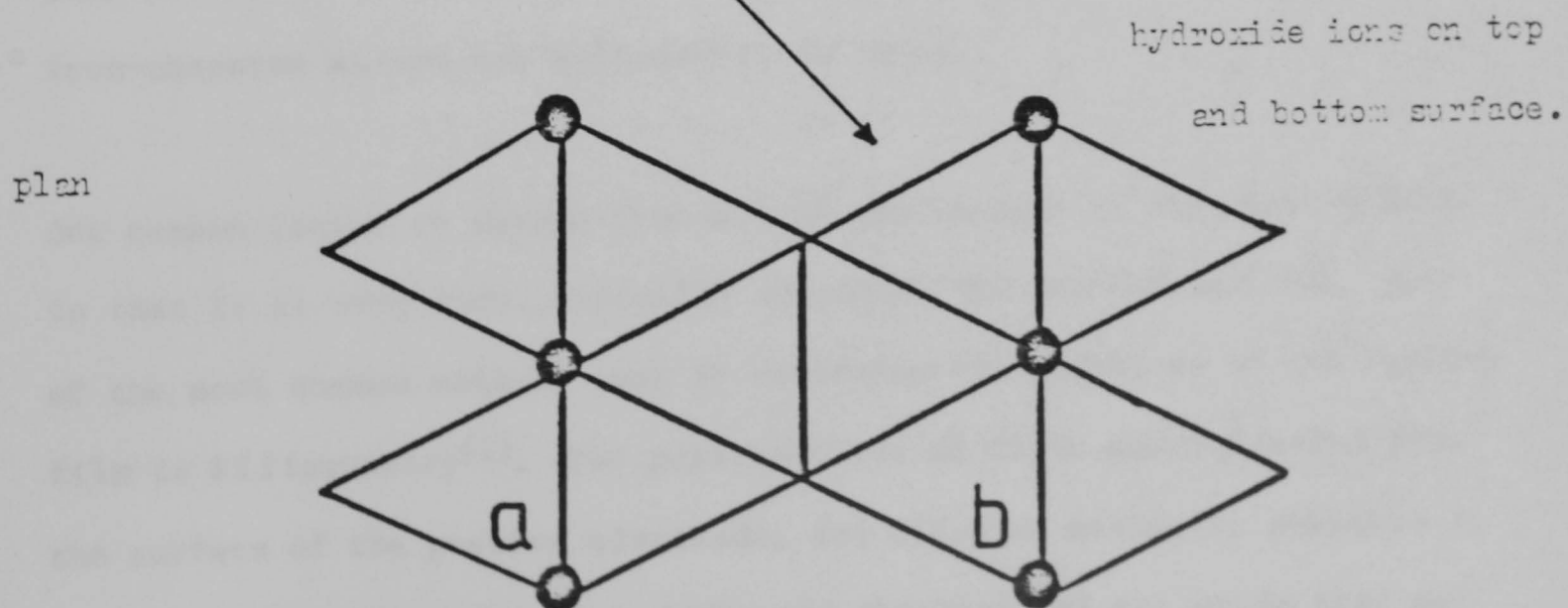
It has been previously been mentioned that the electronic transport properties of the passive film are important in determining the ability of the oxide to act as an effective passivator. The presence of two oxidation states in Magnetite is very important in this respect. Two ions in different oxidation states can exchange states and a conduction process akin to the 'hole' transport mechanism seen in 'p' type semiconductors can occur. This is responsible for the electrical conduction of Magnetite being some six orders of magnitude greater than either of the other two oxides containing ions of one oxidation state only. Clearly this changed conduction will have a deteriorative effect upon the passivation properties of a Magnetite film.

Finally we should review the structure of γ iron oxy hydroxide FeOOH . This is a complex layer structure which, unlike the previous oxides that have been described, is not based upon the close packing of oxygen ions. Each layer is best considered to be made up of distorted octahedral units. At the centre of each octahedral unit is an Fe^{3+} , which is surrounded by four oxygen ions and two hydroxide groups, located on the lower edge of the octahedron. Each of the layers referred to above is then constructed by the stacking of these octagonal cells as shown in Fig. (1.10)

Figure (1.10). Plan and elevation of the layered structure of γ -FeOOH
lepidocrocite.



iron ions at the centre of each octahedra



in such a way that the top and bottom layers are made up of the hydroxide ions which are then able to bond to the top surfaces of other similar layers and so build up the complete structures.

The directional nature of these interlayers O-H-O hydrogen-like bonds causes the distortion of the octahedral units, and accounts for the non-closest packing of hydroxide ions on the bonding surface of each layer. The two layers of oxygen ions sandwiched in the middle of each layer can, however, be regarded as a cubic close packing of oxygen ions. For the sake of completeness it is worth noting that the α form of FeOOH is based upon the hexagonal close packing of oxygen ions and it is not surprising to find that dehydration on the α and γ forms of FeOOH leads to the formation of the α and γ forms of Fe₂O₃.

1.9.2 Previous Studies of the Passive Film Formed on Fe

This section is not intended to provide a complete overview of all of the previous studies that have been undertaken upon the passive film formed on iron, but to provide a basic appreciation of the pertinent features. This is the basic film upon which the more protective films found on the iron-chromium alloys are believed to be based.

One common factor to emerge from all of the studies of the passive film is that it is very thin, typically somewhere between 10Å and 50Å. One of the most common methods used to determine the thickness of the passive film is Ellipsometry⁽¹⁾. Two polarisations of light are reflected from the surface of the passive electrode, and compared making it possible to determine both the refractive index and thickness of any oxide that may

be present upon the alloys surface. Using this method Kruger⁽²⁾ studied the film formed on iron, in air-saturated sodium nitrite solution, and found that the thickness of the film ranged between 15Å and 40Å, depending upon the exact conditions used. Similar results have been obtained by Sata and Kudo⁽³⁾, who applied the same technique to iron passivated in neutral borate solution. This latter study was able to use the measured value of refractive index of the passive film to infer Maghematite or Magnetite as possible candidates for the passive film.

The thin nature of the passive film, together with the fact that oxygen is readily evolved from the passive surface when the sample is polarised into the transpassive region, has been taken to indicate that the film must be a good electron conductor. Ion conductors such as γ -Al₂O₃, do not evolve oxygen under anodic polarisation; instead the oxide film thickens by the outward migration of aluminium cations brought about by the applied electric field. Thus the limited thickness and easy passage of electrons through the film confirm its nature as that of an electron conductor.

Other more direct methods have been used to study the composition and thickness of the films found on iron following its passivation. These are the ESCA (Electron Spectroscopy for Chemical Analysis)⁽⁴⁾ surface sensitive methods. Generally the surface under investigation is excited in some way, X-rays in the case of XPS (X-ray Photo-electron Spectroscopy) and a beam of electrons in the case of AES (Auger Electron Spectroscopy). As the surface atoms relax, following their excitation, they emit photo-electrons and Auger electrons of characteristic energy. Analysis of the emitted electron spectrum then allows the composition of the surface layer to be determined. The surface sensitivity arises

because of the small mean free path of the emitted electrons in the bulk material, which causes the spectrum to be dominated by the emissions from the surface layers. Using the Auger technique Seo⁽⁵⁾ and his co-workers were able to confirm the results presented above, concluding the film to have a composition compatible with $\text{Fe}_2\text{O}_3/\text{Fe}_3\text{O}_4$ type.

Evidence to support the presence of Fe_2O_3 or Fe_3O_4 in the passive film had earlier been provided by Foley, Kruger and Bechtoldt⁽⁶⁾. This extensive work studied the structure of the passive film formed on iron in sulphuric acid, sodium hydroxide and basic borate solution, under active, passive and transpassive conditions, (see Fig. 1.6). With the film still in contact with the iron substrate, they used the sensitive transmission electron diffraction technique to determine the structure of the passive film. Using this technique they were able to distinguish between the two cubic oxides Fe_3O_4 and $\gamma\text{-Fe}_2\text{O}_3$ and concluded that the presence of $\gamma\text{-Fe}_2\text{O}_3$ could be correlated with the presence of the passive state. They also confirmed the coexistence of $\gamma\text{-Fe}_2\text{O}_3$ and Fe_3O_4 in some passive films.

The above observations are in agreement with the recent review of the subject given by Cohen⁽⁷⁾. In his review Cohen provides six possible structures for the passive film on iron. They are all based upon layers of the cubic oxides Fe_3O_4 and $\gamma\text{-Fe}_2\text{O}_3$. Cohen's⁽⁸⁾ own work concerning the two-stage cathodic reduction of the passive film lends extra support to this duplex structure, which had previously been seen elsewhere by Cohen⁽⁹⁾ and proposed by Vetter⁽¹⁰⁾.

To summarise so far the passive film on iron would appear to be of the order of 50\AA thick, and be composed of a layered structure of cubic oxides $\gamma\text{-Fe}_2\text{O}_3$ and Fe_3O_4 , with the Fe_3O_4 next to the iron. The association of the $\gamma\text{-Fe}_2\text{O}_3$ with the passive film is reasonable when we contemplate its expected higher electrical resistance compared to that of consequent improvement of isolation of iron from the environment. Additionally the view that the passive film must be a good electrical conductor, because of the large currents which are seen to pass easily through the film in the transpassive region, need no longer apply. Following Foley's work⁽¹¹⁾, it is now known that the high resistance Fe_2O_3 is not present in the transpassive region and so the large currents passed in the transpassive region have no implications for the conductivity of the passive film. Other workers have detected species such as hydrogen and water in the passive film. An interesting observation in the paper by Foley⁽¹¹⁾ is that the structure of the $\gamma\text{-Fe}_2\text{O}_3$ seen in the passive films may be better described as a lithium spinel LiFe_5O_8 (only in this case the lithium ion would be replaced by a hydrogen ion). This structure can be expected to generate extra reflections in the diffraction pattern, such as those reported in the work by Foley et al. Many workers including Hoar⁽¹²⁾ and Evans⁽¹³⁾ have produced evidence that when iron is passivated in chromate solution, chromium becomes incorporated into the passive film, which is in agreement with the view that chromate inhibitors work by modifying the structure of the passive film.

In conclusion, the evidence so far indicates that the passive film formed on iron is thin, may well be based upon the cubic $\gamma\text{-Fe}_2\text{O}_3$, but includes extra water and even atomic hydrogen. Chromium may be expected to occur when it is present in the electrolyte. Thus the passive film on iron

would appear to have a far from simple structure.

One major criticism of the works that have been reviewed is that all of the techniques used, except Ellipsometry, require that the passive film must be isolated and placed in the drying environment of a vacuum before it is studied. The question of the integrity of this dehydrated film arises. A technique is needed which does not require the sample to be removed from the passivating electrolyte solution: one recently applied to the passive film formed on iron in borate solution is Mossbauer spectroscopy⁽¹⁴⁾.

The interpretation of a Mossbauer spectrum is quite complex; however, the basic principle is as follows. During radioactive decay a nucleus can emit γ -rays of characteristic energy. These γ -rays can be expected to excite other similar nuclides by the inverse process of emission. During the emission, the nucleus will suffer some recoil due to the requirement that momentum should be conserved. Because of the Doppler shift, this recoil leads to a small change in the energy of the γ -ray.

The absorption spectrum of the nucleus will be modified by the its environment. For example, the structure may impose restrictions upon the allowed recoil of the absorber, while any magnetic field within the sample may modify the spectrum. Thus, by varying the velocity of the emitting radioactive source, the energy of the emitted γ -ray can be tuned, and as long as the absorbing nucleus contains similar nuclides, the characteristic absorption spectra of different compounds can be obtained.

Using this technique, O'Grady⁽¹⁵⁾ studied the passive film formed on electrodeposited iron 57, a suitable radioactive isotope of iron. Because of the long mean free path of the rays in water it was not necessary to remove the sample from the passivating solution, thus O'Grady was able to study the films both in situ, i.e. wet and ex situ, i.e. dry. He found that when the films had been dehydrated they displayed an absorption spectrum that was typical of $\gamma\text{Fe}_2\text{O}_3$. When the films were wet, he was unable to correlate directly the observed spectrum with that obtained from any of the known oxides or hydroxides.

He concluded that the passive film must have a structure that was easily dehydrated and that a possible structure might be composed of amorphous chains of iron (III) oxides bonded together by water molecules. The basic building block of the structure proposed contained four iron ions octahedrally co-ordinated to oxygen containing species such as water and hydroxide groups. Each of these units was then connected to other similar units by water molecules, to form the passive film. Dehydration would then involve the removal of these bridging waters, and the re-ordering of the basic units could provide a Face Centred Close packing of oxygen ions, which is the basis of the iron oxides previously described.

1.9.3 Electron Configuration and Oxygen Adsorption

While, as was stated earlier the present understanding of the passivating process is that it was based upon the properties of a three dimensional oxide present upon the alloys surface, there have been other models proposed. These are the adsorbed film model and the electron configuration theory of Uhlig⁽¹⁷⁾. While these ideas are no longer taken to represent the mechanism of passivation, they may be relevant to the early stages of 'bulk' passive film formation, and so they will be described here and put into context with the current view of passivity. In order to explain the sudden increase in corrosion resistance of the alloys at critical compositions, Uhlig proposed his electron configuration theory.

The electronic structure of the transition metals is such that they have incomplete 'd' shells. Uhlig associated the presence of these vacant electron states with the passivity of the transition metals since unfilled 'd' states were thought to enhance the chemisorption of oxygen, which perhaps blocked defect sites likely to be preferentially corroded and prevented the hydration of the iron ions but did not lead to the formation of a true 3-dimensional oxide film. Because the chromium incorporated into an iron-chromium alloy could share electrons with the iron, it could promote the number of 'd' shell vacancies in the iron and so increase the passivity of the alloy. However when the iron/chromium ratio became too great, the chromium could absorb no more electrons and so with fewer spare states in the iron 'd' band, the chemisorption of oxygen fell and with it the passivity of the alloy.

The theory satisfied the critical composition of several alloy systems including iron-chromium, where it predicted a critical composition of 16% atomic chromium. It was less successful with other alloy systems, and the XPS work of Asami⁽¹⁶⁾, who studied the photo-electron emission spectrum of a range of iron-chromium alloys, found that the electronic structure of the alloys changed very little about the critical composition. He therefore concluded that the electron configuration theory could not account for the change in corrosion-behaviour of the iron-chromium system. His work shows that the binding energy of the Fe2P2/3 electron of iron contained in the passive film changes dramatically at an alloy composition of 12% atomic chromium, lending support to the view that it is a change in the passive film that enhances the corrosion resistance and not a change in the alloy.

There has been from time to time some uncertainty about the nature of the passive film found on the chromium rich alloys. Was it an adsorbed layer of oxygen, or was a true 3-dimensional oxide required for passivity? In interpreting their electrochemical data, King and Uhlig⁽¹⁷⁾ concluded that the film was an adsorbed monolayer of oxygen as described above. Aronowitz and Hackerman⁽¹⁸⁾ believed that the film was composed of an adsorbed layer of oxygen through which cations migrated to form a 3-dimensional oxide. The picture has now been clarified by the work of Frankenthal⁽¹⁹⁾.

Frankenthal studied the passivation of an Fe24Cr alloy in sulphuric acid in great detail. He found that there are in fact two types of passive film: a so-called primary film that forms within a few mV of the passivation potential and a secondary film, responsible for lasting passivation, that forms at higher potentials.

The primary film contained less than one oxygen atom per surface atom and was easily removed by cathodic reduction. The secondary film was a true 3-dimensional film, that increased in thickness with potential and time. It was this secondary film that was taken to be responsible for lasting passivation due to its resistance to cathodic reduction.

This result is in agreement with the conclusion reached by Aronowitz and Hackerman⁽¹⁸⁾ who included an adsorbed layer of oxygen in their description of the passive film formation. The picture of passivation presented above may be summarised as follows.

An initial film forms that is composed of adsorbed oxygen atoms, the adsorption of which may well be influenced by the surface crystallography and even the electronic state of the surface. Once passivity has been established by this film it can become thicker. This results in a final film some 20\AA thick, depending upon prevailing conditions. It is this film that is responsible for the corrosion resistance of the alloy, and it is the subject of this work. What follows is a review of the structure and composition of it as previously reported.

1.9.4 The Passive Film formed on Iron Chromium Alloys

We have previously seen that the corrosion resistance of the iron-chromium alloys increases dramatically when the chromium content of the alloy exceeds some 12% atomic chromium. We have also seen that it is the nature of the passive film which determines the corrosion resistance of the alloy. It is not surprising, therefore, to discover that the structure, nature and composition of the passive films can be seen

to change as the chromium content of the alloy exceeds 12% atomic chromium.

In common with the passive films on iron, the passive films on iron-chromium alloys are thin, typically less than 50Å. Additionally, the films become thinner as the chromium content of the alloy increases. Work by Ambrose and Kruger reported in the paper by Revesz and Kruger⁽²⁰⁾ demonstrates this reduction in film thickness very clearly. The maximum film thickness of 26Å has been formed on pure iron while the minimum film thickness of 18Å was formed on the alloy containing 25% atomic chromium.

The chemical composition of the film is seen to undergo a major change at the critical alloy composition. For low chromium alloys there is very little chromium contained in the film. The electron spectroscopic study of Tjong et al⁽²¹⁾, showed, that for an alloy containing 3% atomic chromium, negligible amounts of chromium were incorporated into the film. Alloys containing between 9-18% atomic chromium displayed an enrichment of chromium in the film above that found in the bulk of the alloy. This work was carried out in borate buffer solution; however, similar results were obtained by Halliday and Frankenthal⁽²²⁾, who characterised the passive film on a range of iron chromium alloys containing up to 24% atomic chromium, passivated in sulphuric acid.

The study by Tjong indicated that the increase in chromium content of the passive film was accompanied by a rise in the amount of bound water in the passive film. This was based on careful study of the oxygen photo-electron spectrum, which indicated the presence of O-H type bonds. As we shall see later the presence of chromium in the film is thought

to enhance the amount of water contained in the film, and so the correlation of the chromium content and water content is expected. Similar results have been presented by Asami⁽¹⁶⁾, who has employed the XPS technique to study the passivation of a range of iron-chromium alloys in sulphuric acid. The latter paper concludes that the corrosion resistance of the high chromium content Fe-Cr alloys is attributed to the protective nature of hydrated chromium oxy-hydroxide, which was seen to be the main constituent for alloys containing over 12% atomic chromium.

An earlier paper by Asami⁽²³⁾ demonstrated that the increase in the amount of Cr^{3+} in the film correlated with a decrease in the amount of Fe^{3+} in the film. The Cr^{3+} prevented the oxidation of Fe^{2+} , because of its greater tendency to oxidise. This would have a beneficial effect on passivation because the mechanism of auto-reduction of the passive film implied by equation (1.7) would not be able to take place in the absence of Fe^{3+} .

The recent Auger work by Mitrovic-Scepanovic⁽²⁴⁾ confirms the enrichment of chromium in the alloy but disagrees about the type of film present. The Mitrovic-Scepanovic work concluded that the film is based upon mixed cubic oxides, of the form $(\text{FeCr})_2\text{O}_3$ or FeCr_2O_4 and an outer layer of $(\text{FeCr})_2\text{O}_3$, depending upon the potential at which the passivation took place, the single layer being favoured by lower potentials. The difference between the results of these two studies is surprising since the only major difference between the two works was that Asami had used an alloy containing just 2% less chromium (at 24% chromium). This level of total chromium content would not be expected to cause any major changes to the passive film's corrosion behaviour.

In the electrochemical study by Heumann⁽²⁵⁾ in which the electrochemical behaviour of CrOOH and Cr_2O_3 was compared with the behaviour of the passive film on a 27% atomic chromium alloy, it was concluded that the passive film contained CrOOH . Thus the ESCA techniques and the electrochemical studies appear to agree that chromium enrichment of the passive film takes place on alloys containing over 12% atomic chromium. The XPS studies show that there are O-H type bonds present in the passive film which may be taken to indicate the water or hydroxide ions are incorporated into the passive film on iron-chromium alloys containing over 12% atomic chromium.

The picture presented so far indicates that the passive films formed on iron-chromium alloys with less than 12% atomic chromium are essentially like those found on iron, except that some Fe^{3+} ions have been replaced by Cr^{3+} ions. Alloys containing over 12% atomic chromium would appear to form cubic oxides similar to those on iron except that they are rich in chromium. As with iron, there is evidence once more to suggest that the films may be hydrated, as they almost certainly contain O-H type bonds. Another similarity with the iron films is that the literature mentions the possible presence of CrOOH . Apart from chromium enrichment, the only other real difference appears to be more evidence to support the view that water is contained in the passive film on FeCr alloy and that many of the structures may be hydrated.

So far all the results presented have been based upon composition information gained from spectroscopic methods. Much greater differences between the films formed on iron and those formed on chromium rich iron-chromium alloy are seen when the structure of the film is studied with the aid of transmission electron diffraction. Such a study has been made

upon a range of alloys containing up to 24% atomic chromium by McBee and Kruger⁽²⁶⁾. As we would expect, the films found on iron in this study were identical to those reported earlier by Foley, Kruger and Bechtoldt: the passive films associated with $\gamma\text{Fe}_2\text{O}_3$.

Similar results were obtained for an alloy containing 5% atomic Cr. For alloys containing over 5% atomic chromium extra reflections that identified the film as $\gamma\text{Fe}_2\text{O}_3$ were no longer present. This indicated that the passive film formed on alloys containing over 5% atomic chromium was in some way different from the film formed on low chromium alloys.

The films formed on the higher chromium alloys could be identified with a spinel structure. This is somewhat confusing because in earlier work on iron it had been the inverse spinel type film that had been associated with the passive state; now it appears that the more protective film formed on the chromium containing alloy is based upon the Fe_3O_4 structure that had been previously associated with the active or transpassive state. They showed too that the lattice parameter of the spinel type passive film increased as the chromium content of the alloy increased. They were, however, unable to match the measured lattice parameter with any of the known iron or iron-chromium alloys, implying that the passive film could not be correlated with any of the known bulk oxides. They found additionally that as the chromium content of the alloy rose so the low index (less densely packed) planes of the alloy lost any epitaxial relationship with the passive film, until by the time the alloy contained 19% atomic chromium, there were only two planes displaying a diffraction pattern indicative of an orientated oxide.

Their results may be summarised as follows; on iron the passive film was a crystalline oxide, with a well defined epitaxial relationship with respect to the alloy substrate. As the chromium content of the alloy increased so the film became polycrystalline and began to lose its epitaxial relationship with the substrate. It was further seen that the number of planes displaying no oxide patterns increased until the alloy containing 24% atomic chromium displayed no oxide diffraction pattern at all.

Taking these results together, McBee and Kruger concluded that the passive films formed on Fe-Cr alloys were becoming amorphous as the chromium content increased. They therefore proposed that it was the amorphous nature of the passive film which led to the films formed on chromium rich alloys having a better corrosion resistance than the crystalline oxides formed on low chromium alloys.

A similar conclusion has been reached by Okamoto⁽²⁷⁾. In his paper on the structure of the passive film formed on an 18.80 Austenitic stainless steel, he concludes that the most important parameter controlling the corrosion resistance of the alloy is the amorphous nature of the passive film. In the same paper he also reports some direct evidence for the presence of water in the film. Based upon a radioactive tracer method, the amount of water contained in the passive film was seen to vary as a function of the passivating potential. From this Okamoto proposed that water played an important role in the passivation mechanism and film repair. Electron diffraction work was quoted which demonstrated that the passive film displayed no distinct diffraction pattern and was therefore amorphous in structure.

The conclusion must be that the passive film formed on corrosion resistant alloys is possibly amorphous, contains Fe and Cr, and is probably hydrated or at least contains O-H type bonds. The only structure-study of the films however assumed an amorphous layer because of the absence of a diffraction pattern. Diffraction is not an ideal tool with which to study thin non-crystalline oxide films. It has been the aim of this work to develop the new EXAFS technique to study the amorphous films found on the chromium rich alloys, and provide the much needed structural examination of the corrosion-resistant passive films.

Before describing the results of this EXAFS study, the phenomenon of EXAFS will be described.

1.10 Extended X-Ray Absorption Fine Structure

Traditionally, the structure of matter has been investigated from two distinct stand points. Spectroscopy has been used to study the electronic structure while diffraction techniques have been applied to the study of geometric structure. EXAFS, essentially a spectroscopic method, bridges this distinction by providing information about the local atomic environment of the X-ray absorbing atom, through a detailed examination of the form of the X-ray absorption spectrum.

The X-ray absorption spectrum of iron, in the vicinity of its 'K' edge, is shown in Fig. (1.11). Below the absorption edge, the X-rays interact with low energy core levels within the atom, this provides a smooth background absorption of X-rays. When the X-ray energy exceeds that of the ionisation energy of the 'K' shell level, a photo-electron can be generated thus causing the X-ray absorption to rise. In order to understand the presence of the oscillations seen in the absorption coefficient above the edge, it is necessary to study the photo-electron after its emission from the absorbing atom.

Following its generation the photo-electron will propagate out from the central absorbing atom, with a wavenumber given by equation (1.8)

$$k = \left(\frac{2me(\hbar\omega - E_0)}{\hbar} \right)^{1/2} \quad (1.8)$$

with ω the X-ray energy

E_0 the ionisation energy of the edge.

A fraction of this photo-electron wave will then be backscattered from the surrounding atoms, as shown in Fig. (1.11). This backscattering sets up a standing wave pattern with that part of the photo-electron still emerging from the absorbing atom. As we shall see later it is the overlap of this standing wave pattern and the original 'K' shell wave function that determines the probability of X-ray absorption.

This standing wave pattern will be determined by; the local atomic arrangement of the scattering atoms, their scattering factor and the wavelength of the photo-electron. It is these parameters which combine to form the Extended X-ray Absorption Fine Structure, the oscillations seen above the absorption edge. It is not unreasonable, to expect, given the details of the electron scattering process, that we should be able to determine the local atomic environment of the absorbing atom through a study of its X-ray absorption spectrum. Full details of both the experimental technique and the analysis of the EXAFS spectra are given later. However, before reviewing the EXAFS study of the passive films formed on iron we will briefly describe both.

We have seen that the passive films formed on iron-chromium alloys are of the order of 30\AA thick. This is far too small for the X-ray absorption spectrum to be measured by a simple transmission experiment. Following the absorption of an X-ray the absorption atom will be in an excited state. It can relax out of this state by emitting a fluorescence X-ray or an Auger electron. These two processes are shown schematically in Fig. (1.12). Thus it is possible to measure the absorption of X-rays by counting these emissions, known respectively as Fluorescence and Electron yield modes. These are the two methods that have been used to determine the X-ray absorption spectra of the passive film formed on iron. The fact that the fluorescence X-rays can pass easily

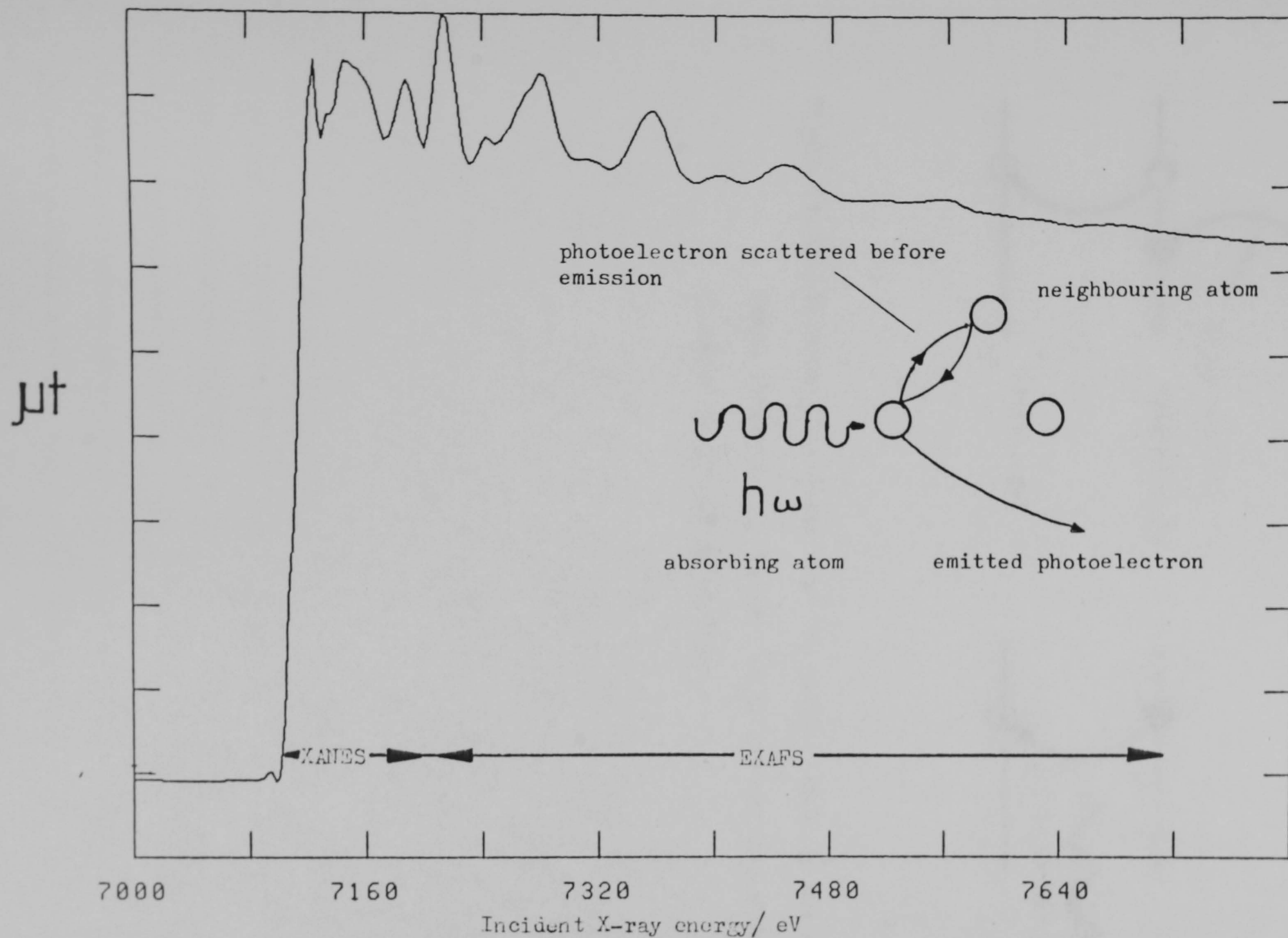


Figure (1.11). The X-ray absorption spectrum of iron about its 'K' edge and the mechanism of EXAFS generation.

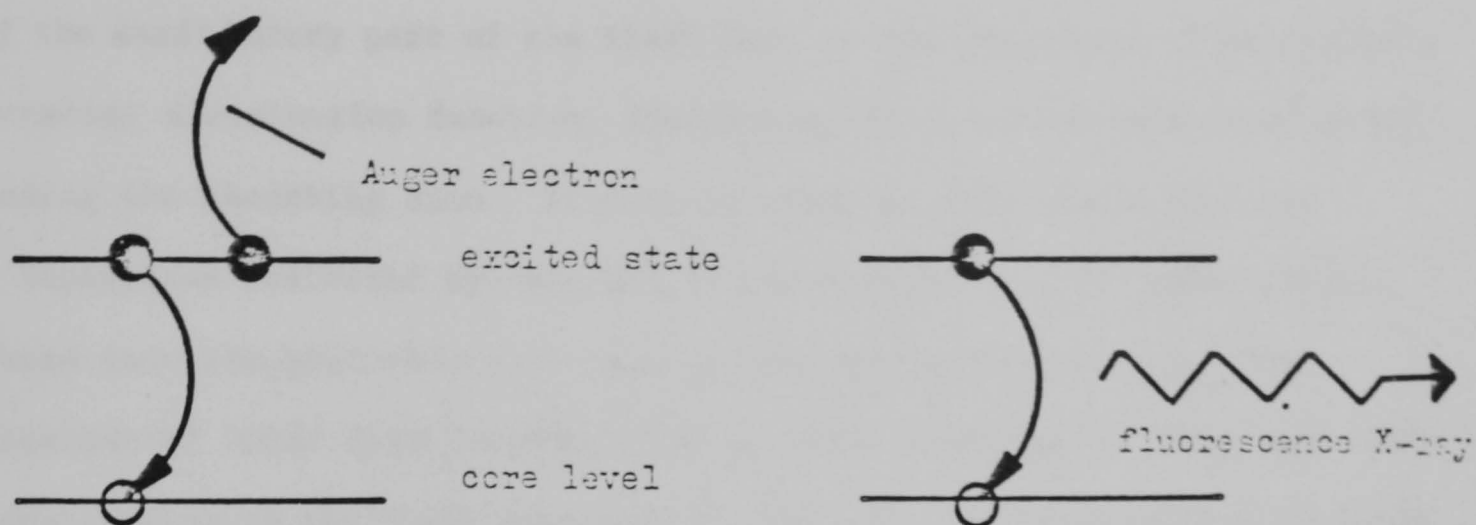


Figure (1.12). Following the decay from the excited state to the core level excess energy is removed by the emission of an Auger electron or fluorescence X-ray.

through typical aqueous passivating solutions makes possible the study of the passive film while it is still in the passivating solution.

A simple method of analysing the EXAFS data involves taking the Fourier transform of the oscillatory part of the EXAFS part of the spectrum. This yields a pseudo-radial distribution function, indicating the relative numbers of atoms surrounding the absorbing atom. It must be noted at this stage that the atomic separation indicated by this RDF is uncorrected for the phase shifts introduced into the photo-electron wave by the scattering process. The determination of 'true' bond lengths will be dealt with later. Thus with this basic description of the EXAFS phenomena we will now review the previous EXAFS studies of the passive film formed on iron.

1.10.1 Previous EXAFS Studies of Passive Films

The technique of EXAFS has already been applied to the study of surface oxides. Forty et al⁽²⁸⁾ has recently used the technique to study the structure of the anodic oxide on bulk aluminium. Using the total electron yield mode they were able to obtain an EXAFS spectrum that was largely unaffected by any contribution from the aluminium substrate, because the oxide was sufficiently thick to dominate the total yield spectrum.

One method which would ensure sufficient surface sensitivity involves measuring the absorption edge of the oxygen contained in the oxide film. This, however, is not possible in the case of iron-chromium alloys because of the close proximity of the iron and chromium 'L' edges to the oxygen 'K' edge. The close proximity of the edges causes interference and prevents a simple analysis of the spectrum.

To ensure sufficient surface sensitivity and observe the passive film formed on iron-chromium alloys, it is usual to work with 'ultra thin' alloy substrates less than 50\AA thick. Following passivation we can then expect that the film will be almost completely converted to passive oxide film, and so expect the EXAFS spectrum to be completely dominated by the passive film. A similar approach has been adopted in the Mossbauer work that has been mentioned earlier.

The lack of sufficient surface sensitivity to deal directly with the passive film on bulk alloys is aptly demonstrated by the work of Davoli et al⁽²⁹⁾. In their study they used the total electron yield method to monitor the 'natural oxide' on bulk iron. While they indicated Fe-O bond lengths consistent with the presence of Fe_3O_4 , they concluded that the sampling depth of the technique was some 200\AA , thus justifying the use of the thin alloy substrates described above for passive film studies.

There have been attempts to avoid the use of the thin substrates described. Bosio⁽³⁰⁾ used a REFLEXAFS technique, so-called because the X-ray beam was incident upon the surface of the passivated alloy at an angle less than the critical angle for total external reflection. Under this condition the X-ray beam penetrates less than 30\AA into the surface thus ensuring that it is only the oxide that contributes to the measured Fluorescence spectrum. While they reported data for several different passive films, it was clear from their results that this was a new technique, which required further refinement before it could be used to provide substantial improvements over the thin substrate method.

A most useful series of experiments has been performed by Long^(31,32,33) and her co-workers. In the first experiments they passivated thin films of iron in sodium nitrite and in potassium chromate solutions. Using a variant of the total electron yield method they were able to study the films in a helium filled detector chamber that did not subject them to the drying environment of a vacuum. The bond lengths determined in the study indicated that the passive films were spinel-like in structure. They determined that the film grown in the chromate solution incorporated some 12% atomic chromium. It displayed somewhat broader peaks in the radial distribution function than the nitrite passivated film, indicating that the structure was more disordered than in the film formed in nitrite solution. This incorporation of chromium has been reported by other workers and chromate is thought to inhibit corrosion by modifying the passive film in some way.

More recently the same authors have applied the Fluorescence mode to study the structure of the film while it is still in contact with the passivating solution. These in situ studies⁽³³⁾ have revealed significant structural differences between these in situ films and those just described. The main difference was seen to be a greater degree of disorder in the in situ i.e. wet films, than had been seen in the previous ex situ films. It was further seen that the disorder was greatest in the chromate passivated film. This was taken to indicate that the chromium contained in the passive film caused a disordering of the film structure, the apparent re-ordering of the film structure shown in the ex situ films was accounted for by assuming that water had been removed from the film. This water was then held to be responsible for introducing additional structural disorder.

Hoffman⁽³⁴⁾ has used the same basic technique as Long et al and reached similar conclusions. He emphasises that the substrate thickness must be carefully controlled if the interpretation of the spectra is to be unambiguous.

1.11 Summary

We have seen that the passive films formed on iron and iron-chromium are thin, typically ranging in thickness from between 20\AA and 50\AA , and that they may conveniently be divided into two groups. Those formed on alloys containing less than 12% atomic chromium, are based upon the passive films found on pure iron; that is, they are based upon the cubic oxides Fe_2O_3 and Fe_3O_4 , with some evidence to indicate that FeOOH may be present. The incorporation of water, in the form of O-H, and the incorporation of chromium into the passive film, have been observed. It appears that water can be removed from the film by the drying environment of a vacuum or dry gas atmosphere. This water can be associated with a degree of structural disorder in the film which is lost when the water is removed. Disorder can also be correlated with the presence of chromium in the film.

The films formed on chromium rich alloys tend to be rather thinner than those described above, having a limiting thickness of 19\AA . They display a marked enrichment of chromium in the passive film above that of the chromium content of the alloy. More evidence is available here to indicate that water is contained in the film. The disordering effect of the chromium is very clearly demonstrated by the formation of a completely amorphous film on a 24% atomic chromium alloy.

It was stated earlier in this work that it is important that the structure of the passive film should be understood, if progress is to be made in understanding the corrosion process. It appears that no direct structural investigation has been undertaken upon the passive film formed on the iron-chromium alloys. The electron diffraction work of McBee concluded from the absence of a diffraction pattern that the film was amorphous.

Thus the aim has been to take the EXAFS technique previously used by Long et al, in the study of the passive film formed on iron, to good effect, and apply it to the study of the passive films formed on a range of iron-chromium alloys containing up to 29% atomic chromium. These alloys have been passivated in sulphuric acid to determine the structure of the film inferred to be present upon the 24% chromium alloy of McBee's⁽²⁶⁾ work. The alloys have been passivated in chromate and nitrite to allow a comparison to be made with Long's work, thus allowing the effect of the increasing chromium content of the alloy upon the film structure to be observed directly. The effect of chromium in the solution has been determined by the use of these two electrolytes. The two modes of the EXAFS technique have been used, the electron yield mode requiring the sample to be exposed to the drying environment of a vacuum while the fluorescence measurement has been made with the sample in air. Thus the effect of dehydration upon the film structure can be determined.

1.12 Thesis Plan

The following chapter puts the EXAFS phenomenon on to a theoretical basis, and relates to the structure of the absorbing material. Chapters 3 and 4 describe in detail the experimental methods used to obtain the EXAFS from the passive films, and the methods used to extract structural information from the experimental dataset.

Chapter 5 contains the results of the EXAFS study of the passive films that have been formed on Fe-Cr alloys passivated in 0.1 M NaNO_2 , 0.05 M K_2CrO_4 and 1M H_2SO_4 . Chapter 6 discusses these results and offers some conclusions about the nature of the passive film and the suitability of the EXAFS technique as a probe of its structure. Finally some suggestions for the future work using this technique concludes Chapter 6.

2. EXAFS Theory

2.1 Introduction

In the previous chapter we have seen that the structure of the passive film formed on an alloy plays an important role in determining the corrosion resistance. The work of McBee and Kruger⁽²⁶⁾ showed clearly that there is a tendency for the films formed on iron-chromium alloys to become amorphous when the atomic fraction of chromium contained in the alloy approached 20%.

Their work served to indicate the problems that are associated with using diffraction techniques to study non-crystalline materials because the claim that the film had become amorphous on an alloy containing 25% atomic chromium, was based upon the absence of a diffraction pattern. The phenomena of EXAFS was then introduced as a technique that could deal equally with crystalline and amorphous materials. To understand this and the benefits that it offers over traditional diffraction methods, it is necessary to have a theoretical model for the EXAFS phenomenon. This theoretical basis will also be of use in the chapters dealing with the analysis and interpretation of the EXAFS spectra.

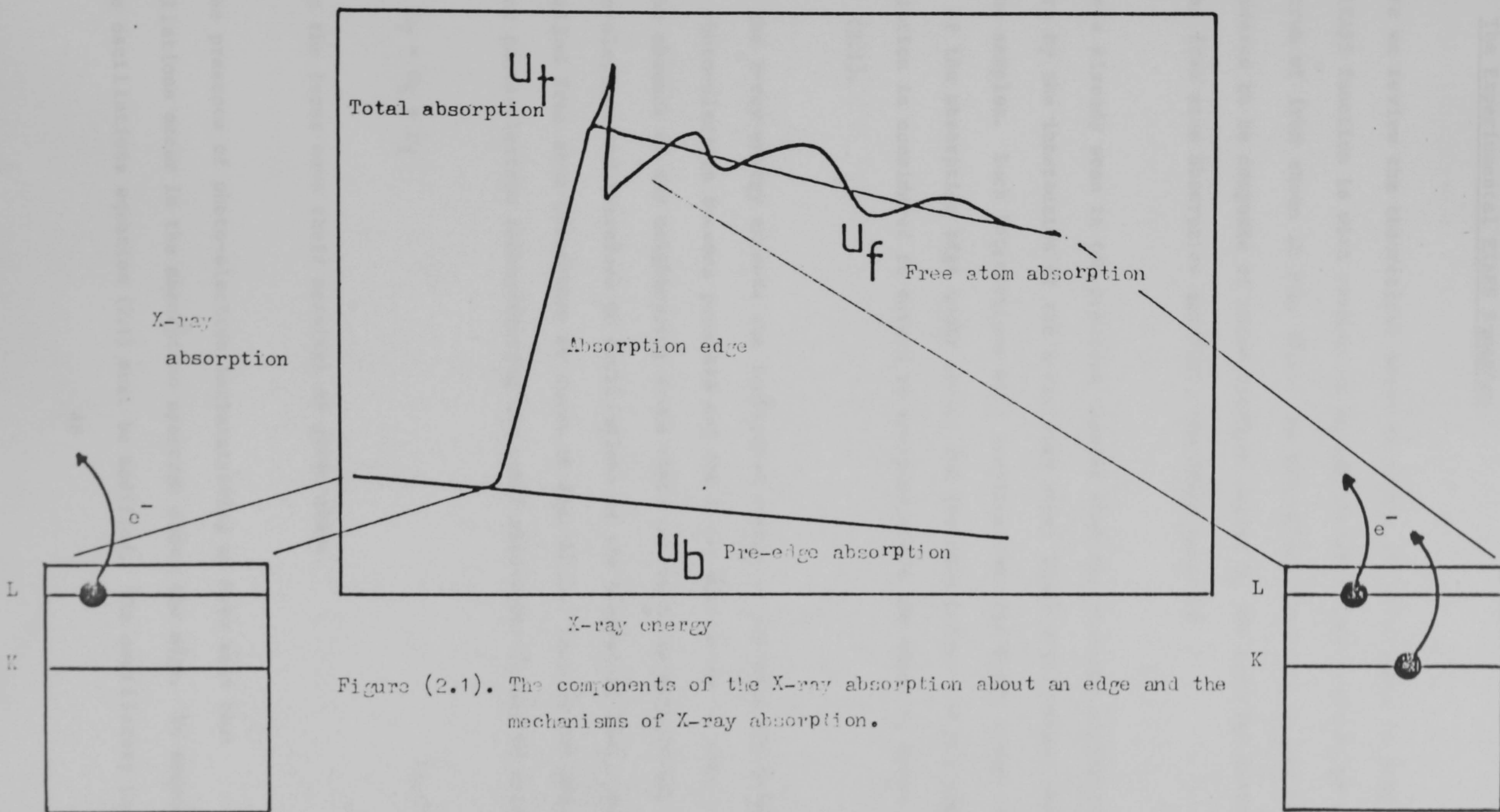


Figure (2.1). The components of the X-ray absorption about an edge and the mechanisms of X-ray absorption.

2.2 The Experimental EXAFS Function

Before we review the theoretical basis of EXAFS, it is intended to show what the EXAFS function is with respect to an experimental data set such as the spectrum of iron shown in Fig. (2.1). An absorption spectrum, U_T may be considered to be composed of three distinct parts; U_b the pre-edge absorption, U_f the free atom absorption and $X(E)$, the EXAFS function.

We have already seen in the previous chapter that the pre-edge absorption U_b occurs by the interaction of the X-ray with other lower energy edges contained in the samples. Such interactions will continue when the X-ray energy exceeds that of the absorption edge under study, and for this reason the pre-edge absorption is considered to extend to energies above the edge, as shown in Fig. (2.1).

When the X-ray energy exceeds the ionisation energy of the edge the generation of a photo-electron becomes possible and the X-ray absorption is seen to rise. In the absence of any neighbouring atoms there can be no backscattering of the photo-electron and therefore no oscillations in the absorption spectrum. This so-called free atom absorption is shown in Fig. (2.1). Thus in the absence of any photo-electron backscattering the total absorption U_T may be written as

$$U_T = U_b + U_f \quad (2.1)$$

where the terms have their meanings as given above.

In the presence of photo-electron backscattering we have seen that oscillations occur in the absorption spectrum above the edge. To account for these oscillations equation (2.1) must be modified. The oscillatory nature of

the absorption has now been incorporated by the term $1+X(E)$ with $X(E)$, the EXAFS function, given as a function of the photo-electron energy, E , which is given by equation (2.2).

$$E = \hbar\omega - E_0 \quad (2.2)$$

$\hbar\omega$ - the X-ray energy

E_0 - the energy corresponding to the ionisation energy of the edge under investigation.

Thus it is possible to write the total X-ray absorption in U_T as

$$U_T = U_b + U_e (1 + X(E)) \quad (2.3)$$

and so the EXAFS function maybe written as

$$X(E) = (U_T - U_b)/U_e - 1 \quad (2.4)$$

Equation (2.3) is therefore the analytic representation of the raw spectrum shown in Fig. (2.1a). The above has referred to the EXAFS oscillations as a function of the X-ray energy, it is more usual however to express them as a function of the photo-electron wavenumber, given by equation (2.5)

$$k = \left(2m/\hbar^2 (\hbar\omega - E_0) \right)^{1/2} \quad (2.5)$$

where $\hbar\omega$ is the X-ray energy and E_0 is the ionisation energy corresponding to the absorption edge.

It is this function $X(k)$ that contains information about the local atomic environment of the absorbing atom and it is this function that we will

describe theoretically in this chapter. The next chapter will deal with its extraction from the raw EXAFS data, and the extraction of bond lengths from it.

2.3 X-Ray Absorption

Usually an analysis of X-ray absorption is based upon the dipole approximation, to describe the interaction between the X-ray and the atom. Such a description gives the probability of X-ray absorption as

$$P = \frac{2\pi e^2}{m c^2 \omega} |M_{fi}|^2 \rho(E_f) \quad (2.6)$$

$\rho(E_f)$ is the density of available states at the final energy of the photo-electron which is given as

$$E_f = \hbar\omega - E_0 \quad (2.7)$$

with $\hbar\omega$ the energy of the incident X-ray and E_0 the corresponding energy to the absorption edge. The matrix element M_{fi} is given as:-

$$M_{fi} = \langle \psi_f | \underline{E} \cdot \underline{r} | \psi_i \rangle \quad (2.8)$$

ψ_i and ψ_f are the initial and final states respectively of the photo-electron and \underline{E} is the electric polarisation vector of the X-ray. It is clear from the above that the form of the X-ray absorption spectrum is determined by both $\rho(E_f)$ and M_{fi} . For reasons that will become apparent later, it is convenient to divide the post edge part of the spectrum shown in Fig. (2.1) into two parts, as shown in Fig. (2.2).

Features close to the edge in the so-called XANES (X-ray Absorption Near Edge Structure) part of the spectrum are largely determined by the form of $\rho(E_f)$, which is rapidly varying in this part of the spectrum. Additionally it should

be noted that the photo-electron because of its low kinetic energy in this part of the spectrum has a very long mean free path, consequently it suffers multiple scattering before escaping from the local atomic grouping, as shown in Fig. (2.2).

At higher energies, in the EXAFS part of the spectrum, the higher kinetic energy and lower mean free path of the photo-electron ensure that it undergoes only single scattering events before leaving the local atomic grouping. This is important, as we shall see the model used to describe the EXAFS part of the spectrum is based upon the photo-electron only undergoing a single scattering event, as shown in Fig. (2.2). We consider that any structure in the absorption spectrum is determined by M_{Fi} , because $\rho(E_f)$ may be approximated by a free electron density of states

$$E = E_0 + \hbar \frac{k^2}{2m_e} \quad (2.9)$$

which is essentially featureless.

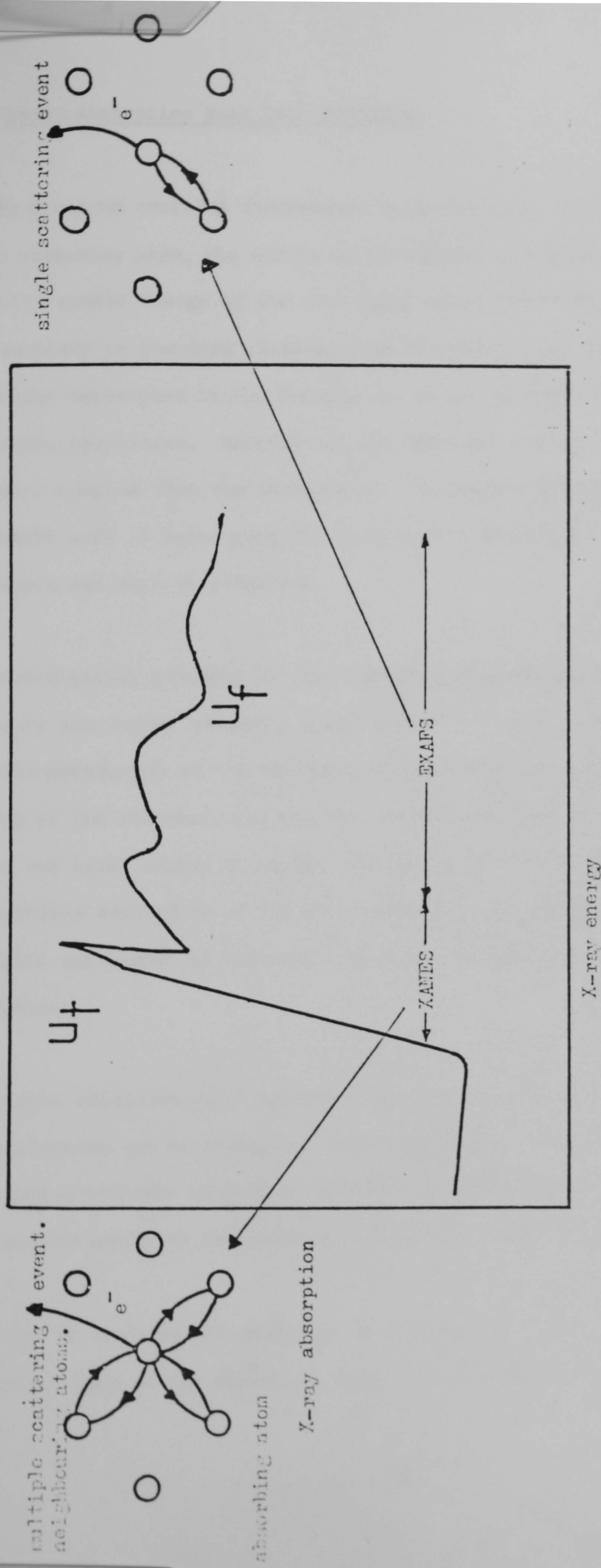


Figure (2.2). The photo-electron scattering mechanisms in the EXAFS and XANES regions of the absorption edge.

2.4 X-ray Absorption Near Edge Structure

A XANES spectrum contains information regarding the co-ordination geometry of the absorbing atom, the nature of unoccupied electronic states and the effective atomic charge of the absorbing atom. This information is complementary to the data obtained from the EXAFS spectrum, and is of particular importance in the description of any passive film structure and electronic properties. Analysis of the features seen in the XANES region is much more complex than the analysis of the EXAFS features. For this reason most XANES work is based upon the qualitative comparison of spectra obtained from known and unknown compounds.

The co-ordination geometry of the absorbing atom manifests itself in the XANES region by the number of sharp peaks present. These 'shape resonances' occur when the wavelength of the emitted photo-electron is less than the interatomic spacing of the absorber, and the photo-electron is of insufficient energy to escape the local atomic grouping. The local co-ordination geometry influences the multiple scattering of the photo-electron, so determining both the intensity and number of resonant conditions compatible with strong X-ray absorption.

The dipole selection rule restricts the type of final states into which the photo-electron can be injected. Thus comparison of the different edges contained within the absorbing material can yield useful information about the type and occupancy of the possibly electronic states available.

Finally, by studying the position of the edge it is possible to determine the oxidation state of the absorbing atom. It has been shown, however (33), that

the exact position of the edge is determined not just by the oxidation state, m , but by the co-ordination, n , of the absorbing atom and the degree of covalency, c , of the bonds that the absorbing atom has formed. It has been shown that the change in edge position ΔE may be given as:-

$$\Delta E \propto m - n c \quad (2.10)$$

Thus it can be seen that the data potentially available from the XANES region are very valuable, especially when they are taken in conjunction with the data available from an EXAFS study.

However the technique is very complex and requires that the features in the XANES spectrum must be positively identified before structural data can be extracted. It has therefore been felt that any XANES analysis should be left to a later study when the EXAFS results from this study may help in the identification of the features contained in the XANES spectra.

2.5 Extended X-ray Absorption Fine Structure

We have now seen what the EXAFS function is in terms of an experimental spectrum. We have also seen through the matrix element, M_{fi} , how X-ray absorption is related to the overlap of the initial and final state of the photo-electron wave function. We have further seen that this final state is no more than a standing wave pattern, generated by the outgoing and back-scattered photo-electron wave interfering as shown in Fig. (2.3). The standing wave pattern will be determined by the local atomic arrangement of the scattering atoms, their scattering factors and the wavelength of the photo-electron. It is the aim of this section to show the relationship between these three parameters and the EXAFS function and demonstrate how structural information can be extracted from the experimental data.

2.5.1 The Theoretical EXAFS Function

The first successful description of the EXAFS function was provided by Sayers et al⁽³⁵⁾ in 1971. This description has been fully developed more recently by both Ashley and Doniach⁽³⁶⁾ and Lee and Pendry⁽³⁷⁾.

Following these two works the EXAFS function for a polycrystalline or amorphous sample is given as equations 2.11, 2.12, and 2.13.

It follows from the above description in equation (2.8) that in single crystal samples the X-ray absorption depends upon the angle between the electric polarisation vector of the incident X-ray and the bonds contained in the sample. Since we shall see later, the radiation source usually used in EXAFS experiments provides radiation that is strongly

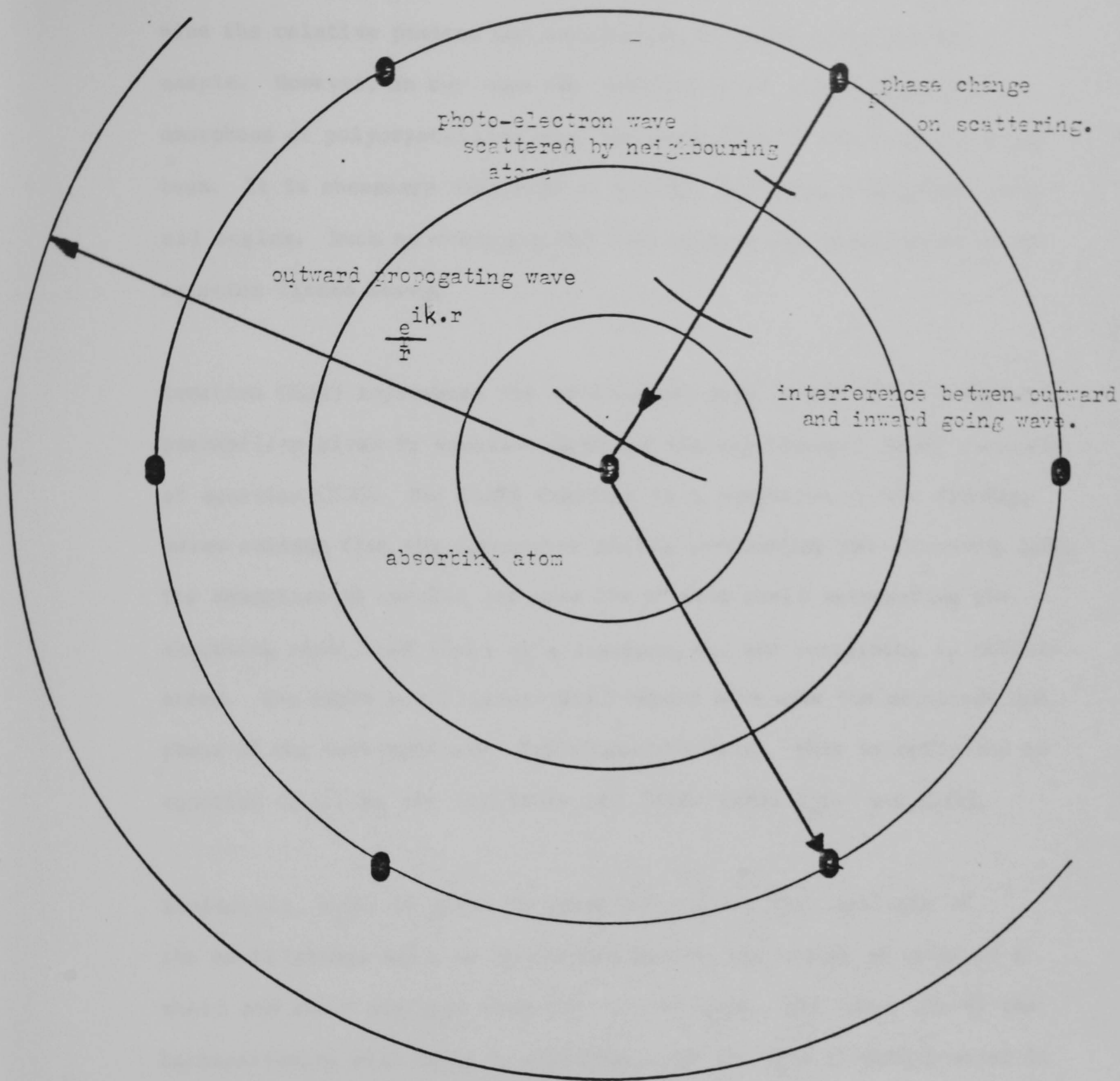


Figure (2.3). Schematic diagram of the interference between the outward going and back scattered photo-electron wave.

polarised in the plane of the source, this effect can be used to determine the relative position and orientation of atoms contained in a sample. However, in our case the samples to be investigated are amorphous or polycrystalline over the dimensions of the incident X-ray beam. It is necessary therefore to average the X-ray absorption over all angles. Such an averaging has been used in the formulation of the equation listed above.

Equation (2.11) represents the oscillatory part of the X-ray absorption probability given by equation (2.6) and the experimental EXAFS function of equation (2.4). The EXAFS function is a summation of the standing waves arising from the successive shells surrounding the absorbing atom. The summation is carried out over the i^{th} atom shell surrounding the absorbing atom, each shell at a distance, r_i , and containing N_i similar atoms. The EXAFS oscillations will depend both upon the magnitude and phase of the back-scattered photo-electron wave. This is reflected in equation (2.11) by the amplitude and phase terms $A_i(k)$ and $\phi_i(k)$.

Explicitly, $A_i(k)$ is given by equation (2.12). The amplitude of the oscillations will be determined by both the number of atoms in a shell and their distance from the central atom. The magnitude of the backscattering will also be dependent upon the type of atom present in the shell, this effect is accommodated by the scattering factor $F_i(k)$.

Finally, in the description of the amplitude function $A_i(k)$ there are two exponential damping terms. The first of these, a Debye-Waller factor, accounts for the reduction in EXAFS amplitude due to structural disorder contained in the sample, both thermal and static, such as we can expect to find in amorphous materials. The final exponential term containing

$$\chi(k) = \sum_i A_i(k) \sin(\phi_i(k)) \quad (2.11)$$

$$A_i(k) = \frac{N_i}{k r_i^2} |F_i(k)| e^{-2\sigma_i k} e^{-2\gamma r_i} \quad (2.12)$$

$$\phi_i(k) = 2kr_i + 2\delta_{\ell=1} + \text{Arg}(F_i(k)) \quad (2.13)$$

$$\psi(r, \theta) = e^{i k r \cos \theta} + \frac{F(k, \theta)}{r} e^{i k r} \quad (2.14)$$

$$e^{i k r \cos(\theta)} = \sum_{\ell=0}^{\infty} (2\ell+1) i^{\ell} J_{\ell}(kr) P_{\ell}(\cos(\theta)) \quad (2.15)$$

$$\psi(r, \theta) = \sum_{\ell=0}^{\infty} a_{\ell} R_{\ell}(kr) P_{\ell}(\cos(\theta)) \quad (2.16)$$

$$\frac{1}{r^2} \frac{d}{dr} \left(r^2 \frac{dR}{dr} \right) + \left\{ -\frac{\ell(\ell+1)}{r^2} + \frac{2m}{\hbar^2} (E - V(r)) \right\} R = 0 \quad (2.17)$$

reflects the finite coherence length of the photo-electron wave, and the possibility of incoherent elastic scattering which increases with the distance travelled by the photo-electron. In the original work of Sayers et al⁽³⁵⁾ this term was included as an empirical damping factor. However the more recent works have included this damping by adding an imaginary component to the photo-electron energy, E . In this case γ may be associated with $\xi / (2E)^{1/2}$. γ is often referred to as the inelastic mean free path of the photo-electron.

The phase of the final state of the photo-electron wave is given by equation (2.13). The term $2kr_i$ relates to the phase change in the photo-electron following its propagation to and from the surrounding shell, and an additional phase change when it is scattered from the atoms contained in the surrounding shell. This phase change is described by the argument of the scattering factor, a term not included in the original work of Sayers. The photo-electron also suffers a phase change of $\delta_{\ell=1}$ when it leaves and re-enters the absorbing atom.

Because the electron is initially in an $\ell = 0$ state, the photo-electron must necessarily be in an $\ell = 1$ state. As we shall see in the section dealing with electron scattering, it is possible to show that an electron in an ℓ state with angular momentum $\hbar\sqrt{\ell(\ell+1)}$ will suffer a phase change of δ_{ℓ} . These δ_{ℓ} define the scattering factor $F_1(k)$ and $\delta_{\ell=1}$ represents the phase shift that a photo-electron suffers as it both enters and leaves the central atom since the photo-electron must be in an $\ell = 1$ state. This explains the $2\delta_{\ell=1}$ term contained in equation (2.13). It is necessary to have information about these phase factors for all of the atoms contained in the sample.

The phase factors and scattering factors are of great importance in the description of the EXAFS function. For this reason the basics of electron scattering will be presented in the next section together with the scheme used to determine the phase factors for a wide range of atoms.

2.5.2 Electron Scattering

The description of the EXAFS function presented in the previous section assumes that the photo-electron wave can be treated as a plane wave during its interactions with both the central atom and the atoms contained in the surrounding shells. Under this approximation the scattering process may be viewed as shown in Fig. (2.4).

A plane wave of momentum k travelling in the z direction is incident upon an atom (a scattering potential) located at the origin. The scattered wave, represented by spherical waves, propagates out from the scattering atom. Such a state may be described by equation (2.14), which is written using spherical polar co-ordinates. The angular dependence of the phase and amplitude of this scattered wave is given by $F(k, \theta)$. Since the scattering potential is assumed to be spherically symmetric, the scattering factor $F(k, \theta)$ can have no ϕ dependence and so it must be a function of θ only.

All three terms contained in (2.14) must be solutions of the Schroedinger time independent wave equation. Further it is possible to show that as $r \rightarrow \infty$ and $\psi(r)$, the scattering potential also tends to zero, so it is possible to write the incident plane wave as a sum of Legendre polynomials $P_\ell(\cos\theta)$ and Spherical Bessel functions $J_\ell(kr)$, which are

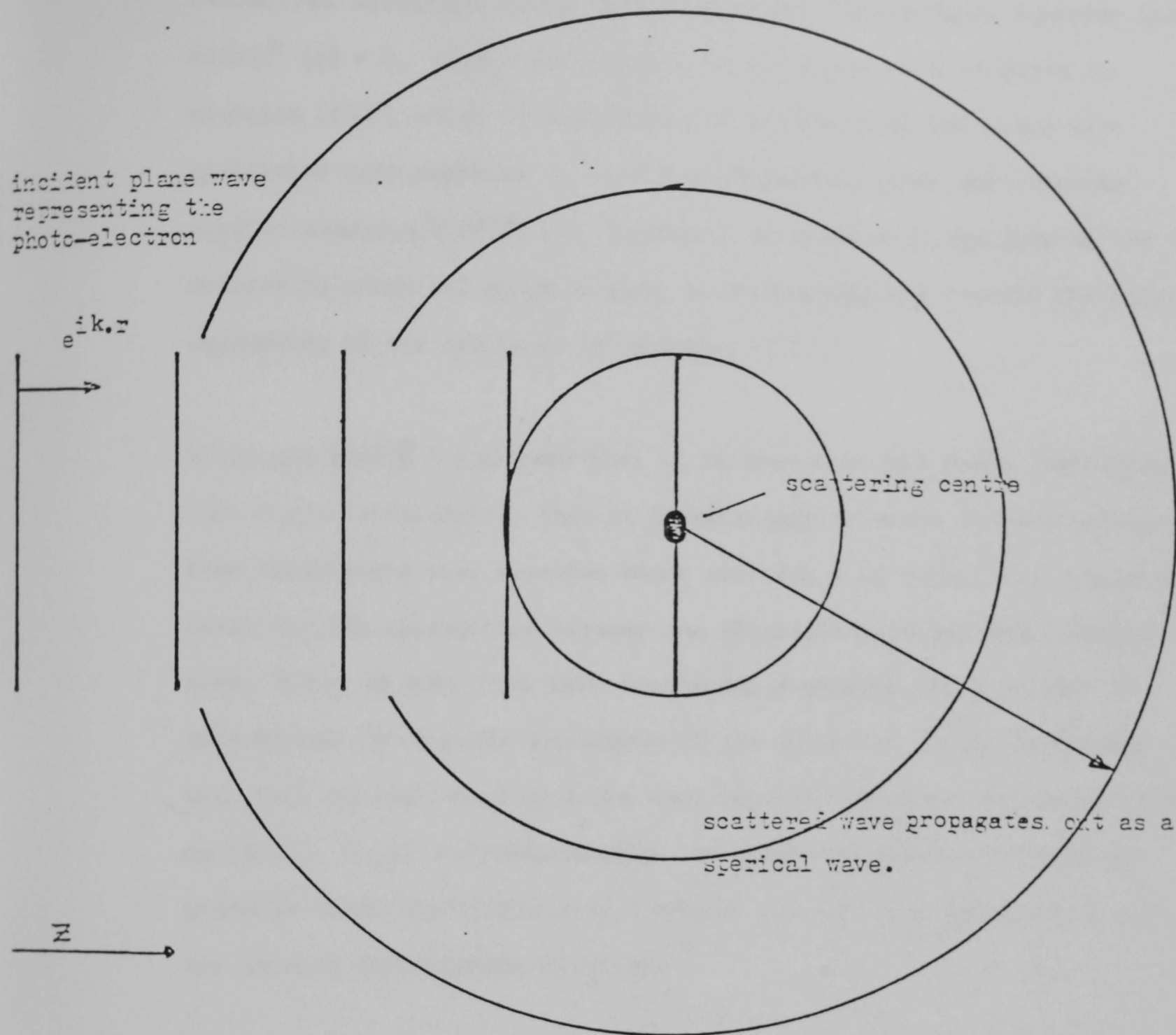


Figure (2.4). The model used to determine the electron atom scattering factors.

themselves solutions of the time independent Schroedinger equation (2.27) with $\mathcal{V}(r) = 0$. Such a description of the plane wave is given in equation (2.15), which is equivalent to representing the plane wave associated with momentum k , as a set of partial waves each with an angular momentum $\hbar\sqrt{\ell(\ell+1)}$. It should be noted that the form of the scattering potential plays no part in determining the form of the angular dependence of the solutions of equation (2.15).

If we now seek $\psi(r, \theta)$ such that it is true over all space, including that region where $\mathcal{V}/=0$, then it is necessary to solve the Schroedinger time independent wave equation which includes a potential that adequately describes the interaction between the photo-electron and the scattering atom. Since we know that this scattering potential plays no part in determining the angular dependence of the solution, it can be assumed that this solution must have the same angular dependence as the solutions in (2.15). It is not unreasonable to propose a solution, $\psi(r, \theta)$ as given by (2.16) where Q_ℓ is some constant and R_ℓ is a solution of 2.17, the reduced Schroedinger equation.

Because R_ℓ must hold over all space, it must be true for that region of space where $\mathcal{V}(r) \rightarrow 0$ i.e. $r \rightarrow \infty$. That is, $R_\ell(kr)$ and $J_\ell(kr)$ are both solutions of the same differential equation. It is not surprising, therefore to find that in the limit $r \rightarrow \infty$, the solution R_ℓ becomes (2.18).

$$\underline{R_\ell = \frac{\sin(kr - \pi/2 + \delta_\ell)}{kr}} \quad (2.18)$$

They are very similar to the spherical Bessel functions of (2.15) in the limit $r \rightarrow \infty$. It will be apparent that away from the scattering potential

the only difference between the two solutions is one of phase, which is given by δ_l .

Returning to the original equation (2.14) which represents the scattering process, we may rewrite it in terms of (2.15), (2.16) and (2.18). It is then possible to solve the scattering factor $f(\theta, k)$ in terms of the phase factor δ_l , as shown in equation (2.19).

$$f(\theta, k) = \frac{1}{2ik} \sum_{l=0}^{\infty} (2l+1)(e^{2i\delta_l} - 1) P_l(\cos \theta) \quad (2.19)$$

This then is the scattering factor seen in equations (2.12) and (2.13) of the EXAFS function. It is determined by the phase factors δ_l , which are obtained by solving the reduced Shroedinger equation (2.17) with a potential $\mathcal{V}(r)$ that adequately describes the interaction between photo-electron and the scattering atom in question and solving equation (2.17) in the case where $\mathcal{V}(r) = 0$. The phases of the two solutions are then compared in the limit $r \rightarrow \infty$, and the phase factor δ_l so obtained.

Before leaving this section, it should be noted that δ_l represents the phase change that a wave associated with an angular momentum $\sqrt{L(L+1)}$ would suffer during scattering from a potential $\mathcal{V}(r)$. Thus for a photo-electron with $L = 1$, which is the case for 'K' edge studies, $2\delta_l = 1$ represents the phase change associated with the photo-electron propagation out of and into the central atom. In order to interpret the EXAFS data, we need to know $f(\theta, k)$ for the backscattering atoms, and also for the central absorbing atom.

The development of a suitable interaction potential $\mathcal{V}(r)$ will now be presented along with the scattering factors for Fe and O.

2.5.3 The Phase and Amplitude Functions

As we have seen in the last section, calculation of the phase factors begins by assuming the form of the interaction potential between the atom and the photoelectron. Early attempts to determine the phase shifts met with only limited success, because they failed to include exchange and correlation effects in the potential.

While the electrostatic potential due to the electron orbitals within the scattering atom can be calculated from known wave functions it is necessary to include the fact that the electron orbitals will be disturbed by the incoming electron. These 'correlation' effects can be expected to be smaller for fast incident electrons since the atomic orbitals may not have sufficient time to respond.

Lee and Beni⁽³⁸⁾ have given a suitable potential that includes these effects, to provide a suitable description of electron-atom scattering. Based on this work Teo and Lee⁽³⁹⁾ have tabulated the back-scattering factor for over half of the atoms in the periodic table, $f(\pi, k)$ (since $\theta = \pi$ rads, for backscattering) together with the central atom phase shifts $\delta_l = 1$. Since the central atom (atomic number Z) is ionized it is necessary to describe it by wave functions derived for the $(Z + 1)$ ion.

By way of an example we include the back-scattering functions of oxygen and iron following Teo and Lee⁽³⁹⁾ shown in Fig (2.5).

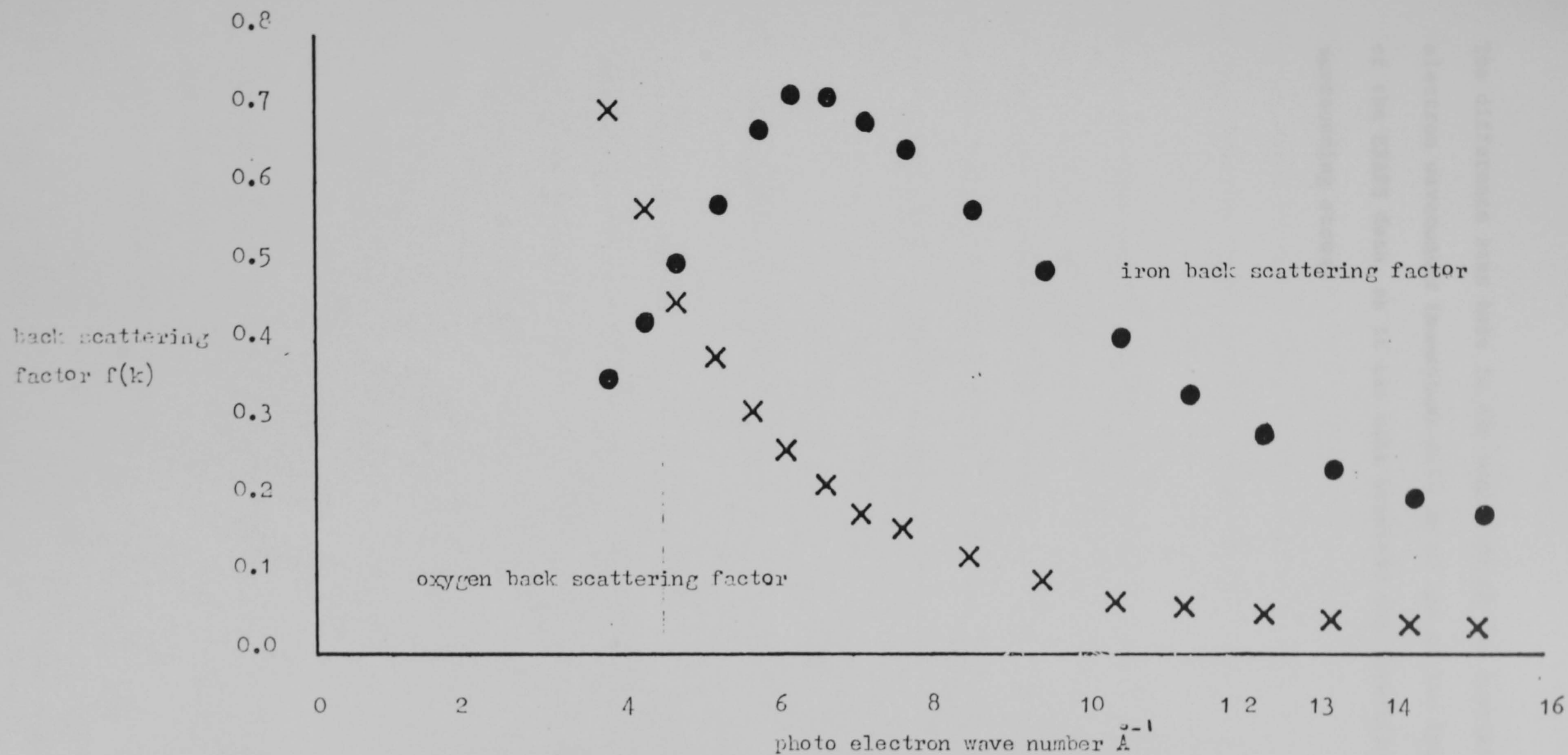


Figure (2.5). The back scattering factors of oxygen and iron after Teo and Lee (39).

The difference seen here in the magnitude of the scattering at low electron wavenumber (momentum) will be of use in the interpretation of the EXAFS data, as it can make possible the identification of the surrounding atoms.

2.6 Interpretation of EXAFS Spectra

It will be clear from equation 2.11 and its description that a wealth of data regarding the local atomic environment of the absorbing atom are contained within the EXAFS function. This section will deal with the extraction of these data from the experimentally derived EXAFS function.

There are two main methods available, a real space analysis that leads to a radial distribution function, obtained by the Fourier transformation of the EXAFS data, and a modelling routine based upon theoretical scattering data. While these two methods are introduced separately it should be realised that in practice most EXAFS analysis proceeds by a combination of both.

2.6.1 The Fourier Transform

Returning to equation (2.11), the basic EXAFS description, it will be apparent that in the absence of any scattering phase shift a Fourier transform of it will result in a series of Gaussians that peak at bond lengths r_i , see equation (2.20).

$$F(r) = \frac{1}{\sqrt{2\pi}} \int_{k_{\min}}^{k_{\max}} \chi(k) e^{i k r} d(2k) \quad (2.20)$$

The amplitude of each Gaussian will be proportional to $A_i(k)$, reflecting the attenuation of the peak due to the static and thermal structural disorder in the sample, and the number of atoms in the shell.

Each peak will be further broadened because of the necessity to work with an EXAFS function of only limited 'k' range. Such a broadening has been discussed by Sayers⁽⁴⁰⁾, and is given as equation (2.21).

$$\Delta r = \frac{3.8}{\Delta k} \quad (2.21)$$

That such a broadening should occur is a natural result of the Fourier transform. The decay of the EXAFS function also generates other unwanted features in the resulting distribution function, in the form of side bands on each of the main peaks. This can be overcome by weighting the experimental data set by a factor of k^n , so as to bias the high energy end of the spectra. The parameter n is chosen to provide EXAFS oscillations that are independent of photo electron energy. Following ⁽³⁹⁾, n is given in Table (2.1). Thus the final transform taken is

$$F(r) = \frac{1}{\sqrt{2\pi}} \int_{k_{min}}^{k_{max}} \chi(k) k^n e^{ikr} d(2k) \quad (2.22)$$

The above description the Fourier transform technique has chosen to ignore the presence of any phase shift of the scattered photo electron. The presence of any such shift will lead to the peaks in the distribution function being moved away from their true position. Sayers⁽⁴¹⁾ has shown that if the phase function can be written as

$$2\delta_{L=1} + \text{Arg}(F_i(k)) = -ak + b \quad (2.23)$$

Then the structural features contained in the distribution function will be shifted by an amount Δr

$$\Delta r = \frac{a}{2} \quad (2.24)$$

n	atomic number range
3	$2 < 36$
2	$36 < 2 < 57$
1	$2 > 57$

Table (2.1). Weighting factors 'n' of k^n
after Teo and Lee⁽³⁹⁾.

However it is possible to determine this shift by comparing the distribution function of the unknown sample with that obtained from a model compound of similar chemical composition, so that the same phase shifts are involved, and known structure. It is then possible to correct the unknown distribution function with the shifts derived from the model compound data.

2.6.2 Further Methods of EXAFS Analysis

It will be apparent from the above description of the Fourier transform analysis route that limitations are imposed by the inherent nature of the Fourier transform introducing artefacts into the radial distribution function. Additionally, the limited resolution of this Fourier transform implied by equation (2.21), makes difficult the interpretation of distribution functions from samples containing closely spaced or overlapping co-ordination shells.

To overcome these problems other methods of analysis have been developed. Whatever method is employed, there is still the need to obtain information about the form of the scattering factor. In the above Fourier transform method this was included in the analysis by the comparison of the unknown and known radial distribution functions. In making such a comparison it is assumed that the electron scattering is determined largely by electrons contained within the core of the scattering atom and that the electrons involved in chemical bonding play only a small part. It is thus assumed that the scattering is independent of the chemical state of the scattering atom. Such a procedure is known as chemical transferability and has been justified⁽⁴²⁾.

It will be evident that each peak in the distribution function from the different co-ordination shells containing different atoms will be shifted from their true positions by a different amount. A more sophisticated variant of the Fourier transform technique known as single shell analysis seeks to determine the true position of each peak separately.

Each peak in the distribution function is isolated and back Fourier transformed into 'k' space, thus generating the 'EXAFS' for a single co-ordination shell, the phase of which is given by equation (2.25).

$$\phi_i(k) = 2kr_i + 2\delta_{L=1} + \text{Arg}(F_i(k)) \quad (2.25)$$

If a pair of equations of the form (2.25) are obtained for similar shells from a model and unknown compounds, then the scattering factor can be removed by subtraction as shown in equation (2.26).

$$2k(r_1 - r_2) = \phi_1(k) - \phi_2(k) \quad (2.26)$$

In the absence of any suitable model compounds it would be possible to use the theoretical values given by Teo and Lee, and subtract the theoretical phase factors due to scattering from the experimentally obtained phase. This immediately shows up one problem common to all EXAFS analysis: when the experimental data were converted from X-ray energy to photoelectron wavenumber the threshold energy E_0 was used to define 'k'. In general ' E_0 ' is not determined simply by the ionisation energy of the excited core level, the mean interatomic potential seen by the photoelectron, and the work function of the material also has been involved. In general we have no prior way of determining E_0 from

the features seen in the absorption edge, and so we must assume that E_0 is uncertain by an amount ΔE_0 . Under these conditions it can be shown that 'k' will also be in error by

$$k' = \left(k^2 - \frac{2\Delta E_0}{7.62} \right)^{1/2}$$

Thus in order to ensure that the subtraction of the scattering phase (experimental or theoretical) is successful, it is necessary to employ some iterative procedures in the choice of E_0 . Several choices of E_0 are made and E_0 chosen when the best fit to the straight line of equation (2.22) is obtained. This method has been used to analyse the results obtained and is more fully described later.

2.6.3 Modelling

The most successful method of extracting the data contained in an experimental EXAFS function is based upon modelling the unknown EXAFS function using theoretically or experimentally determined scattering information. Some guess is made about the structure of the unknown material, which is generally based upon the results obtained from the Fourier analysis, previously described.

An iterative procedure is then employed, to obtain the best fit based on least square deviation, between the theoretical EXAFS model and the experimental dataset. The values of disorder, co-ordination number and bond length may then be taken from the theoretical dataset. Modelling the whole of an EXAFS dataset is very complex due to the large number of parameters available for iteration. Because of this it is usual to attempt to model individual EXAFS of single co-ordination shells as generated in the Single Shell analysis of the Fourier transform analysis.

While this method is the most reliable and accurate method described, time has precluded it from being employed to analyse the data obtained in this study. What follows is therefore concerned with the Fourier transform analysis of EXAFS data.

3. Experimental Methods

We start with a description of the preparation and passivation of the thin alloy substrates. The remainder of the chapter deals with the experimental methods used to measure the EXAFS of the passive oxide film.

3.1 Sample Preparation

It has been seen in the previous chapters that the fluorescence and total electron yield EXAFS measurement modes are sensitive to passive film structure. It has been seen too that the sampling depth of the two modes is greater than the typical thickness of passive film. For this reason it has been found necessary to ensure that the sample should contain as little unoxidised metal as possible, so that the measured EXAFS is dominated by the passive film structure. Since the passive films are known to be approximately 30Å thick, it is implied that the unpassivated alloy substrate should be no more than 25Å thick.

The EXAFS technique can sample the structure of the passive film over an area of approximately two square cm, and so to ensure the maximum sensitivity of the technique, it is important that this full sampling area should be utilised. Thus we require a sample that is uniformly thin over several square cm. Such a sample precludes the use of bulk alloy samples that have been mechanically or chemically thinned since these methods can only provide such thin samples over very small areas of less than a square mm. Suitable samples can be prepared by thermal evaporation.

3.1.1 Thermal Evaporation

The technique basically involves generating a vapour of the alloy or metal to be prepared and allowing it to condense on to a cold substrate. The vapour is produced by heating the material to be deposited, in a tungsten filament under a vacuum. A schematic diagram of the apparatus used is shown in Fig. (3.1).

While the conventional thermal technique has produced good samples, it is not immediately obvious that it can produce alloys of any composition. This is because the formation of alloys requires that the constituents should be deposited together. Now because the deposition rates of the metals can differ by many orders, certain alloy compositions may not be achievable. The technique also suffers because the high temperatures involved in melting the alloys leads to mechanical instability of the filaments which can lead to uncertainties in the alloy composition. It is for this reason that much time was spent in trying to develop the alternative method of Ion-Beam-Sputter-Deposition. This new technique removes the above problems by generating the vapour by Ion-Beam-Sputtering a target of the material to be deposited. Since the deposition rates of many materials are very similar under these conditions, almost any alloy composition can be obtained. Because the method is much more stable, many of the uncertainties regarding alloy composition are removed. While this technique did produce iron, nickel and iron-nickel alloy films the low deposition rates and poor vacuum present in the sputtering system lead to the oxidation of any sputtered chromium. For this reason the iron-chromium alloys were prepared by conventional thermal evaporation, even though the uncertainties

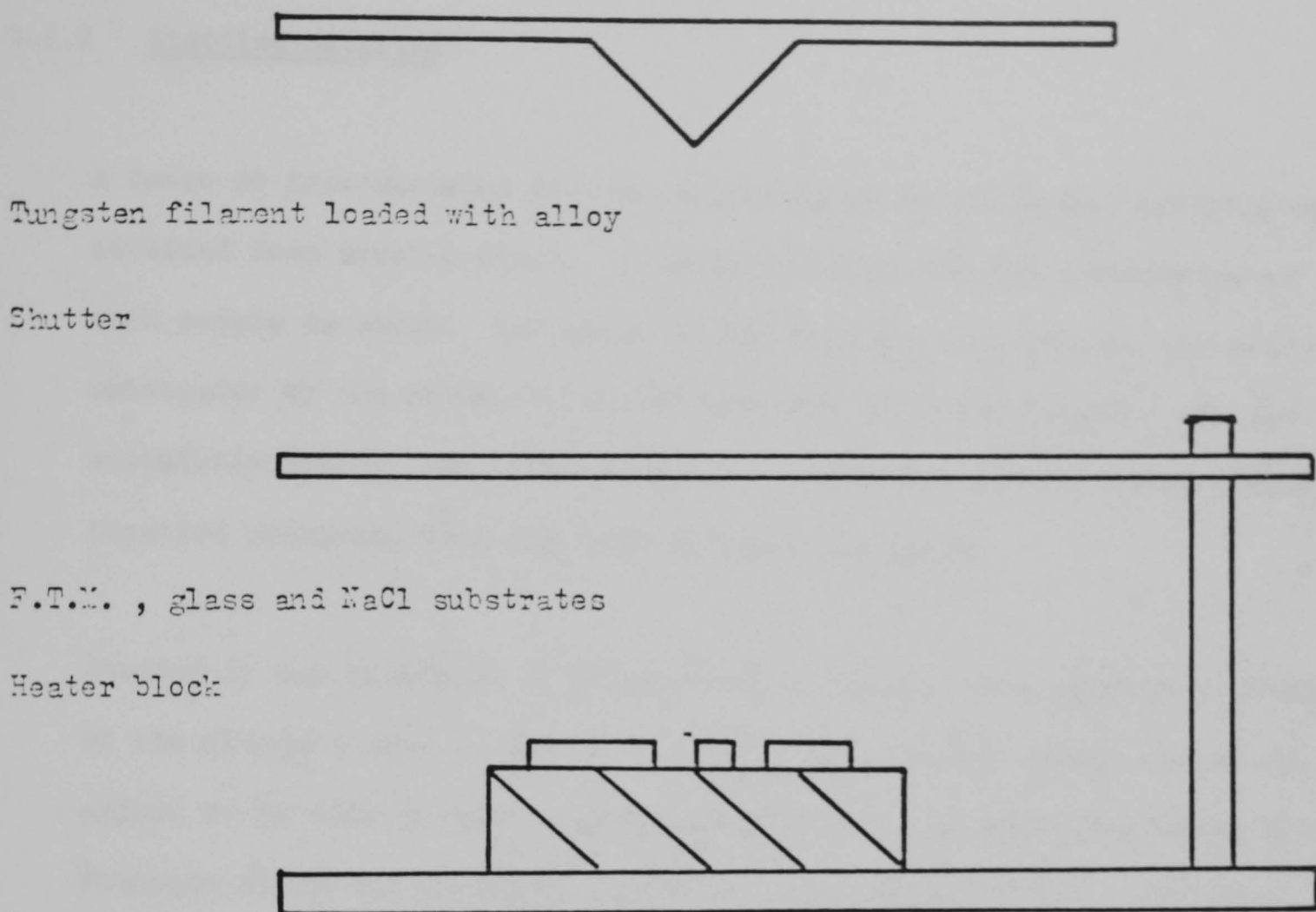


Figure (3.1). Schematic representation of the apparatus used for the thermal evaporation of the alloy samples.

inherent in the method required that many alloy samples had to be produced in order to obtain samples of the required composition.

3.1.2 Starting Material

A range of iron-chromium alloys containing up to 25% atomic chromium were obtained from British Steel. A table (3.1.) giving the composition of each sample is shown. Initially it had been hoped to prepare the alloy substrates by the co-deposition of iron and chromium; however, the low deposition rate of the chromium and the consequent instabilities thereby incurred prevented this approach from being adopted.

Instead it was necessary to prepare the alloys by the evaporation of one of the alloys listed in Table 3.1. Under equilibrium conditions we can expect to be able to predict the composition of the deposited alloy as a function of the bulk evaporating alloy composition. However, in this study the evaporation conditions were not in any sense equilibrium conditions. This was caused by the tendency of the chromium to react with the tungsten filament, and the variability of the heating effect of the filament, due to the instability of the system at elevated temperatures.

To avoid these problems the alloys were evaporated under a wide variety of conditions, such as deposition rate and the time during which the sample was deposited. This led to the formation of many thin alloy substrates of widely differing composition, from which suitable samples were selected.

nominal composition of alloy	analysis of alloy							
	Cr	Si	Sn	P	S	Mo	Ni	C
Fe	0.02	0.31	0.03	0.003	0.02	0.05	0.02	0.004
Fe5Cr	4.18	0.16	0.08	0.005	0.02	0.02	0.02	0.004
Fe10Cr	11.2	0.21	0.08	0.005	0.02	0.02	0.02	0.006
Fe15Cr	14.2	0.19	0.08	0.005	0.03	0.02	0.02	0.007
Fe20Cr	20.3	0.26	0.08	0.005	0.03	0.02	0.02	0.006
Fe25Cr	24.6	0.25	0.07	0.005	0.03	0.02	0.02	0.005

Table(3.1). Analysis of the bulk alloys used in the electrochemical study and used to prepare the thin alloy films.

3.1.3 Evaporation of Alloy Films

Small pieces of alloy were cut from the bulk alloy sample. Each piece was in some 2mm in diameter, washed ultrasonically in acetone to remove any gross contamination, and finally soaked in boiling methanol. They were then etched in dilute nitric acid to remove any inorganic debris left over from the cutting process. Finally the sample was washed thoroughly in running deionised water. To ensure complete cleaning of the sample the whole washing process was then repeated.

Because of the tendency of the chromium to react with the tungsten filament it was necessary to use a new filament for each deposition. Following their formation the filaments were found to be heavily blackened with oxide. The most effective method found to remove this scale required the heating of the filament to white heat under a vacuum. After this heat cleaning the freshly cleaned pieces of bulk alloy were loaded into the filament together with the glass and sodium chloride substrates. The NaCl substrates were included to allow the spatial uniformity of composition of the glass grown film to be determined (see below).

Glass microscope slides were used as substrates upon which to grow the thin alloy films since they would contribute no structure to the EXAFS spectrum and offered a readily available smooth substrate. Each was thoroughly washed and degreased before being mounted into the evaporator. Around each glass substrate, six pieces of sodium chloride were placed as shown in Fig. (3.2). As we shall see later these six samples were suitable for observation in the TEM, and were able to provide information about composition, structure and contamination of the glass formed film.

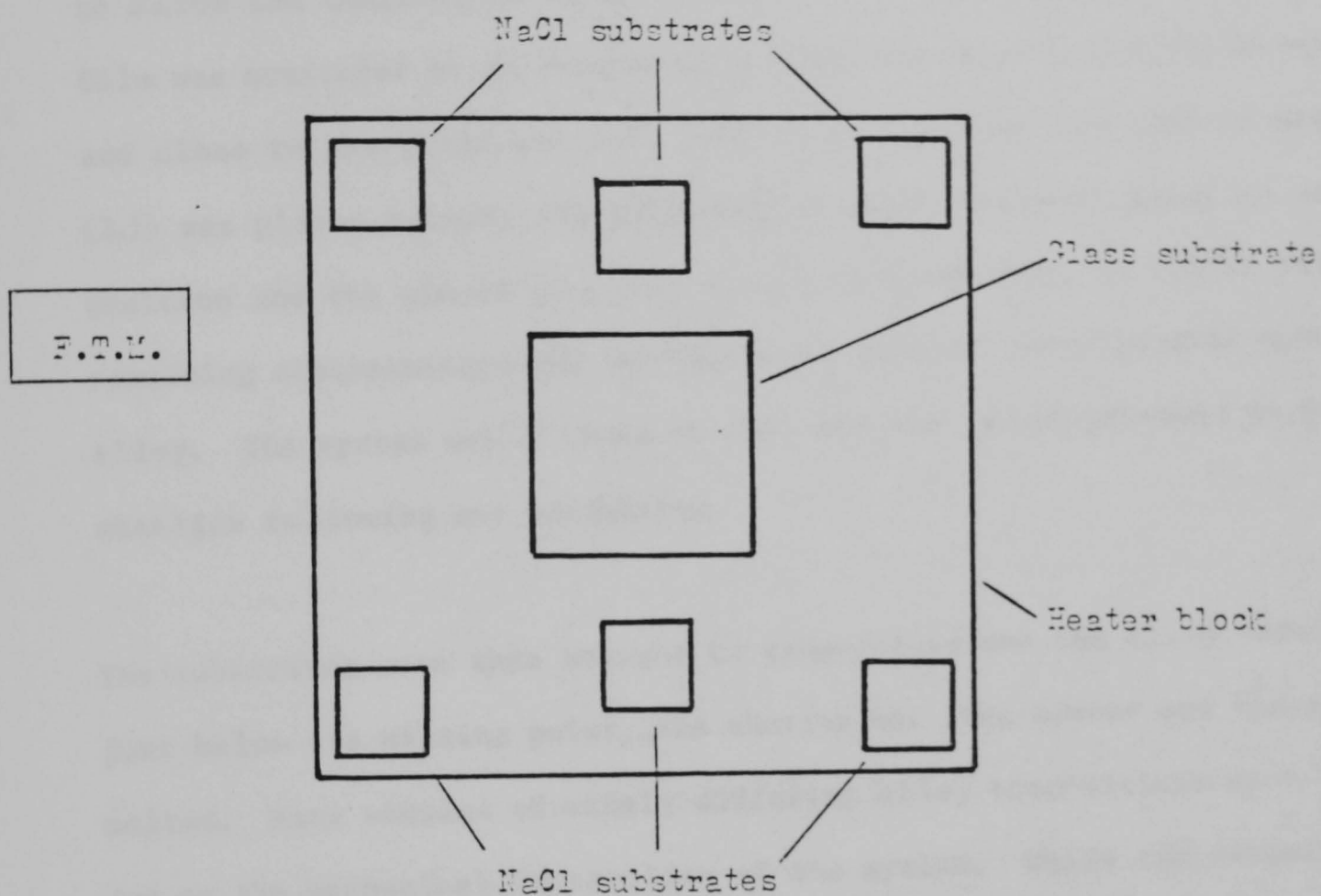


Figure (3.2). The spatial arrangement of the film thickness monitor (F.T.M.) and the glass and NaCl substrates, used during alloy film evaporation.

In order to ensure that the films were of uniform thickness and "pin hole" free, it was necessary to heat the substrates to 100°C. This was accomplished by placing the glass and NaCl substrates on a stainless steel electrically heated substrate table, which contained a thermocouple to allow the temperature to be measured. The thickness of the deposited film was monitored by an Edwards film thickness monitor placed alongside and close to the glass and NaCl substrates. The shutter seen in diagram (3.1) was placed between the substrates and the filament prior to deposition and the pieces of alloy heated to white heat, to remove any remaining contamination and decompose any natural oxide present upon the alloy. The system was allowed to cool and the vacuum pressure to re-stabilise following any outgassing.

The substrates were then brought to temperature and the alloy heated to just below its melting point, the shutter was then opened and the alloy melted. Many samples of widely differing alloy compositions were formed due to the mechanical instability of the system. While the composition was a function of the initial alloy composition and the temperature of the evaporation, the most profound effect upon the composition of the alloy film was seen to be due to the rate at which the chunks of bulk alloy were melted. The rate of melting was difficult to control since it depended upon the manner in which each piece of bulk alloy sat upon the tungsten filament. Following the deposition of the thin alloy film the system was allowed to cool to room temperature and the samples transferred to a vacuum desiccator, to await characterisation and passivation.

3.1.4 Alloy Film Characterisation

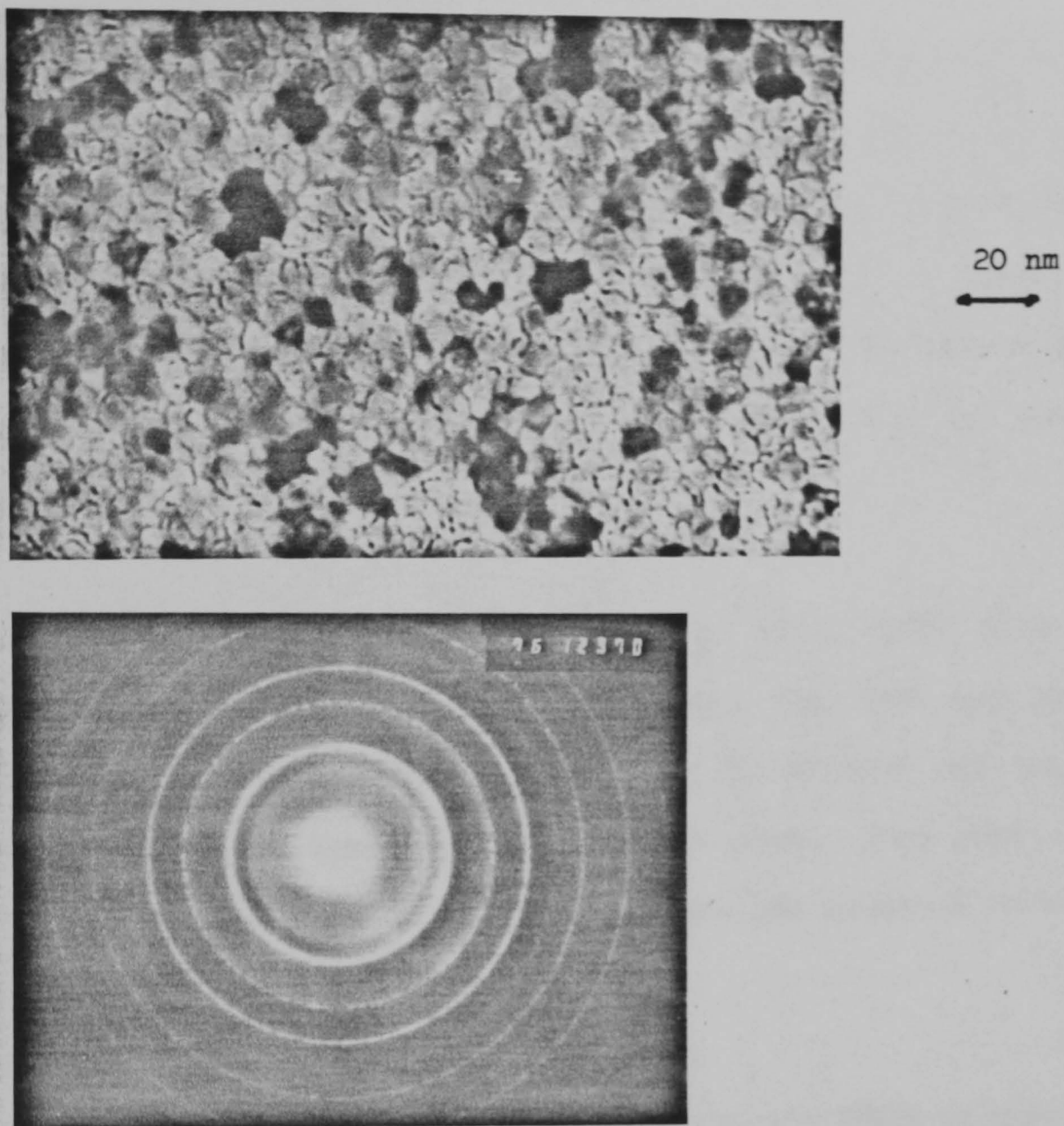
Attempts were made to characterise the composition and morphology of the alloy films formed on glass using Scanning Electron Microscopy. However, the thinness of the alloy films caused the analysis to be dominated by the glass substrate. To overcome this problem, at the same time as the alloy was deposited on to the glass substrate it was deposited on to the six NaCl substrates. The NaCl could be dissolved in water and the thin alloy film mounted on to a gold microscopy grid for observation in the Transmission Electron Microscope.

The Transmission Electron Microscope provides information about the structure, composition and degree of oxidation of the films formed on the NaCl substrates. Analysis of the electron diffraction pattern provides positive identification of the structure of the alloy and any oxide that may be present. Additionally, analysis of the X-rays emitted from the sample (EDAX) provides information about the chemical composition of the film. In principle this method can be used to determine the oxygen content of the film; however, the particular X-ray detector available was unable to cope with the soft X-ray emissions from any oxide that may have been present, and so oxide presence was determined by the nature of the electron diffraction pattern.

In the absence of the glass substrate, the T.E.M. observations allowed the structure, composition and degree of oxidation of the alloy to be assessed. The presence of six such samples placed about the glass substrate allowed the compositional uniformity of the alloy to be determined.

A typical electron micrograph of an alloy film containing 15% atomic chromium is shown in Fig. (3.3), together with its corresponding electron diffraction pattern. It should be noted that the film is uniform and "pin hole" free. The diffraction pattern may be interpreted as the B.C.C. structure of the iron-chromium alloys. The diffraction pattern also indicates that there is very little oxide present within the sample. Dark field electron microcopy has shown that the individual crystal size is of the order of 50\AA . EDAX measurements of the composition of the films indicated that the composition of the samples was uniform over the six NaCl grown samples to better than 1% atomic chromium, across the whole of the set. From this it was inferred that the glass grown film had a similar compositional uniformity.

In order to check the similarity of the corrosion behaviour of the thin films to the bulk alloys, the electrochemistry of each was compared. Since as we shall see later the electrochemical behaviour of the bulk alloys in sulphuric acid is indicative of the composition of the alloy, electrochemical scans of the bulk and thin alloys in sulphuric acid were taken. The EDAX results and electrochemical behaviour compared well with the bulk alloys for the thin films containing over 10% atomic chromium while the much greater dissolution currents encountered in the low chromium passive alloys lead to the total dissolution of the alloy film before its electrochemical nature could be fully determined. This fact was sufficient to confirm the alloys to be of a low chromium content.



Figure(3.3). Transmission electron micrograph and diffraction pattern from a thin (30Å) alloy film(Fe15Cr).

3.1.5 Sample Passivation

The samples to be used for the chromate and nitrite studies were placed in sample jars containing 0.05 molar potassium chromate solution and 0.1 molar sodium nitrite solution respectively. It was found necessary to ensure that each sample remained in the solution for at least one month, in order that there should be sufficient passive film oxide present for the EXAFS to be dominated by the passive film and not the remaining alloy.

Samples for the sulphuric acid study were kept under vacuum until just before the EXAFS measurements were to be made. They were then removed from the vacuum and cathodically reduced in 2M sulphuric acid at -1.0V S.C.E., to ensure the removal of any surface oxide. They were anodically polarised for 30 minutes to ensure the formation of a true three dimensional passive oxide film.

Following passivation and immediately prior to the EXAFS measurement being made the samples were washed in deionised water and dried in nitrogen. They were then mounted in the EXAFS equipment and the EXAFS measurement begun.

3.2 EXAFS Measurement

A schematic diagram of the apparatus used to measure the Fluorescence and Total electron yield EXAFS of the passive films is shown in Fig. (3.4).

Polychromatic radiation from an X-ray source, in this case the synchrotron radiation source at Daresbury, is monochromatised by a crystal monochromator. The intensity of this monochromatic X-ray beam I_0 is then monitored by the Incident ionisation chamber. Only a small fraction of the incident beam is absorbed here, just sufficient to ensure a reliable measure of incident intensity.

In the case of the Total Electron Yield measurements the incident beam then passes through a thin Mylar window and on into a vacuum chamber. This is a Turbo Molecular pumped chamber with a background pressure of 10^{-6} Torr. The beam impinges on the passive film sample, which is held at an angle of 60 degrees to the incident beam to maximise the amount of sample analysed. As previously described in Chapter 1, the absorption of the X-ray beam is accompanied by the emission of electrons from the passive film. These electrons are detected and counted by the channeltron electron detector. Finally, the signal produced by the channeltron is processed before being passed into the computer, which controls the experiment and data acquisition.

In the case of the Fluorescence measurements no vacuum chamber is needed, and following the I_0 ionisation chamber the X-ray beam impinges directly on the sample, which again is held at 60 degrees to the line of X-ray incidence. This time the X-ray absorption generated Fluorescence X-rays are detected by four scintillation detectors, arranged to collect as many of the emitted X-rays as possible.

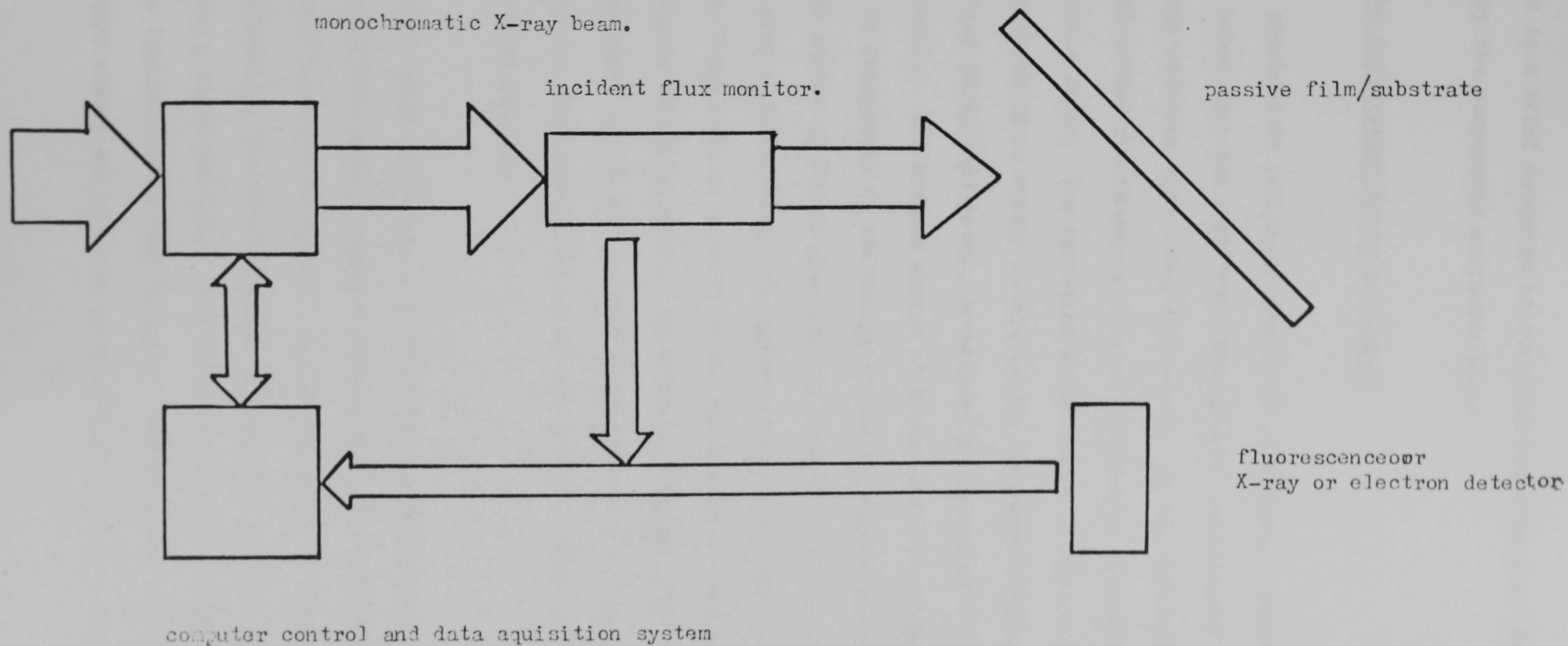
white X-ray radiation from the S.R.S.

crystal monochromator under vacuum.

monochromatic X-ray beam.

incident flux monitor.

passive film/substrate



computer control and data aquisition system

fluorescence or
X-ray or electron detector

Figure (3.4). Schematic representation of the EXAFS equipment used for both the fluorescence and total electron yield measurements.

This then is a brief overview of the EXAFS measurements. We will now describe more fully the components mentioned above.

3.2.1 The Synchrotron Radiation Source

The synchrotron radiation source and traditional laboratory X-ray sets are based upon the same basic phenomenon; accelerated electric charge radiates electromagnetic waves. In the laboratory X-ray set this acceleration occurs when a beam of high energy electrons impacts on a suitable anode. The radiation so generated is characterised by peaks corresponding to energy levels within the anode material and a smoothly varying background level, determined by the energy of the incident electrons. The maximum energy of X-rays that can be generated in this way is determined by the energy of the incident electron beam, while the total number of X-rays generated is related to the total power of the incident electron beam. The maximum X-ray flux that is available from these X-ray sets is limited by the maximum power that the anode can dissipate before it melts. In order to increase this level, anodes are often water cooled and in some cases the anode is designed to rotate, to spread out the heating effect of the electron beam and so reduce the chance of melting.

However, even with these modifications the X-ray intensity is such that it would take several weeks to obtain an EXAFS spectrum of sufficient quality to allow structural information to be extracted from it. Additionally, the characteristic peaks present in the spectrum can severely limit the range over which EXAFS data can be collected. With these limitations in mind it is not surprising to find that the advances in EXAFS theory and practice have largely reflected the availability and

development of the synchrotron radiation source, which does not suffer from these drawbacks.

In the synchrotron radiation source ⁽⁴⁵⁾ electrons moving at relativistic energies are held in near circular orbits by strong magnetic fields. Consequently the electrons suffer an acceleration and can be expected to emit electromagnetic radiation. Classically we would expect that an observer outside the orbit of the electron would see the dipole radiation field of the electron at the orbital frequency.

However, since the electron is moving at relativistic speeds the field seen by the observer should be obtained by applying a Lorentz transform to the classical dipole radiation field generated by the orbiting electron. Under this Lorentzian transformation the radiation pattern generated by the electron becomes thrown forward in the direction of travel of the electron. This results in the observer seeing a series of short flashes each time the radiation "beam" passes them. Thus the observer sees a whole series of frequencies at the harmonics of the fundamental electron orbit frequency.

Additionally all these harmonics are Doppler shifted towards a higher frequency due to the relativistic motion of the electron. Thus the output spectrum contains X-rays at harmonic frequencies of the orbiting electron right up into the hard X-ray regions of the spectrum.

In a real synchrotron machine, bunches of electrons not single electrons generate the radiation. Each of these electrons wobbles very slightly about its orbit, changing slightly the frequency of the emitted radiation. Since the output of the synchrotron is the sum of the

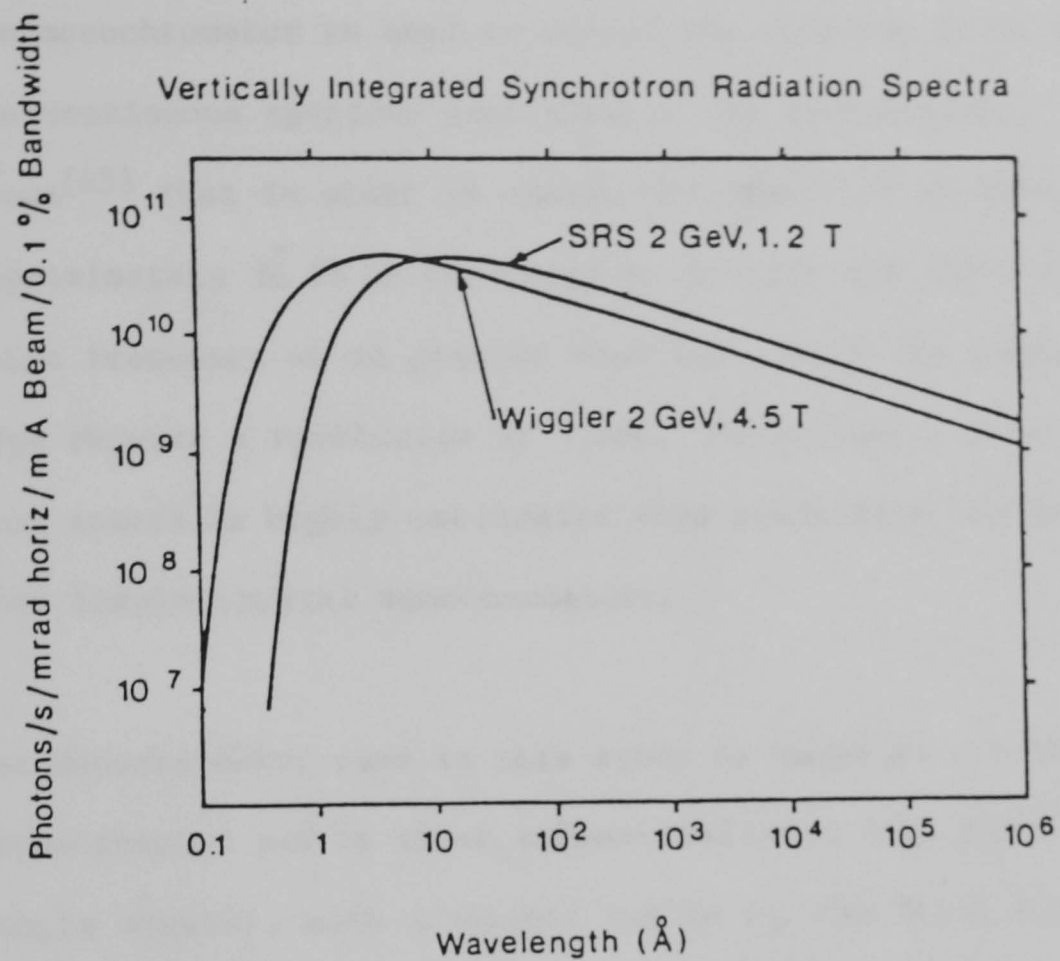
emissions from all of the electrons, the individual harmonic lines become smeared out. This results in a continuum of radiation that extends up to an energy related to the kinetic energy of the electron and given by equation (3.1).

$$\lambda_c = \frac{2.35 (R(m)) \text{ \AA}}{[E(\text{Bev})]^3} \quad (3.1)$$

The spectrum of radiation generated by the Daresbury S.R.S. is given in Fig. (3.5). It should be noted that the spectrum is smooth, there being no characteristic peaks, and that a high intensity is maintained up to the hard X-ray region.

As well as providing an intense smooth spectrum, the radiation is well collimated and strongly polarised in the plane of the orbit. The source has a typical divergence of 10^{-4} mrad. and it is possible to use simple monochromators without the penalty of low efficiency to select specific X-ray wavelengths, thus generating a simple high intensity tunable X-ray source. Additionally, the strong polarisation of the X-ray source allows the anisotropies of materials to be investigated. It should be noted that the radiation above the orbit plane is circularly polarised and may be of use in other structural studies.

Thus because of the high brightness of the source and the smooth nature of the spectrum all of the results presented in this work were obtained using the S.R.S. at Daresbury. This allowed individual spectra to be obtained for each sample in a period of about ten hours.



Figure(3.5). The radiation spectrum of the S.R.S. at Daresbury.

3.2.2 The Monochromator

The monochromator is used to select the required X-ray wavelength from the continuous spectrum generated by the synchrotron. It can be shown⁽⁴³⁾ that in order to ensure the detection of bond lengths up to approximately 3\AA it is necessary to collect the EXAFS data with an energy point frequency of no greater than 5eV, while the features in the near edge require a resolution of 1.0eV. Fortunately, because the synchrotron source is highly collimated this resolution can be easily obtained from simple crystal monochromators.

The monochromator used in this study is known as a channel cut crystal monochromator and is shown schematically in Fig. (3.6). Made from a single crystal, with a channel cut in it, the first crystal face disperses the X-rays according to the usual Bragg relationship given below in equation (3.2).

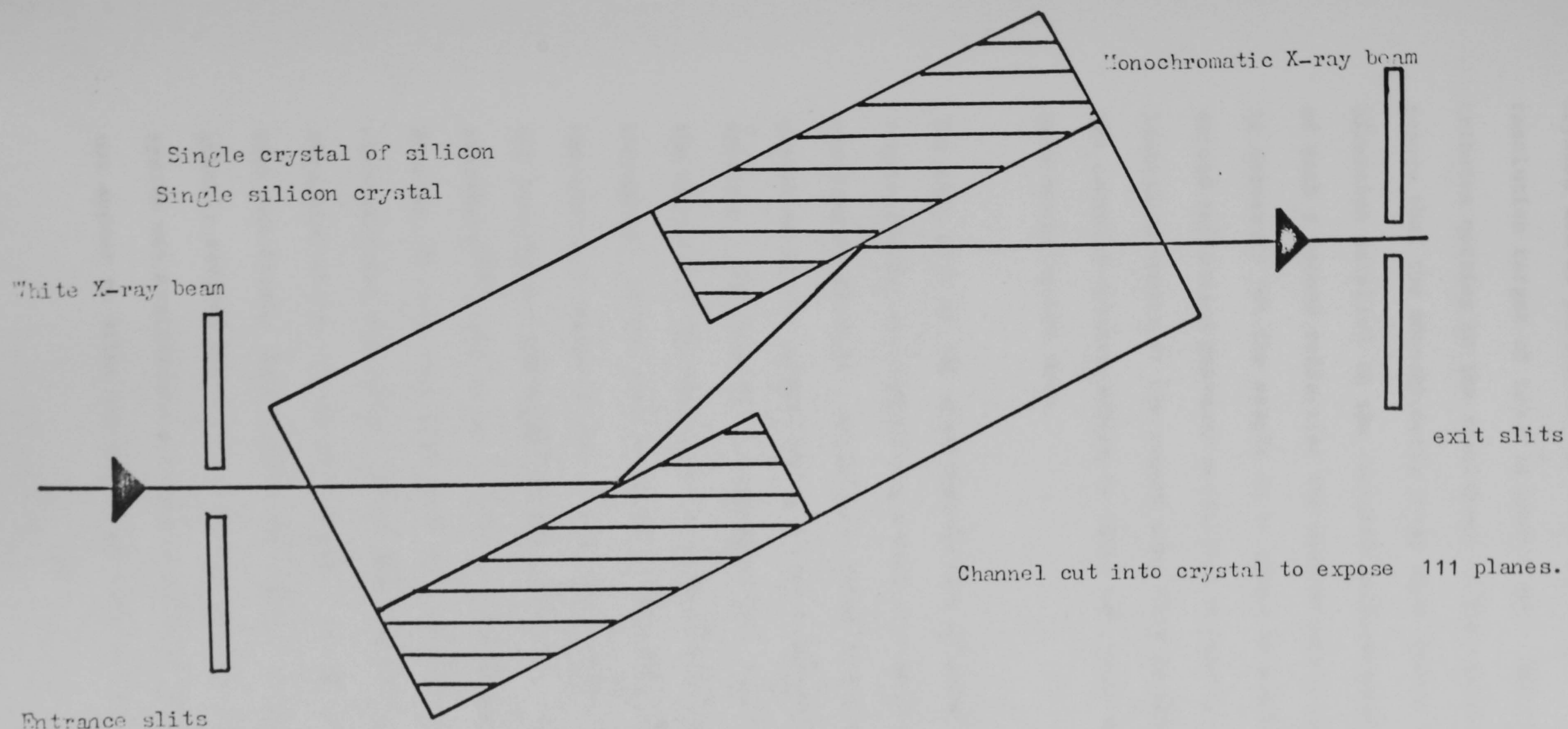
$$n\lambda = 2d \sin \theta \quad (3.2)$$

The resolution of a single crystal monochromator is given by equation (3.3).

$$\frac{\Delta \varepsilon}{\varepsilon} = \cot \theta \Delta \theta \quad (3.3)$$

$\Delta \theta$ = Divergence of Source

Given that the monochromator uses silicon $\langle 111 \rangle$ crystal planes and that the divergence of the X-ray source is about 10^{-3} mrad and that the



Figure(3.6). Schematic diagram of the channel cut monochromator used to select X-ray energy.

crystal can be positioned to about 1.0 mrad, it can be seen that the resolution target of 1.0eV is easily met. The second crystal face contributes nothing to the resolution of the system, its purpose is to ensure that the monochromatic X-ray beam leaves the monochromator in a direction parallel to the incident poly-chromatic beam. In the absence of such a second reflection the monochromatic beam is swept about, and it is necessary for the sample to be moved to ensure alignment. While the second reflection prevents rotational movement, there is still some lateral movement of the output beam. This is easily dealt with by using the computer control system to raise and lower the sample as the X-ray beam moves up and down.

The exit slit of the monochromator was adjusted to ensure that only the required X-ray wavelength could pass through the system. Other wavelengths obviously satisfy the Bragg equation for other plane spacings contained in the crystal and can lead to spurious glitches in the EXAFS spectrum. The form of the equation (3.2) also suggests that harmonics of the required X-ray energy can also be present in the output of the monochromator. In the case of the iron edge this harmonic energy is above the critical energy of the source and so need not be of concern here. Our results for the EXAFS of pure iron agree well with those published elsewhere⁽⁴⁴⁾, and so our neglect of the higher harmonics is justified. However, in case they proved to be a problem, an order-sorting monochromator was available. Based upon the double crystal monochromator described above, the second crystal face may be rotated out of parallel with the first. This causes the harmonic response of the system to be greatly reduced with respect to the required wavelength. While this system was available the added complexity of alignment and running did not appear to offer any advantage over the conventional monochromator,

which produced good results.

3.2.3 Incident Flux Monitor

The purpose of this detector is to measure the incident flux of the monochromatic X-ray beam falling on the sample. Essentially a tube with beryllium (X-ray transparent) windows on each end, the detector is filled with a Helium-Argon gas mixture that absorbs a small fraction of the incident beam. The absorbed X-rays ionise the gas and under the action of the applied potential a current flows through the detector. It is then assumed that this current is a proportional measure of the incident X-ray flux passing through the detector. It is important that the correct fraction of X-rays are absorbed by the detector, too small a fraction, and the signal measuring I_0 will be subject to much noise, while too much absorption will reduce the incident flux to such an extent that the signals measuring the fluorescence or electron yield will be heavily degraded. Theoretical figures have been given by Store et al⁽⁴³⁾ for the fraction of X-rays that should be absorbed to ensure a maximum signal to noise ratio for the EXAFS spectra. In the experimental system used here it was found that an absorption of about 10% led to a noise free measurement of I_0 with the maximum fluorescence and electron yield signal being generated.

The current from the ionisation chamber was fed into a Keithley ammeter with a transconductance of 10^8V amp.^{-1} . This signal was then used to drive a voltage to frequency converter, the pulses from which were counted by the data acquisition computer. Because of current leakage through the ionisation chamber some counts were recorded in the absence of any incident beam. It was therefore necessary to remove this

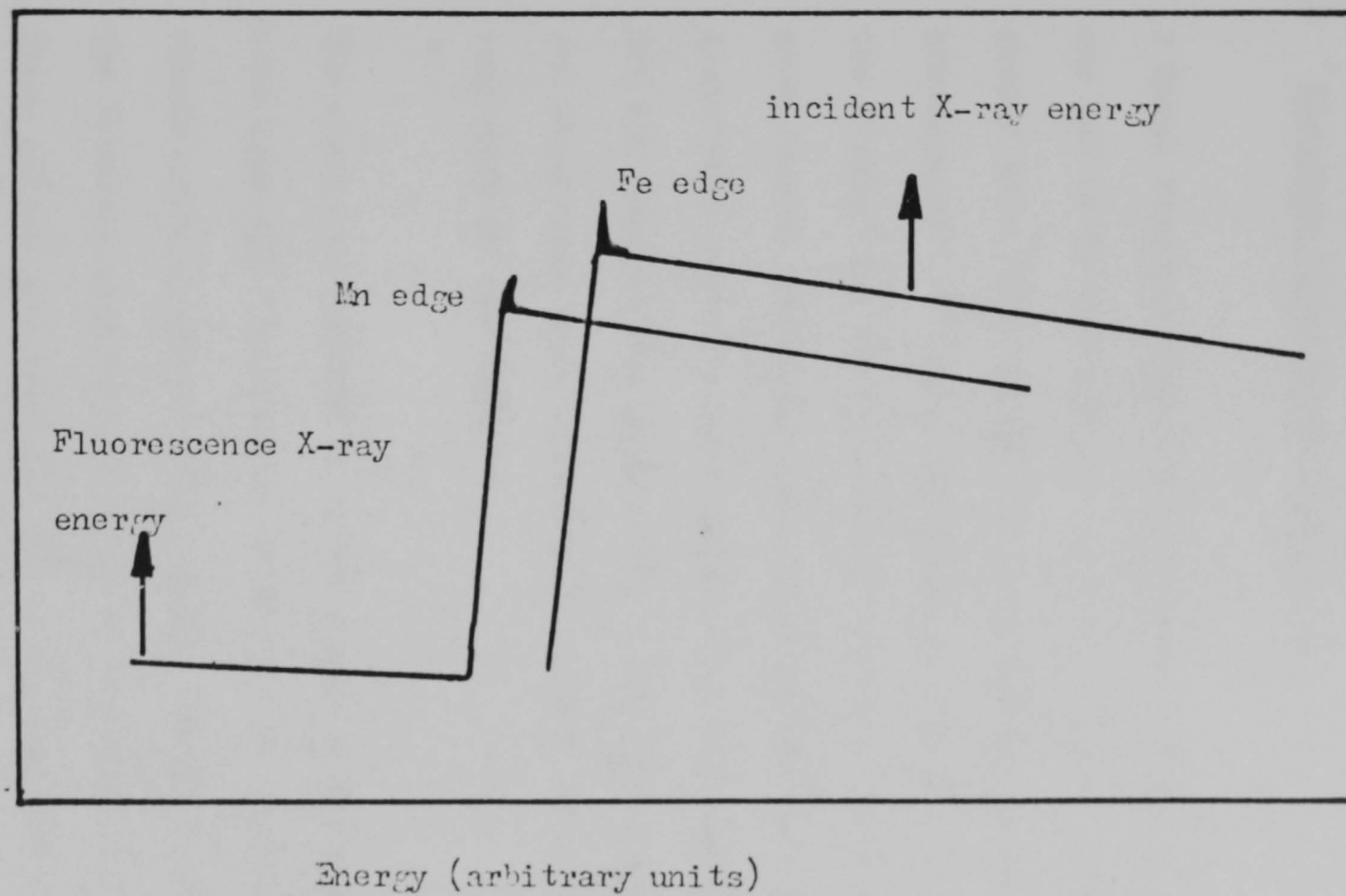
background level from any recorded data.

3.2.4 Fluorescence X-ray Detection

The Fluorescence X-ray system used in this study was that provided on EXAFS station 7.1 at the S.R.S. at Daresbury. The Fluorescence X-rays were detected by four scintillation detectors arranged about the sample so as to maximise the solid angle subtended to the sample ensuring the detection of the maximum number of Fluorescence X-rays. In order to maximise the signal-to-noise ratio on the measured signal, it is necessary to prevent any X-rays from the incident beam entering the detectors. This is accomplished by the use of low pass (z-1) filters, placed in front of the detectors. As an example of these filters we may look at the use of the manganese (z-1) used during the study of the iron absorption edge. The effect is summarised by the diagram in Fig. (3.7), which shows the X-ray absorption spectrum of iron and manganese in the vicinity of the iron edge. Since iron and manganese are next to each other in the periodic table we can expect their 'K' edges to be close to each other, the manganese edge being at a somewhat lower energy than the iron edge. The diagram reveals that any X-ray of above the energy of the iron edge will be heavily absorbed by the manganese since it is above the manganese absorption edge. However the Fluorescence X-rays generated by the absorption of the incident X-ray beam will pass through the manganese filter since they have an energy well below that of the absorption edge in the manganese. Hence only Fluorescence X-rays contribute to the detected signal.

A prealigned set of electronics was provided by Daresbury Laboratory to process the signal generated by the fluorescence detector. The processed

X-ray absorption
(arbitrary units)



Figure(3.7). The use of a manganese (Z=1) filter heavily attenuates any scattered incident X-rays but allows easy passage of the fluorescence X-ray.

counts were then fed into the data acquisition computer. Using this system it took approximately five hours to collect a good quality spectrum, each datum point in the spectrum representing 10^7 counts.

3.2.5 Electron Yield Detection System

A Total Electron Yield EXAFS system was not available at Daresbury and so one had to be constructed. A small vacuum chamber was built, which was pumped by a Turbo Molecular pump and was capable of reaching a vacuum pressure of 10^{-6} mbar, as shown in Fig. (3.8). A Mylar window allowed the X-rays easy entry into the chamber, while allowing the formation of a good vacuum. An aluminium sample holder was used so that any of the X-ray beam that may have spread over the edge of the passive film sample did not lead to the generation of any structure in the collected data, the absorption coefficient of aluminium being essentially featureless in this part of the spectrum.

The electrons emitted from the sample were detected by a Mullard channeltron type XBL-25, operated in the pulse counting mode as indicated by the channeltron diagram of Fig. (3.10). In this mode each electron entering the detector generates a pulse in the output voltage of the channeltron. These pulses are then fed into a preamplifier having a voltage gain of 10^6 . Because there is always some noise on the output of the preamplifier, it is necessary to pass the signal through a pulse height discriminator. This ensures that only pulses whose height is compatible with their being generated by an electron emitted from the sample are passed onto the counting circuits of the computer. Those pulses whose height is too small or too large are neglected. The setting-up of this pulse height discriminator is time consuming and complex. However, once

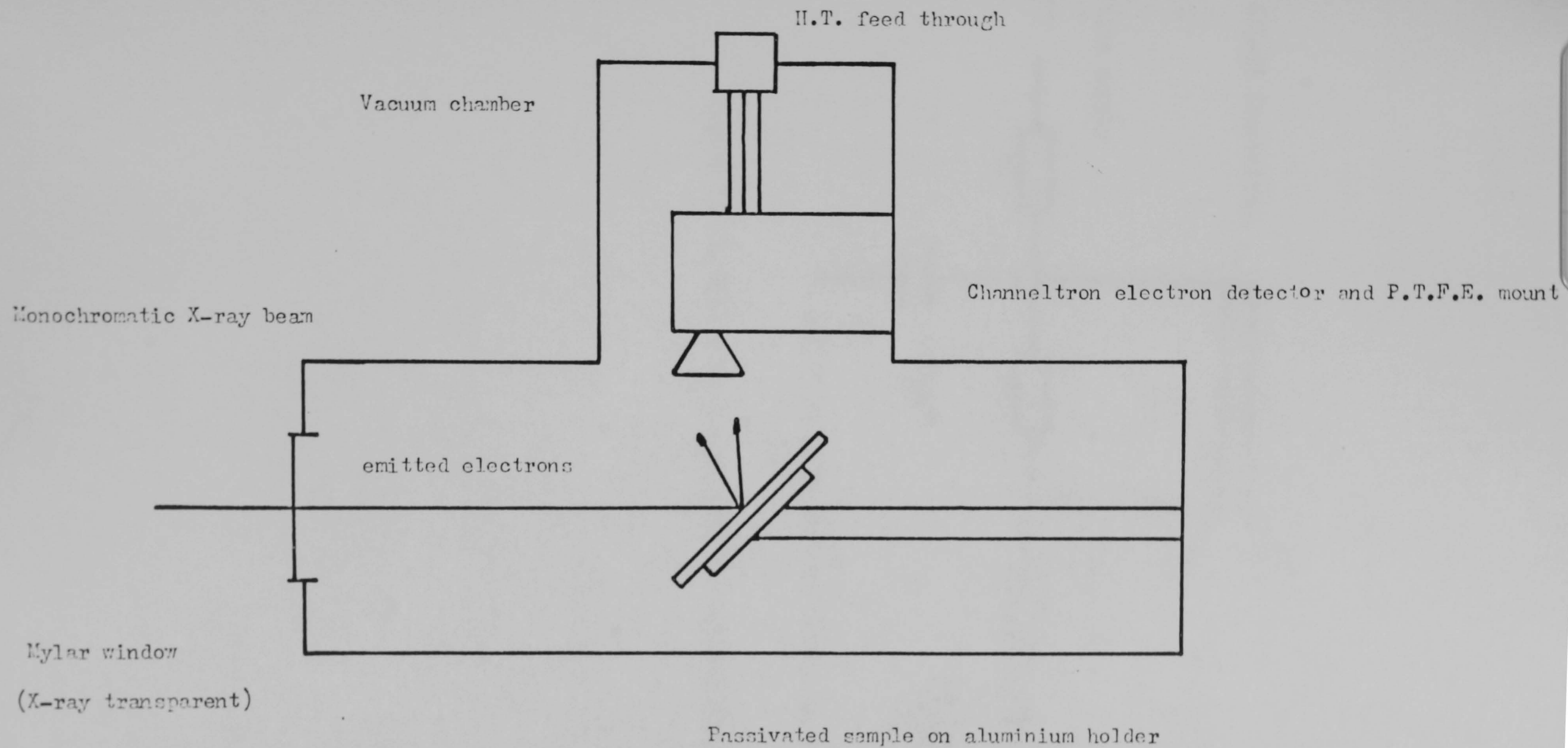


Figure (3.8). Schematic diagram of the vacuum chamber built for the total electron yield EKAES measurements.

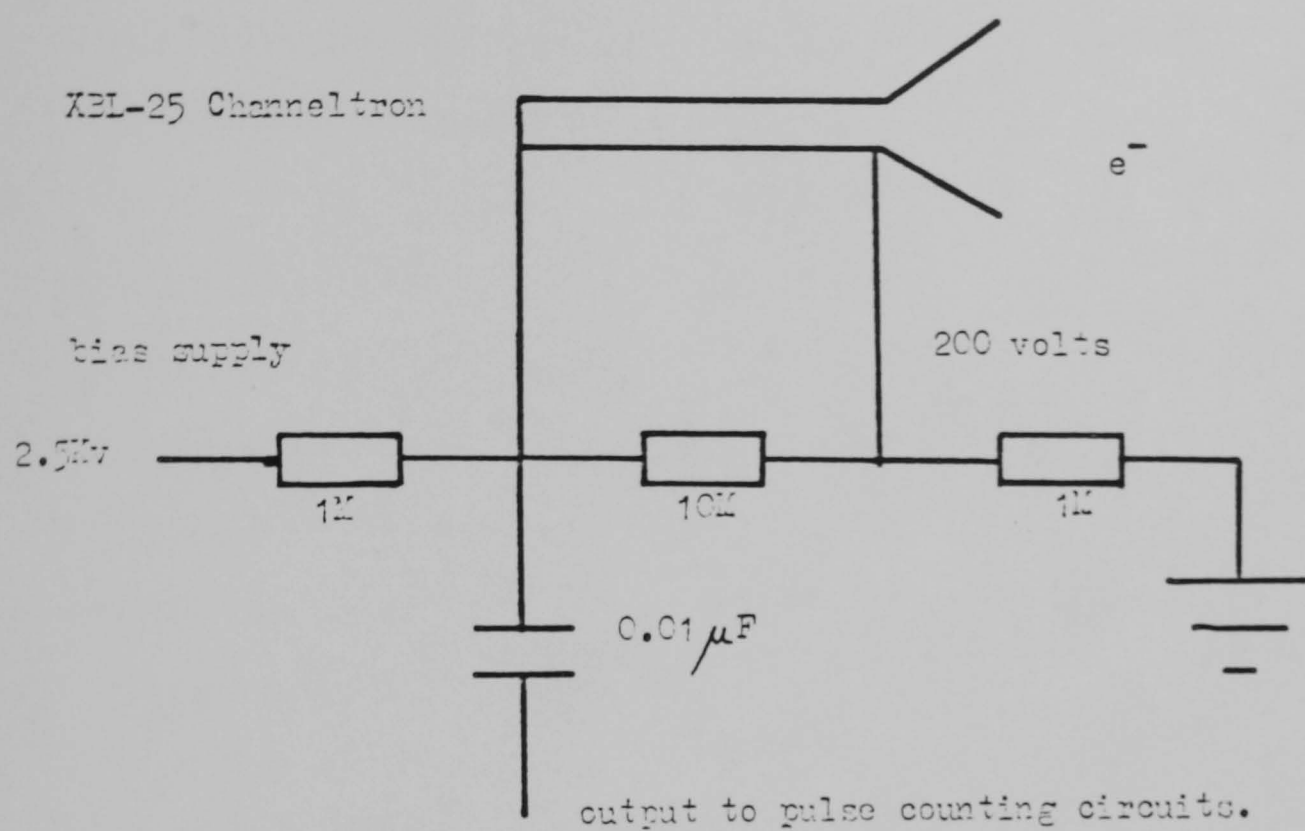


Figure (3.6). Bias circuit used with the Mullard XBL-25 channeltron.

set correctly good quality spectra were easily obtained by collecting data over several hours, typically each point in the spectrum resulting from 10^6 electron counts.

3.3 Data Collection

X-ray absorption data were collected over approximately an 800eV range extending from 100eV below the absorption edge to 700eV above the edge, Measurements were made every 3 to 5eV, except in the immediate vicinity of the edge when data were collected every 1eV.

In order to ensure that the EXAFS data was of sufficient quality to allow bond length determination, it is necessary to make sure that each point contained in a dataset has a sufficiently low signal-to-noise ratio. In the existing experimental arrangement this required that each point must be counted on for approximately one minute. This means that it would take many hours to obtain a completed spectrum for one sample. The lifetime of the stored beam on the S.R.S. is on the same timescale, and intermittent beam losses can reduce the "beam time" further. This means that in any experiment one could only rely on the presence of the beam for times of up to one hour. It was therefore experimentally prudent to take several one hour scans of a sample and average the results at the end. Thus if the beam were lost during a run, only that one hour's worth of data was lost, the remaining scans being unaffected.

The selection of X-ray wavelength and associated movement of the sample, together with the data acquisition were accomplished by the local computer system provided by Daresbury. This ran a suite of programs that could deal with both the Fluorescence and Total Yield experiments, and transfer of the experimental data to the main computer for storage and analysis.

3.4 Averaging and Calibration

Before dealing with the analysis of the EXAFS, it is necessary to average and calibrate the single scans that make up a complete dataset for each sample. This task was performed using a suite of programs available at Daresbury, two major features of which will be outlined here.

Since some backlash and thermal drift may be present in the monochromator, it is necessary to align the separate scans before averaging. The shifts involved may only be small, typically less than 2eV, however they do prevent chemical information being obtained from the position of the absorption edge. Since the monochromator was calibrated with metallic chromium or iron at the start of every session, it is more likely that the first experimental scan will be the most accurately calibrated. For this reason all other scans were aligned to it.

The suite of programs also allowed the removal of background effects from the measuring system, such as the absorption in air of the X-rays. To do this a scan is made over the same data range with no sample present. This normalisation spectrum may then be subtracted from the averaged spectrum described above.

4. EXAFS Analysis

4.1 Introduction

This chapter describes how structural information contained in the EXAFS spectrum is obtained from the experimental dataset. The starting point for the analysis route is the calibrated and averaged spectrum described at the end of Chapter 3. The analysis route may be described in three stages: smoothing, background subtraction and finally Fourier transformation to generate a pseudo-radial distribution function (R.D.F.).

There is a need to correct the bond lengths indicated by these pseudo R.D.F.'s because of the shifts introduced by the phase change that the photoelectron suffers upon scattering from neighbouring atoms. The determination of these correction factors for all the atom pairs studied is presented.

Finally, the errors present in any bond length determination are also evaluated. One cause of error is uncertainty in the choice of the edge position E_0 . The effect of this choice has been investigated by the use of the single shell analysis method. This method allows the comparison of individual bond-length peaks in the model compound and unknown R.D.F.'s to be compared in a more precise manner than the simple comparison of R.D.F.'s. The chapter concludes with a table listing the correct factors for all the atom pairs investigated in this way, and the errors inherent in the bondlength determinations.

4.2 Data Smoothing

As an example of the calibrated and averaged datasets described at the end of Chapter 3, the EXAFS from a nitrite passive iron film is shown in Fig. (4.1). While the EXAFS oscillations are clearly visible, it is apparent that a considerable amount of high frequency noise is present upon the signal. This noise can cause considerable difficulty in the latter stages of the analysis, where as we shall see later it is necessary to 'weight' the higher energy end of the spectrum with respect to the lower energy end and truncate the data. This whole process is made much more difficult in the presence of any noise.

For this reason the data were Spline smoothed using a routine available at the Daresbury laboratory. This essentially removed the high frequency noise but left unaffected the EXAFS oscillations. The effect of this smoothing may be seen in Fig. (4.2), where the EXAFS dataset for the nitrite passivated film is superimposed upon a smoothed version of the same dataset. The effect of this routine upon the radial distribution function and the measured bond lengths is described later.

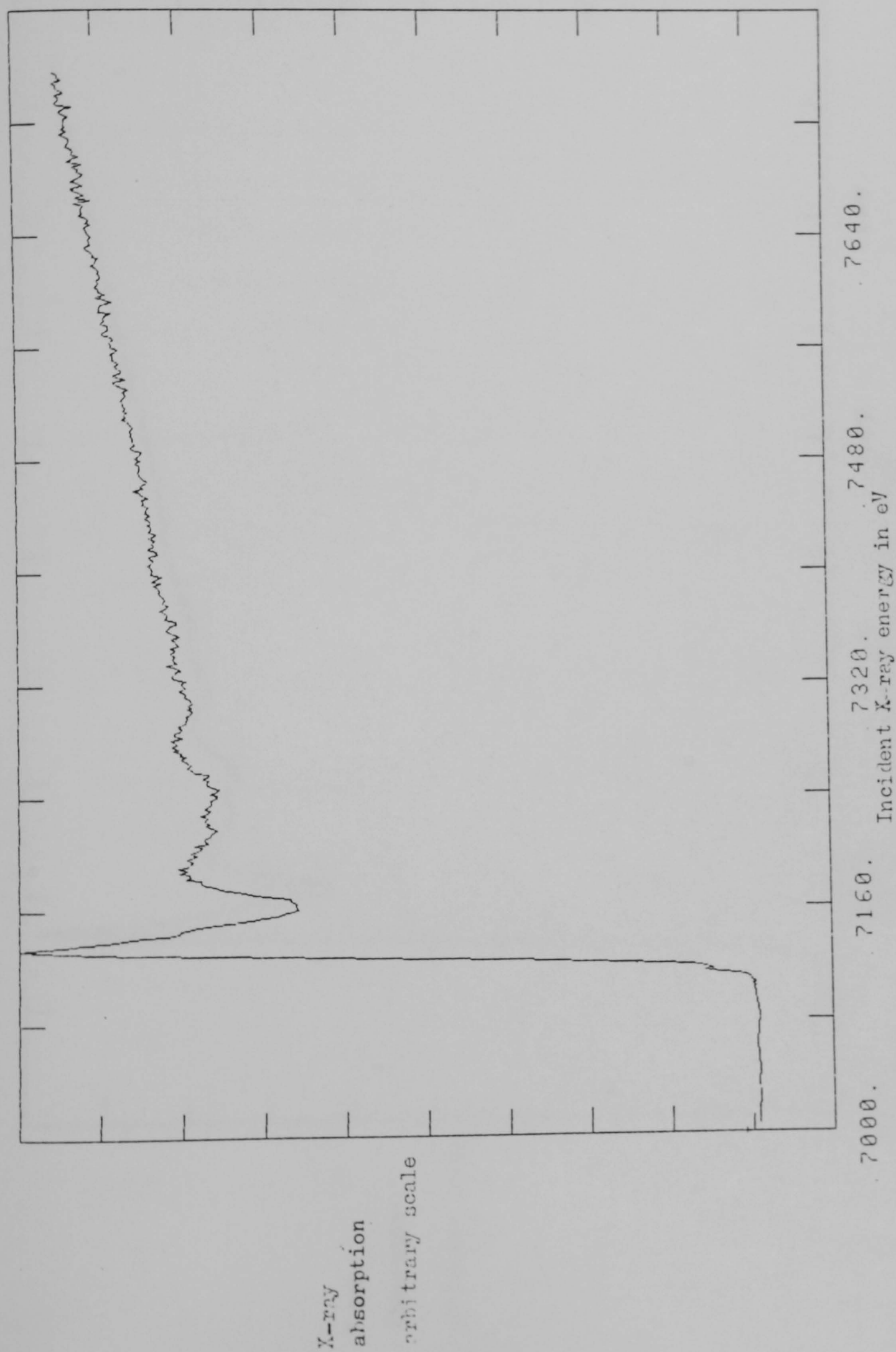


Figure (4.1). EXAFS spectrum of a nitrite passivated iron film, showing the presence of high frequency noise.

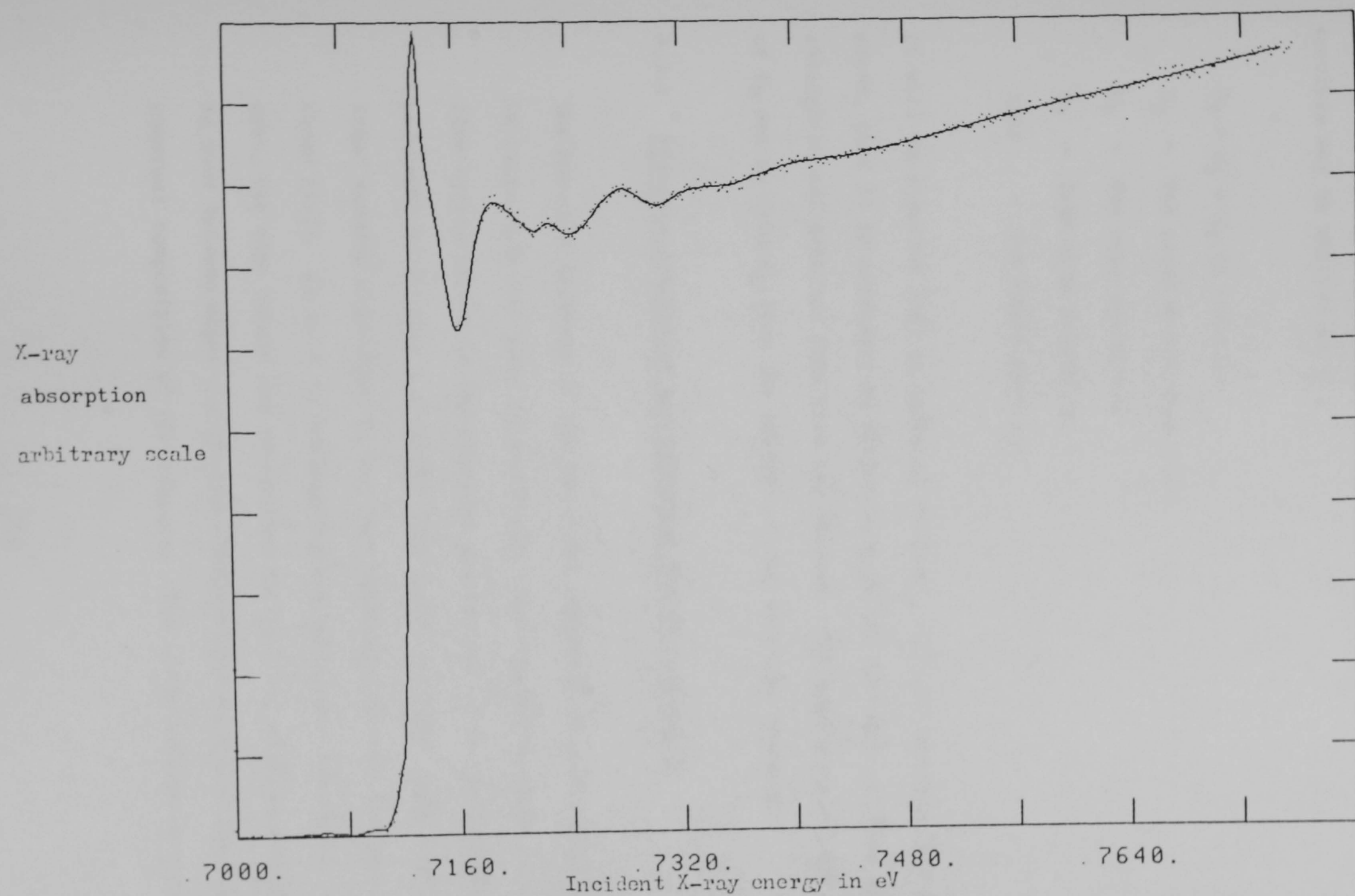


Figure (4.2). The smoothing effect of the Daresbury spline routine upon the high frequency noise seen in the spectrum of figure (4.1).

4.3 Background Removed

It will be recalled from Chapter 2 that the experimental X-ray absorption spectrum may be written as U_T

$$U_T = U_b + U_f (1 + X(\xi)) \quad (4.1)$$

U_T - The total X-ray absorption

U_b - Pre edge absorption

U_f - Free atom absorption

$X(\xi)$ - The EXAFS function

It will be apparent that in order to isolate the EXAFS function $X(\xi)$ from the above, that it is necessary to determine both the pre-edge and free atom absorption and subtract them from the dataset. The approximation and removal of U_b and U_f from U_T form the subject of the next two sections.

4.3.1 Pre-edge Absorption Approximation and Normalisation

The smoothed datasets of the two model compounds Fe and $\alpha\text{-Fe}_2\text{O}_3$ are shown in Figs.(4.3a and 4.3b) respectively, superimposed on each is a straight line approximation to the pre-edge absorption. This approximation was generated by fitting a straight line to the pre-edge region (X-Y) using a least squares algorithm; U_b was then extrapolated over the whole dataset range (X-Z). As well as subtracting the background absorption from the data, the edge height was normalised to it. This allowed comparisons to be made between edges and provided information regarding the relative chemical composition of the samples. Thus a new dataset is generated

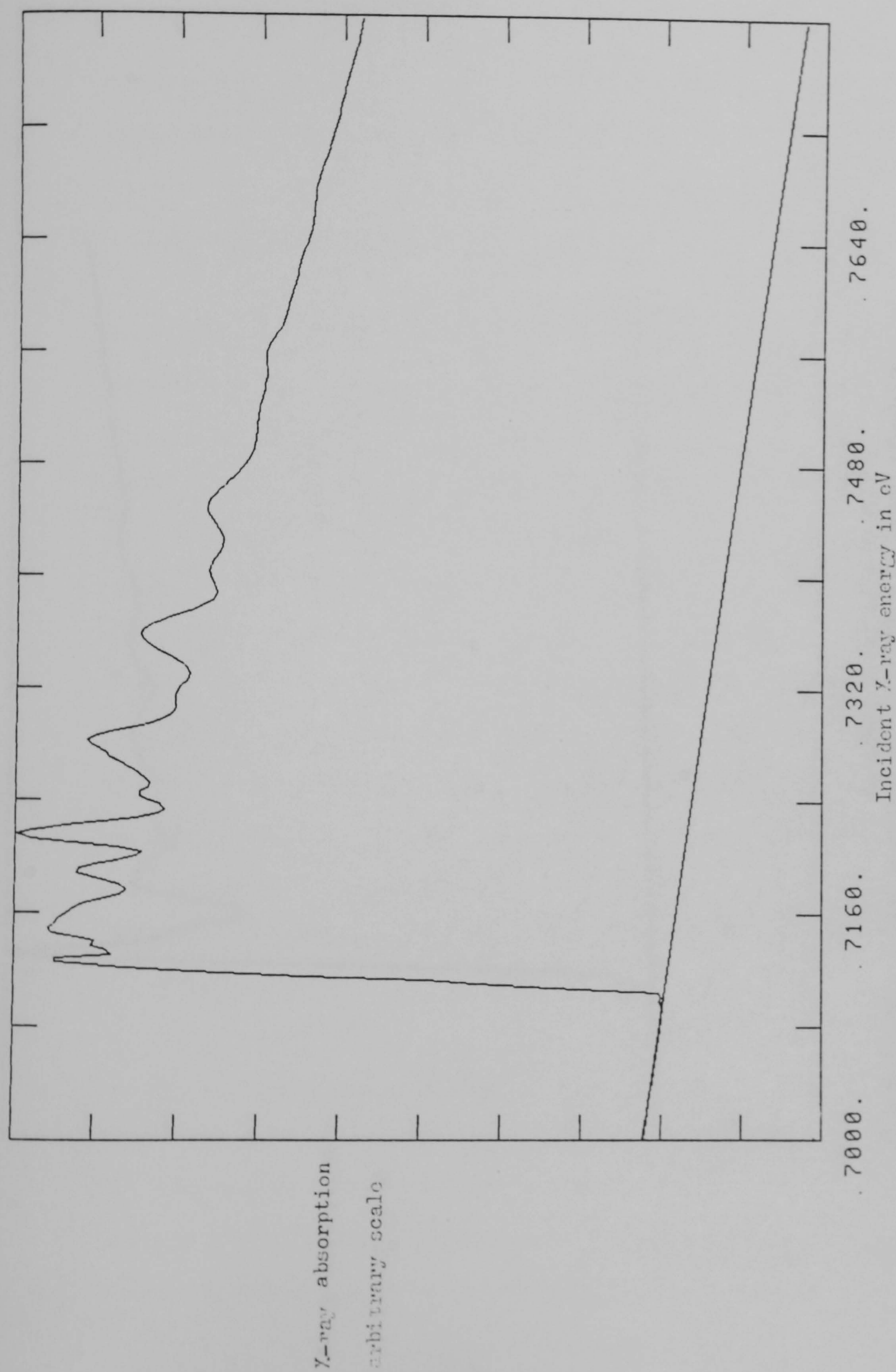
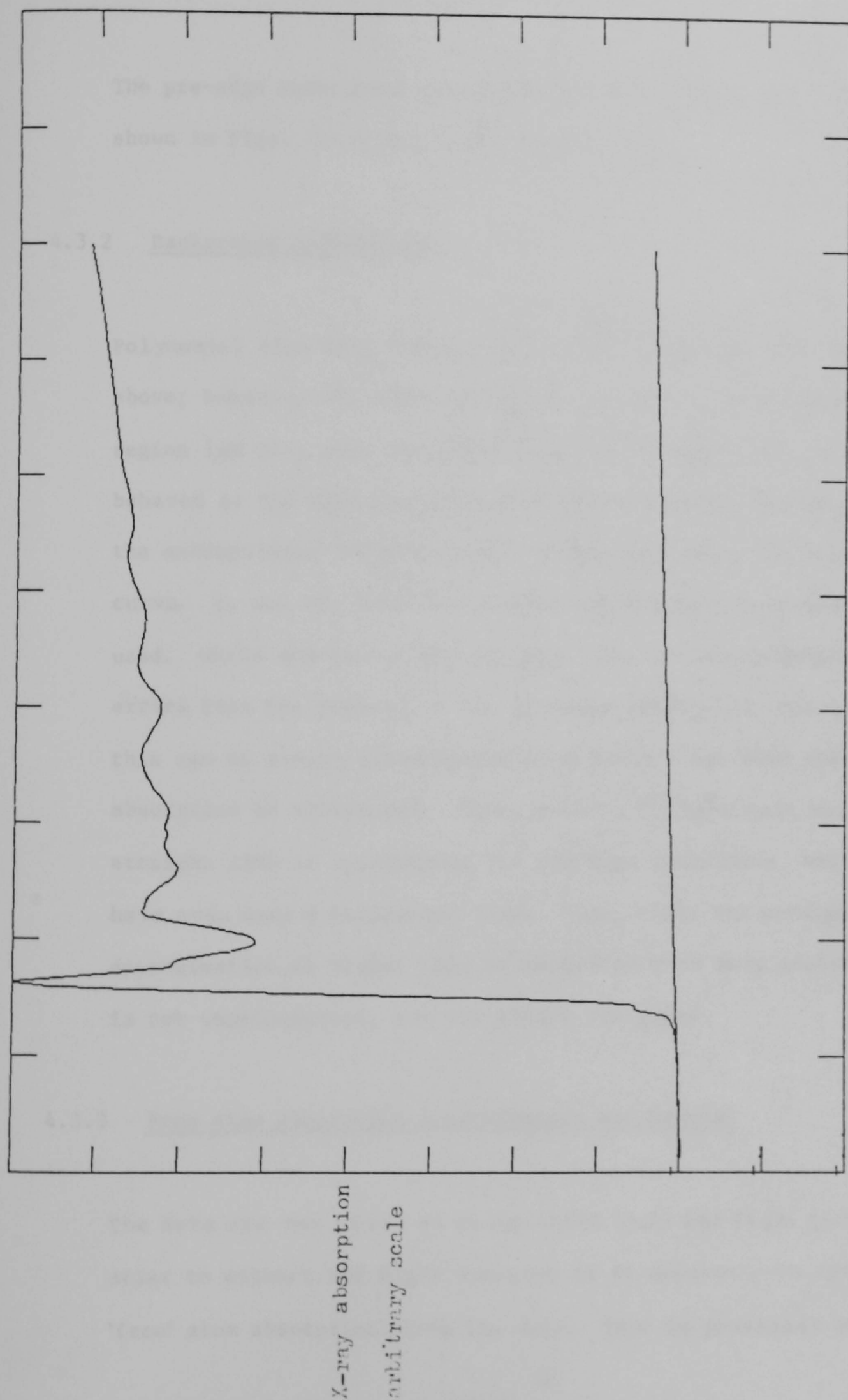


Figure (4.3a). Spline smoothed 'K' edge EXAFS spectrum of pure iron.



7000. 7160. 7320. 7480. 7640.
Incident X-ray energy eV

Figure (4.3b). Spline smoothed 'K' edge EXAFS spectrum of $\alpha\text{Fe}_2\text{O}_3$.

as

$$U_T - U_b = U_f (1 + X(E)) \quad (4.2)$$

The pre-edge subtracted and normalised data for Fe and $\alpha\text{-Fe}_2\text{O}_3$ are shown in Figs. (4.4a and 4.4b) respectively.

4.3.2 Background Subtraction

Polynomial fits were tried instead of the straight line described above; however, the short region of the data recorded in the pre-edge region led to a poor quality fit and the extrapolated curve being badly behaved at the high energy part of the spectrum. Indeed, in some cases the extrapolated curve was seen to intersect with the total absorption curve. It was for this reason that the straight line approximation was used. While the use of the straight line obviously introduces some errors into the removal of the pre-edge absorption from the dataset, this can be easily accommodated at a later stage when the free atom absorption is subtracted. Other workers⁽⁴⁴⁾ have made use of a straight line to approximate the pre-edge absorption, while some⁽⁴⁵⁾ have even used a horizontal line. Thus, while the straight line approximation is cruder than we should perhaps have wished to use it is not unprecedented, nor its effect too great.

4.3.3 Free Atom Absorption Approximation and Removal

The data are now given as in equation (4.2) and Figs. (4.4a, 4.4b). In order to extract the EXAFS function it is necessary to remove U_f (the 'free' atom absorption) from the data. This is generally not known and

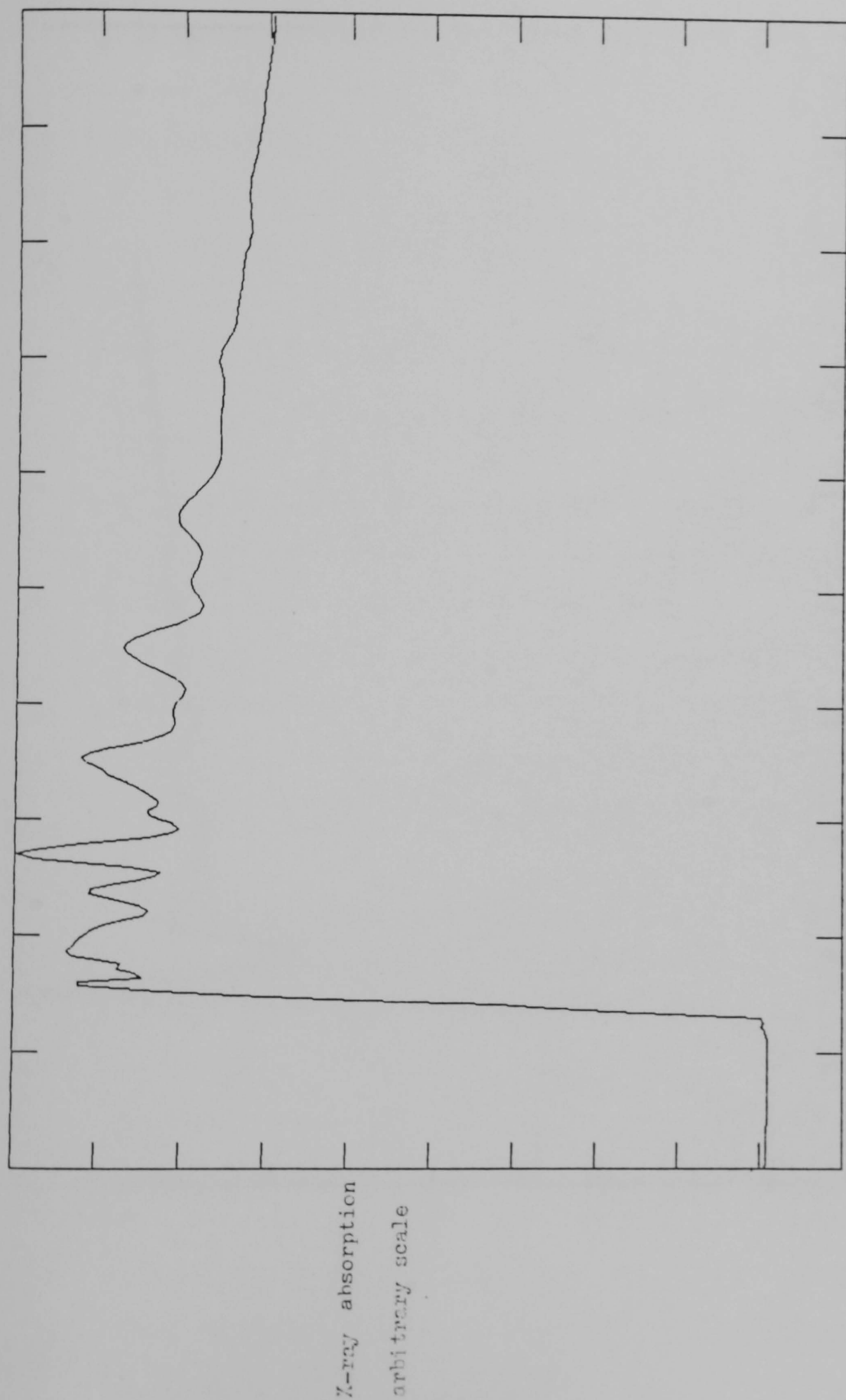


Figure (4.4a). Pre-edge absorption subtracted and normalised spectrum of the iron 'K' edge.

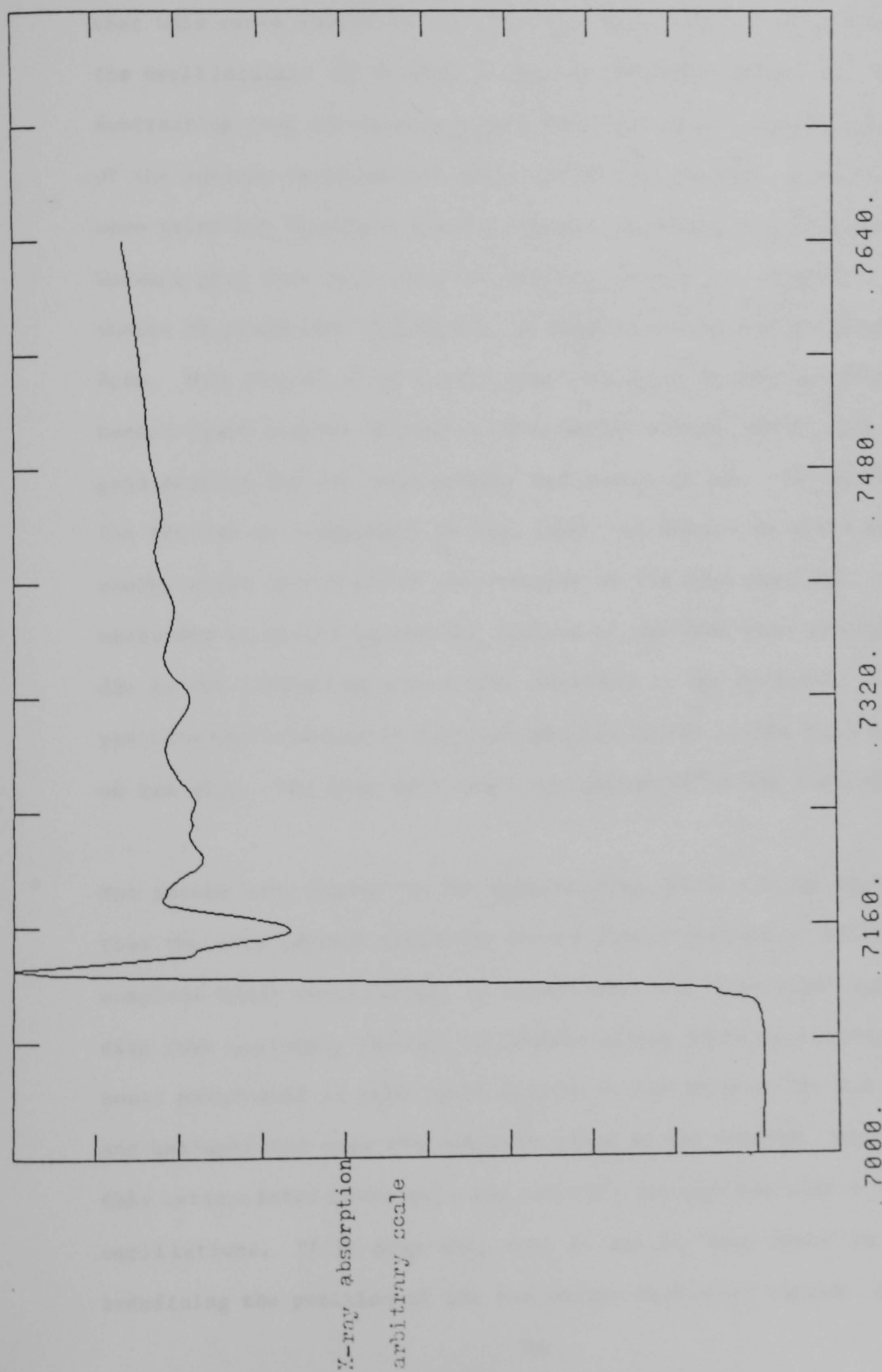


Figure (4.4b). Pre-edge absorption subtracted and normalised spectrum of the iron 'K' edge in $\alpha\text{-Fe}_2\text{O}_3$

and must be obtained empirically. The approach adopted is to determine it as follows. A curve is least squares fitted to the dataset such that it passes through the middle of the EXAFS oscillations. It is important that this curve should be sufficiently 'rigid' that it does not follow the oscillations. If it were to follow the oscillations its subsequent subtraction from the dataset would introduce errors into the amplitudes of the various oscillations contained in the dataset. Several methods were tried for fitting a suitable curve. A spline routine available at Warwick gave some good results; however, it was very sensitive to the choice of parameters that had to be made to select its stiffness and form. This proved to be a very time consuming process and so a polynomial least squares fitting routine was developed, which gave equally good results but was much quicker and easier to use. The operation of the routine is summarised in Fig. (4.5). It should be noted that the energy scale is now given with respect to the edge position. This was necessary to ensure successful fitting of the free atom absorption curve, due to the limited atom numerical accuracy of the computer. The edge position was arbitrarily but consistently chosen as the half height point on the edge. The free atom curve was generated in the following way.

Two points were chosen in the dataset, Fig. (4.5). It is important that the data between these two points should contain at least one complete EXAFS oscillation, to ensure that the 'free atom' approximation runs uniformly through the middle of the EXAFS oscillations. A cubic polynomial is then least squares fitted between the two points and extrapolated over the complete range of the dataset. Hopefully, this extrapolated curve will run smoothly through the middle of the oscillations. If it does not, then it can be 'fine tuned' by redefining the position of the two points initially chosen. Suitable

X-ray absorption
arbitrary scale

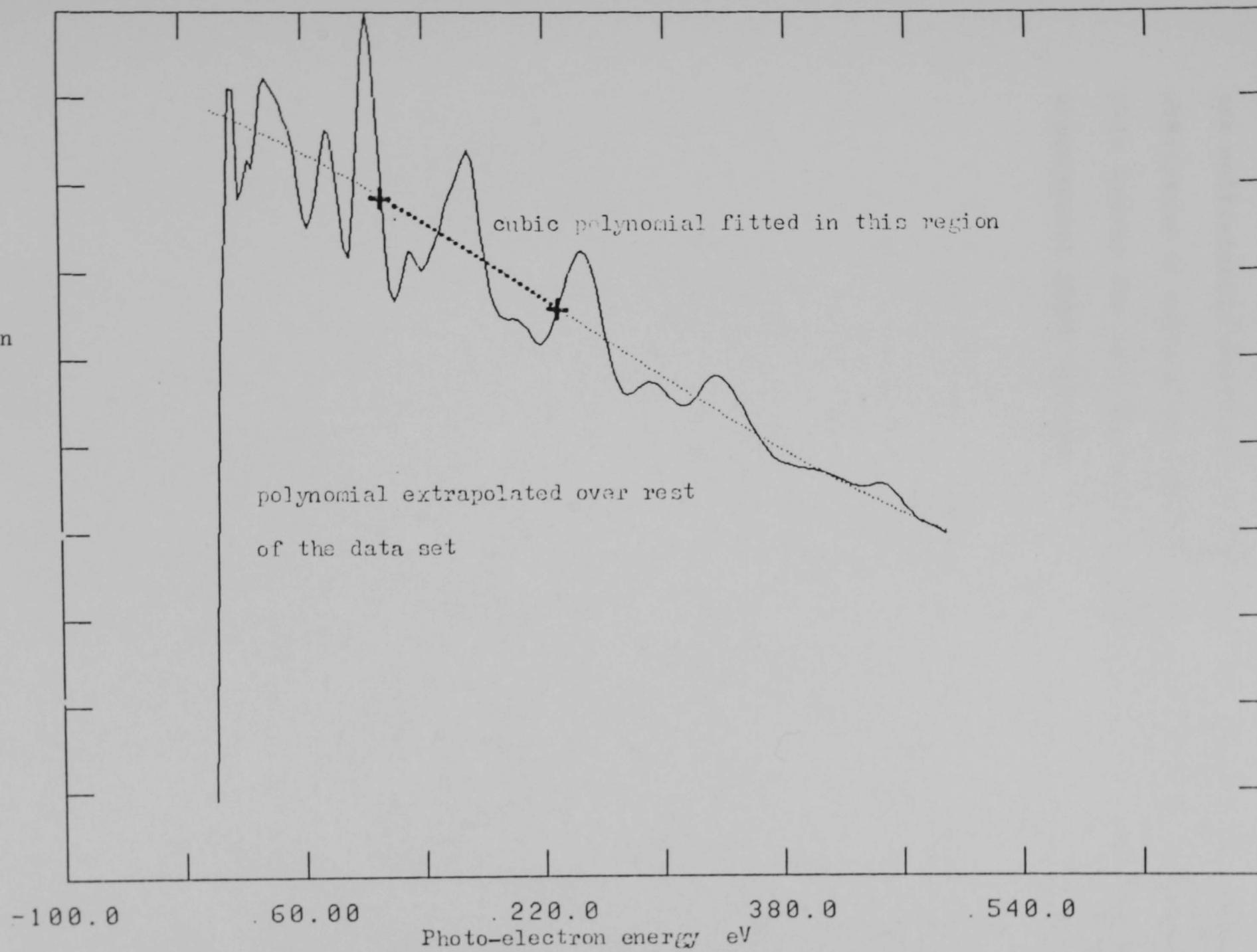


Figure (4.5). Cubic polynomial fit to approximate the free atom X-ray absorption.

approximations to the free atom absorption for the two model compounds of Fe and α -Fe₂O₃ are shown in Figs. (4.6a, 4.6b) respectively. It should be noted that these curves run through the middle of the oscillations but are sufficiently stiff not to follow them. Again this extrapolated absorption is subtracted from the data, and the data normalised to it. This leaves the data as shown in Figs. (4.7a, b). The result is the experimental EXAFS function.

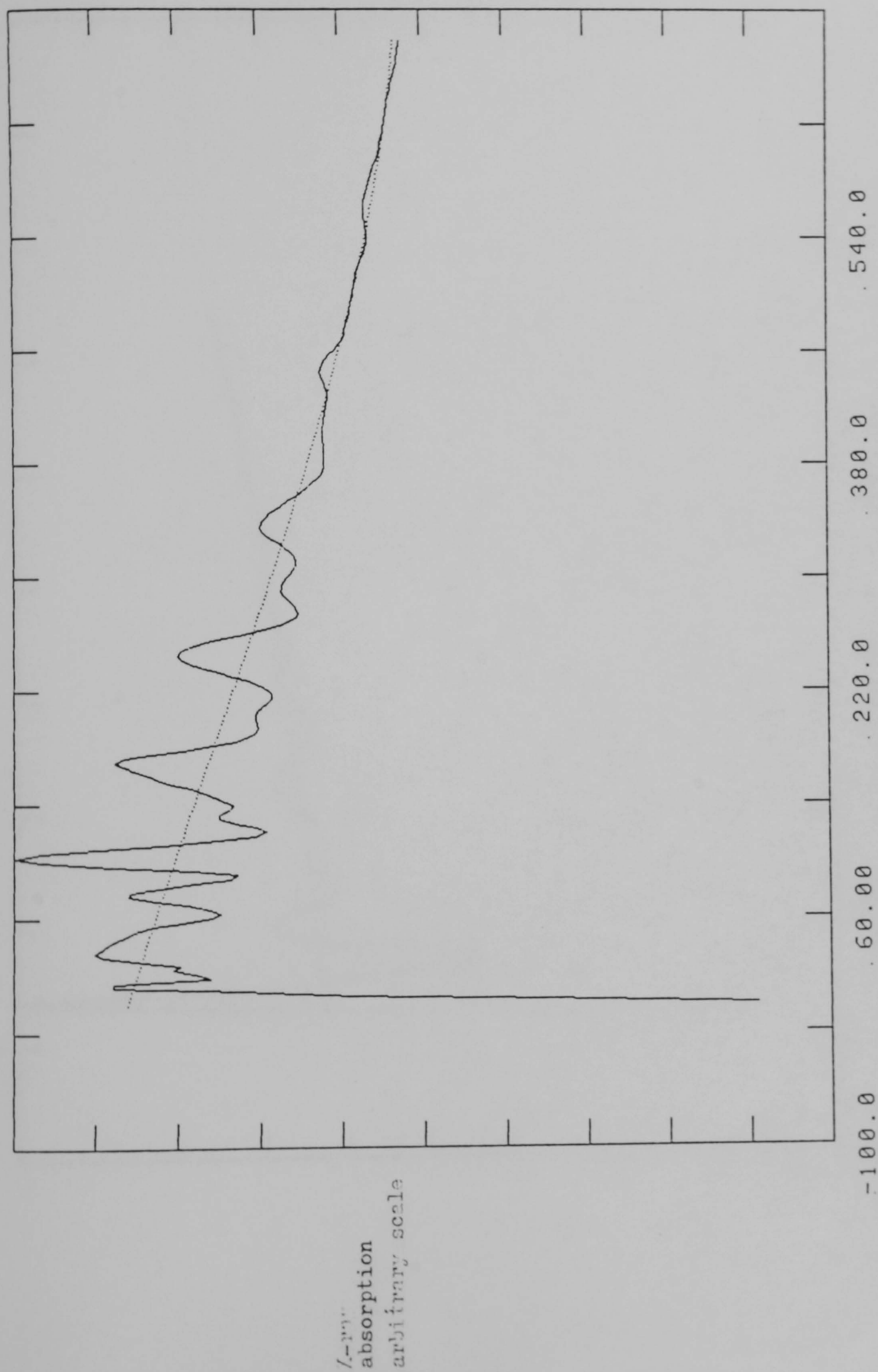


Figure (4.6a). Free atom X-ray absorption approximation generated in the analysis of iron K edge EXAFS.

X-ray
absorption
arbitrary scale

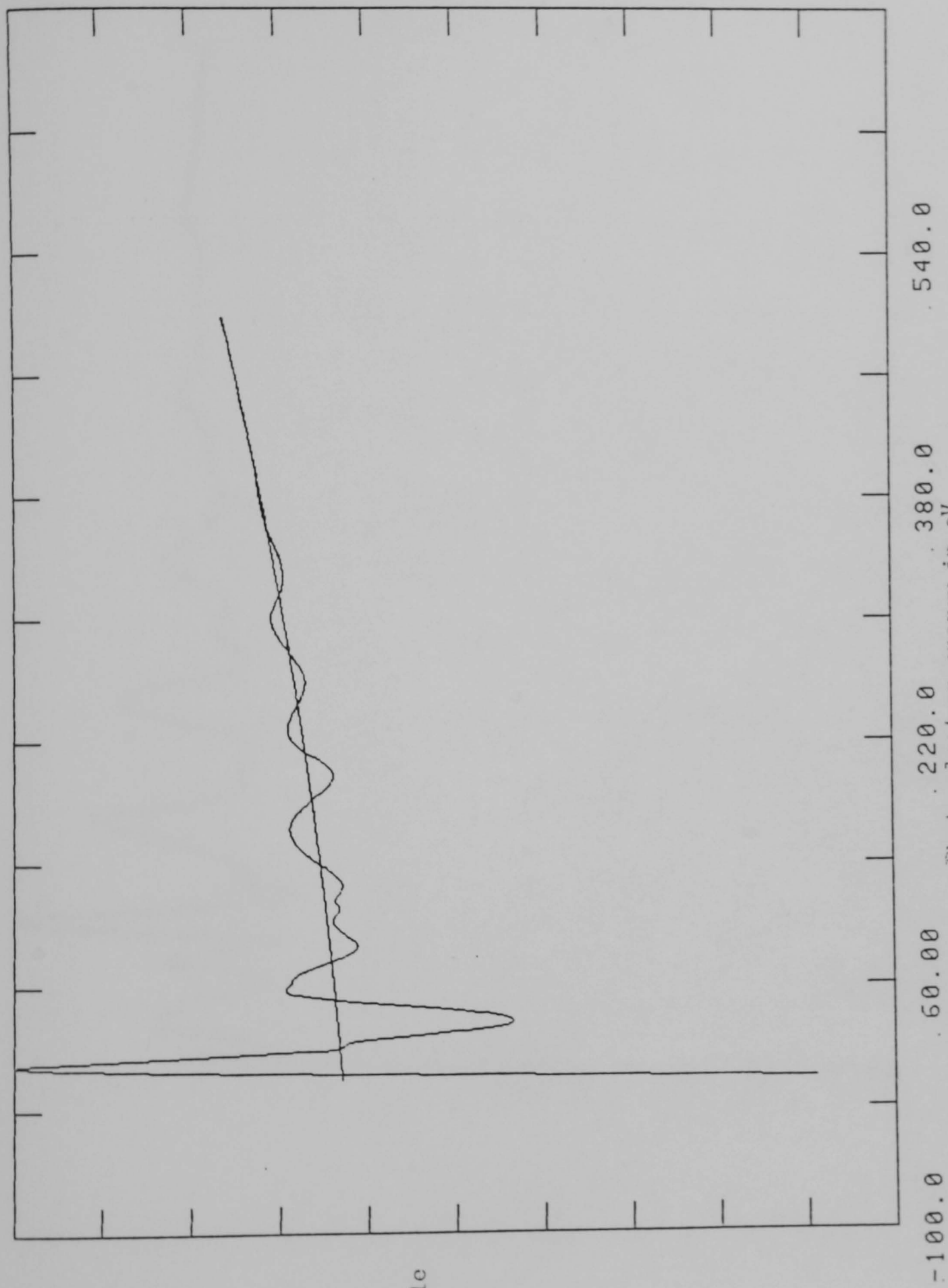


Figure (4.6b). Free atom X-ray absorption approximation generated in the analysis of $\alpha\text{-Fe}_2\text{O}_3$.

K- $\mu\mu\gamma$
absorption
arbitrary scale

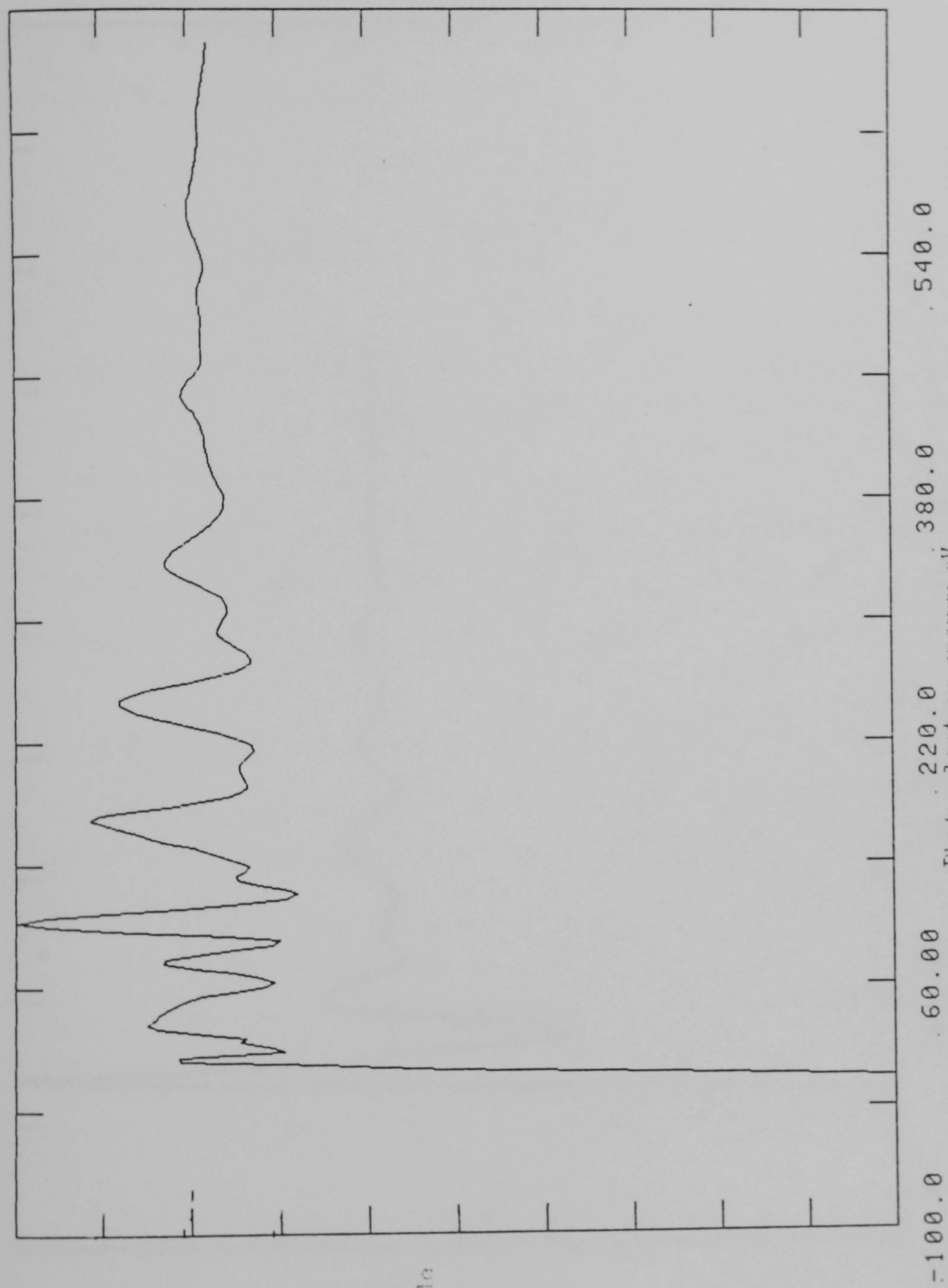


Figure (4.7a). The experimental EXAFS function of iron.

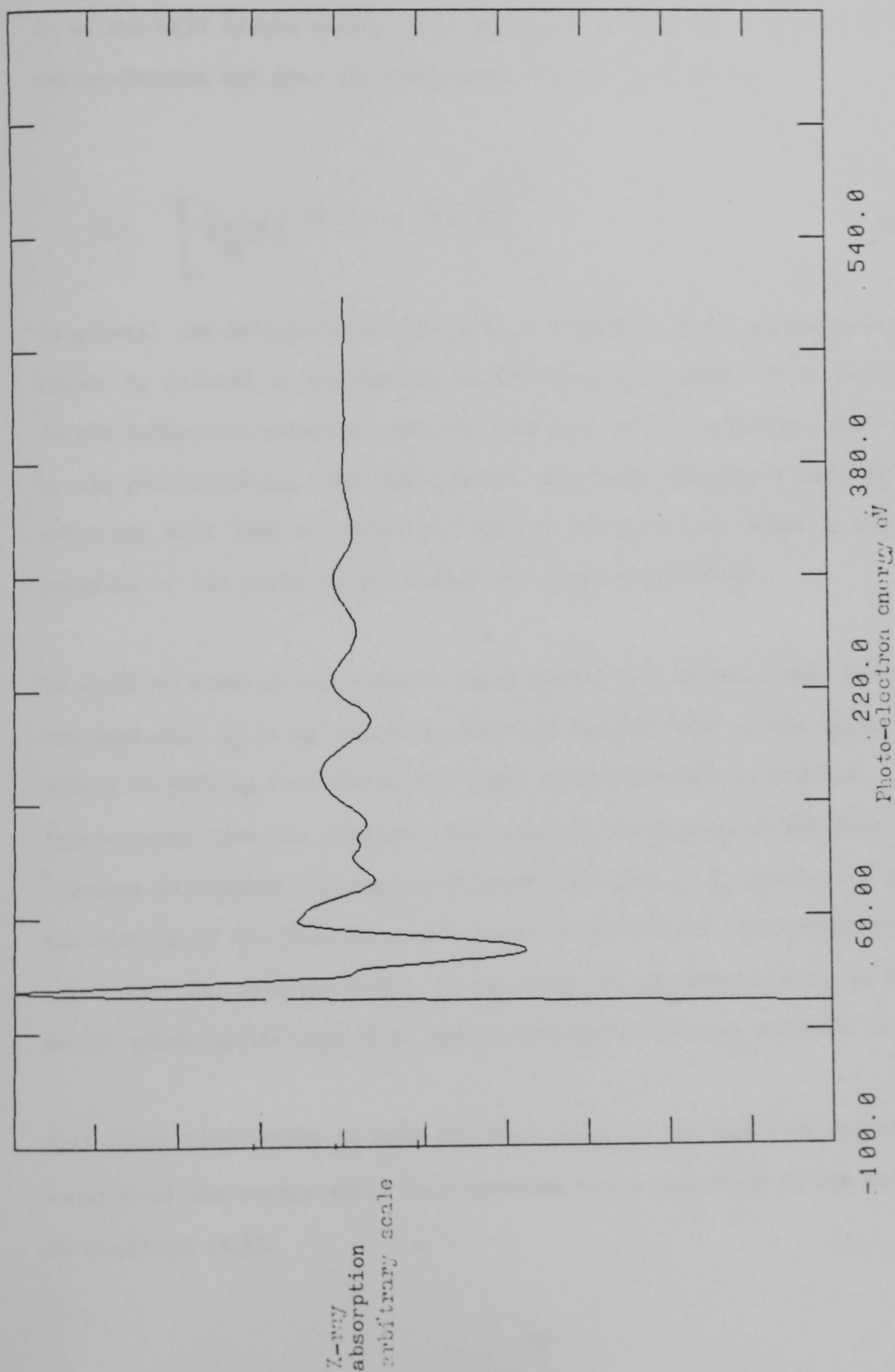


Figure (4.7b). The experimental EXAFS function of $\alpha\text{-Fe}_2\text{O}_3$.

4.4 Conversion to Momentum Space and The E₀ Problem

In the previous sections we had to define the edge position and chose to place it at the half height point. This not only defines the energy, E of the photo-electron but also its wavenumber k which is given by

$$k = \left[\frac{2m_e}{\hbar} (\hbar \omega - E_0) \right]^{1/2} \quad (4.3)$$

In general the definition of the zero of momentum of the photoelectron cannot be related to any feature in the absorption edge. It is related to the ionisation potential and the mean interatomic potential experienced by the photoelectron. For this reason the choice made above will be in error and will lead to errors in both the photoelectron momentum and the position of the peaks in the radial distribution function.

In order to minimise and control these errors all datasets were treated in the same way, E₀ being chosen at the half height point on the edge. The effect of varying this choice was later investigated by a routine incorporated into the program. Prior to the conversion of the data to photo-electron wavenumber the program allowed the value of E₀ previously defined in the fitting of the free atom absorption to be varied. The effect of these variations and thus the effect of any error in the choice of E₀ as the half height point on the edge have been investigated and are reported later.

With these limitations in mind the next stage of the analysis was the conversion of the energy scale to a momentum scale according to the relationship in equation (4.3).

Again the effect of this part of the data analysis is shown with reference to the two model compounds Fe and $\alpha\text{-Fe}_2\text{O}_3$ in Figs. (4.8a, and b).

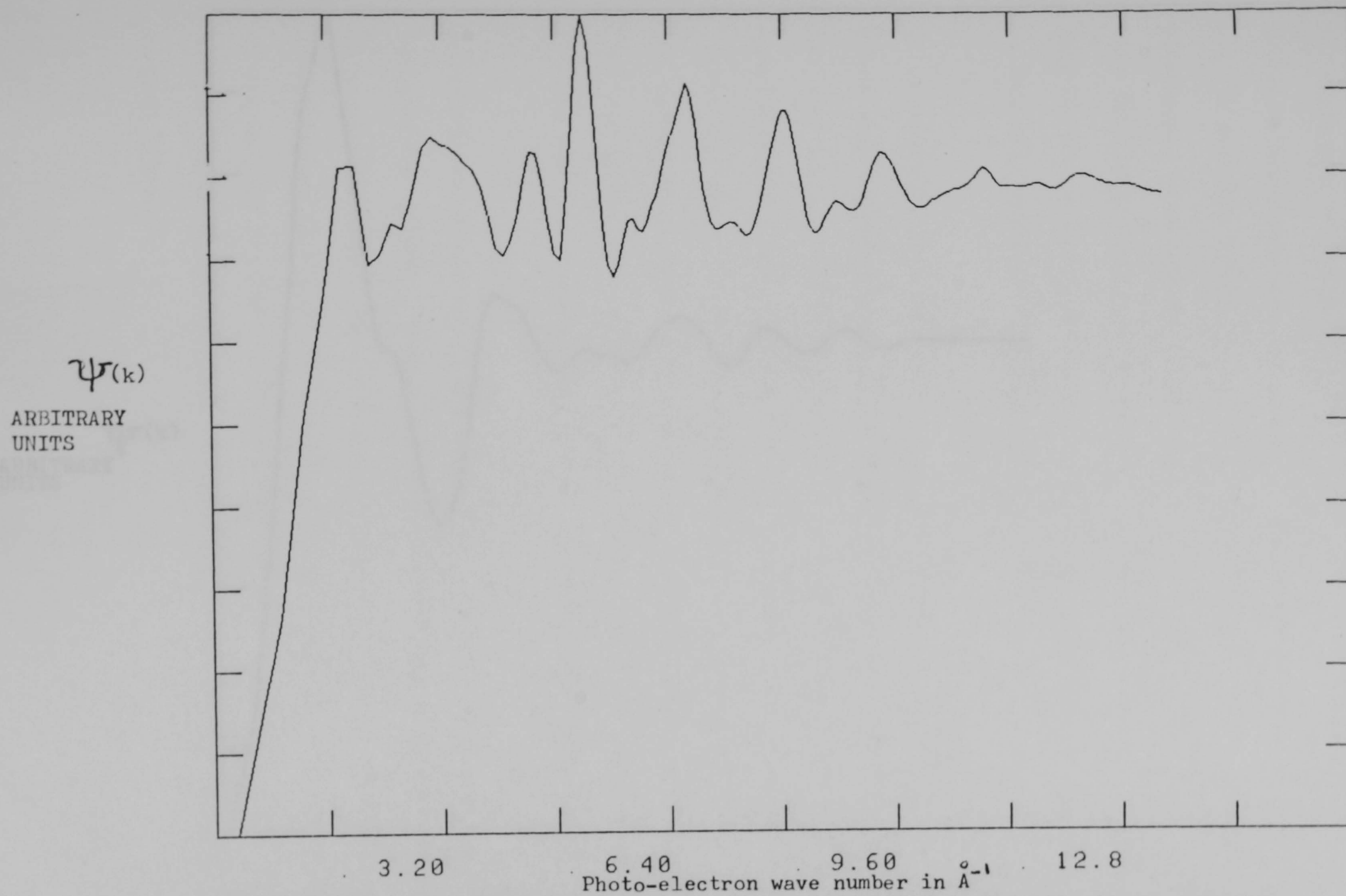


Figure (4.8a). The EXAFS function of Iron as a function of photo-electron wavenumber.

ARBITRARY
UNITS $\chi(k)$

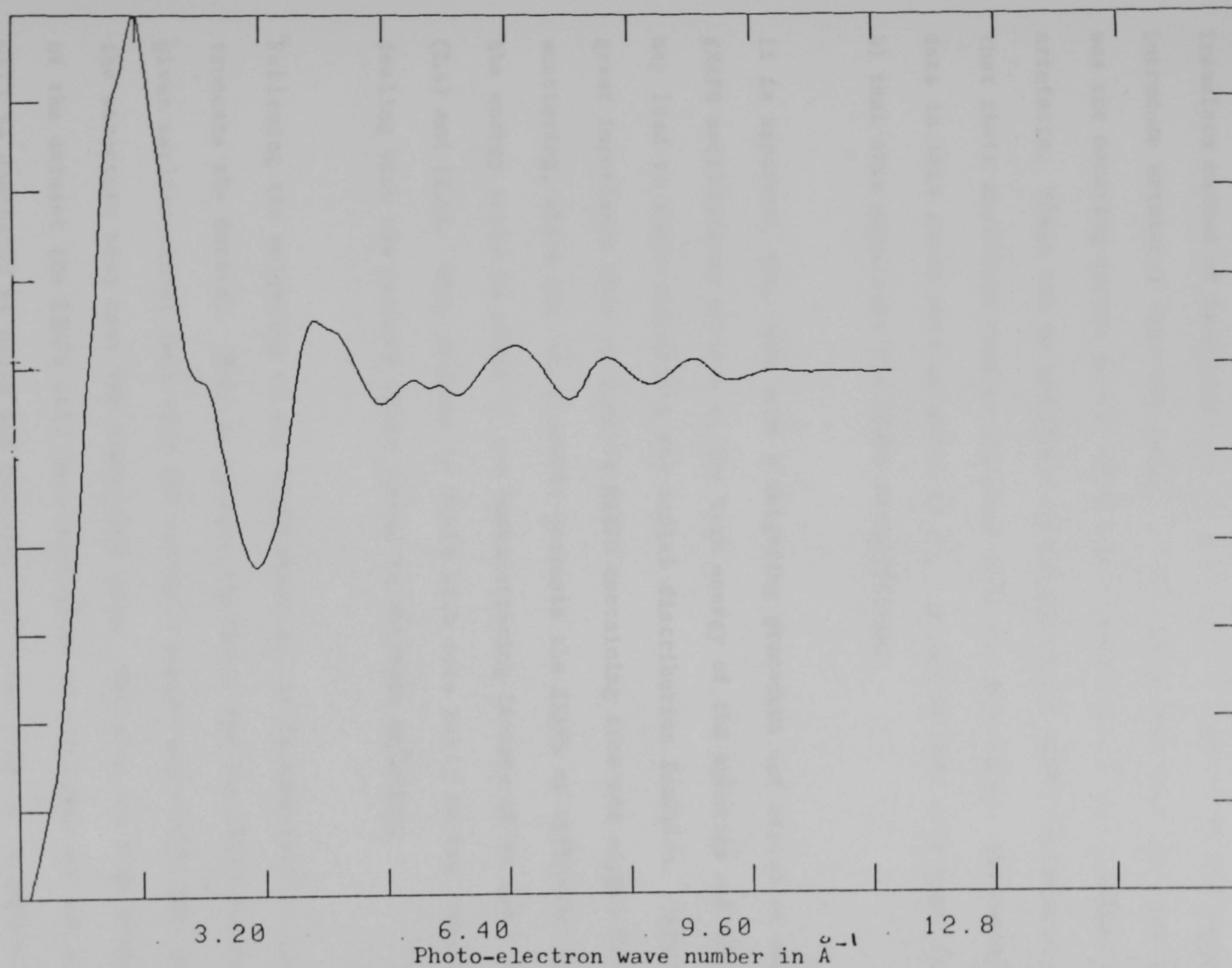


Figure (4.8b). The EXAFS function of $\alpha\text{-Fe}_2\text{O}_3$ as a function of photo-electron wavenumber.

4.5 Weighting and Data Truncation

It will be recalled from Chapter 2 that a disadvantage of the Fourier Transform method of data analysis is that the very nature of the transform can introduce artefacts into the radial distribution function. One such problem was the decaying nature of the EXAFS oscillations which can generate sideband artefacts. These can be minimised by weighting the EXAFS oscillations such that their amplitude remains constant over the data range. Following⁽³⁹⁾ the data in this study were weighted by k^2 . It can be seen from Figs. (4.9a and b) that this equalises the EXAFS oscillations.

It is apparent, too, that such a weighting procedure can emphasise unduly any EXAFS oscillations present at the high energy of the spectrum and that this may lead to their dominating any radial distribution function. This is of great importance when we analyse EXAFS containing iron and oxygen back-scattering, where the two elements dominate the EXAFS at different parts of the energy scale as shown by the backscattering factors of Fe and O in Figs. (2.4) and (2.5). This problem is dealt with more fully in the results section dealing with the passive films formed in chromate solution.

Following the weighting of the EXAFS function, it is necessary to limit or truncate the dataset. This is because the model for the EXAFS function given earlier cannot deal with the multiple scattering events that determine the structure seen near the absorption edge. While at the high energy end of the dataset the EXAFS will have diminished in amplitude and the spectrum will be dominated by noise and features left over from the background removal routines.

$k^2 \chi(k)$

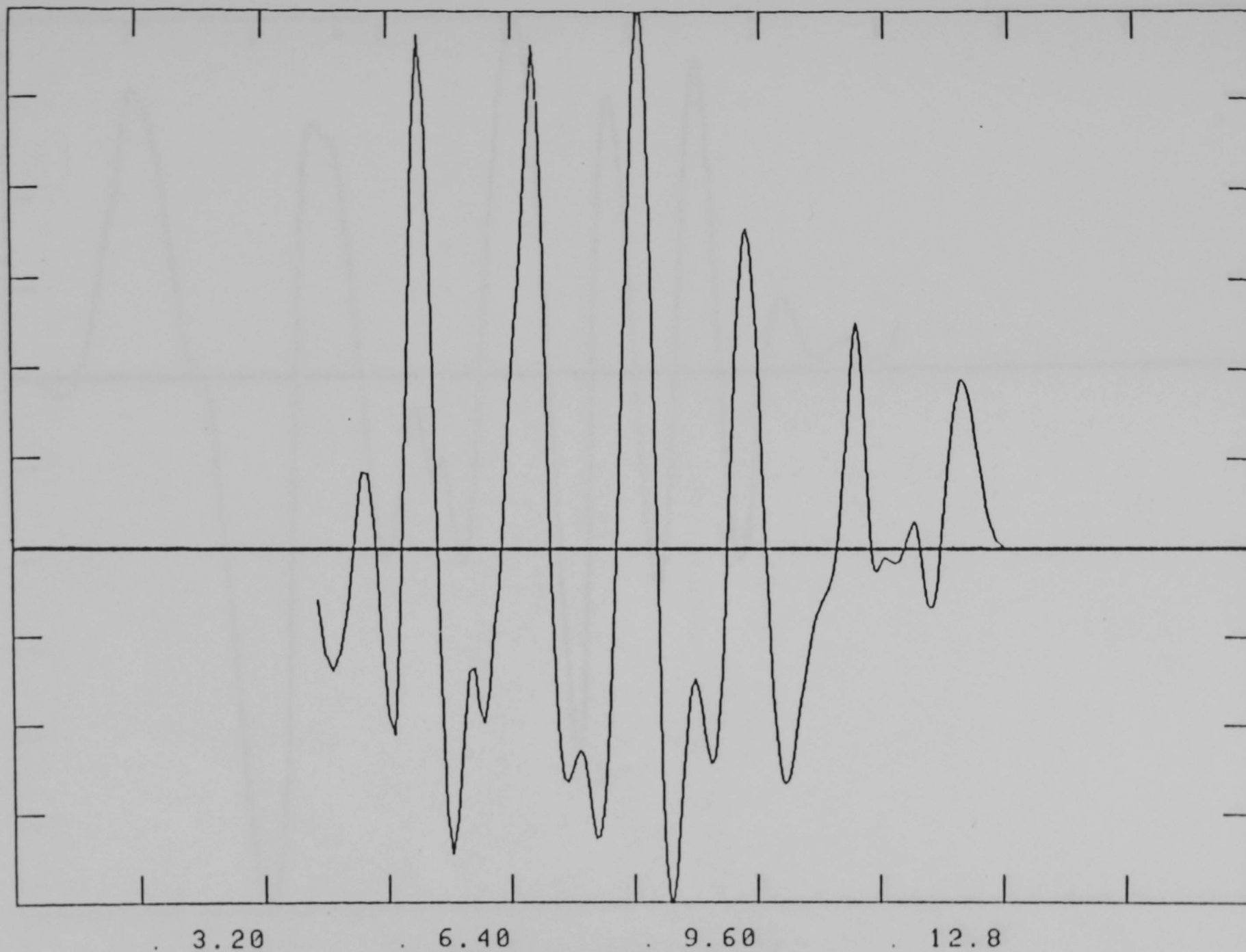
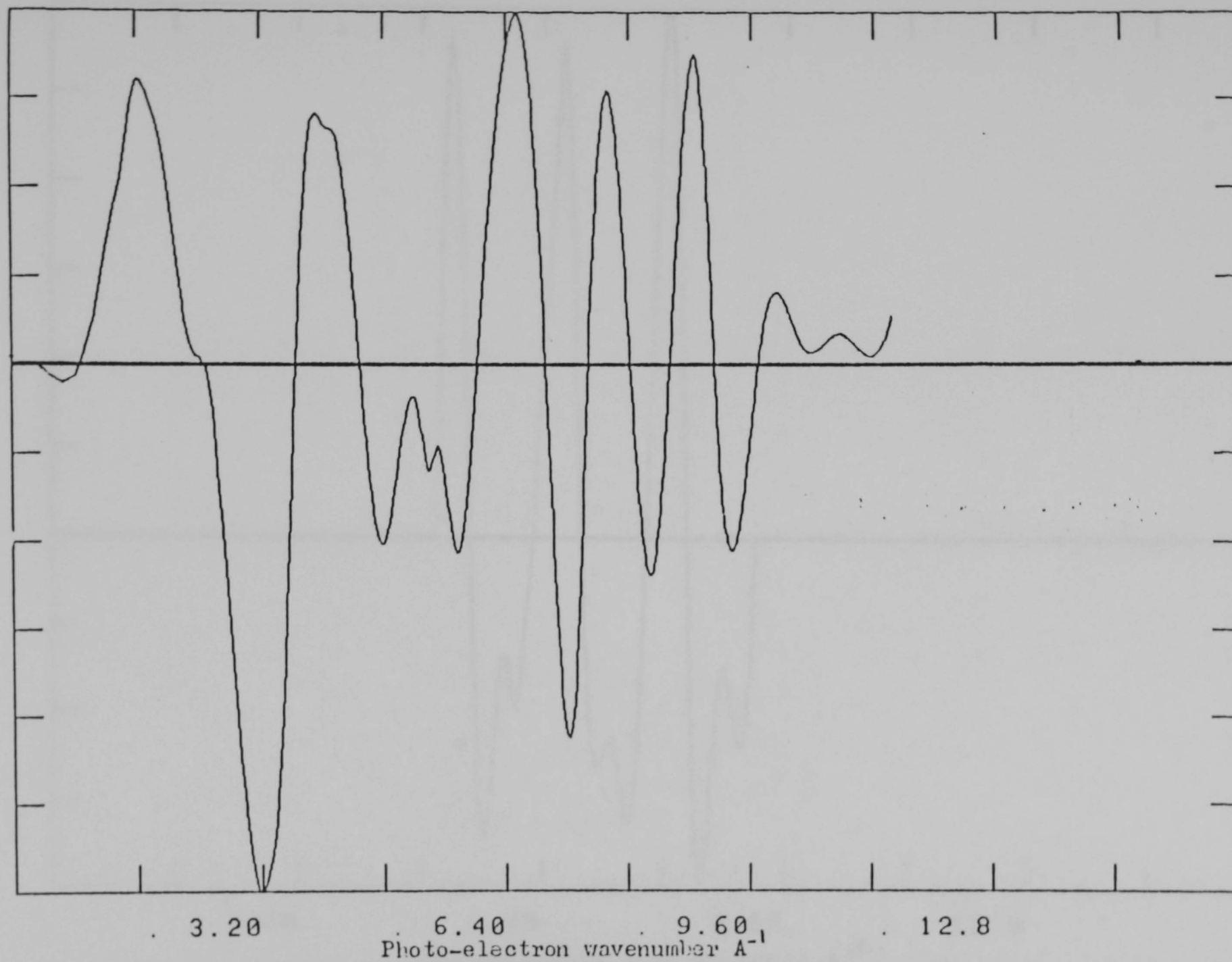


Photo-electron wave number in \AA^{-1}

Figure (4.9a). The weighted EXAFS function of iron as a function of photo-electron wavenumber.

$k^2\chi(k)$



Figure(4.9b). The weighted EXAFS function as a function of photo-electron wavenumber, of $\alpha\text{-Fe}_2\text{O}_3$

$$k^2\chi(k)$$

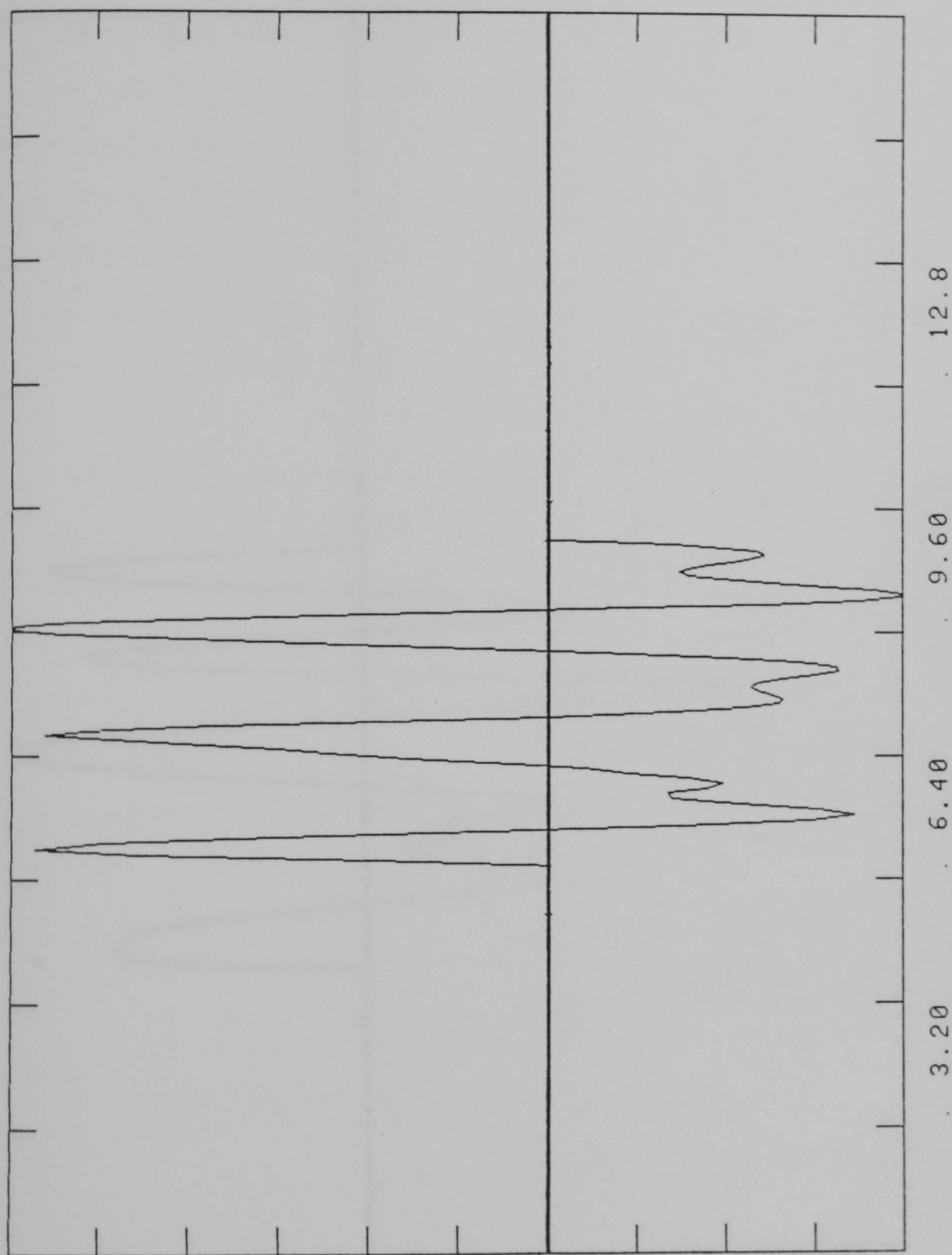
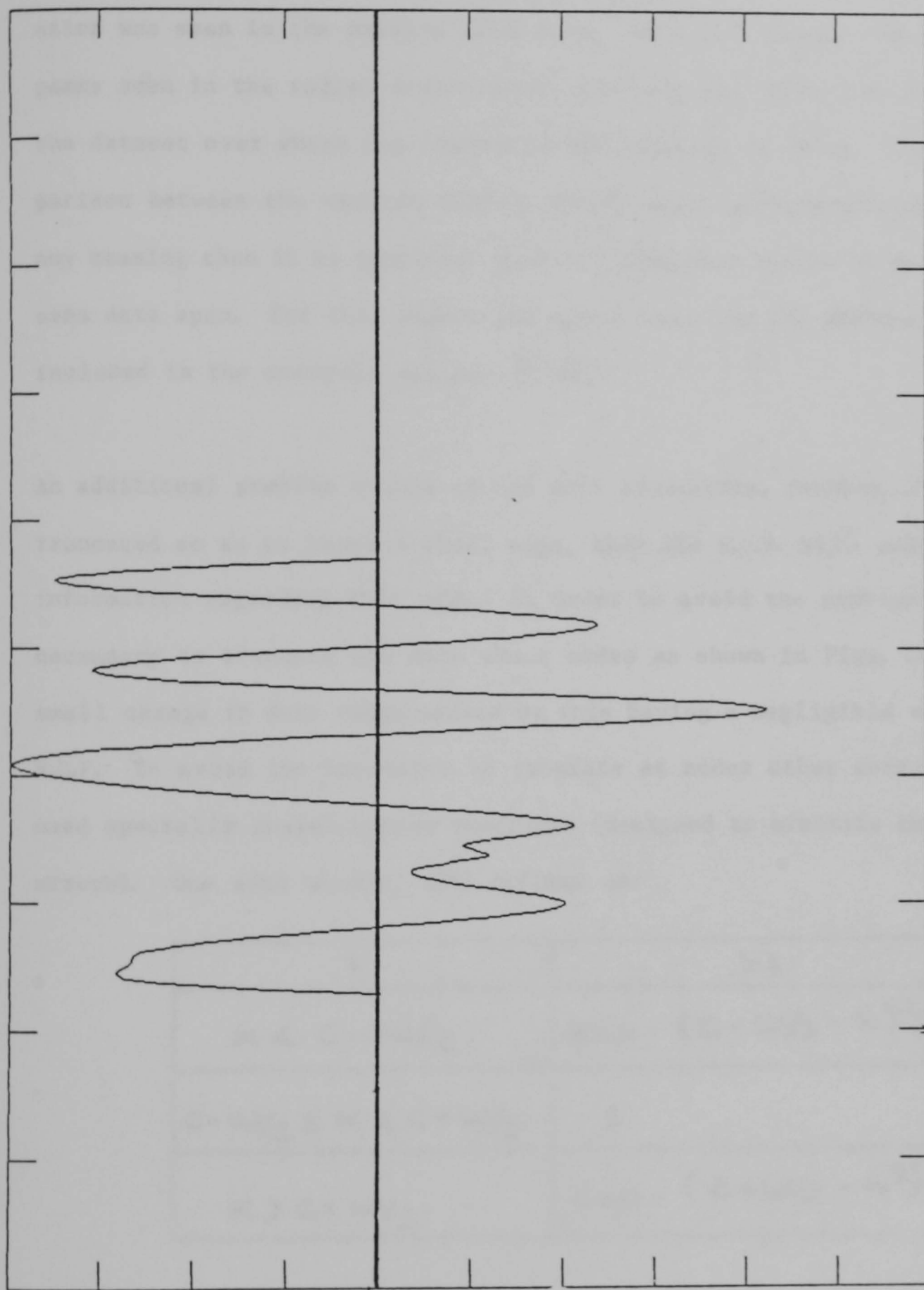


Photo-electron wave number in \AA^{-1}

Figure (4.10a). The weighted EXAFS function of iron as a function of photo-electron wavenumber.



3.20

6.40

9.60

12.8

Photo-electron wavenumber \AA^{-1}

Figure(4.10b) The weighted EXAFS function as a function of photo-electron wavenumber, of $\alpha\text{Fe}_2\text{O}_3$

For this reason the minimum photoelectron momentum that could be incorporated into the analysis was 2\AA^{-1} . The maximum value that could be incorporated into the analysis was determined by the minimum momentum at which an EXAFS oscillation was seen in the passive film data. This was because the width of the peaks seen in the radial distribution function are determined by the width of the dataset over which the Fourier transformation is taken. Thus if comparison between the various R.D.F.'s of the model and passive films is to have any meaning then it is important that all analysis should be made over the same data span. For this reason the upper limit on the photoelectron momentum included in the analysis was put at 8\AA^{-1} .

An additional problem occurs in the data truncation, because if the data are truncated so as to leave a sharp edge, then the R.D.F. will contain spectral information regarding this edge. In order to avoid the problem it is necessary to truncate the data about nodes as shown in Figs. (4.10a, b), the small change in data range caused by this having a negligible effect upon R.D.F. To avoid the necessity to truncate at nodes other workers⁽⁴⁶⁾ have used specially shaped window functions (designed to minimise these truncation errors). One such window, $W(k)$ defined as:

k	$W(k)$
$k < c - w/2$	$\exp - (c - w/2 - k)^2 / \sigma^2$
$c - w/2 \leq k \leq c + w/2$	1
$k > c + w/2$	$\exp - (c + w/2 - k)^2 / \sigma^2$

C = centre of window

W = width of window

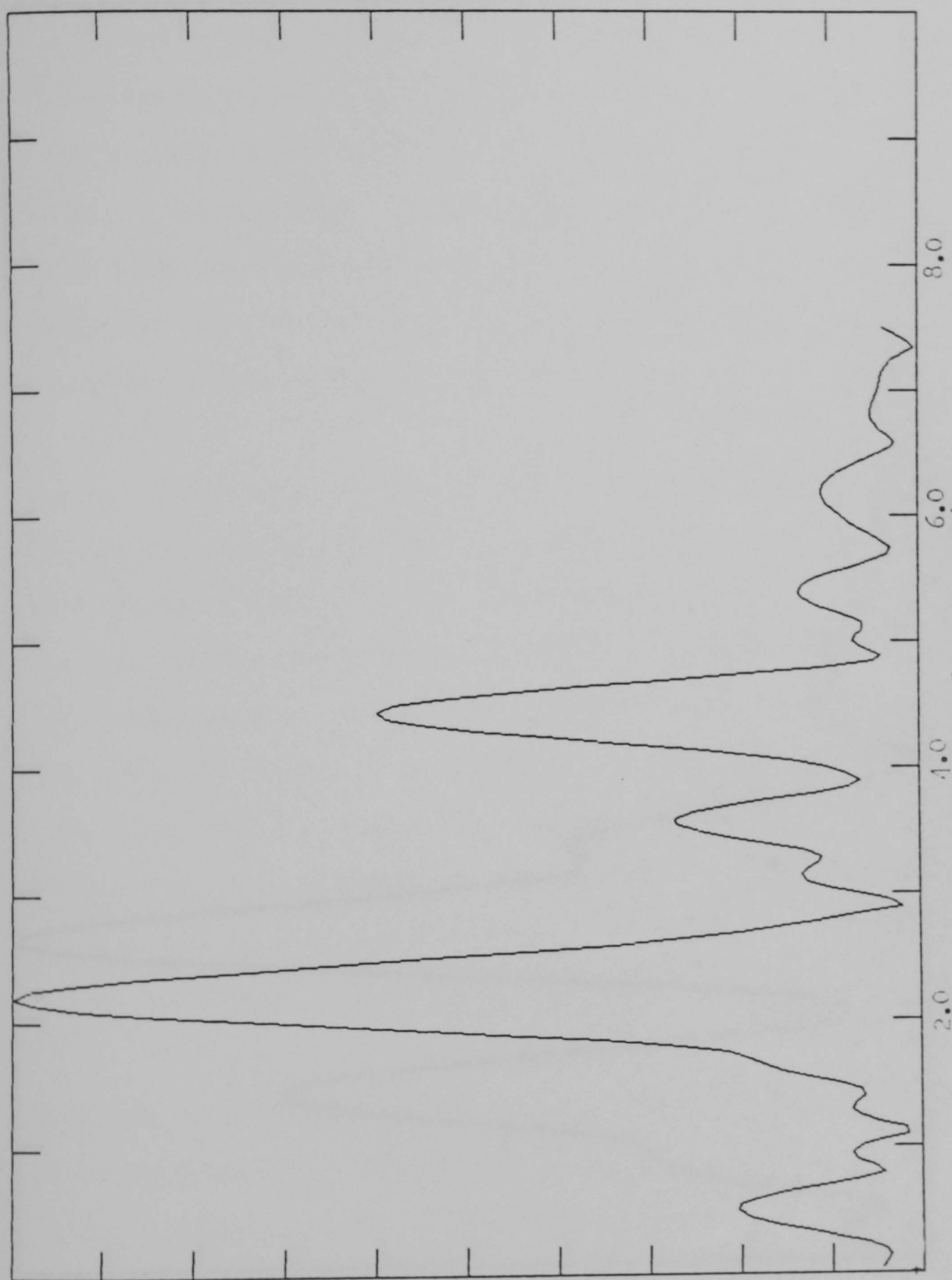
σ^2 = edge smoothness factor

this was tried; however its enhancement of the results was not readily apparent and its further use was not entertained.

4.6 Fourier Transformation

Following the truncation of the data it was Fourier transformed using a conventional routine. This generated a Pseudo Radial Distribution Function. Figures (4.11a and b) show the resultant pseudo R.D.F. of Fe and \propto Fe₂O₃ respectively. It must be remembered that each peak is shifted with respect to its true position by the phase change of the photoelectron during scattering. The remaining sections of this work deal with the comparison of the R.D.F. obtained from the model compounds to elucidate both the correction factors and the accuracy with which the bond lengths of the unknown material can be quoted.

arbitrary scale



Figure(4.11a). Pseudo- radial distribution function of iron.

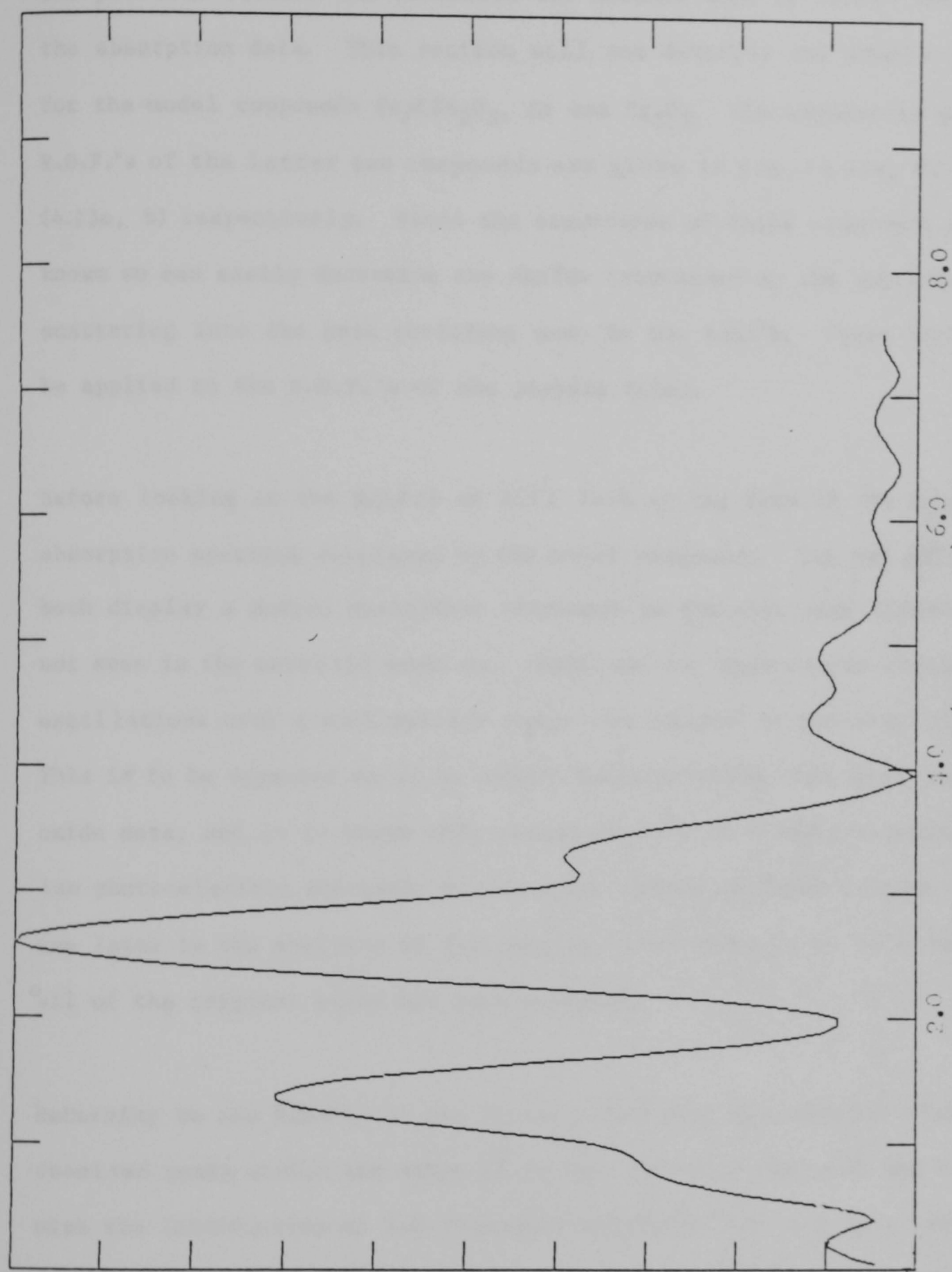


Figure (4.11b). Pseudo radial distribution function of $\alpha\text{-Fe}_2\text{O}_3$.

4.7 Model Compound Results

The previous section has described the methods used to obtain the R.D.F. from the absorption data. This section will now describe the R.D.F.'s so obtained for the model compounds $\text{Fe}_3\text{AlFe}_2\text{O}_3$, Cr and Cr_2O_3 . The absorption data and the R.D.F.'s of the latter two compounds are given in Fig. (4.12a, b) and Fig. (4.13a, b) respectively. Since the structures of these compounds are well known we can easily determine the shifts introduced by the photo-electron scattering into the peak positions seen in the R.D.F.'s. These shifts can then be applied to the R.D.F.'s of the passive films.

Before looking at the R.D.F.'s we will look at the form of the X-ray absorption spectrum displayed by the model compounds. The two oxide samples both display a marked absorption resonance in the near edge structure that is not seen in the metallic samples. Additionally, both oxides display EXAFS oscillations over a much smaller range than is seen in the metallic samples. This is to be expected as it is oxygen backscattering that will dominate the oxide data, and it is known that oxygen is only an effective backscatterer at low photo-electron energies, unlike iron. These two observations will be of use later in the analysis of the passive films where it is believed that not all of the original alloy has been oxidised.

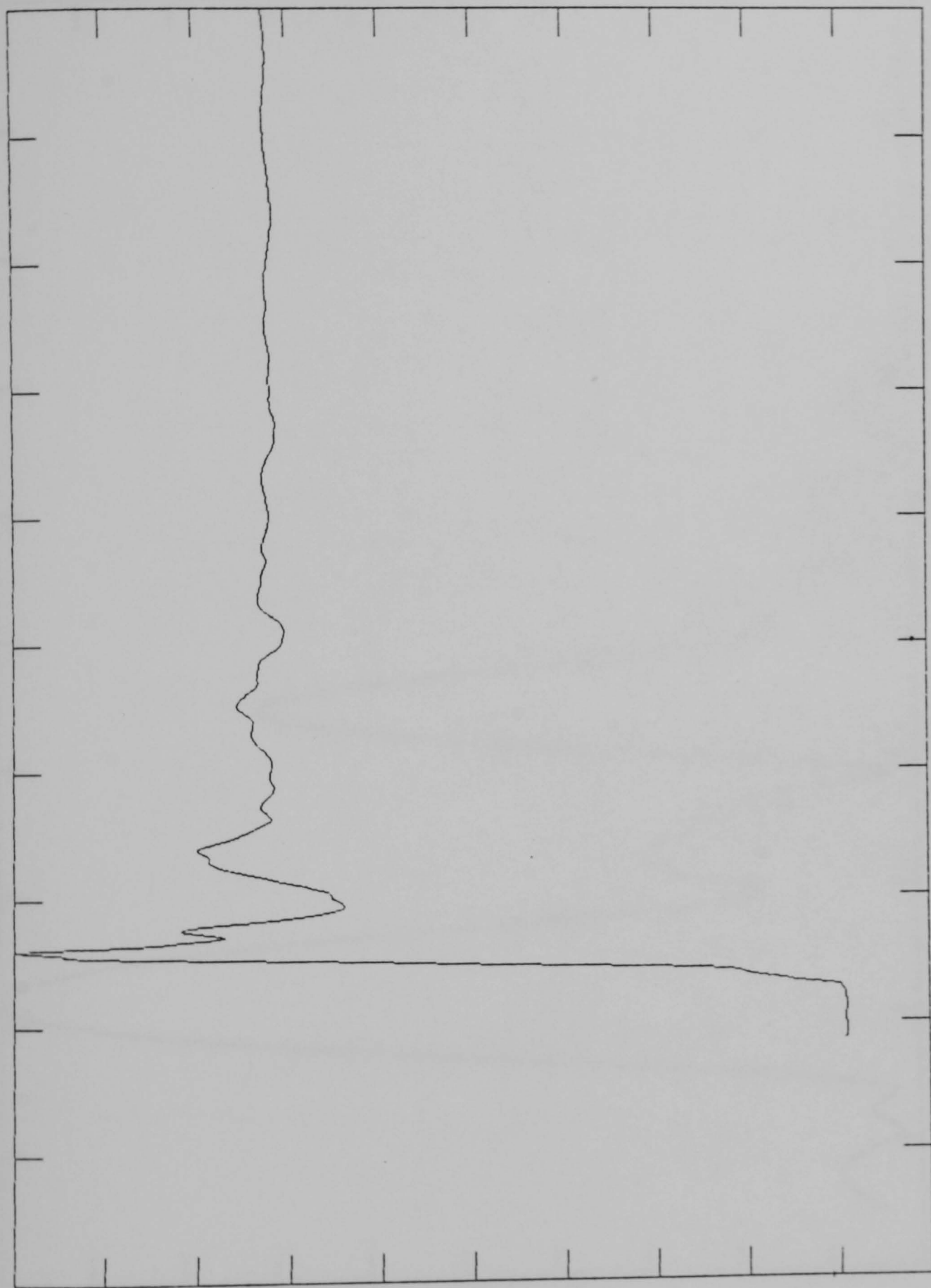
Returning to the R.D.F.'s, it can be seen that they all display clearly resolved peaks within the range 1\AA to 6\AA . Features below 1\AA may be associated with the introduction of low frequency artefacts into the data during background subtraction. Features above 6\AA can be ascribed to high frequency errors such as truncation.

X-ray absorption
arbitrary scale



5800. 5960. 6120. 6280. 6440.
Incident X-ray energy eV
Figure (4.12a). The X-ray absorption data obtained from chromium metal about its 'K' edge.

X-ray
absorption
arbitrary
scale



5800. 5960. 6120. 6280. 6440.
Incident X-ray energy eV
Figure (4.12b). The X-ray absorption data obtained from Cr_2O_3 about its 'K' edge.

arbitrary scale

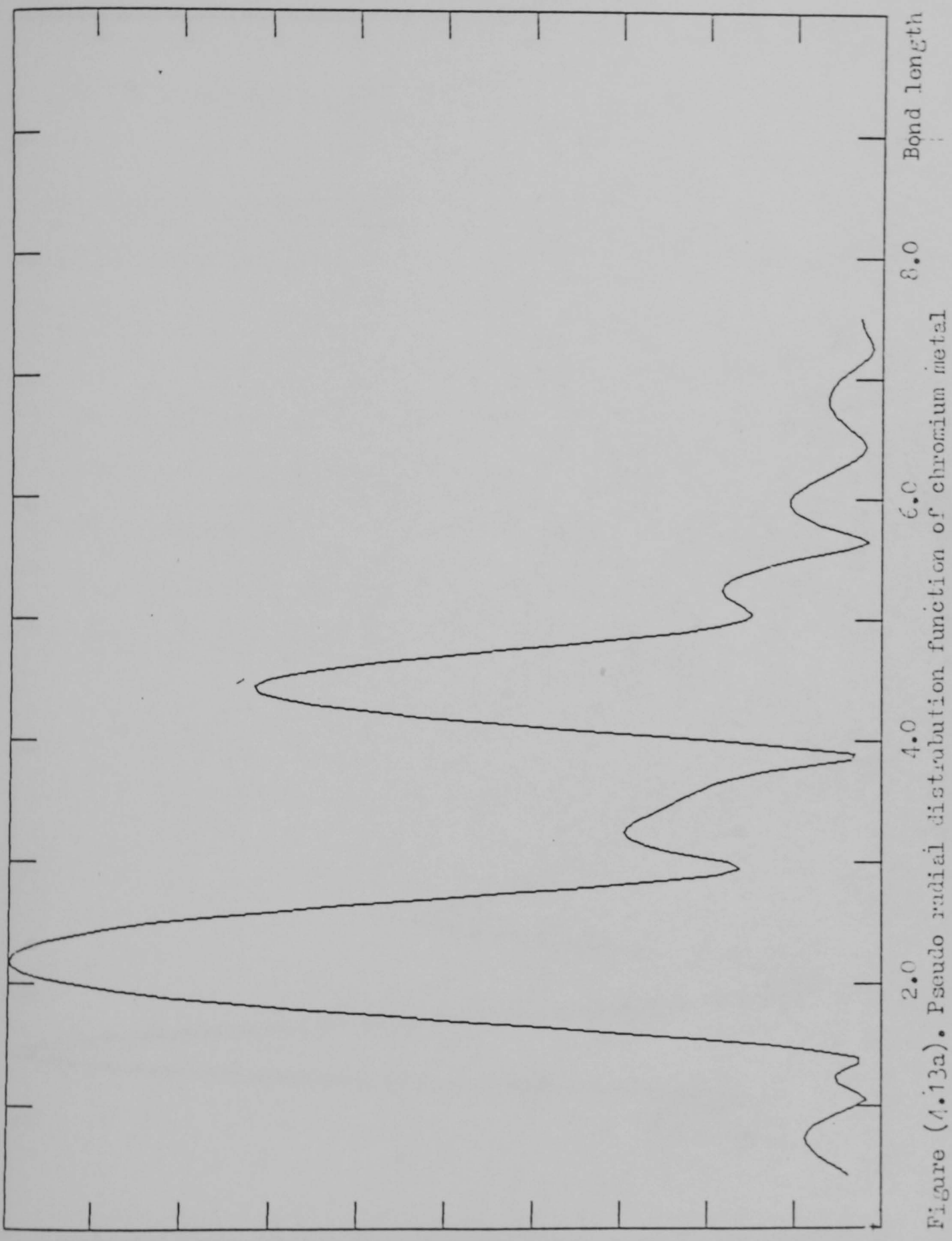


Figure (4.13a). Pseudo radial distribution function of chromium metal

χ arbitrary scale

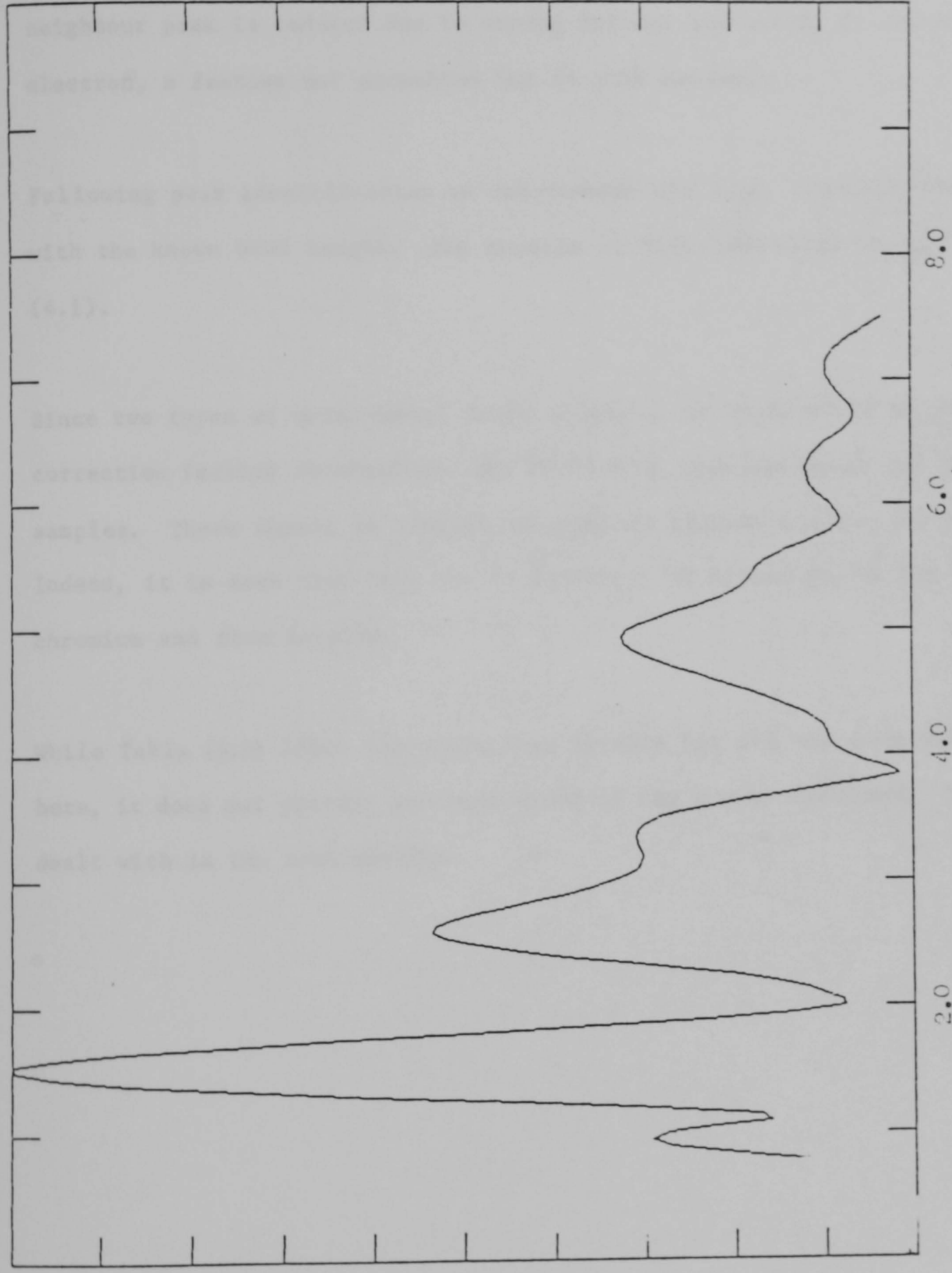


Figure (4.13b). Pseudo radial distribution function of Cr_2O_3

Since the structure of each compound is well known we may easily identify each peak with a particular atom pair contained in the sample. It should be noted that in the two B.C.C. metals Fe and Cr shown here the second nearest neighbour peak is reduced due to strong forward scattering of the photon-electron, a feature not accounted for in this analysis.

Following peak identification we can compare the R.D.F. indicated bond length with the known bond length. The results of this comparison are given in Table (4.1).

Since two types of metal-metal bonds exist, it is interesting to compare the correction factors obtained for the Fe-Fe bond from the metal and oxide samples. These should be similar if chemical transferability can be applied. Indeed, it is seen that they are in agreement by within $\pm 0.03\text{\AA}$ for both the chromium and iron samples.

While Table (4.1) lists the correction factors for all the atom pairs studied here, it does not provide any indication of the errors involved. These are dealt with in the next section.

Sample	Bond	Known bond length in A	Measured bond length in A	correction A
Fe	Fe-Fe	2.432	2.15	0.305
α Fe ₂ O ₃	Fe-Fe	2.915	2.63	0.285
	Fe-O	1.985	1.50	0.485
Cr	Cr-Cr	2.498	2.19	0.319
Cr ₂ O ₃	Cr-Cr	2.930	2.59	0.34
	Cr-O	1.995	1.54	0.46

Table (4.1). Comparison of the bond lengths determined from the pseudo R.D.F.'s with the known bond lengths of the model compounds, and the consequent correction factors.

4.8 Errors due to the choice of E_0

The R.D.F.'s generated in the previous section are not unique. The peak position may easily be adjusted by changing the weighting factor 'n', the range over which the data is analysed, or the exact value of E_0 chosen in the determination of the photo-electron wavenumber. Any comparison between R.D.F.'s can only be valid when they have been prepared in exactly the same way.

While it is easy to arrange for the weighting factor and data range to be kept constant during the analysis of several datasets, the same similarity cannot be arranged for E_0 . Since we have no way of fixing E_0 to a particular feature in the absorption spectrum.

To determine what effect variation of E_0 has upon peak position, R.D.F.'s of $\alpha\text{-Fe}_2\text{O}_3$ were obtained for a range of E_0 values from 10eV below the half edge height position to 10eV above. A graph of the Fe-O bond length as a function of E_0 is given in Fig. (4.14). This shows that over the 20eV range, that the peak position may shift by up to 0.07\AA . Clearly it is important to know how closely each dataset is aligned to the model compound to determine how far the peaks may have been shifted. This may be determined by single shell analysis.

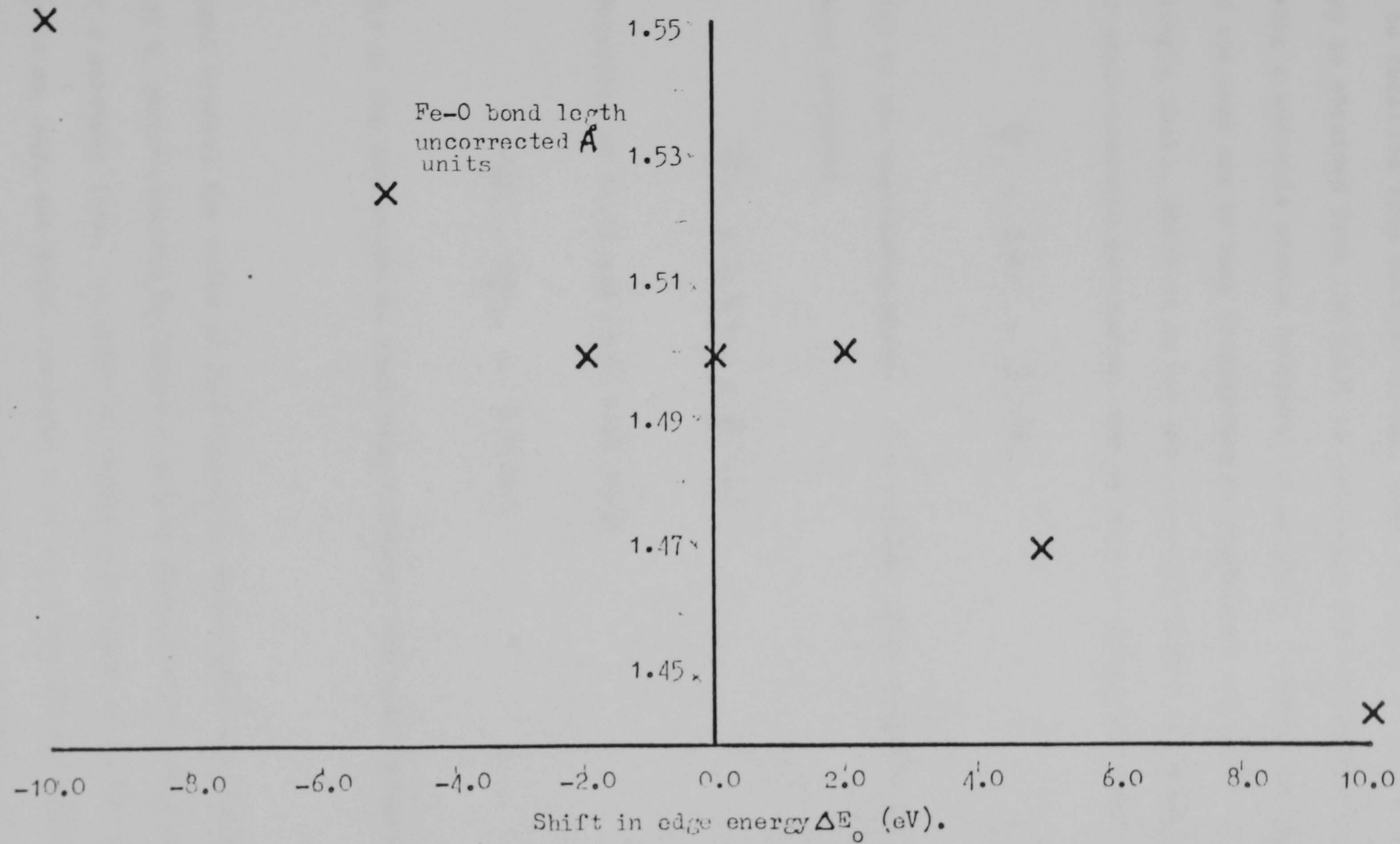


Figure (4.14). Variation of bond length(Fe-O) of the model compound Fe_2O_3 with ΔE_0 .

4.9 Single Shell Analysis

It will be recalled from section (2.6.2), that the EXAFS of a single atom pair shell may be obtained from the R.D.F. by isolating the relevant peak in the R.D.F. using a suitable window function, to minimise truncation errors. Once isolated the peak may be back transformed to regenerate the EXAFS oscillation of the single shell, which if E_0 has been properly chosen to yield the true value of photo-electron wavenumber, can be used to obtain the phase function.

$$\psi_i = 2kr_i + \phi_i(k) \quad (4.4.)$$

where $\phi(k)$ is the scattering phase. If a similar phase function is obtained for a model compound

$$\psi_m = 2kr_m + \phi_i(k) \quad (4.5)$$

The subtraction of (4.4) and (4.5) will yield

$$\psi_i - \psi_m = 2k\Delta r \quad (4.6)$$

where Δr is the difference in bond length between the model compound and the sample.

In general however the value of E_0 originally chosen will not provide the true value of k , photo-electron wavenumber, and so equation (4.6) will not have the form of a straight line. In order to obtain a straight line, it is necessary to vary E_0 on, say, the model compound so as to align the two datasets. At this point not only can we obtain the difference in bondlengths Δr from

equation (4.6), but also ΔE_0 the shift in E_0 required to align the two datasets.

Such an analysis was carried out on the Fe-Fe, Cr-Cr bonds in the metal compounds and on the Fe-O, Cr-O bonds contained in the model compounds and several passive films. The results are summarised in Table (4.2). The shifts associated with the Fe-Fe and Cr-Cr bonds obtained by this method can be seen to be within 0.04\AA of those obtained by simple comparison of the R.D.F.'s, and within 0.001\AA of the true value. This discrepancy can easily be accounted for when it is seen that the datasets were out of alignment by some 8eV, which with reference to Fig. (4.14) indicates an uncertainty in bond length of 0.05\AA . The passive films are seen to be misaligned by some +5eV which indicates a bond length error of 0.03\AA . These results are summarised in Table (4.2) which lists the correction factors for all the atom pairs studied here along with their uncertainties.

Samples compared	Bond studied	Δr_{known} Å	Δr by R.D.F. comparison Å	Δr by single shell analysis Å	R.D.F. error Å	S.S.A. error Å	Required ΔE shift in S.S.A. eV
Cr Cr_2O_3	Cr-Cr	0.432	0.4	0.41	-0.032	-0.02	-5.0
Fe $\alpha\text{Fe}_2\text{O}_3$	Fe-Fe	0.433	0.48	0.42	-0.047	-0.03	-3.0
$\alpha\text{Fe}_2\text{O}_3$ Fe [*]	Fe-O	N/A	0.04	0.03	$\pm 0.03^{**}$	N/A	+5.0
Cr_2O_3 Cr ^{***}	Cr-O	N/A	0.20	0.15	$\pm 0.04^{****}$	N/A	+7.0

Fe^{*} iron sample passivated in nitrite solution. ** error determined with reference to Figure (4.14).

Cr^{*} chromium edge in an Fe16Cr alloy passivated in nitrite solution. **** determined as above.

Table (4.2). Comparison of the correction factors obtained by R.D.F. comparison and single shell analysis (S.S.A.), together with the uncertainties present in the correction factors.

4.10 Conclusion

We have seen how the R.D.F. may be obtained from the X-ray absorption data and how comparison of the R.D.F.'s from the model compounds allows the correction factors to be arrived at. It has been seen that the single shell analysis route can determine more accurately these correction factors and the value of ΔE_0 the misalignment between two datasets. Based on these values ΔE_0 some uncertainty may be placed upon the correction factors obtained here. Since more accurate results obtained by the single shell analysis cannot help identify the exact film structure it was decided to analyse the data obtained by simple comparison of the R.D.F. based upon the correction factors of Table (4.3).

Additionally, the large number of datasets to be compared prevented a more detailed analysis taking place because of the limited time available.

Atom pair	correction factor in A	error in A
Fe-Fe	0.285 [*]	± 0.05
Fe-O	0.485	± 0.03
Cr-Cr	0.34 [*]	± 0.03
Cr-O	0.46	± 0.04

* Correction factors based upon oxide data, since this offers the closest chemical environment to that expected in the passive film.

Table (4.3). Correction factors used in this study.

5. RESULTS

5.1 Introduction

Four alloy compositions were investigated, containing 0, 6, 16, and 29% atomic chromium. While EXAFS measurements of passivated iron films have previously been reported by other workers, they were studied here both for completeness and as a check upon the reproducibility of the EXAFS technique as applied to passive films. The 6 and 16% atomic chromium alloys were chosen because these two compositions straddle the corrosive to resistant transition shown by iron-chromium alloys at 12% atomic chromium, while the final composition of 29% atomic chromium was included as it should lie well within the region where the passive film is expected to be amorphous.

Five sets of samples were prepared in all; two sets were passivated in 0.1M NaNO_2 , two sets in 0.05M K_2CrO_4 and one set was anodically passivated in 2.0M H_2SO_4 . All passivation took place at room temperature and in air saturated solutions, as described in the experimental chapter.

All the EXAFS measurements reported here were made using the S.R.S. at Daresbury. Both the Fluorescence and Total Electron Yield results were made at room temperature. The fluorescence readings were taken in air, while the total electron yield results were taken in a vacuum of 10^{-6} Torr.

5.2 Nitrite Passivated Films

The two sets of nitrite passivated films were studied using both the fluorescence and total electron yield EXAFS modes. In all cases the iron 'K' edge was studied, but in the total electron yield mode the chromium 'K' edge was also measured for the 16 and 29% atomic chromium alloys. In all other cases the yield from the chromium edge was too small to provide a workable signal. The total electron yield results are presented in Section 5.2.1 while the fluorescence results are presented in Section 5.2.2. Section 5.2.3 provides a summary of the results obtained from the nitrite passivated films, together with a comparison of the two measurement modes.

5.2.1 Total Electron Yield Results

The iron 'K' edge X-ray absorption data for the four compositions of 0, 6, 16 and 29% atomic chromium are reproduced in figures (5.1. to 5.4) respectively. The chromium 'K' edge X-ray absorption data for the 16% atomic chromium sample are shown in figure (5.5).

It can be seen that all the X-ray absorption edges display a marked absorption resonance in the near edge region. This is a feature that we have previously associated with oxide samples. The energy range over which the EXAFS oscillations are seen is also reduced with respect to the metallic and oxide model compounds. This may be taken to indicate that the film is oxidised and contains a greater degree of structural disorder than the model compounds.

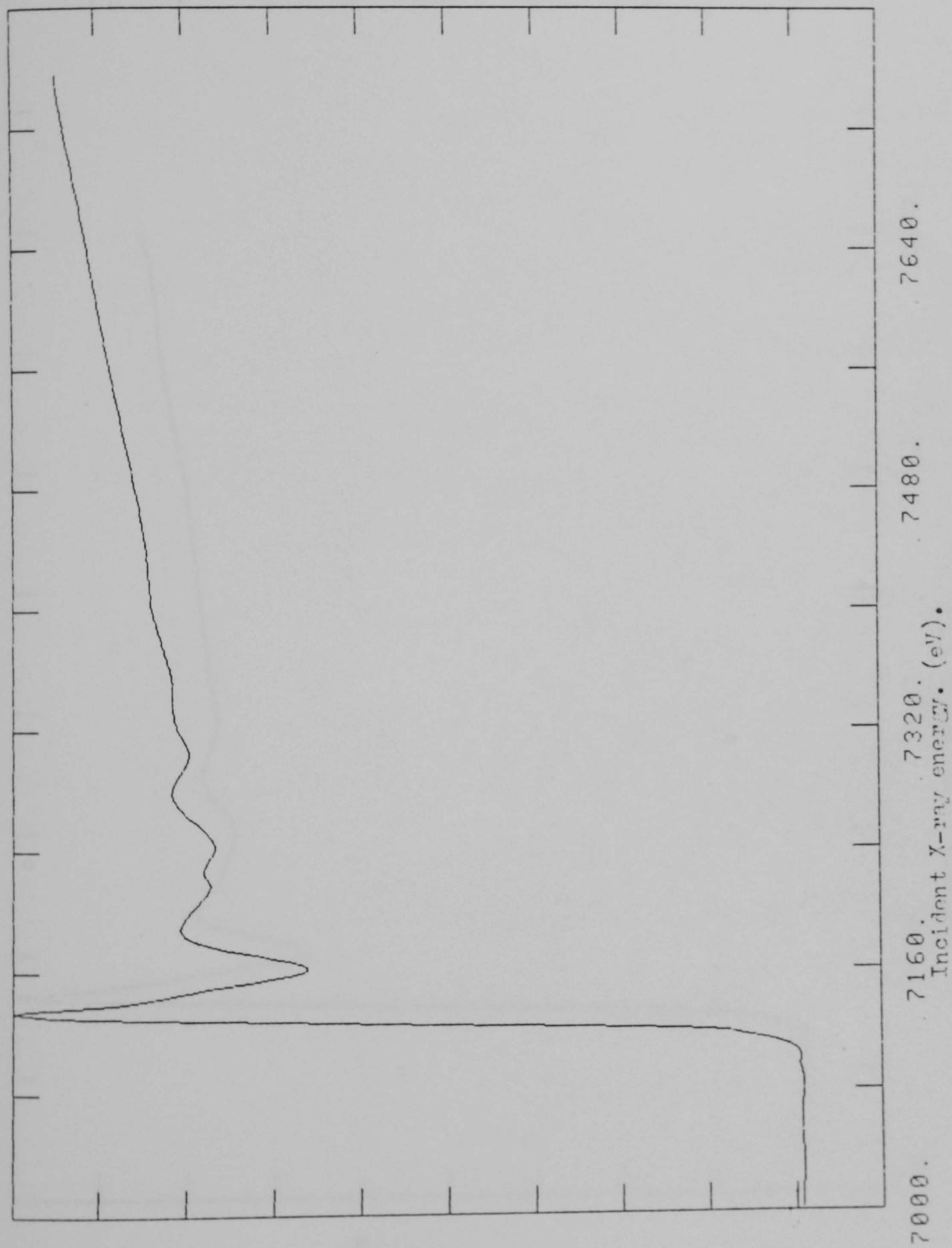


Figure (5.1). The iron 'K' edge X-ray absorption spectrum of an iron film passivated in 0.1 M NaNO_3 measured using the total electron yield mode.

X-ray absorption
arbitrary units

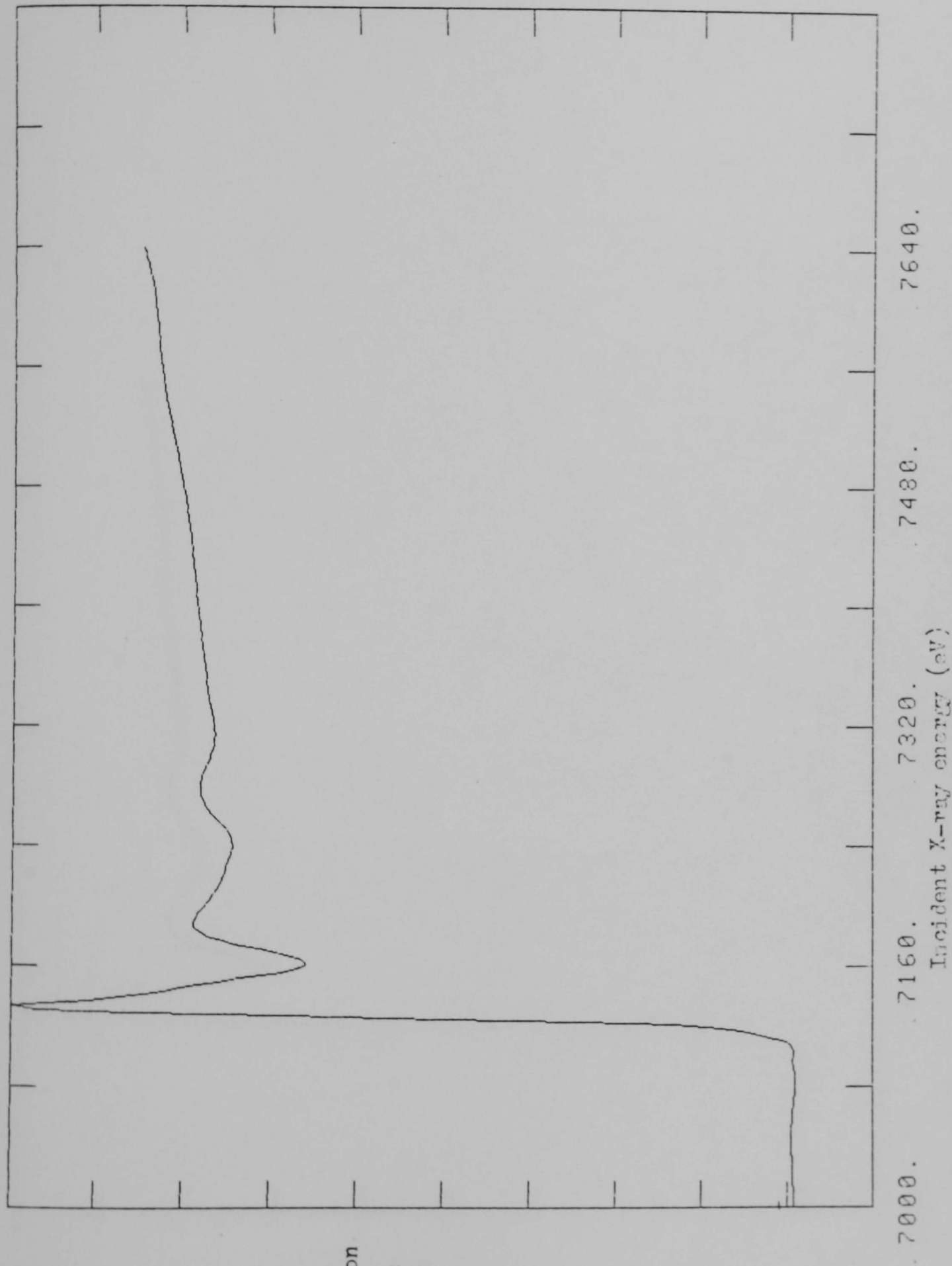


Figure (5.2). The iron 'K' edge X-ray absorption spectrum for an Fe6Cr alloy film passivated in 0.1M NaMO₂, measured using the total electron yield mode.

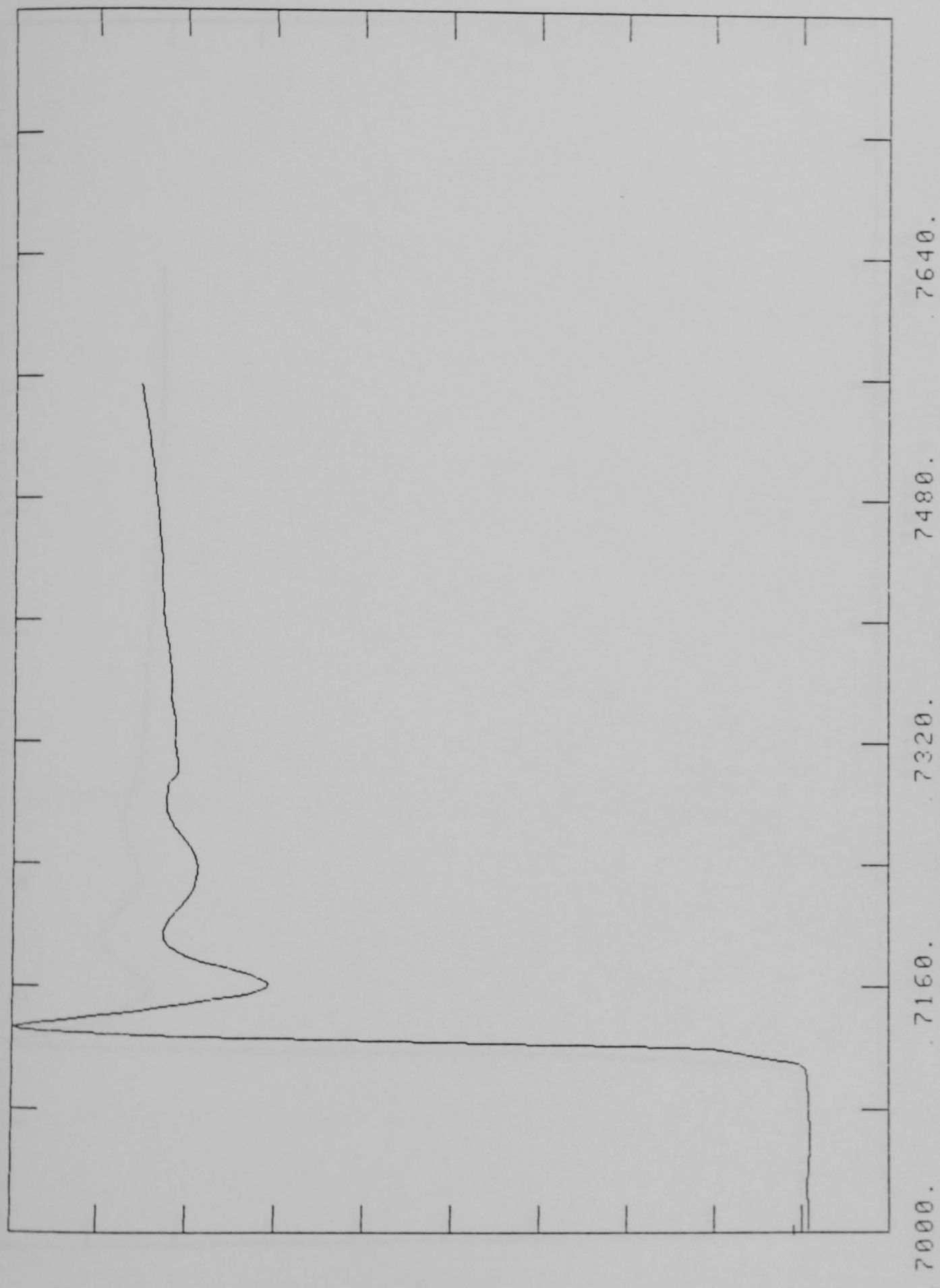
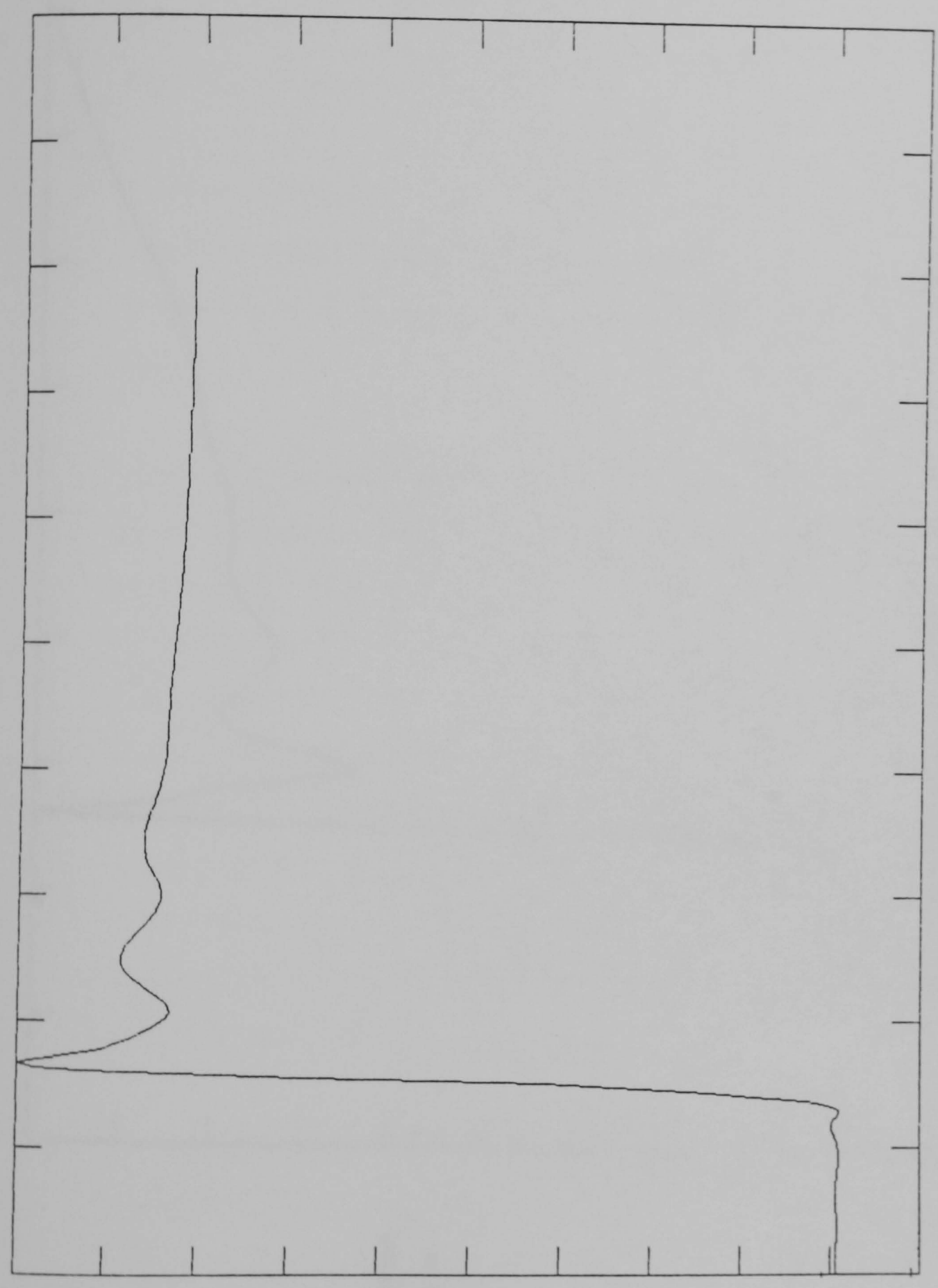


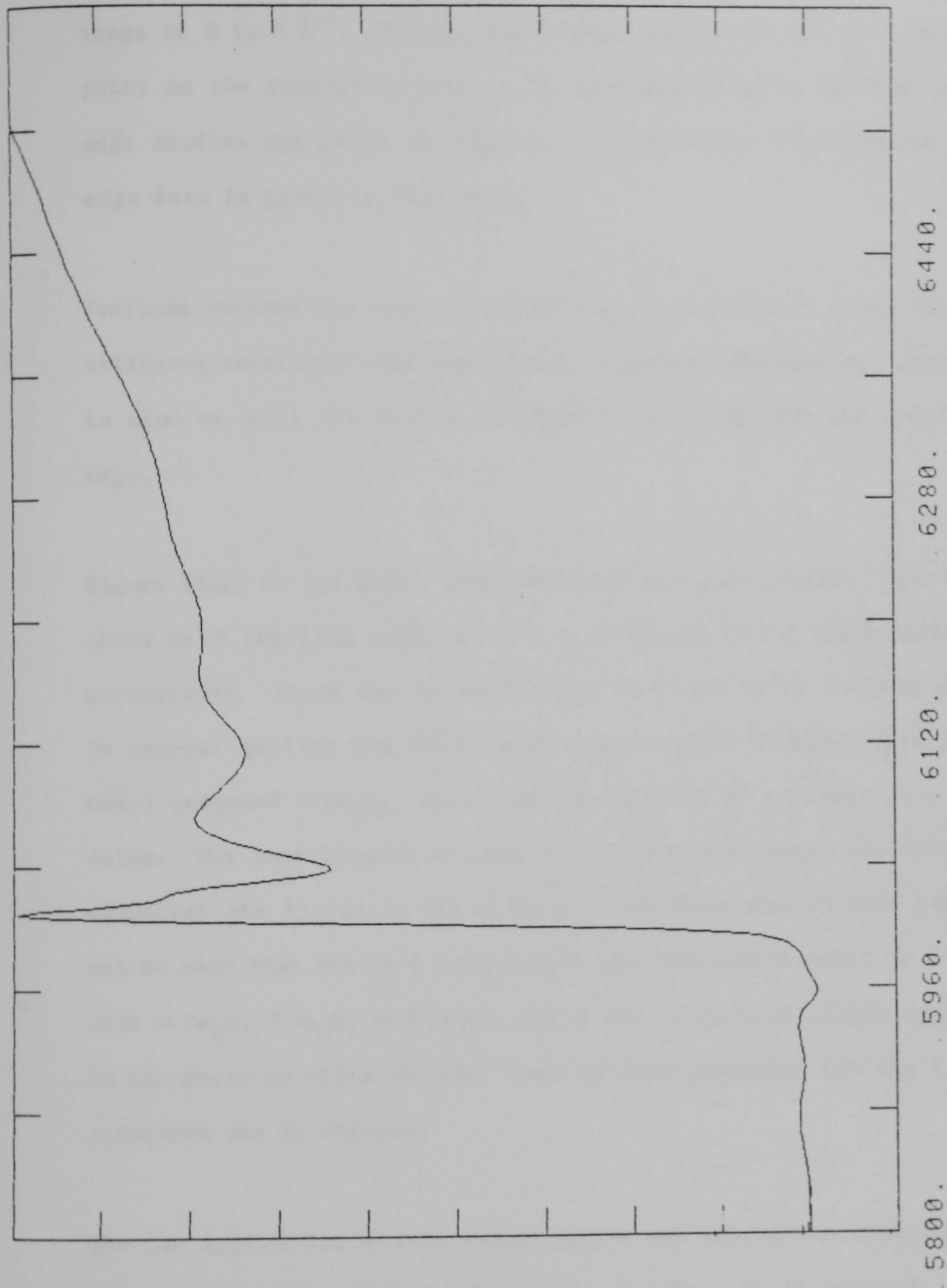
Figure (5.3). The iron 'K' edge X-ray absorption spectrum of an Fe16Cr alloy passivated in 0.1N HNO₃ measured using the total electron yield mode.

X-ray absorption
arbitrary units



7000. 7160. 7320. 7480. 7640.
Incident X-ray energy. (eV)

Figure (5.4). The iron 'K' edge X-ray absorption spectrum for an Fe29Cr alloy film passivated in 0.1M NaNO₂ measured using the total electron yield mode.



X-ray absorption
arbitrary units

Figure(5.5). The chromium 'K' edge X-ray absorption spectrum of an Fe₁₆Cr alloy film passivated in 0.1M NaOH measured using the total electron yield mode.

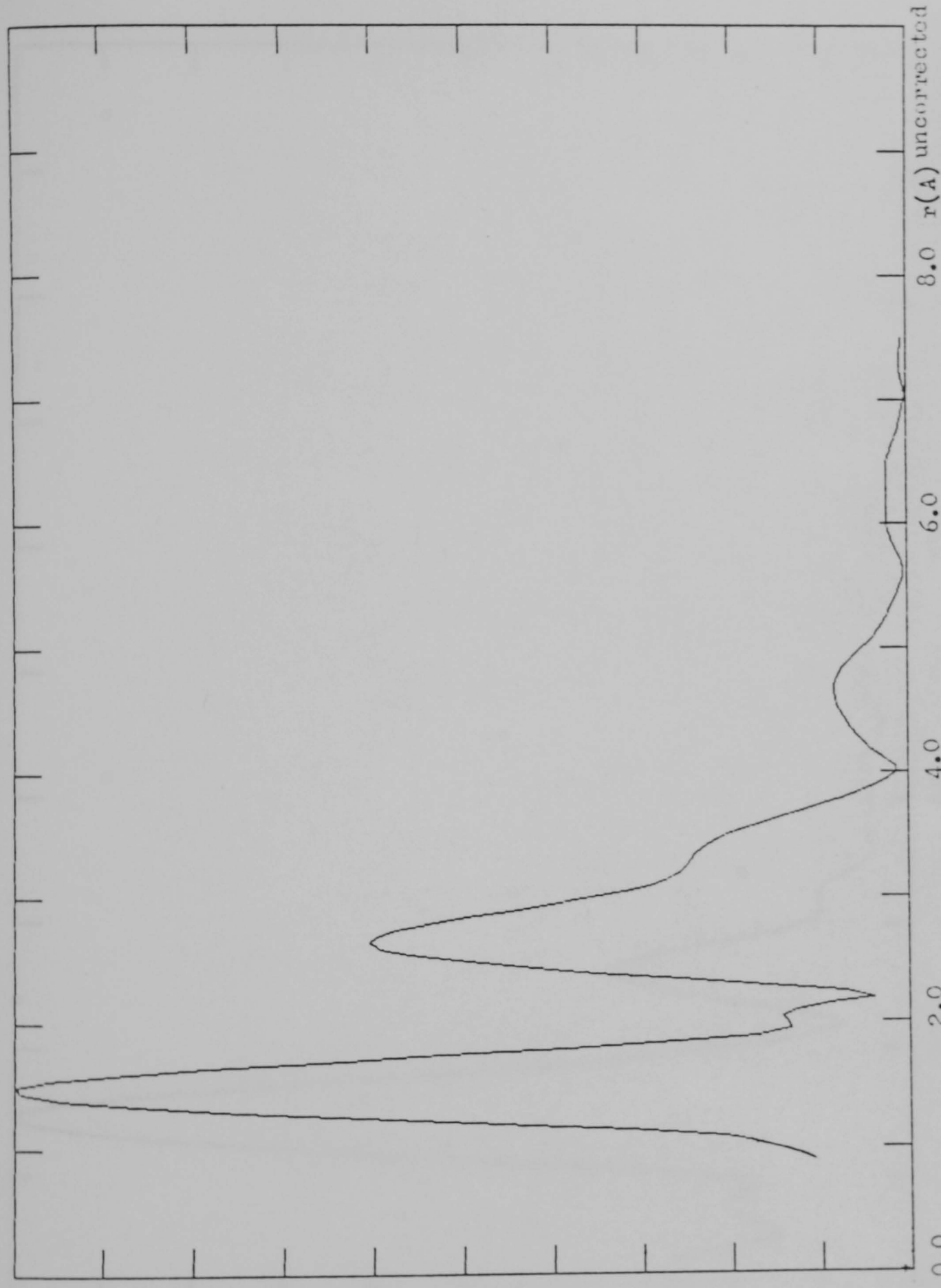
Using the methods described in Chapter 4, R.D.F.'s for the six data sets above were generated using a weighting factor of k^2 and a data range of 3 to 8 \AA^{-1} . E_0 was consistently chosen at the half height point on the absorption edge. The resultant R.D.F.'s for the iron 'K' edge studies are given in figs. 5.6 to 5.9, while the chromium 'K' edge data is given in fig. 5.10.

Features outside the range 1 \AA to 6 \AA may be ascribed to noise and artifacts remaining from incomplete background absorption. With this in mind we will now review the R.D.F.'s obtained from the iron 'K' edge.

Figure (5.6) is the R.D.F. obtained from the iron sample. The function shows well resolved peaks at $1.99 \pm 0.03\text{\AA}$ and $2.96 \pm 0.05\text{\AA}$ (after correction). These may be ascribed to Fe-O and Fe-Fe bonds respectively. In general quality the R.D.F. is not unlike that obtained here for the model compound $\alpha\text{-Fe}_2\text{O}_3$, and as such is typical of a crystalline oxide. The bond lengths of some common iron and oxygen containing compounds are listed in Table (5.1). With reference to this table it can be seen that the Fe-O bond length obtained above could be linked with $\alpha\text{-Fe}_2\text{O}_3$, $\gamma\text{-Fe}_2\text{O}_3$ or $\gamma\text{-FeOOH}$, while the Fe-Fe bond length appears to be too short to allow $\gamma\text{-FeOOH}$. Thus no firm contender for the film structure can be offered.

The two R.D.F.'s for alloys containing 6 and 16% atomic chromium are presented in figs. (5.7 and 5.8) respectively. It is apparent that these two R.D.F.'s are very similar, which is not surprising as the X-ray absorption spectra from which they were obtained are very similar. Fe-O bond lengths of 1.95\AA and Fe-Fe bond lengths of 2.95\AA

$F(r)$
arbitrary units



Figure(5.6). Magnitude of the Fourier transform of iron passivated in 0.1M NaNO_2 by electron yield.

$F(r)$
arbitrary units

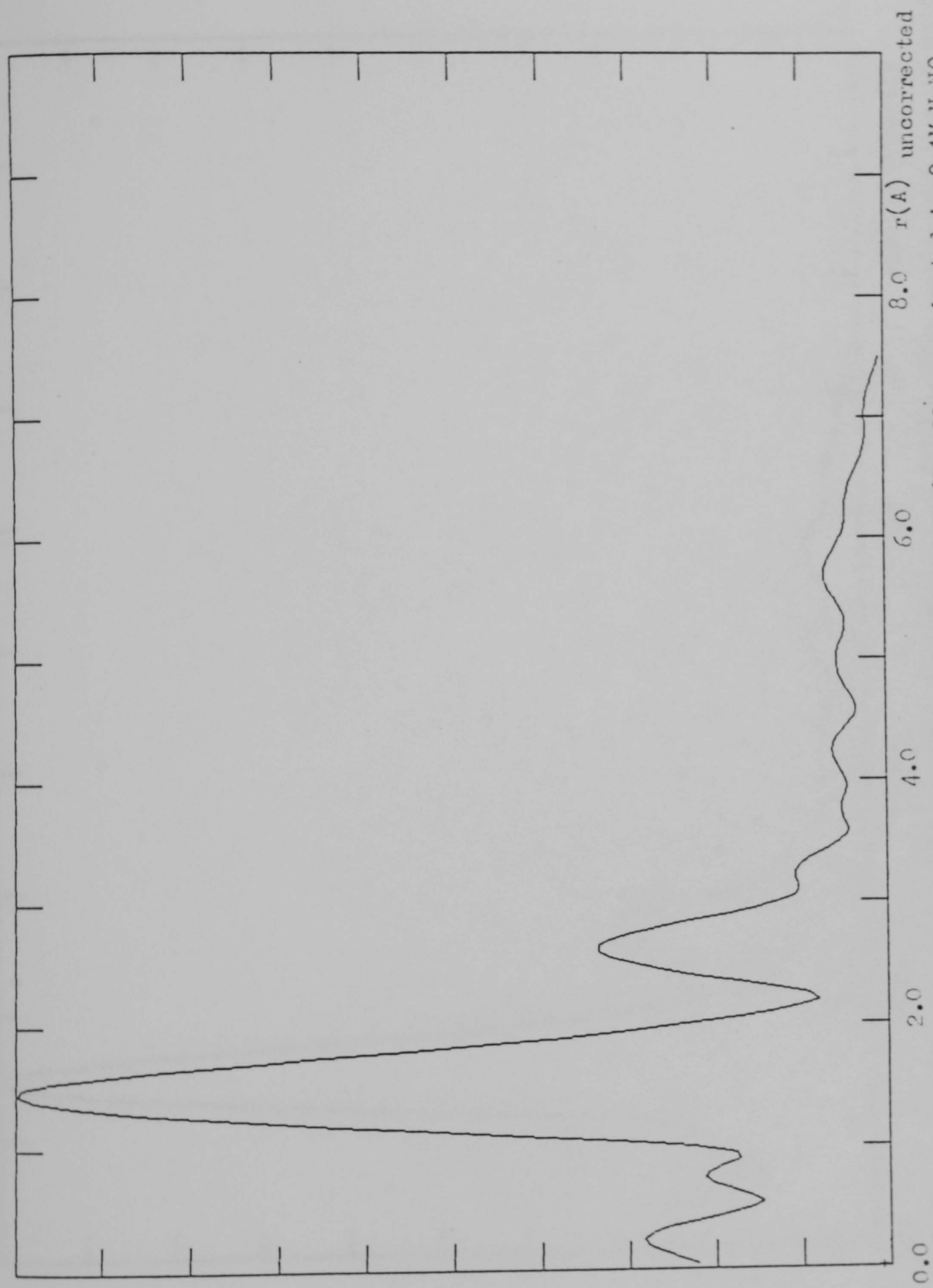
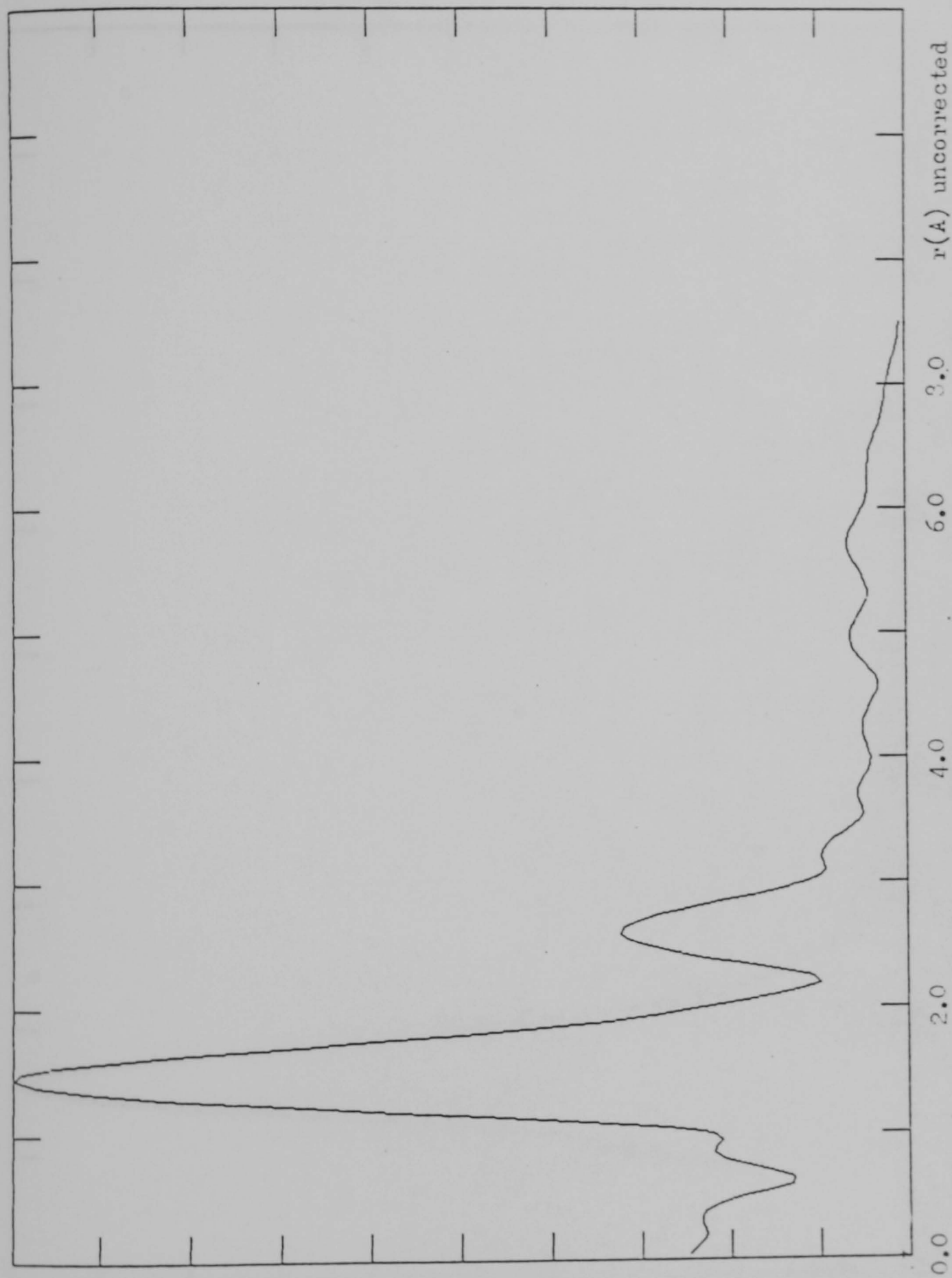


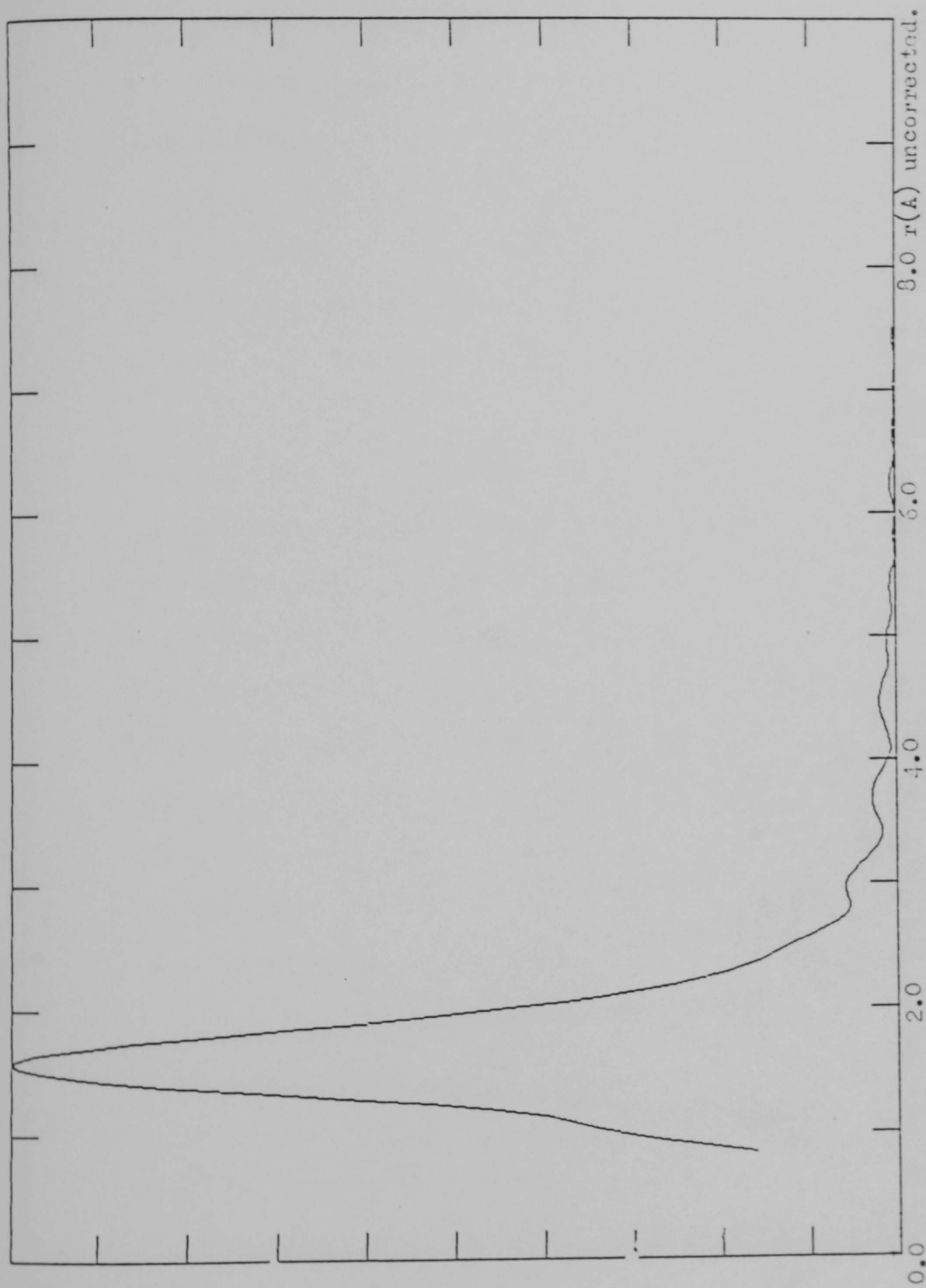
Figure (5.7). The magnitude the Fourier transform of an Fe6Cr alloy, passivated in 0.1M H_2O_2 by electron yield.

$F(r)$
arbitrary units



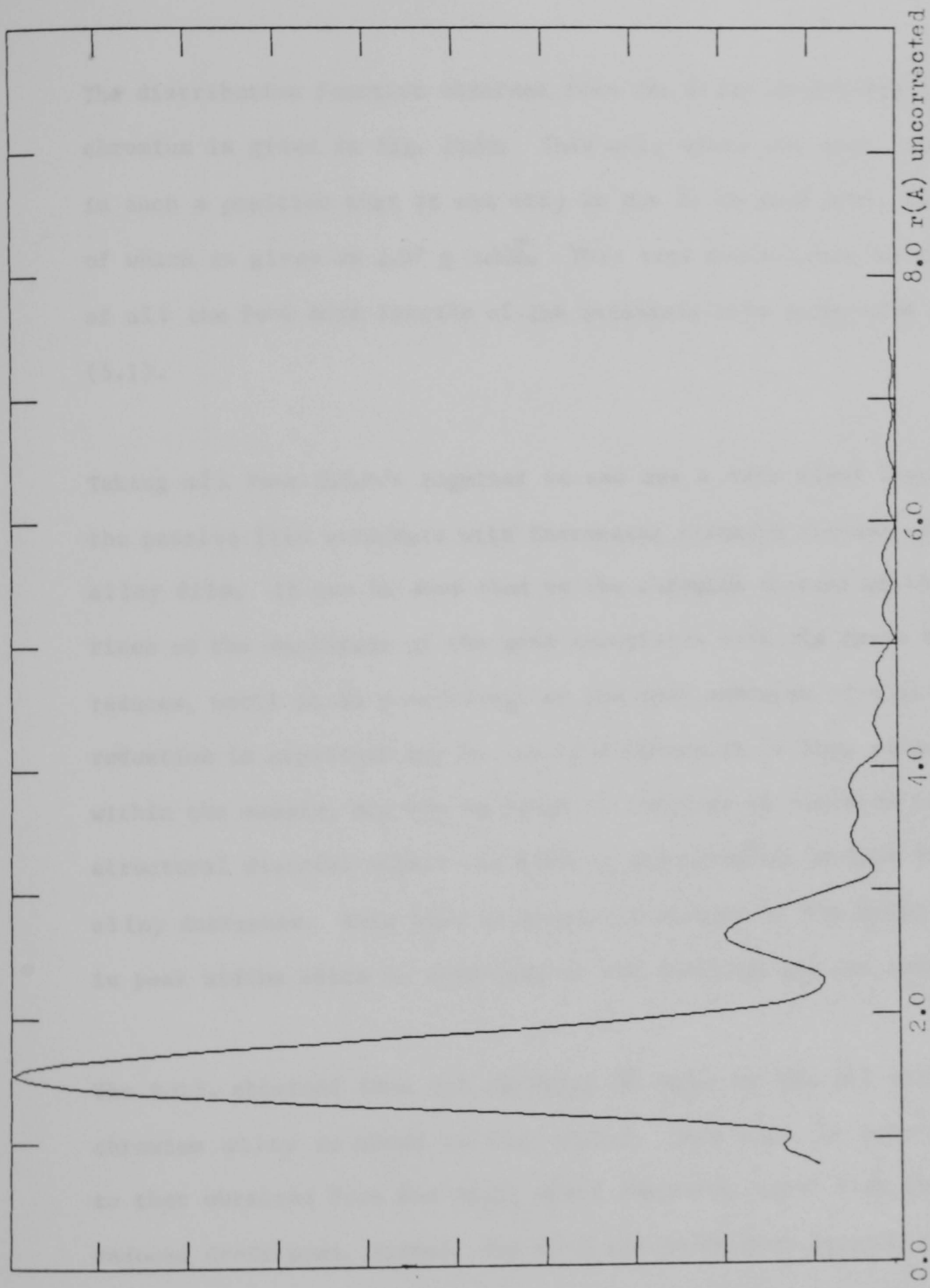
Figure(5.8). The magnitude of the Fourier transform of an Fe16Cr alloy passivated in 0.1M NaNO_2 by electron yield.

$\bar{F}(r)$
arbitrary units.



Figure(5.9). The magnitude of the Fourier transform of an Fe29Cr alloy passivated in 0.1 M HNO_3 by electron yield.

$F(r)$
arbitrary units



Figure(5.10). The magnitude of the Fourier transform of an Fe16Cr alloy passivated in 0.1 m NaNO_2 by electron yield and using the chromium edge.

are indicated in both distribution functions. Again the limited accuracy of the bond length determination prevents a structure being given for the passive film.

The distribution function obtained from the alloy containing 29% atomic chromium is given in fig. (5.9). This only shows one peak, which is in such a position that it can only be due to an Fe-O bond, the length of which is given as $2.07 \pm 0.03\text{\AA}$. This sits comfortably in the middle of all the Fe-O bond lengths of the candidate film structures of Table (5.1).

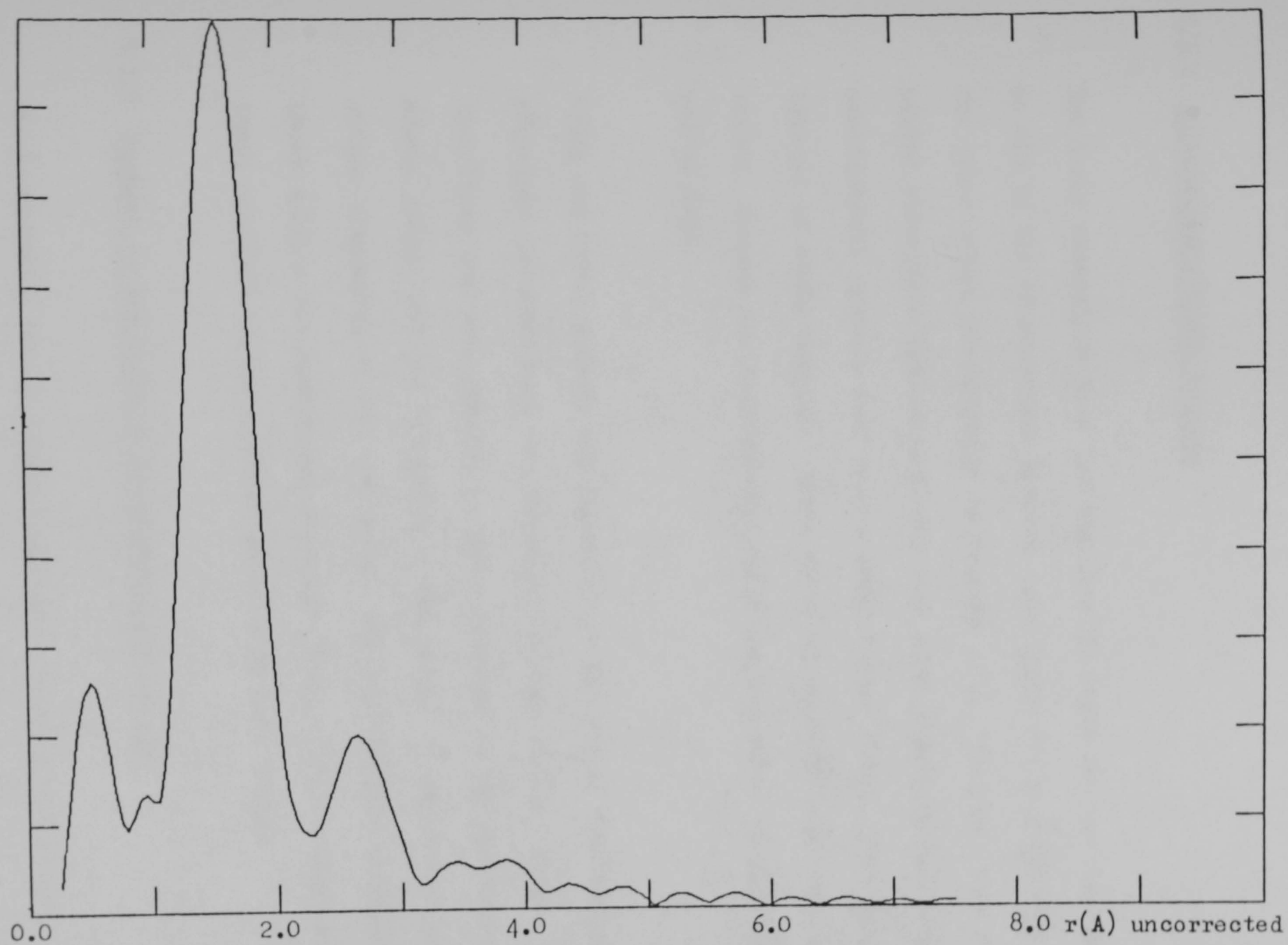
Taking all four R.D.F.'s together we can see a very clear transition in the passive film structure with increasing chromium content of the alloy film. It can be seen that as the chromium content of the alloy rises so the amplitude of the peak associated with the Fe-Fe bond reduces, until it is nonexistent on the most chromium rich alloy. This reduction in amplitude may be due to a reduction in long range order within the sample, and can be taken to indicate an increase in structural disorder within the film as the chromium content of the alloy increases. This view is supported because of the small increase in peak widths which is also seen as the chromium content increases.

The R.D.F. obtained from the chromium 'K' edge in the 16% atomic chromium alloy is shown in fig. (5.11). This R.D.F. is very similar to that obtained from the Cr_2O_3 model compound, apart from the greatly reduced Cr-Cr peak. Indeed, the Cr-O and Cr-Cr bond lengths of 2.91\AA and 2.0\AA are identical within the experimental limits to the Cr_2O_3 data. Again we may interpret the greatly reduced Cr-Cr peak as being

Compound	Fe-O bond lengths	Fe-Fe bond lengths
$\gamma\text{-FeCOH}$	1.93 2.13	3.06
$\gamma\text{-Fe}_2\text{C}_3$	1.82 2.1	2.97 3.46
$\alpha\text{-Fe}_2\text{C}_3$	1.91 2.06	2.93
Fe_3C_4	1.80 2.1	2.97
FeO	2.15	3.05

Table(5.1). Fe-O and Fe-Fe bond lengths found in some common iron compounds.

$F(r)$
arbitrary units



Figure(5.11). The magnitude of the Fourier transform of an Fe16Cr alloy passivated in 0.1 M NaNO_2 by electron yield and using the chromium edge.

indicative of a reduction of long range order within the passive film compared to the model compound. The bond lengths reported above are summarised in Table (5.2).

5.2.2 Fluorescence Yield Results

The X-ray absorption data for the iron 'K' edges are not reproduced here as all of the fluorescence spectra look identical to those reported for the total yield measurements of Section 5.2.1. That is, they display a marked absorption resonance in the near edge structure and have EXAFS oscillations present over only a limit energy range. Thus they are typical of oxide samples. There is no chromium 'K' edge data here either, because the fluorescence yield was too small to provide any useful data.

Using the usual methods and parameters - the radial distribution functions obtained here are presented in fig. (5.12). It can be seen that these are very similar to those obtained in the electron yield study, except for the reduction in the height of the Fe-Fe peak and a slight broadening of all the peaks. The bond lengths determined from these R.D.F.'s are summarised in Table (5.3). Similar bond lengths to those obtained in the electron yield study were found.

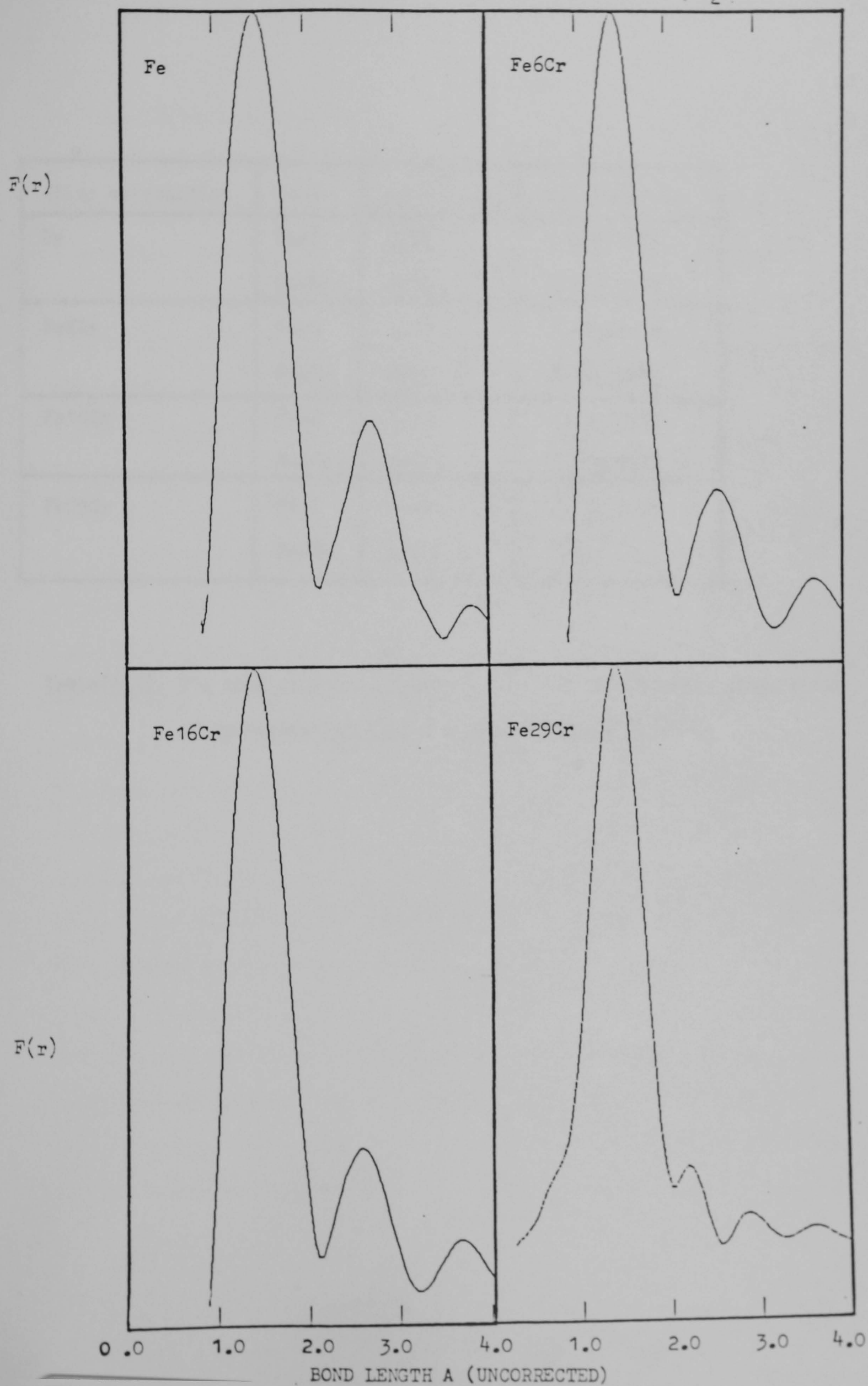
5.2.3 Summary of the Nitrite Passivated Film Results

Qualitatively, the two EXAFS measurement modes have provided the same picture of the passive film formed on Fe-Cr alloys. Both show that as the chromium content of the alloy increases so there is a tendency for the film to lose long range order. The iron samples both yield

Alloy composition	Bond	Measured peak(A)	corrected peak(A)
Fe	Fe-O	1.5	1.99 \pm 0.03
	Fe-Fe	2.67	2.96 \pm 0.05
Fe60Cr	Fe-O	1.46	1.95 \pm 0.03
	Fe-Fe	2.63	2.92 \pm 0.05
Fe16Cr	Fe-O	1.46	1.95 \pm 0.03
	Fe-Fe	2.63	2.92 \pm 0.05
	Cr-O	1.59	2.00 \pm 0.03
Fe29Cr	Fe-O	1.58	2.07 \pm 0.03
	Fe-Fe	N/A	N/A
	Cr-O	1.59	2.00 \pm 0.03

Table(5.2). The bond lengths determined from the total electron yield study of iron-chromium alloys passivated in 0.1M NaNO₂.

Figure(5.12). The magnitudes of the Fourier transforms of Fe-Cr alloys containing 0,6,16 and 29% Cr. Passivated in. 0.1M NaNO_2 by fluorescence y:



Alloy composition	Bond	Measured(A)	Uncorrected(A)
Fe	Fe-O	1.46	1.95 \pm 0.03
	Fe-Fe	2.65	2.94 \pm 0.05
Fe6Cr	Fe-O	1.42	1.91 \pm 0.03
	Fe-Fe	2.59	2.90 \pm 0.05
Fe16Cr	Fe-O	1.42	1.91 \pm 0.03
	Fe-Fe	2.59	2.90 \pm 0.05
Fe29Cr	Fe-O	1.40	1.88 \pm 0.03
	Fe-Fe	N/A	N/A

Table(5.3). The bond lengths determined from the fluorescence yield study of iron-chromium alloys passivated in 0.1 M NaNO₂

R.D.F.'s that were better resolved than any of those presented by Long et al (31).

Two main differences between the two measurement modes exist however. The fluorescence measurements tend to produce R.D.F.'s with slightly (5%) broader peaks than the corresponding electron yield R.D.F. While the bond length obtained from both data sets agree for the samples containing 0, 6 and 16% atomic chromium, a difference is seen in the bond length determined for the chromium-rich alloy. The fluorescence measurement indicates an Fe-O bond length of $1.90 \pm 0.03 \text{ \AA}$ while the electron yield indicates a length of $2.07 \pm 0.03 \text{ \AA}$. All the other Fe-O bond lengths lie about 1.95 \AA within the experimental error of each other.

This result is somewhat surprising because, if as we have seen in Chapter 1. The passive film is to be based upon some oxy-hydroxide structure, (which following O'Grady, may be easily dehydrated), then we might expect that the film measured in the total yield mode would suffer the greatest dehydration. This would imply that we might expect to see a $\gamma\text{-FeOOH} \rightarrow \text{Fe}_2\text{O}_3$ and a shortening of the Fe-O bond in the electron yield result, but a longer Fe-O bond, compatible with the supposed oxy-hydroxide structure, from the fluorescence measurement, where less dehydration can be expected to have taken place. We have seen here, however, that the converse is true.

Finally, we have seen that any chromium contained in the film is oxidised, and appears to be in a chemical environment similar to that found in Cr_2O_3 , except that there is less long range order as indicated by the absence of a substantial Cr-Cr bond.

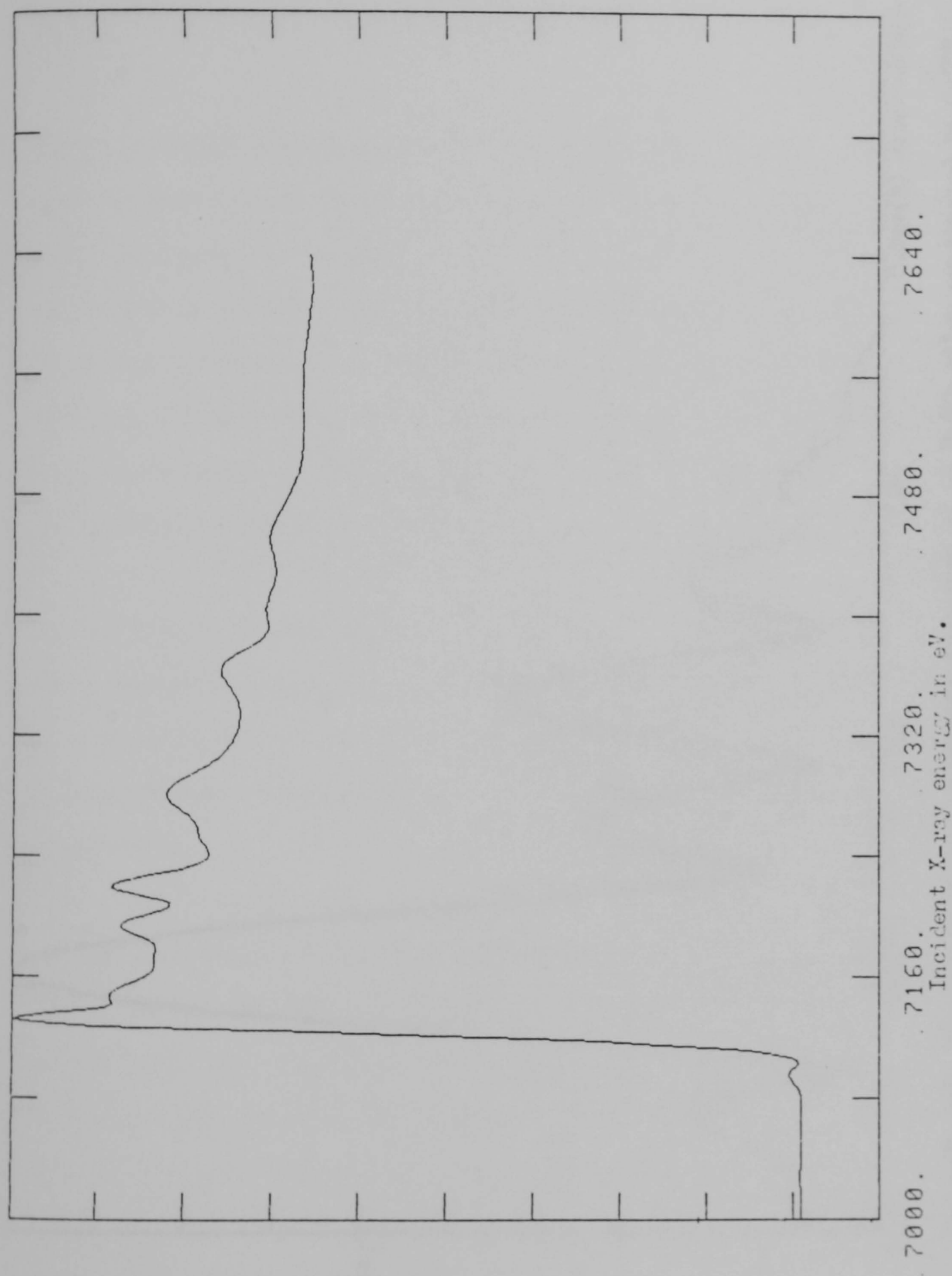
5.3 Chromate Passivated Films

Two sets of alloy films were prepared and passivated in 0.05M K_2CrO_4 solution. One set was studied using the fluorescence mode, while the other was studied using the electron yield mode. The iron 'K' edge X-ray absorption was studied for all the samples while the chromium 'L' edge in the 16 and 29% atomic chromium alloys was studied using the electron yield method. In all other cases the chromium 'K' yield was too low to allow a useful signal to be obtained.

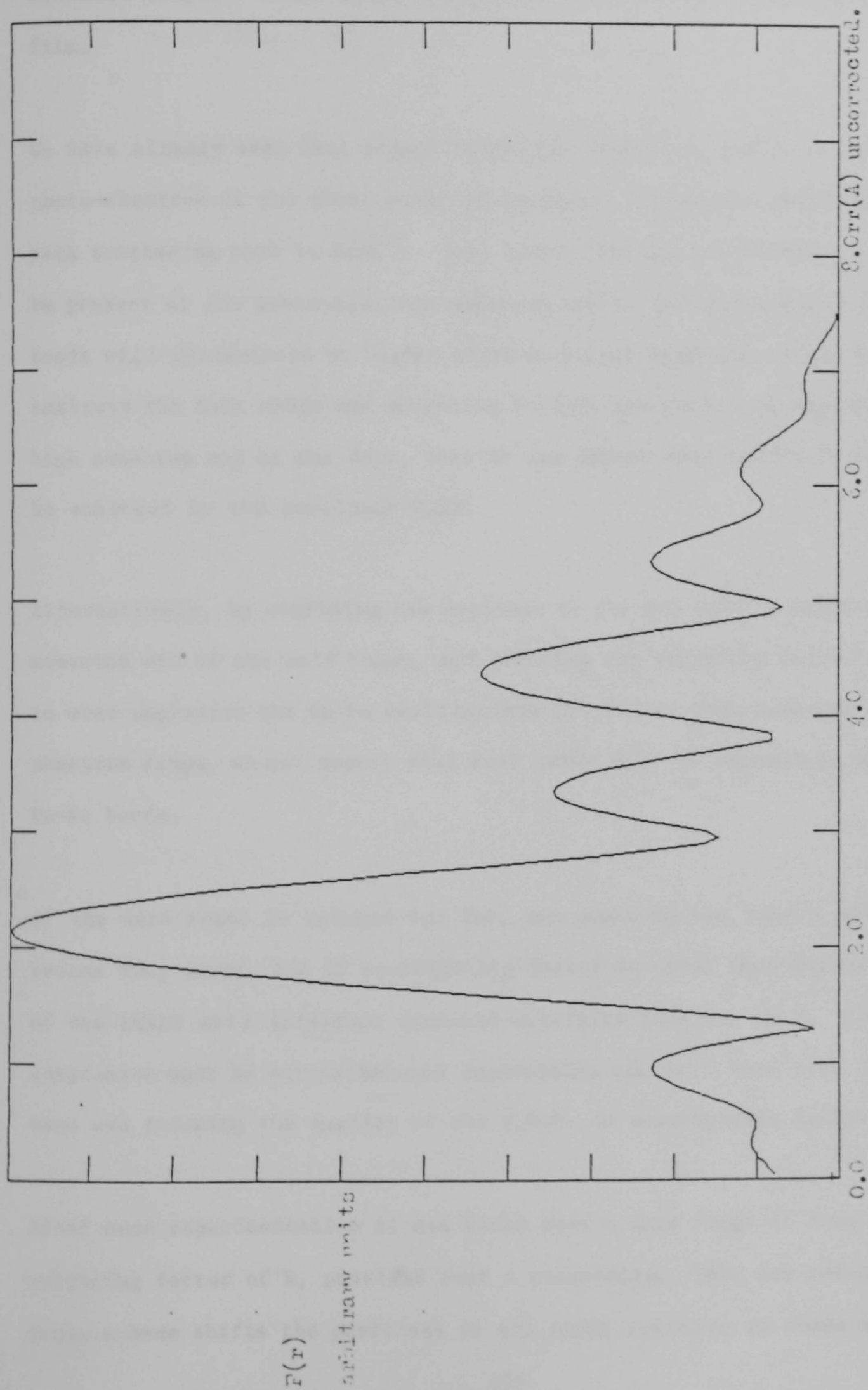
One feature common to all of the samples studied here, was the presence of unoxidised iron, which complicates the interpretation of the passive film EXAFS. This is a problem that has been raised before by Long et al⁽³¹⁾ and Hoffman⁽³⁴⁾.

To illustrate the presence of metallic iron, we shall take as an example, the X-ray absorption data obtained using the electron yield measurement mode from a 6% atomic chromium alloy; this is shown in fig. (5.13). While it can be seen that the near edge structure is indicative of an oxide, it is also clear that the EXAFS oscillations are dominated by metallic iron. The greater sensitivity of the near edge region to any oxide can be ascribed to the much larger back scattering factor of oxygen compared to iron, at the low photo-electron momentum seen in the XANES region. The presence of metallic iron is clearly seen in the R.D.F. of the Fe6Cr alloy shown in fig. (5.14). This is very similar to the R.D.F. of the iron model compound shown in fig. (4.11a).

There are reasons, however, to suppose that some passive film information may be present in the data. The near edge absorption indicates that some



Figure(5.13). The iron 'K' edge X-ray absorption spectrum of an Fe6Cr alloy passivated in 0.05 M K_2CrO_4 measured by total electron yield.



Figure(5.14). The magnitude of the **Fourier** transform of an Fe6Cr alloy passivated in 0.05M K_2CrO_4 measured by total electron yield.

oxidation has taken place, the peaks seen in the R.D.F.'s are more complicated, displaying structures and secondary peaks, not seen in the metallic sample. These extra features may be ascribed to the passive oxide film.

We have already seen that oxygen is only an effective scatterer of the photo-electron at low photo-electron momentum, unlike iron which has a back scattering peak at 6.5\AA^{-1} . This means that any oxide EXAFS will only be present at low photo-electron momentum, while the EXAFS due to Fe-Fe bonds will predominate at higher photo-electron momentum. Thus, if during analysis the data range and weighting factors are chosen to emphasise the high momentum end of the data, then we can expect that any Fe-Fe bonds will be enhanced in the resultant R.D.F.

Alternatively, by confining the analysis to the low ($<7\text{\AA}^{-1}$) photo-electron momentum end of the data range, and reducing the weighting factor so as not to over-emphasise the Fe-Fe oscillations present in high photo-electron momentum range, we can expect that Fe-O bonds will be emphasised against the Fe-Fe bonds.

If the data range is reduced too far, any peaks in the R.D.F.'s will become very broad, and if no weighting factor is used, then the natural decay of the EXAFS will introduce unwanted artefacts into the R.D.F. Thus a compromise must be struck between emphasising the Fe-O bond over the Fe-Fe bond and reducing the quality of the R.D.F. to unacceptable limits.

After much experimentation it was found that a data range of 3 to 7\AA^{-1} and a weighting factor of k , provided such a compromise. This new reduced data range scheme shifts the positions of the peaks relative to those obtained

using the full data range. Thus new correction factors have to be obtained from the model compounds, by analysing the model compounds using the reduced data range the resultant R.D.F.'s are shown in figs. (5.15 and 5.16), with the new correction factors given in Table (5.4).

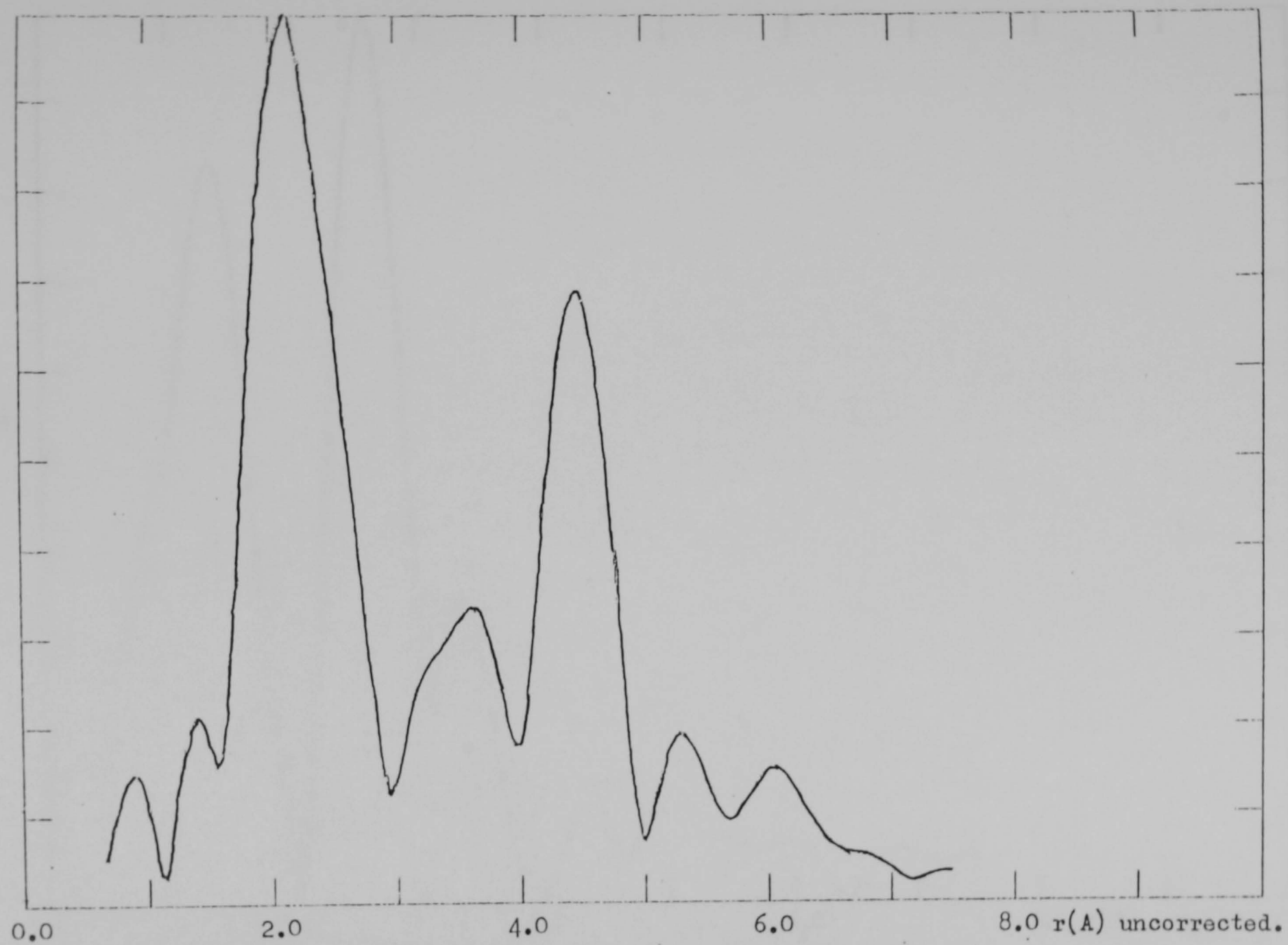
It can be seen that while the peaks are broader than those reported earlier, they are still well resolved and that two oxygen peaks are now visible in the $\alpha\text{-Fe}_2\text{O}_3$ data. It is also clear that it is possible to distinguish between Fe-O bonds in an oxide from the Fe-Fe bonds of metallic iron. However, that it is possible to distinguish between the Fe-Fe bonds in a metal and an oxide is less clear.

Returning to the 6% atomic Cr alloy discussed above, this was re-analysed using the reduced data range scheme and its new R.D.F. shown is in fig. (5.18). Comparison with the iron R.D.F. makes it possible to identify easily the peaks associated with metallic iron, and Fe-O bonds. The close proximity of the Fe-O bond and the first metallic Fe-Fe bond will introduce some error into the position of each peak.

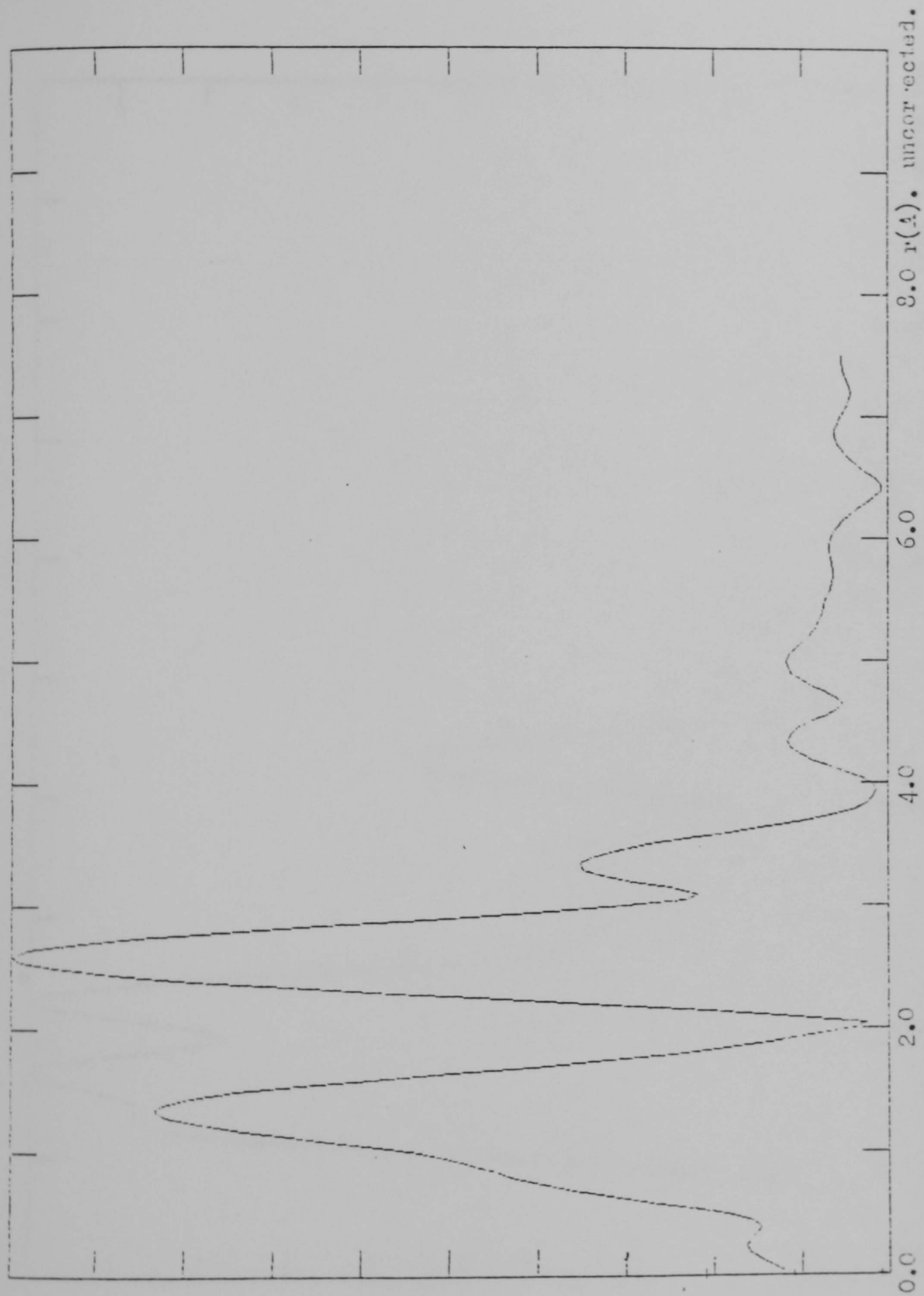
For completeness all the R.D.F.'s generated here using the reduced data range are reproduced in figs. (5.17 - 5.24). The Fe-O bond lengths determined from them are presented in Table (5.5). No attempt was made to determine the (Fe-Fe) bond lengths as these were confused by the presence of some residual metallic iron signal.

The fluorescence measurements indicate that for alloys containing less than 20% atomic chromium that the Fe-O bond length is constant at approximately 2.0Å. The discrepancy seen on the alloy containing 6% atomic chromium is due to the Fe-O peak overlapping with the residual metallic iron peak. The

$F(r)$
arbitrary units

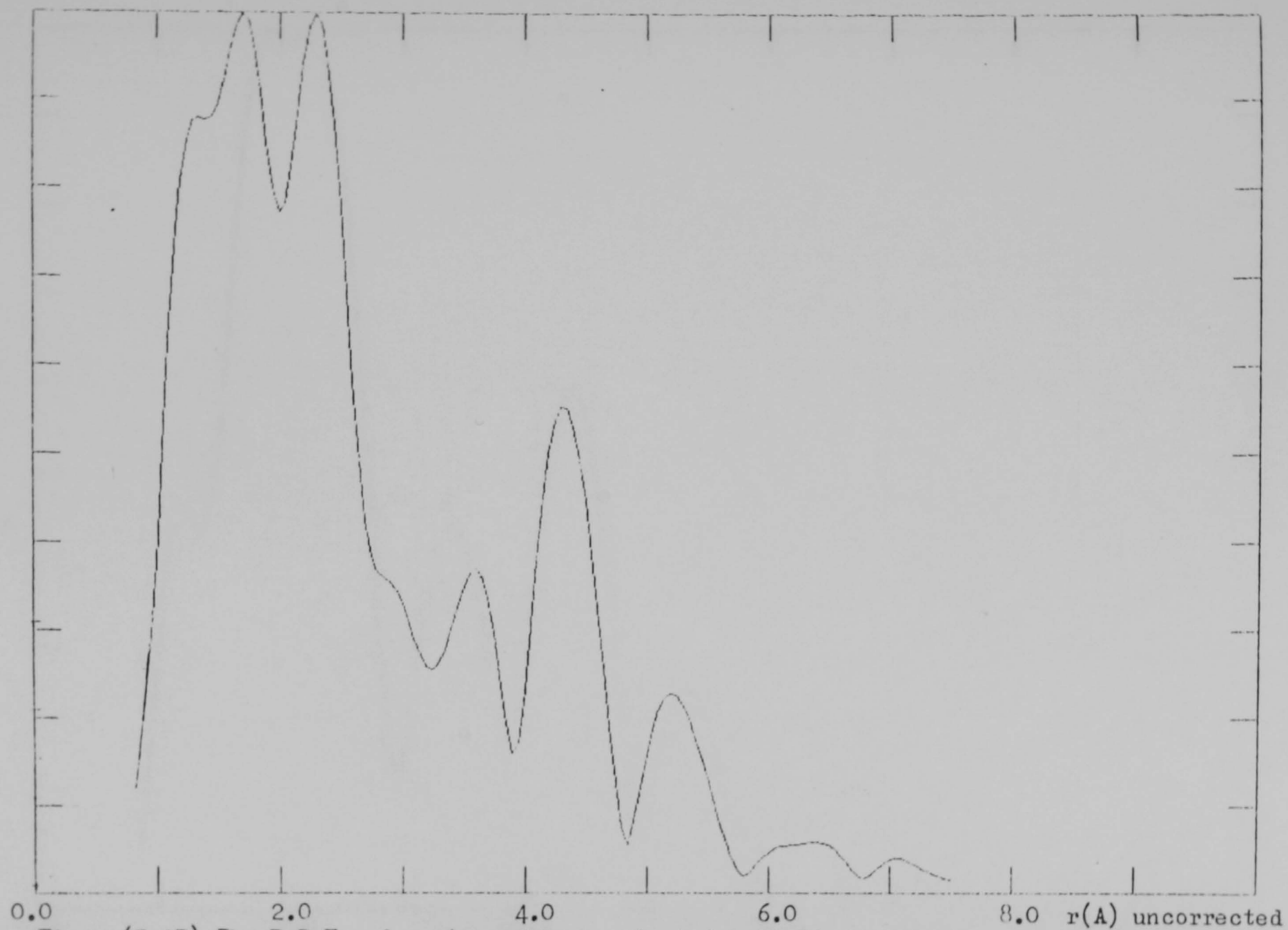


Figure(5.15). The R.D.F. of iron using the reduced data range scheme.



Figure(5.16). The R.D.F. of $\alpha\text{-Fe}_2\text{O}_3$ by the reduced data range scheme.

$F(r)$
arbitrary units



Figure(5.17). The R.D.F. of an iron film passivated in 0.05 M K_2CrO_4 by electron yield and the reduced data range scheme.

$F(r)$
arbitrary units

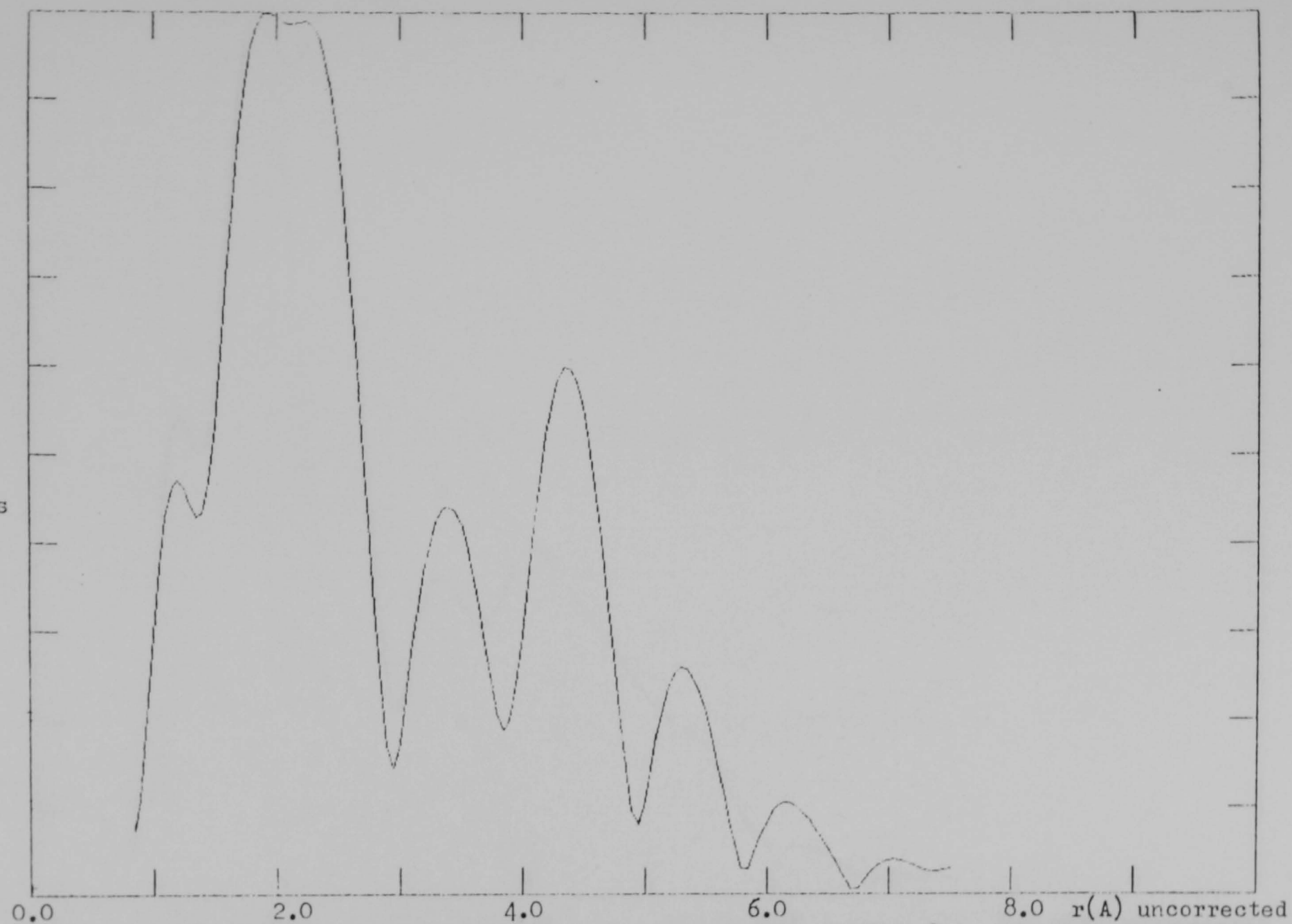


Figure (5.18). The R.D.F. of an Fe6Cr alloy passivated in 0.05M K_2CrO_4 by electron yield

and the reduced data range scheme.

$F(r)$
arbitrary units

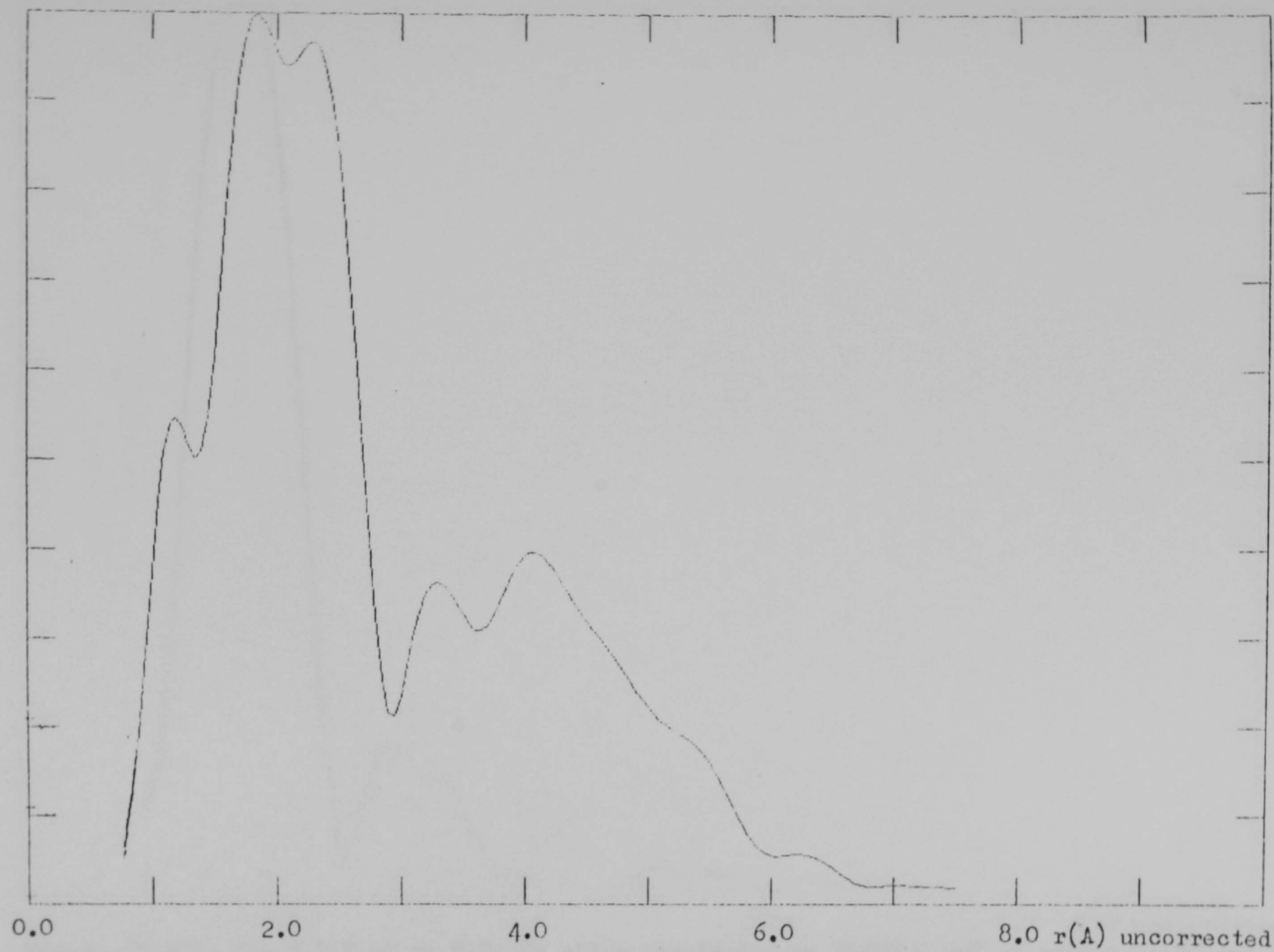


Figure (5.19). The R.D.F. of an Fe16Cr alloy passivated in 0.05M K_2CrO_4 by electron yield and the reduced data range scheme.

$F(r)$
arbitrary units

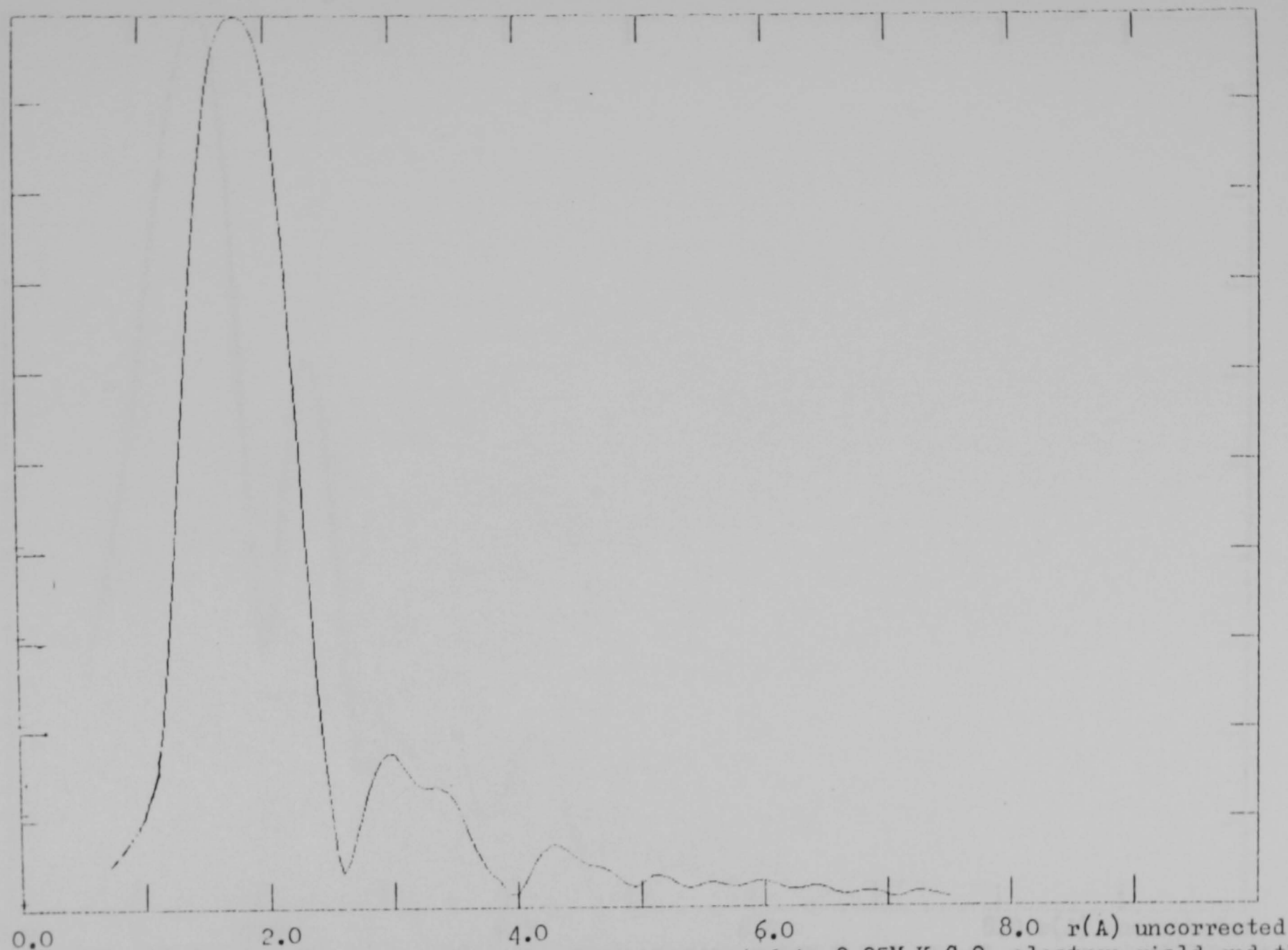
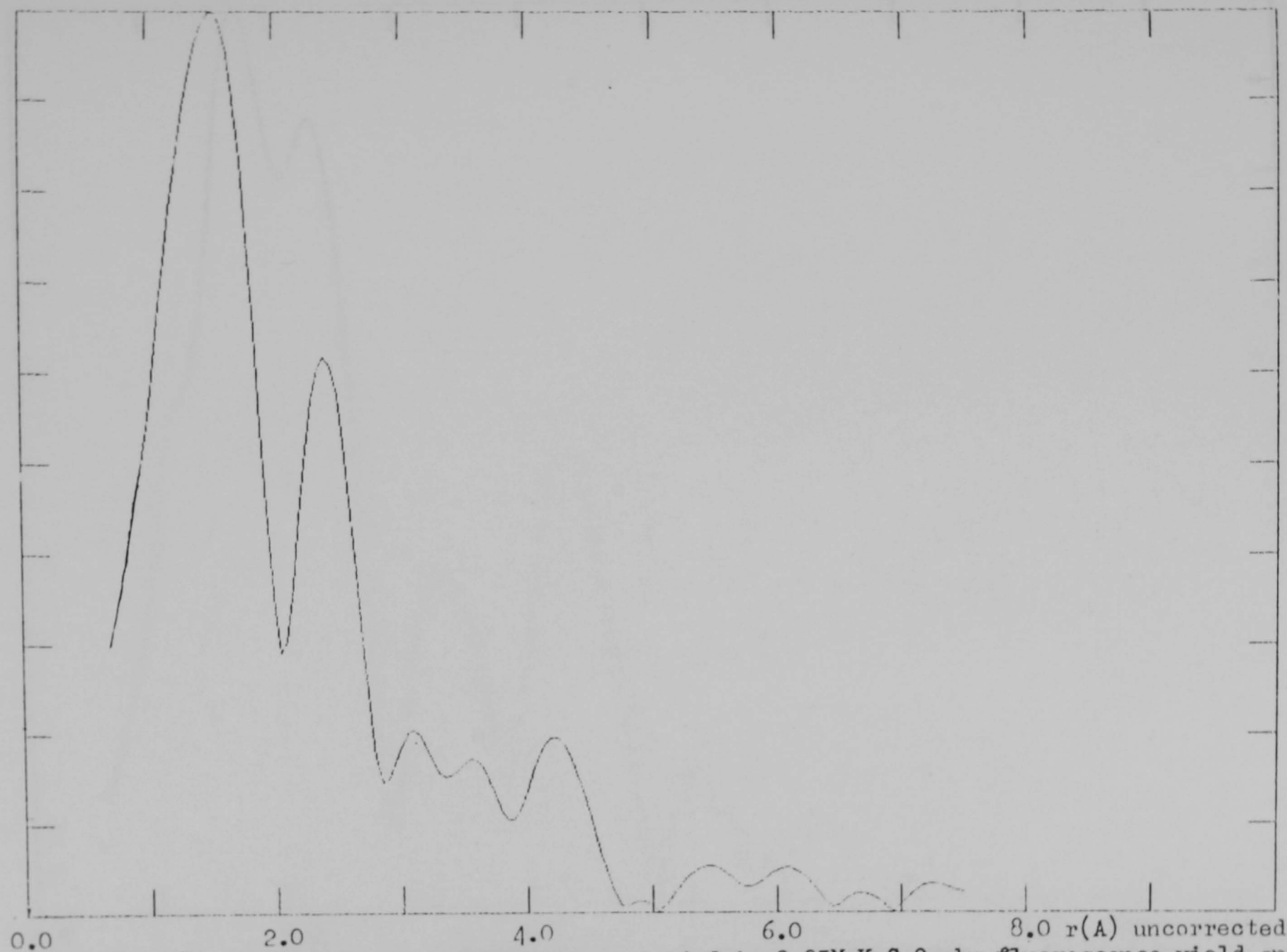


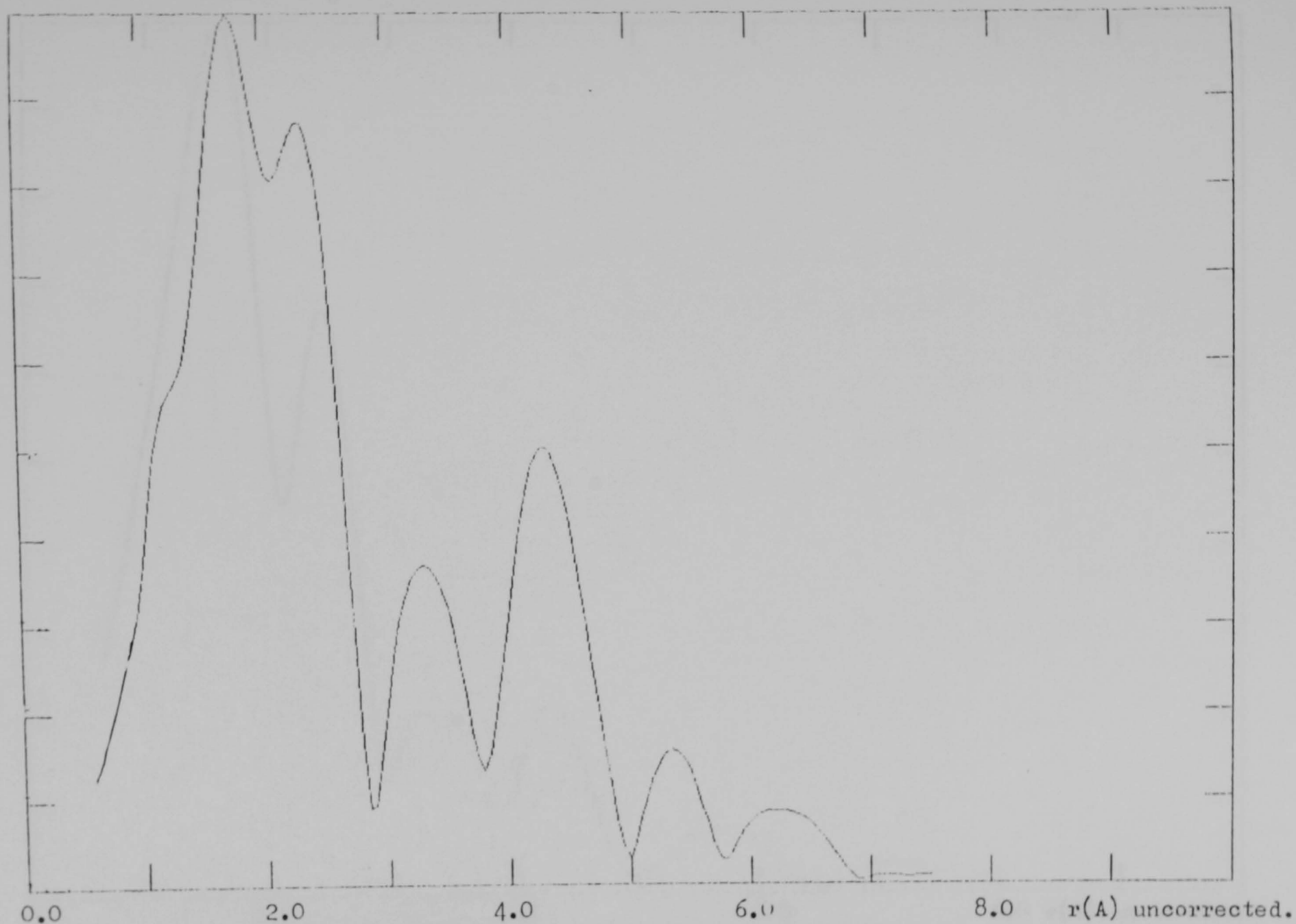
Figure (5.20). The R.D.F of an Fe29 Cr alloy passivated in $0.05\text{M K}_2\text{CrO}_4$ electron yield and the reduced data range scheme.

$F(r)$
arbitrary units

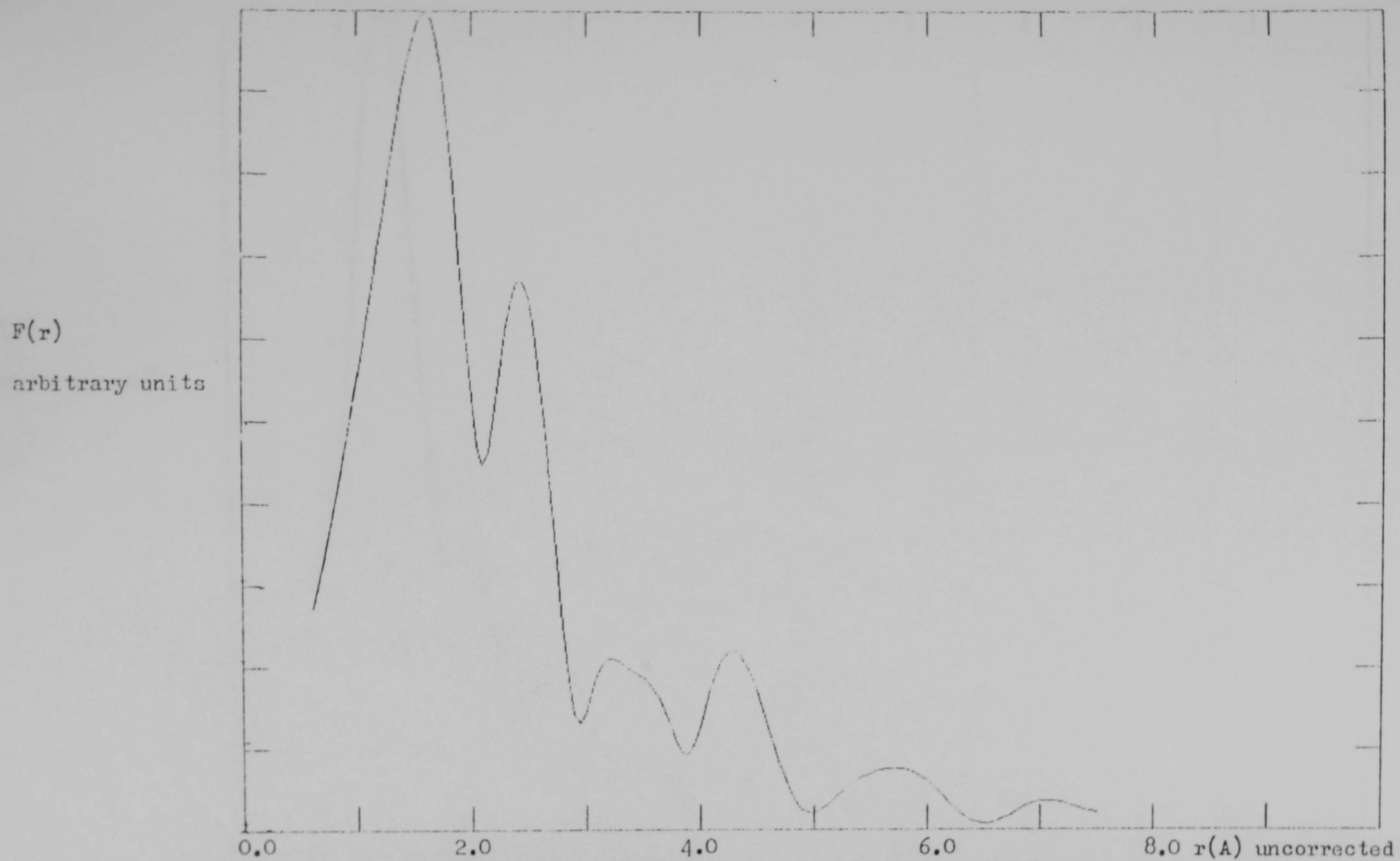


Figure(5.21). The R.D.F. of an iron film passivated in 0.05M K_2CrO_4 by fluorescence yield and the reduced data range scheme.

$F(r)$
arbitrary units



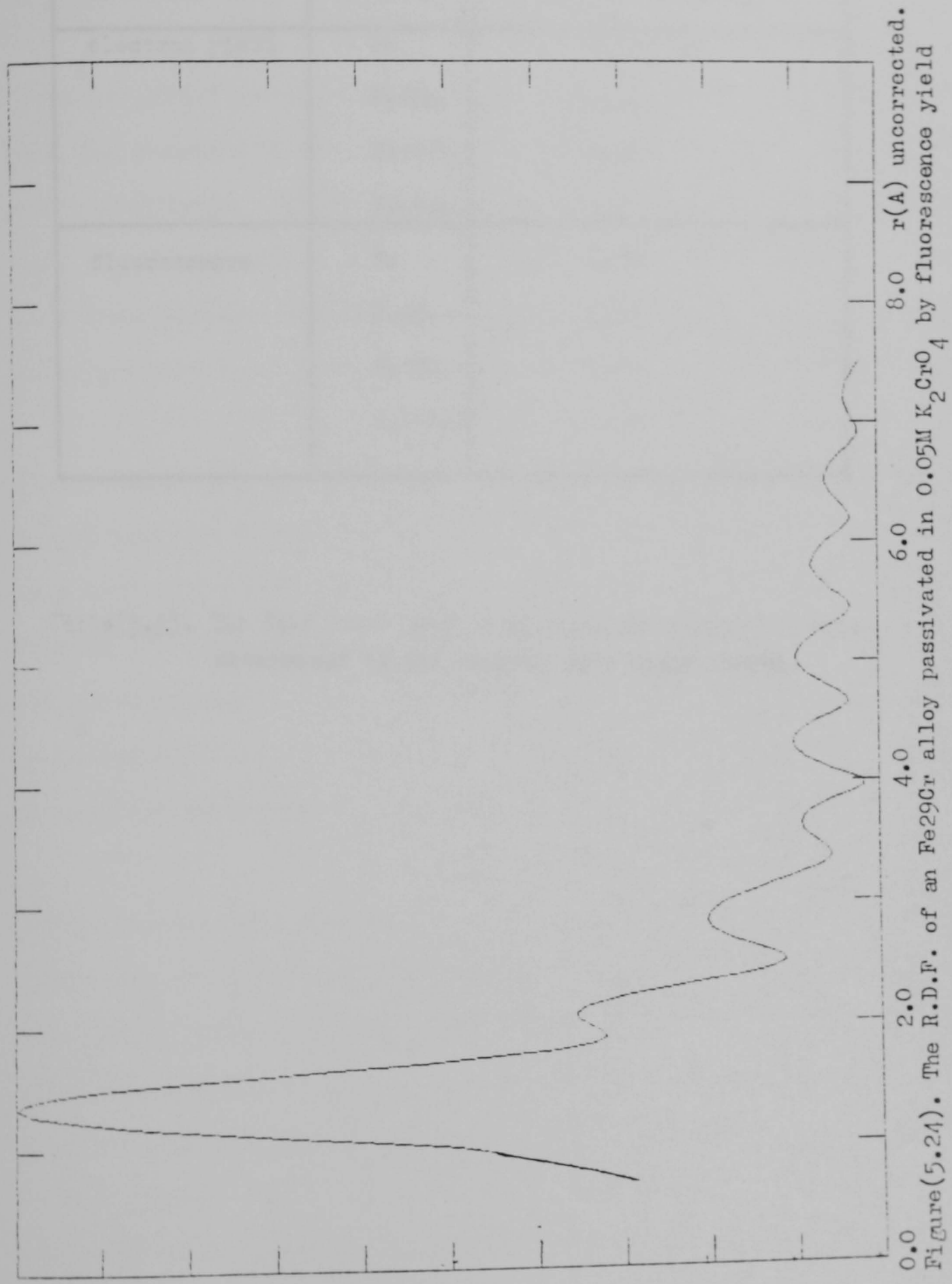
Figure(5.22). The R.D.F. of an Fe6Cr alloy passivated in 0.05M K_2CrO_4 by fluorescence yield and the reduced data range scheme.



Figure(5.23). The R.D.F. of an Fe16Cr alloy passivated in 0.05M K_2CrO_4 by fluorescence yield and the reduced data range scheme.

$F(r)$

arbitrary units



and the reduced data range scheme.

Detection mode	alloy	Fe-O bond length(A)
electron yield	Fe	2.24 \pm 0.2
	Fe6Cr	2.46
	Fe16Cr	2.34
	Fe29Cr	2.32
fluorescence	Fe	2.09
	Fe6Cr	2.32
	Fe16Cr	2.14
	Fe29Cr	1.90

Table(5.5). The Fe-O bond lengths of chromate passivated alloy determined by the reduced data range scheme.

Fe-O bond length seen in the Fe₂₉Cr alloy is reduced compared to those obtained from the low Cr alloys: a feature seen in the fluorescence measurements made upon the nitrite passivated films.

The total yield measurements provide a more complicated picture. For even when the presence of metallic iron is accounted for, the remaining peaks are still structured. Within the limits of the simple analysis method employed here it is not possible to analyse these features any further, except to say that their presence does lend support to the view that chromate passivated films are more complex in structure than the nitrite passivated films.

While similar features were seen in the fluorescence data presented here, it may be that the features in the total yield data are more prominent because they form as a result of the dehydration of the true passive film. Thus because less de-hydration occurs in the fluorescence mode the features do not present themselves so clearly. In order to understand fully the extra peaks and structure seen here a more advanced analysis method, based upon theoretical modelling, is required.

Before leaving this section, it is worth noting that in their in situ EXAFS study Long et al⁽³²⁾ presented R.D.F.'s for chromate and nitrite passivated iron films. These were almost identical to those obtained using electron yield measurements to study iron passivated in chromate solution. In this study we have been able to ascribe the peak labelled Fe (metallic) to residual metallic iron. Long et al however interpret the wide triplet of peaks as being due to the passive film and so infer a large degree of disorder to be present in the passive film. Since Long et al only present data up to 4Å in the R.D.F. one cannot check to see whether there is any indication of a metallic Fe-Fe bond at 6Å. In view of this one may wonder whether the

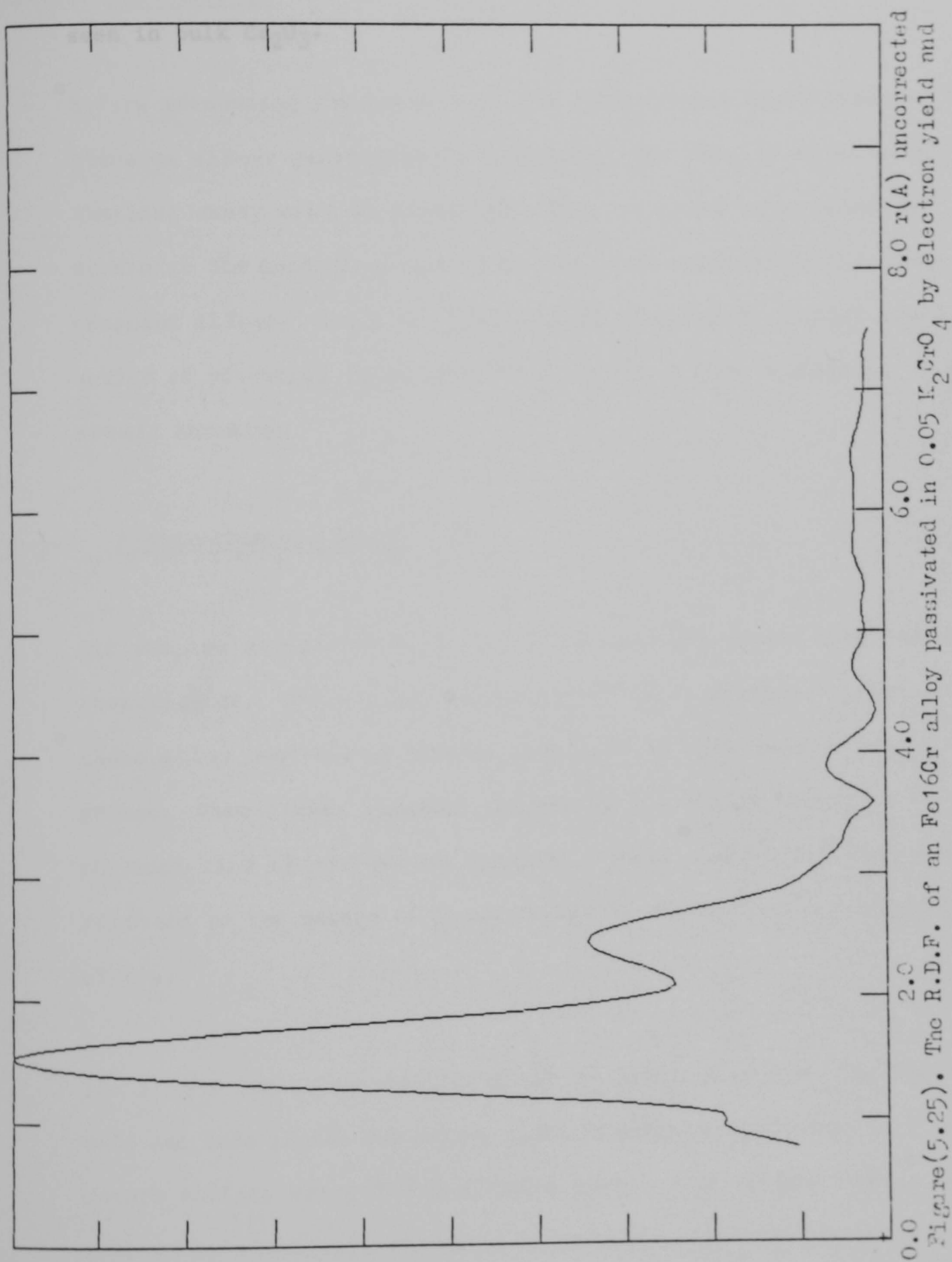
Long et al data should not be interpreted in terms of residual iron rather than a complex film structure.

The two chromium R.D.F.'s indicated Cr-O bonds compatible with Cr_2O_3 , and again showed a reduction in long range order compared to the Cr_2O_3 model compound. The R.D.F. from the Fe16Cr alloy is presented in fig. (5.25). It is interesting to note that despite large quantities of unoxidised iron remaining in the film, the chromium data clearly indicates that all the chromium present is oxidised.

5.3.1 Summary of the Chromate Passivated Film Results

Since the alloy samples used in this study were the same thickness as those used in the nitrite study, we must assume that the presence of the large amount of un-oxidised iron is a result of the chromate formed film's being much thinner than the nitrite formed film's. We have also seen that both the EXAFS and XANES are very sensitive to small amounts of oxide present, since even in the presence of so much un-reacted iron we have still been able to obtain the Fe-O bond length in the passive film.

The analysis of these metallic iron-rich samples indicates that great care must be taken in sample preparation, data analysis and interpretation, if the ambiguous results of Long et al⁽³¹⁾ are to be avoided. The bond lengths determined here for the Fe-O bond are compatible with those on known iron-oxides. However, the large uncertainty in the bond length determination prevents any detailed structure from being presented.



the chromium edge and analysed by the 'full' data range scheme.

Finally it is interesting to note that even though much metallic iron was present in the sample, any chromium present was oxidised, and was sited in a local matrix displaying more structural disorder than that seen in bulk Cr_2O_3 .

5.4 H₂SO₄ Passivated Films

5.4.1 Introduction

Before presenting the results of the fluorescence EXAFS study of iron-chromium alloys passivated in 2.0M H₂SO₄, the results of an electrochemical study will be presented. This study was undertaken to determine the conditions needed to passivate anodically the iron-chromium alloys. Using the bulk alloys provided by British Steel, a series of potential scans were obtained for alloys containing up to 25% atomic chromium.

5.4.2 Electrochemical Study

Six samples containing 0, 5, 10, 15, 20 and 25% atomic chromium were investigated. While other workers^(13,24) have presented results for these alloy comparisons before, they have not all been presented together. When viewed together changes in the anodic behaviour of the chromium rich alloys become apparent. These changes are then seen to be relevant to the nature of films formed on the corrosion resistant Fe-Cr alloys.

The alloys (exact composition given in Table (5.6) some 2mm thick were cut into pieces 2cm x 1cm, and mechanically polished to a mirror smooth surface using 0.05um alumina paste. Any surface damage was then removed by electropolishing. A contact wire was spot welded to the top edge of the sample and an exposed area of 0.5cm² was defined on the polished surface using Lacomite varnish.

Using a standard potentiostat with a saturated calomel electrode and gold counter electrode, the sample was introduced into 2.0M H_2SO_4 at a potential of -0.8V (S.C.E.). The sample was held here for 20 minutes to ensure the cathodic reduction of any surface oxide. The potential was then ramped at 5mVs^{-1} to oxygen evolution at +1.8V (S.C.E.), where it stopped and then ramped back to the cathodic potential.

5.4.2.1 Electrochemical Results

The anodic curves are shown in Fig. (5.26 to 5.31). The behaviour of the alloys containing up to 20% atomic chromium is well known and has been reported elsewhere⁽¹³⁾. As usual the reduction in the iron dissolution peak is matched by an increase in the chromium dissolution peak, which can be seen to maximise on the alloy containing 20% atomic chromium.

Figure (5.31) shows the anodic behaviour of the alloy containing 25% atomic chromium. This curve is in good agreement with that presented by Mitrovic-Scepanovic et al⁽²⁴⁾. It is interesting to note that the peak associated with the dissolution of Cr^{6+} has now reduced in magnitude compared to that seen in the alloy containing 20% atomic chromium. During repeated potential cycling, the chromium dissolution peaks on the alloys containing 20% atomic chromium were found to be reproducible while the peak on the 25% atomic chromium alloy was not.

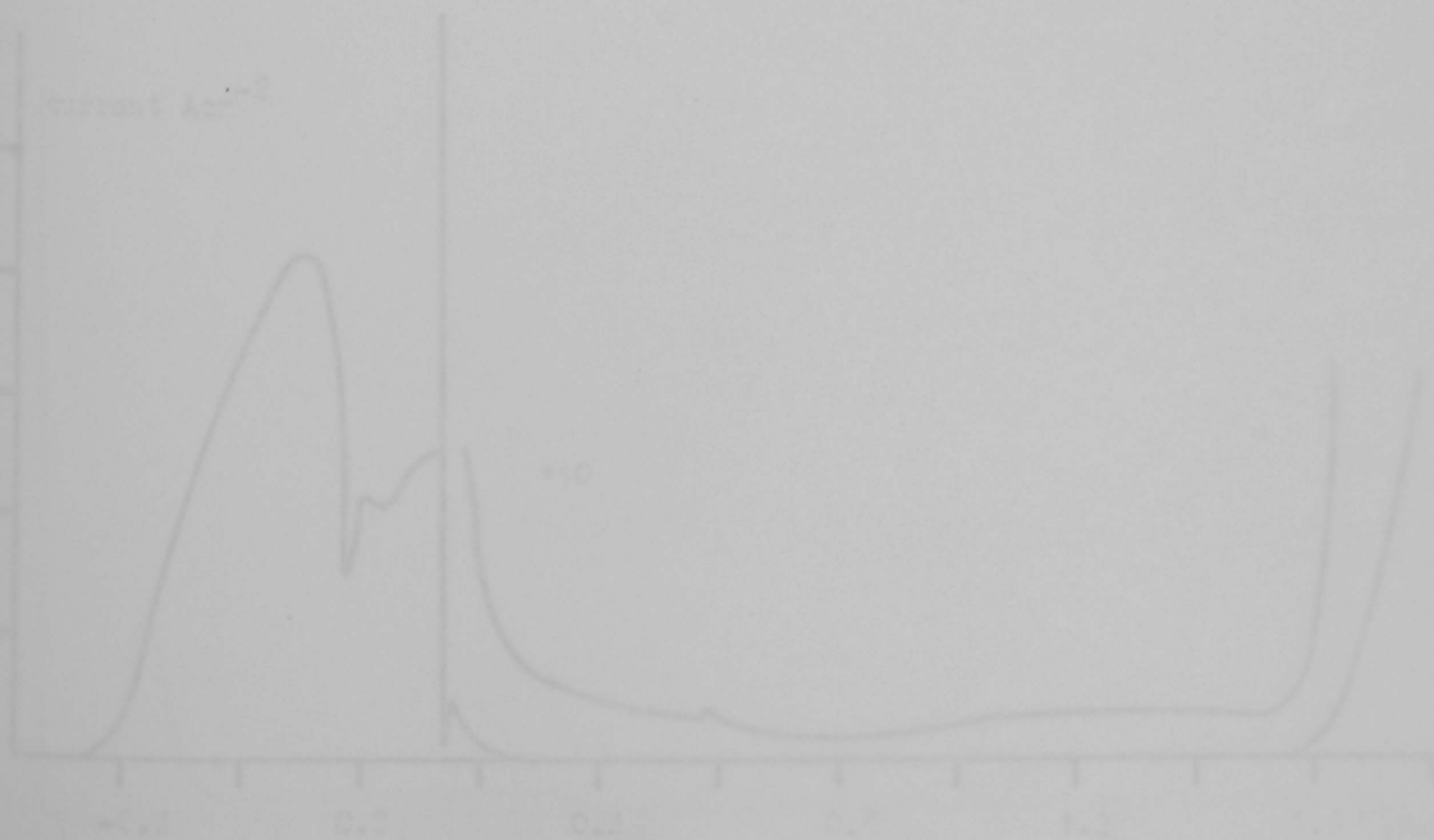
This was taken to indicate that in the chromium rich alloy passivation in the potential region +0.8 to +1.6V (S.C.E.) was more effective. Thus when all the curves are seen together it is apparent that some change has occurred to the passive film as the chromium content of the alloy exceeds 20% atomic chromium.

current Acm-2

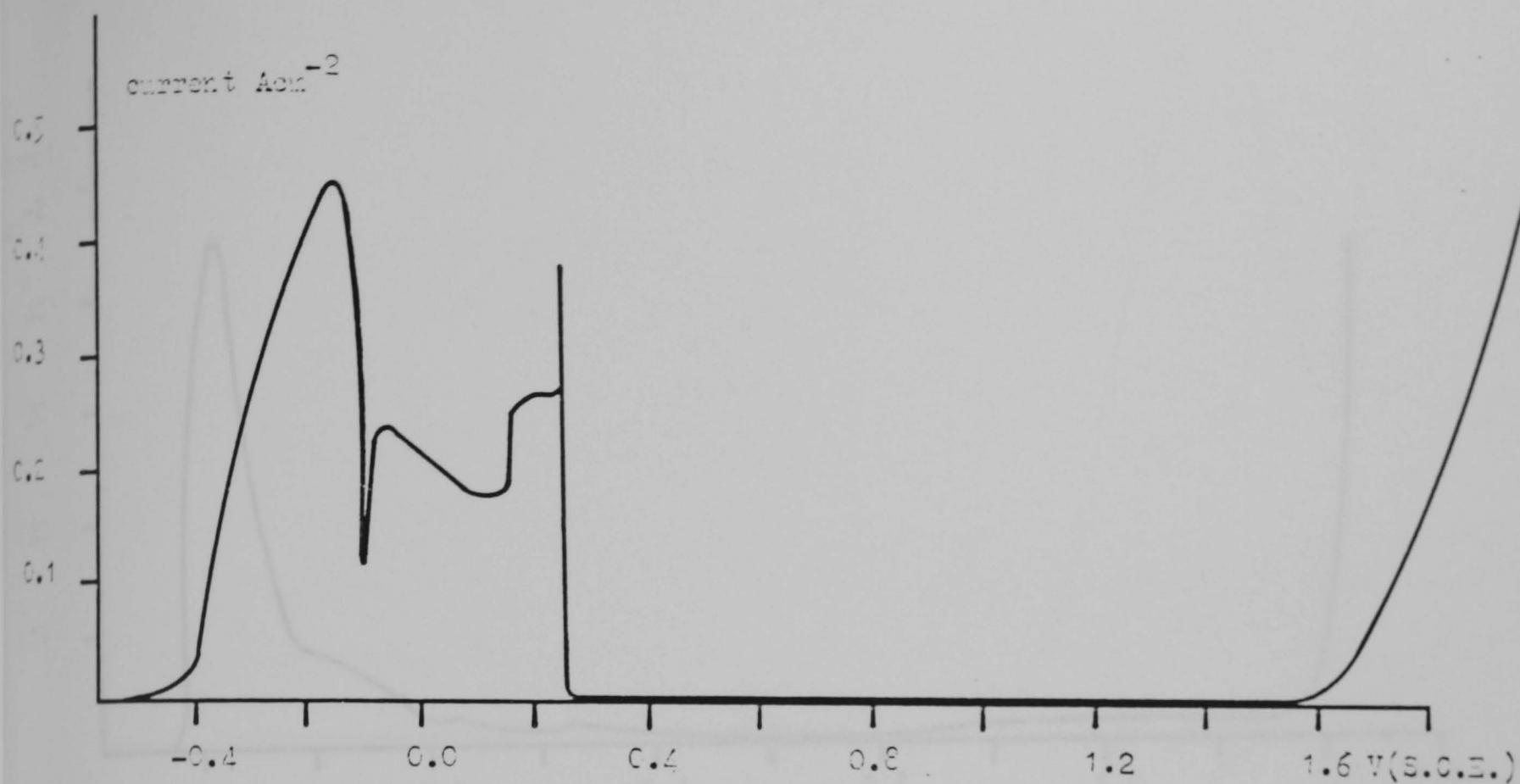
nominal composition of alloy	analysis of alloy							
	Cr	Si	Mn	P	S	Mo	Ni	C
Fe	0.02	0.31	0.03	0.003	0.02	0.05	0.02	0.004
Fe5Cr	4.18	0.16	0.08	0.005	0.02	0.02	0.02	0.004
Fe10Cr	11.2	0.21	0.08	0.005	0.02	0.02	0.02	0.006
Fe15Cr	14.2	0.19	0.08	0.005	0.03	0.02	0.02	0.007
Fe20Cr	20.3	0.26	0.08	0.005	0.03	0.02	0.02	0.006
Fe25Cr	24.6	0.25	0.07	0.005	0.03	0.02	0.02	0.005

Table(5.6). Analysis of the bulk alloys used in the electrochemical study and used to prepare the thin alloy films.

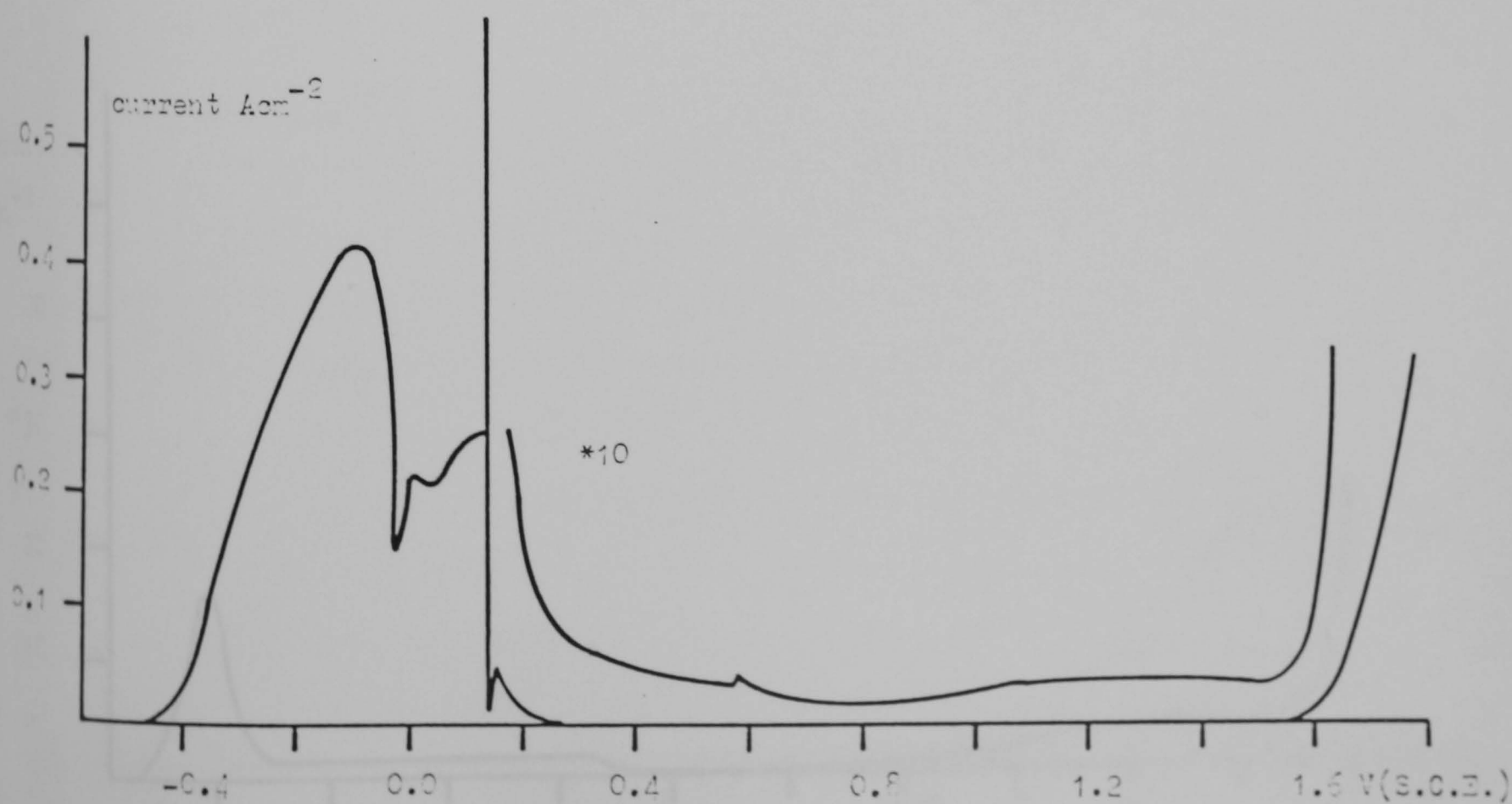
current Acm-2



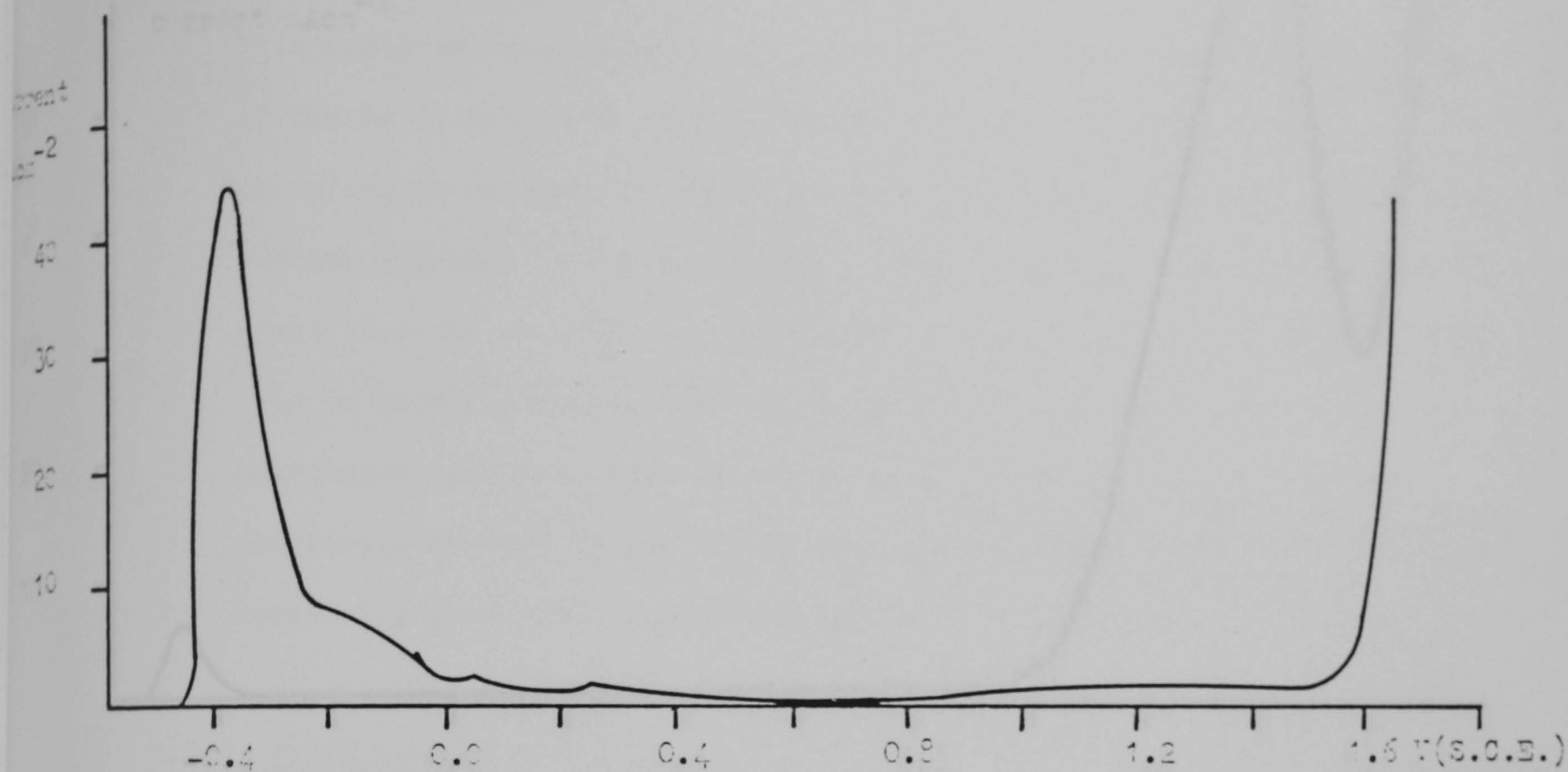
Figure(5.7) The anodic polarization curves of Fe and Fe-Cr alloys in 1M NaCl at 30°C



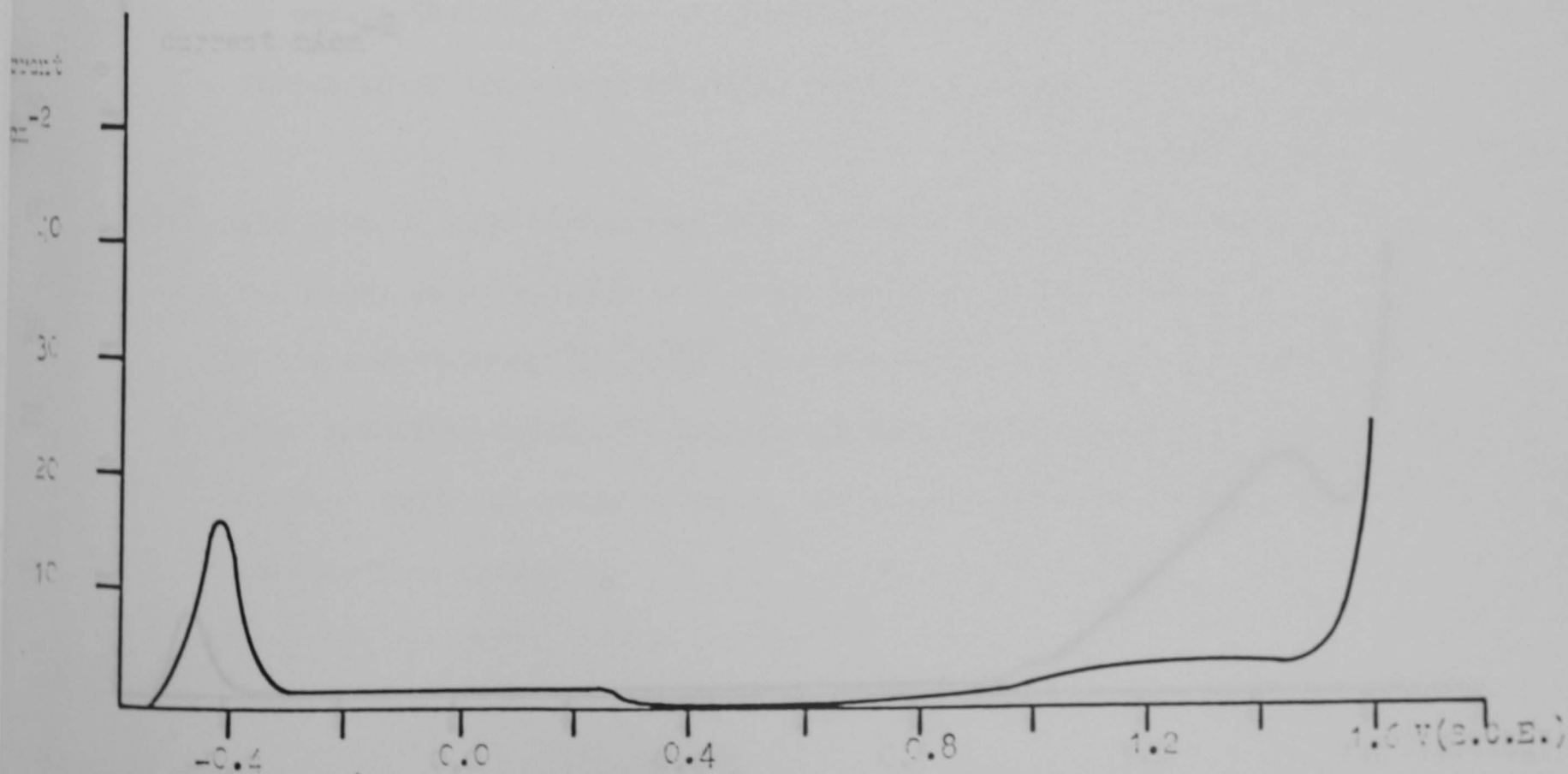
Figure(5.26). The anodic polarisation curve of iron in 2.0M H_2SO_4 at $5mVs^{-1}$



Figure(5.27). The anodic polarisation curve of an Fe50Cr alloy in 2.0M H_2SO_4 at $5mVs^{-1}$

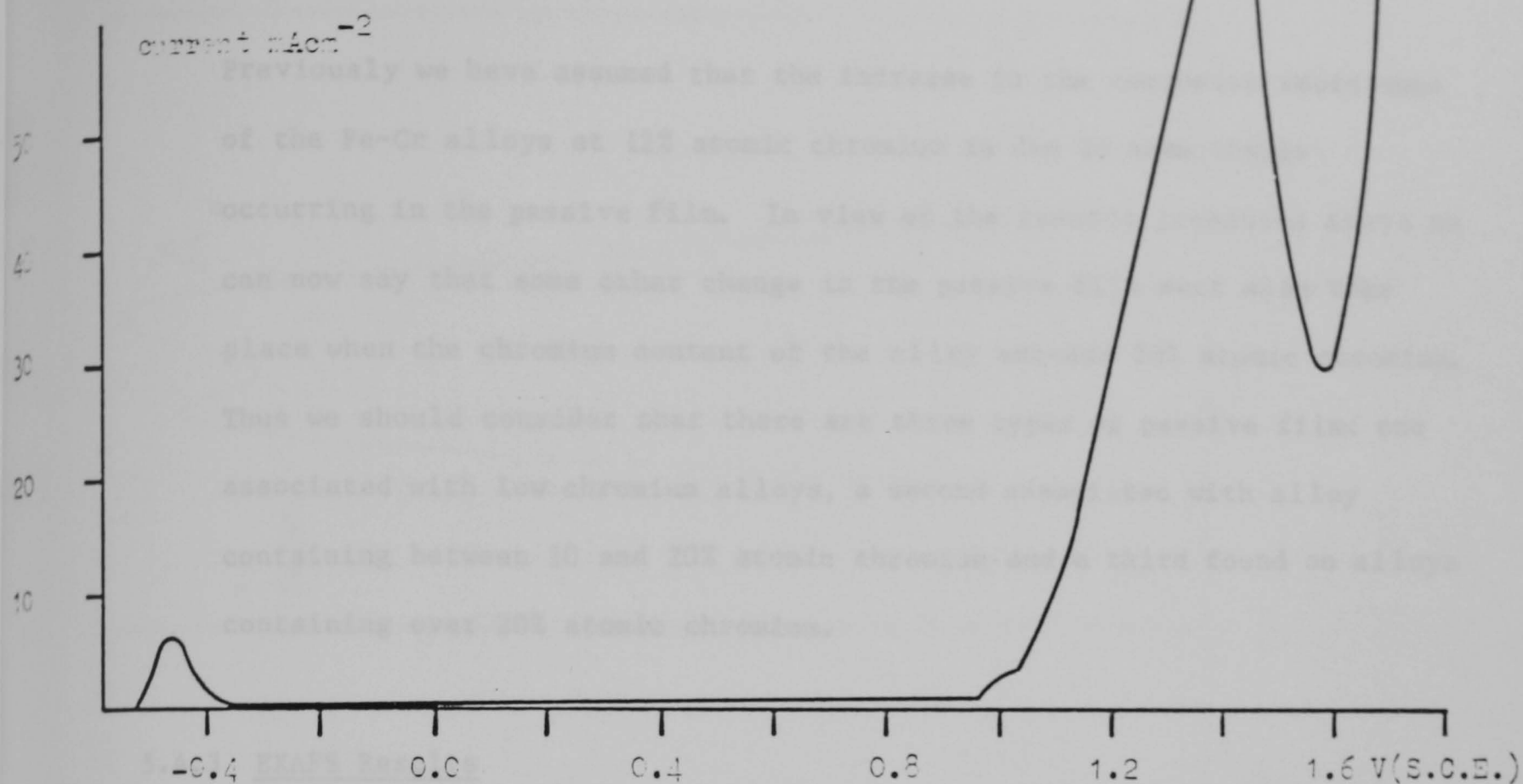


Figure(5.28). The anodic polarization curve of an Fe10Cr alloy in 2.0M H_2SO_4 at $5mVs^{-1}$

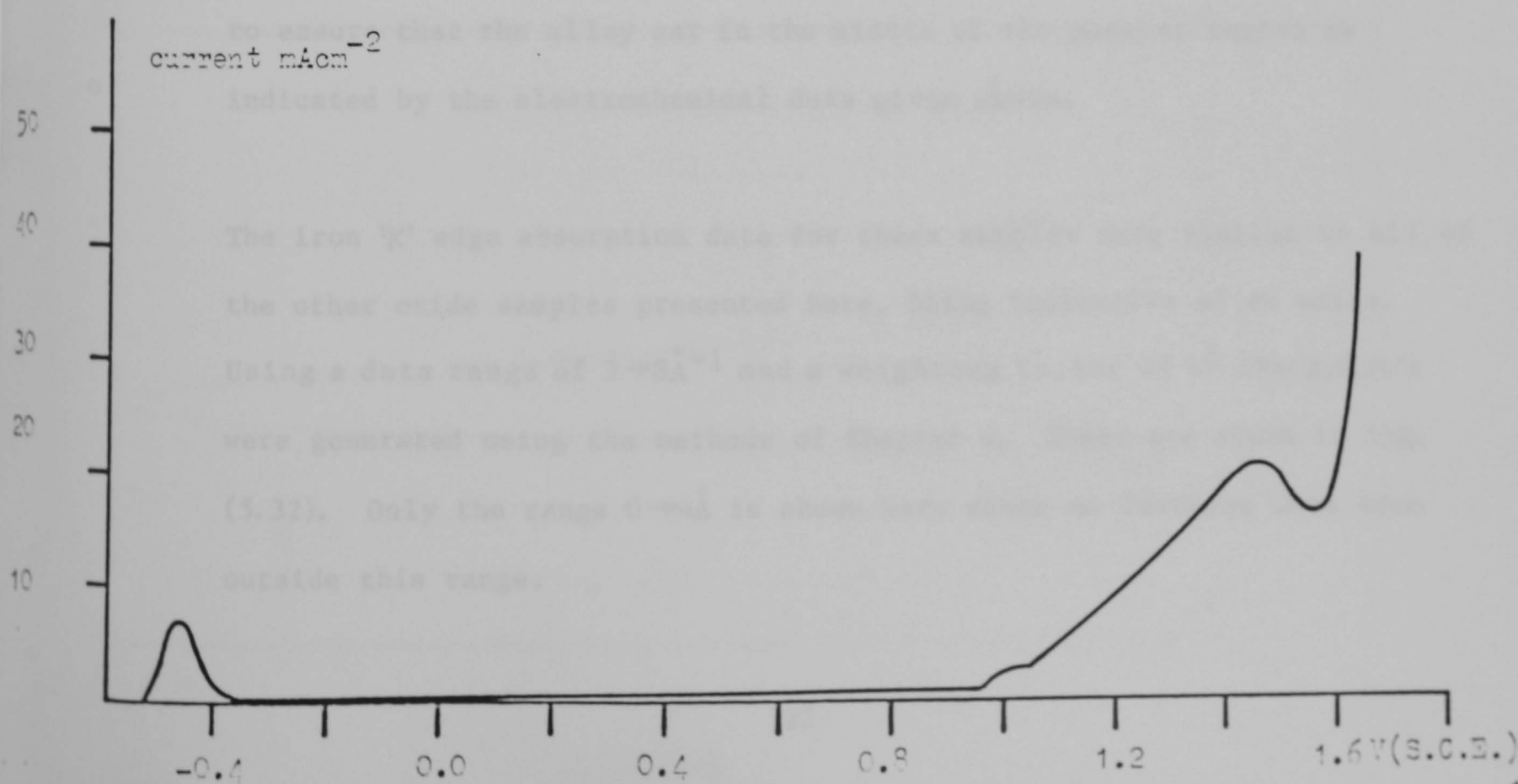


Figure(5.29). The anodic polarization curve of an Fe15Cr alloy in 2.0M H_2SO_4 at $5mVs^{-1}$

5.4.2.2 Conclusion of Electrochemical Analysis



Figure(5.30). The anodic polarisation curve of an Fe20Cr alloy in 2.0M H_2SO_4 at $5mVs^{-1}$



Figure(5.31) The anodic polarisation curve of an Fe25Cr alloy in 2.0M H_2SO_4 at $5mVs^{-1}$

5.4.2.2 Conclusion of Electrochemical Results

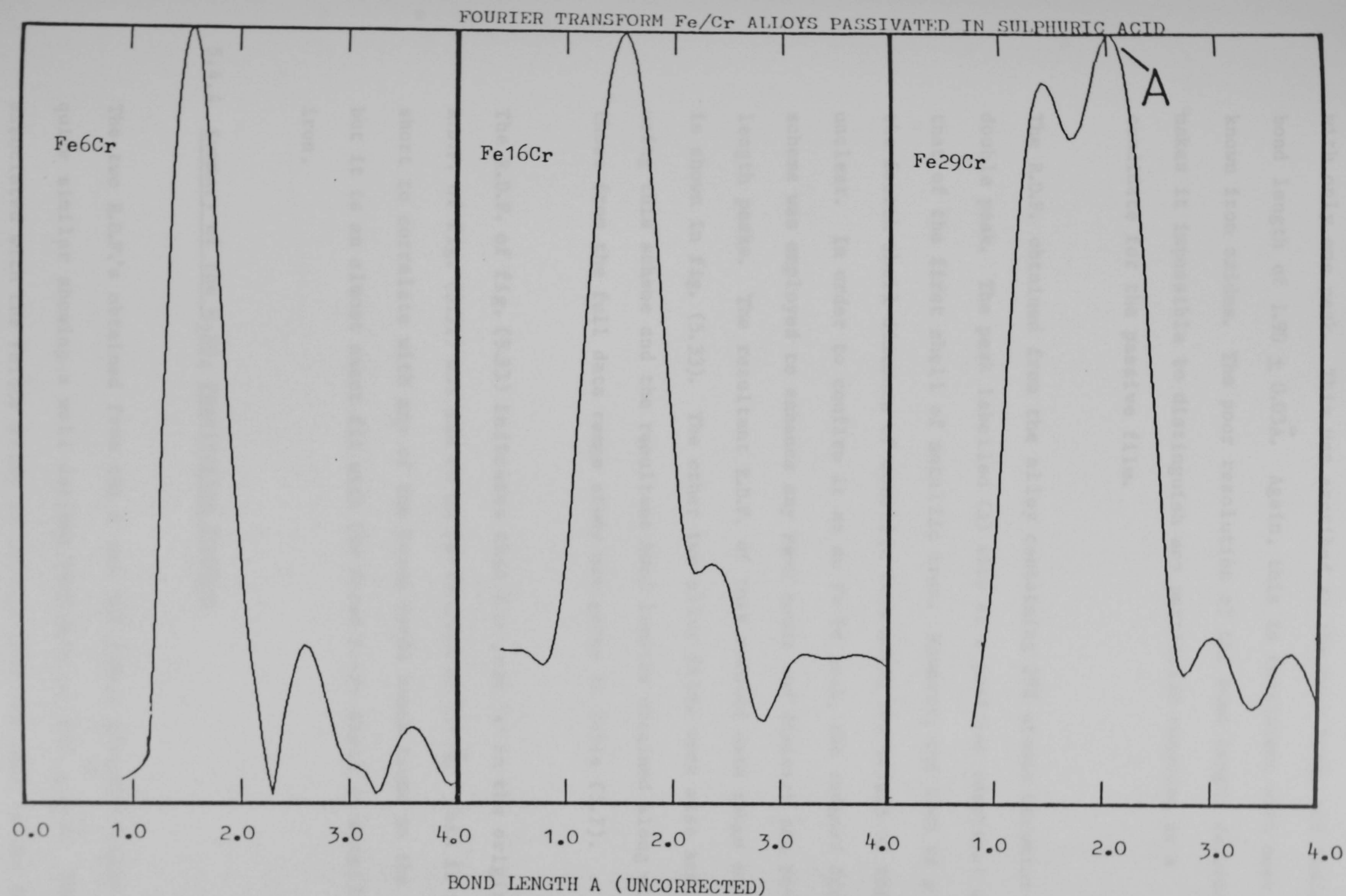
Previously we have assumed that the increase in the corrosion resistance of the Fe-Cr alloys at 12% atomic chromium is due to some change occurring in the passive film. In view of the results presented above we can now say that some other change in the passive film must also take place when the chromium content of the alloy exceeds 20% atomic chromium. Thus we should consider that there are three types of passive film: one associated with low chromium alloys, a second associated with alloy containing between 10 and 20% atomic chromium and a third found on alloys containing over 20% atomic chromium.

5.4.3 EXAFS Results

Attempts to passivate the thin iron sample were unsuccessful due to the high currents involved in passivation, which invariably resulted in the complete dissolution of the alloy film. Alloys containing 6, 16 and 29% atomic chromium were, however, successfully passivated at +0.8V and +0.4V (S.C.E) respectively, for 30 minutes. These potentials were chosen to ensure that the alloy sat in the middle of the passive region as indicated by the electrochemical data given above.

The iron 'K' edge absorption data for these samples were similar to all of the other oxide samples presented here, being indicative of an oxide. Using a data range of $3 \rightarrow 8 \text{ \AA}^{-1}$ and a weighting factor of k^2 the R.D.F.'s were generated using the methods of Chapter 4. These are shown in fig. (5.32). Only the range $0 \rightarrow 4 \text{ \AA}$ is shown here since no features were seen outside this range.

ARBITRARY
SCALE



Figure(5.32). The R.D.F.'s of iron-chromium alloys containing 6,16 and 29% atomic chromium passivated in 2.0M H_2SO_4

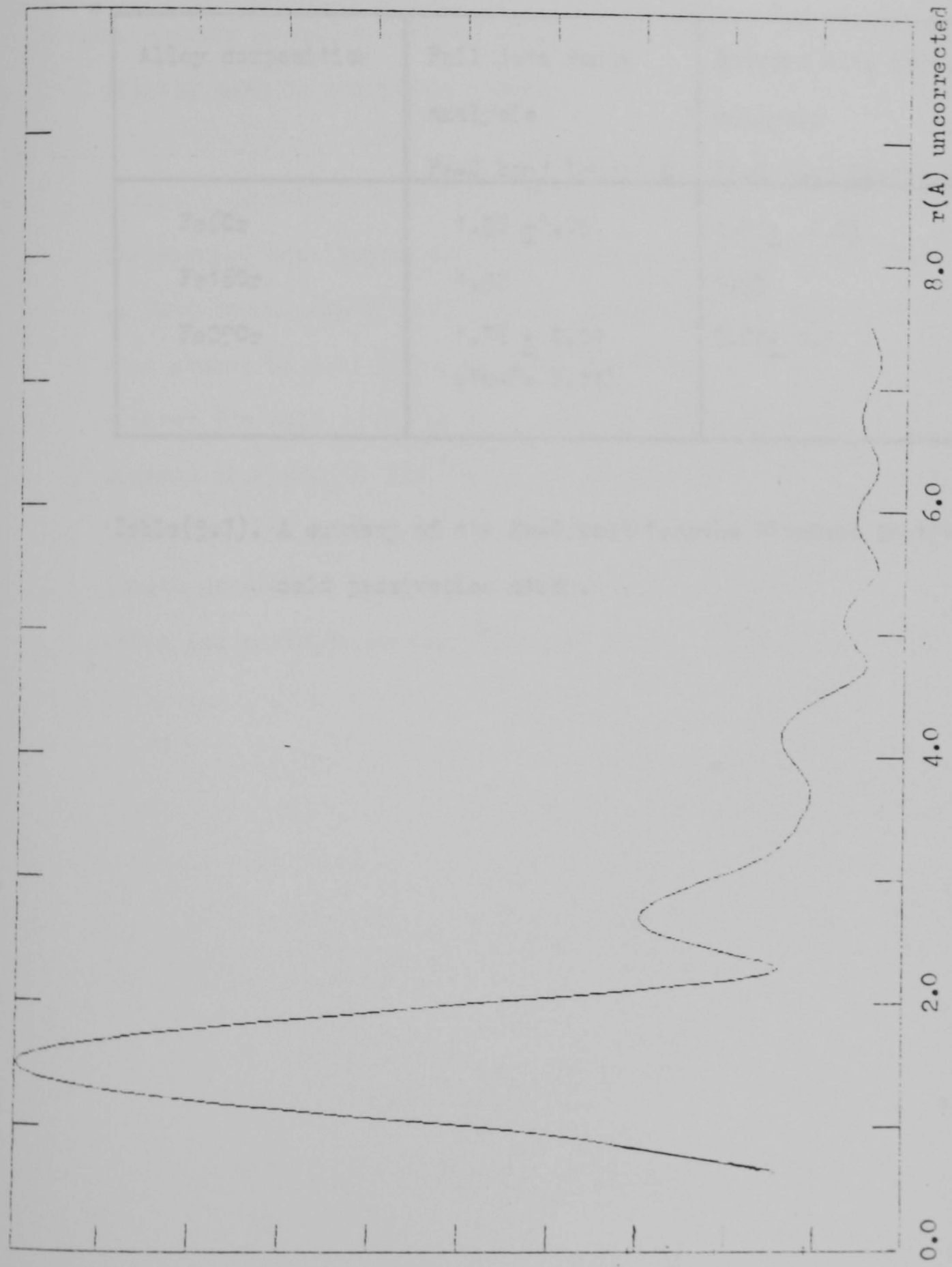
The two alloys containing 6 and 16% atomic chromium displayed R.D.F.'s with only one peak. This was ascribed to the Fe-O bond, and indicated a bond length of $1.90 \pm 0.03\text{\AA}$. Again, this is consistent with most of the known iron oxides. The poor resolution of the bond length determination makes it impossible to distinguish any particular compound as a candidate for the passive film.

The R.D.F. obtained from the alloy containing 29% atomic chromium shows a double peak. The peak labelled (A) sits at a position identical with that of the first shell of metallic iron. However, the lack of a peak at the fourth shell distance of metallic iron makes the origin of this peak unclear. In order to confirm it as an Fe-Fe peak, the reduced data range scheme was employed to enhance any Fe-O bonds and diminish the Fe-Fe bond length peaks. The resultant R.D.F. of this reduced data range analysis is shown in fig. (5.33). The other two alloy films were also analysed using this scheme and the resultant bond lengths obtained along with those from the full data range study are given in Table (5.7).

The R.D.F. of fig. (5.33) indicates that the peak 'A' in the original R.D.F. of fig. (5.32) was due to an Fe-Fe bond of 2.41\AA . This is too short to correlate with any of the known Fe-Fe bonds found in the oxides, but it is an almost exact fit with the first Fe-Fe shell in metallic iron.

5.4.4 Summary of the H₂SO₄ Passivation Studies

The two R.D.F.'s obtained from the 6 and 16% atomic chromium alloy are quite similar showing a well defined Fe-O bond at $1.91 \pm 0.3\text{\AA}$. The peak associated with the Fe16Cr alloy is broader than the peak in the Fe6Cr



Figure(5.33). The R.D.F. of an Fe29Cr alloy passivated in 2.0M H_2SO_4 generated using the reduced data range scheme.

Alloy composition	Full data range analysis Fe-O bond length, Å	Reduced data range analysis Fe-O bond length, Å
Fe6Cr	1.90 \pm 0.05	1.95 \pm 0.05
Fe16Cr	1.90	1.95
Fe29Cr	1.76 \pm 0.09 (Fe-Fe 2.41)	2.07 \pm 0.1

Table(5.7). A summary of the Fe-O bond lengths obtained in the sulphuric acid passivation study.

alloy and so it may be assumed that some greater degree of structural disorder is present in the 16% atomic chromium alloy. The lack of any other longer Fe-Fe bonds may also indicate that the passive film formed on these two alloys in H_2SO_4 is more disordered than the films formed in nitrite solution. These peaks corresponding to Fe-Fe (oxide) were clearly seen in the nitrite data.

Analysis of the R.D.F. of the 29% atomic chromium alloy is less clear. The reduced data range analysis clearly shows that peak 'B' is due to an Fe-O bond length $2.07\text{\AA} \pm 0.1\text{\AA}$. The second 'A' peak due to Fe-Fe bond cannot be correlated with any known oxide structures. It does however fit well with the Fe-Fe bond in metallic iron. However, the absence of a peak at the fourth shell separation of iron makes the interpretation of the origin of this peak unclear. The Fe-O bond length determined from the reduced data range scheme is to be preferred since its position is not distorted by the presence of the Fe-Fe peak.

5.5 Summary of Results

The nitrite passivated films show quite clearly that there is a transition towards an amorphous film as the chromium content of the alloy increases. The accuracy of the bond lengths determined is insufficient to identify a film structure positively; they are, however, comparable with $\alpha\text{Fe}_2\text{O}_3$, $\gamma\text{Fe}_2\text{O}_3$ and FeOOH . Where measured, the chromium edge shows that all chromium contained in the film is oxidised and has a local oxygen environment similar to that in Cr_2O_3 . However, the lack of any longer bonds implies that there is a lack of long range order in the film in the vicinity of the chromium.

The similarity of the two R.D.F.'s obtained from the alloys containing 6 and 16% atomic chromium indicates that the films formed on alloys above and below 12% atomic chromium are quite similar. This is interesting because in the past the increase in corrosion resistance of the Fe-Cr alloys seen at 12% atomic chromium has been thought to occur because of some change in the passive film structure - no such evidence is available from this study.

Only small differences were seen between the measurements made using the two EXAFS modes. The fluorescence measurements producing R.D.F.'s indicating that a somewhat greater disorder is present in the film. A discrepancy was also found between the Fe-O bond length in the film formed on an alloy containing 29% atomic chromium. The total yield results indicating a bond length of $2.07 \pm 0.03\text{\AA}$ while the fluorescence measurements indicated a bond length of $1.9 \pm 0.03\text{\AA}$.

The sulphuric acid passivated samples demonstrated a greater degree of disorder than that seen in the electron yield or fluorescence yield measured nitrite passivated films. The two alloys of 6 and 16% atomic chromium yield

similar results; however, the R.D.F. of the 16% atomic chromium film is somewhat wider. The interpretation of the final 29% atomic chromium film is unclear since the Fe-Fe bond has no clear origin.

The EXAFS results are compatible with the electrochemical results which show that three types of film may be present upon the Fe-Cr alloys depending upon the composition of the alloy. In common with the nitrite study no clear difference can be seen between the films formed on a 6% atomic chromium alloy and 16% atomic chromium alloy. Some change is evident in the film formed on an alloy containing 29% atomic chromium and the low Cr alloys.

The chromate passivation results are of a poor quality because of the amount of unoxidised iron remaining in the sample. However, the reduced data range analysis does indicate Fe-O bond lengths compatible with the known oxides. Since the films used here were the same thickness as those used in the nitrite study it must be concluded that the passive film formed by 0.05M K_2CrO_4 is much thinner than that formed by 0.1M NO_2 solution. We have also seen from this study that great care must be taken in analysing such data if we are to avoid ambiguous results such as those presented by Long et al (31).

6. Conclusion and Discussion

6.1 Introduction

Following the presentation of the results obtained in this study in the previous chapter, we will now discuss them under the following headings; EXAFS as a probe of the passive film structure, their implications for passivation and the structure of the passive film. Finally, some suggestions for future work in this field are made.

6.2 EXAFS as a Probe of the Passive Film Structure

All of the results presented in this work show that using the intense S.R.S. at Daresbury, both the fluorescence and electron yield EXAFS detection schemes are sensitive to passive film structure, even though the amount of film present is very small (10^{16} iron atoms). A comparison between the two detection schemes can only be made for the nitrite passivated films, since the analysis of the chromate passivated film was complicated by the presence of unoxidised iron.

This comparison showed that while the two detection modes provided broadly the same results - an increase in the disorder of the film structure with increasing chromium content of the alloy film - two differences were detected. The fluorescence signal indicated a greater degree of structural disorder in all the films, and a substantial difference was seen between the bond lengths determined for the 29% atomic chromium alloys.

The increase in structural disorder seen in the fluorescence study can be understood in view of the work of O'Grady⁽¹⁵⁾. O'Grady used 'in situ' and 'ex situ' Mossbauer Spectroscopy to show that the passive film on 'in situ' iron could not be identified with any of the known oxides of iron, but the dehydrated 'ex situ' film could have been $\gamma\text{Fe}_2\text{O}_3$. From this it was concluded that the true film was both hydrated and disordered. Since we can expect less dehydration to have taken place in the fluorescence detection system than the total electron yield system, the results presented here would appear to be in agreement with O'Grady's.

The uncertainties in the bond lengths determined in this study are such that for alloys containing less than 20% atomic chromium, both the fluorescence and total electron yield data gave the same result within the experimental limits. However, the fluorescence measurements indicate that the Fe-O bond length in the passivated 29% atomic chromium alloy is shortened with respect to the low chromium alloys, while the electron yield result indicates that it is lengthened.

The transformation $\gamma\text{FeOOH} \rightarrow \gamma\text{Fe}_2\text{O}_3$ as suggested by O'Grady will lead to a change in the mean Fe-O bond length from 2.03\AA to 1.96\AA . Since all the Fe-O bond lengths are shorter in the fluorescence measurements than the electron yield data it is difficult to conclude that less dehydration has occurred in the fluorescence mode.

6.2.1 Conclusion Fluorescence vs Electron Yield

Both the total electron yield and fluorescence yield detection schemes are seen to be sensitive to the passive film. It is apparent that the fluorescence mode yields results indicative of a greater structural disorder than the electron yield results. However, the Fe-O bond lengths determined from the data obtained from the two modes, do not make it clear that any less dehydration has occurred in the fluorescence experiments than the electron yield experiments. This may be because some oxidation of the film occurs in the fluorescence mode due to the samples prolonged exposure to the air.

While neither mode can be favoured over the other, from the results presented here, the ability of the fluorescence mode to be developed for in situ studies makes it a favourite candidate for any future work.

6.3 EXAFS Analysis

Local structural information about the type, number and position of scattering neighbours is available from the EXAFS oscillations as shown by equation (2.12). Using the simple analysis used here only information about type and position of neighbours has been extracted from the data. Also the uncertainties in the bond lengths obtained here are too great to define any film structure.

The use of a more elaborate analysis scheme was ruled out here because of the limited time available. However, a more advanced analysis method using theoretical or experimental scattering data to model the EXAFS data such as that described by Lee and Beni⁽³⁸⁾, could yield the full information available from the data, and improve upon the uncertainties in the bond length determinations. This would allow more precise structures to be proposed for the passive films.

It is apparent that an advanced analysis could deal more fully with the lightly oxidised samples obtained in the chromate study. Since it is able to take a more detailed account of the presence of the unreacted iron. We must conclude therefore that any future work must be based upon a more advanced form of analysis of the EXAFS data.

While no attempt was made here to analyse the X-ray absorption near edge structure, it will be apparent from the chromate study that this region of the X-ray absorption is especially sensitive to any oxide that maybe present. We have previously seen in Section (2.4.) that information regarding oxidation state, co-ordination and nature of the bonding of the absorbing atom, is available from this region of the absorption spectrum..

Thus any future study should seek to analyse fully this region of the data.

6.3.1 Conclusion - EXAFS Analysis

While the simple analysis used here provides a qualitative picture of the passive film, any future work must seek to use a more advanced analysis so that the amount of disorder and bond lengths can be obtained more quantitatively and accurately.

The analysis must include the XANES region, as we have seen this to be very sensitive to the presence of any oxide. The need for careful analysis has been highlighted by this study since it has demonstrated the ambiguous nature of the results presented by Long et al⁽³¹⁾, where the presence of some residual metallic iron may have been mis-interpreted as a complex passive film structure.

6.4 The Nature of the Passive Film

In view of the ambiguous nature of the chromate passivated film results this section is based upon the nitrite and H_2SO_4 studies.

For all the passivated films studied here, very little change in the structure of the local iron environment was seen when the chromium content of the alloy increased from 6 to 16% atomic chromium. Both these alloys displayed more structural disorder than the passivated iron films, but less disorder than the passivated 29% atomic chromium alloys. Where studied, the chromium environment was seen to have less long range order than the corresponding iron environment, with very little change occurring as the chromium content of the alloy increased from 16 to 29% chromium.

The electrochemical study shows that as well as changes in the electrochemical behaviour of the alloys occurring between 5 to 15% chromium which result in greater corrosion resistance, changes also take place at between 20 and 25% atomic chromium. As such the electrochemical data and EXAFS data are in agreement, that three types of film may exist: on iron, a crystalline oxide or hydroxide as reported elsewhere, on resistant chromium alloys containing up to 20%; a film that contains iron in a semi-disordered environment and chromium in a completely disordered environment with only the peak for the oxygen shell well resolved; finally, a film that forms on alloys containing over 20% atomic chromium that contains both iron and chromium in a disordered environment.

That disordered or amorphous films can be correlated with corrosion resistant alloys has been noted before by Hoar⁽⁴⁶⁾ and Leach⁽⁴⁷⁾. One of the rules set out by Hoar⁽⁴⁶⁾ to produce corrosion resistant alloys, the

corrosion resistance of which is based upon a good passive film, was to use an alloy that lead to an amorphous mixed oxide. Since such an amorphous oxide would not contain any grain boundaries 'short circuit' diffusion paths would be reduced and so the isolation of the alloy would be improved. Evidence that such amorphous films exist has already been given by McBee and Kruger (26) and Leach⁽⁴⁷⁾. Evidence that oxide films formed at low temperatures are amorphous has been presented by Fehlner⁽⁴⁸⁾, where the benefits of slower self diffusion and the lack of grain boundaries raised.

One of the most important requirements for the formation of an amorphous film is the need for structural flexibility to be present in the oxide. Evidence to support the view that such flexibility could be provided by the incorporation of chromium into the passive film has been given by Revesz and Kruger⁽²⁰⁾.

Since the free energies of formation of CrO_3 and Cr_2O_3 are quite similar it is possible that various structural conformations of roughly the same energy may exist. Additionally chromium oxides may display different structures due to a ligands such as any water that may be present in the structure. Since these ligand involve both σ and π bonding the stereochemistry of the oxide can be modified without any great change to the bond energy. Finally, the multiple valency of both iron and chromium and the ability to form solid solutions of Fe-Cr oxides will provide additional structural flexibility.

Following the above observations and the results obtained here the following model for the passive film on iron-chromium alloys is proposed.

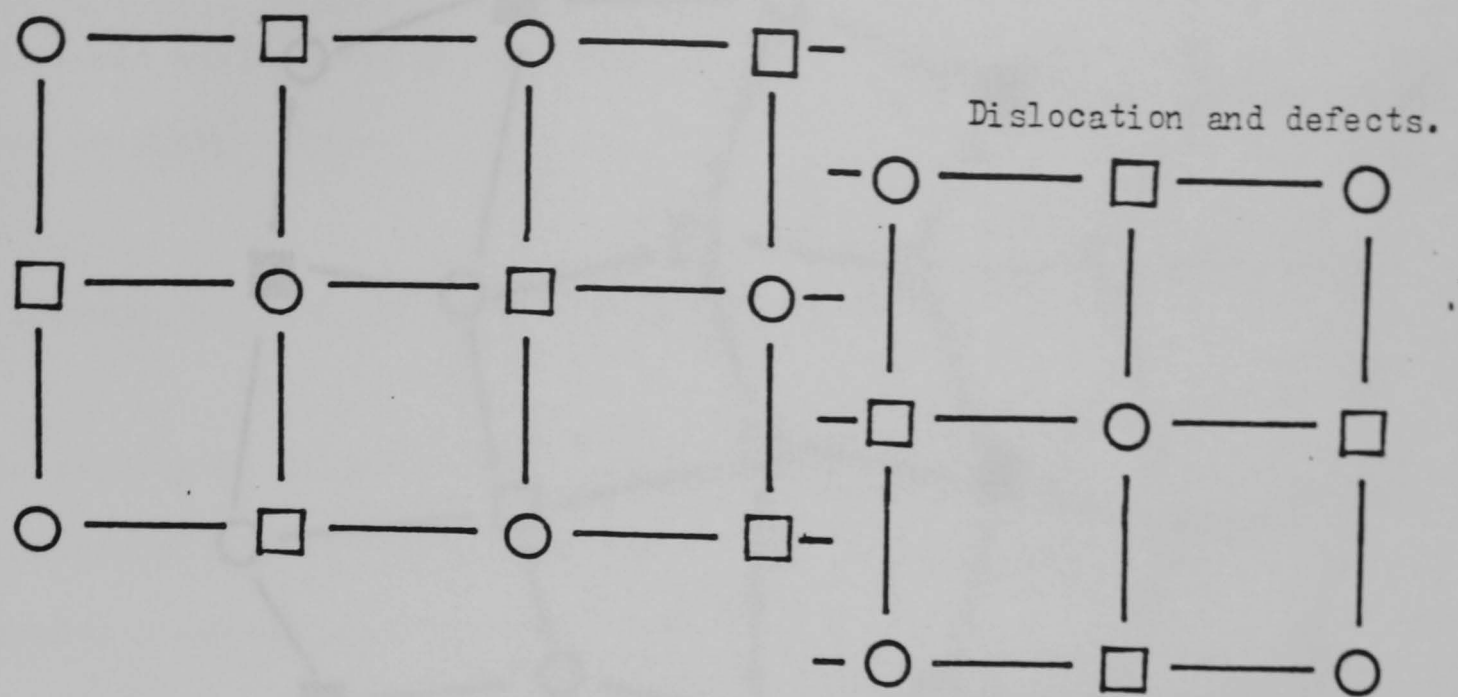
When chromium is not present, the passive film will be a well ordered crystalline oxide, which as $\gamma\text{-Fe}_2\text{O}_3$ or some hydrated compound such as

γ -FeOOH. (The results of this study are not sufficient to say which). Such a film is shown schematically in fig. (6.1a), obviously it will contain various defects and as such would not be an effective passivator. When chromium is incorporated into the film, its greater bonding flexibility allows it to bridge any defect sites more easily, and so the number of defects present is reduced and corrosion resistance improved. It should be noted that bonding flexibility does not necessarily mean a change in bond length, but merely variability of bond angle.

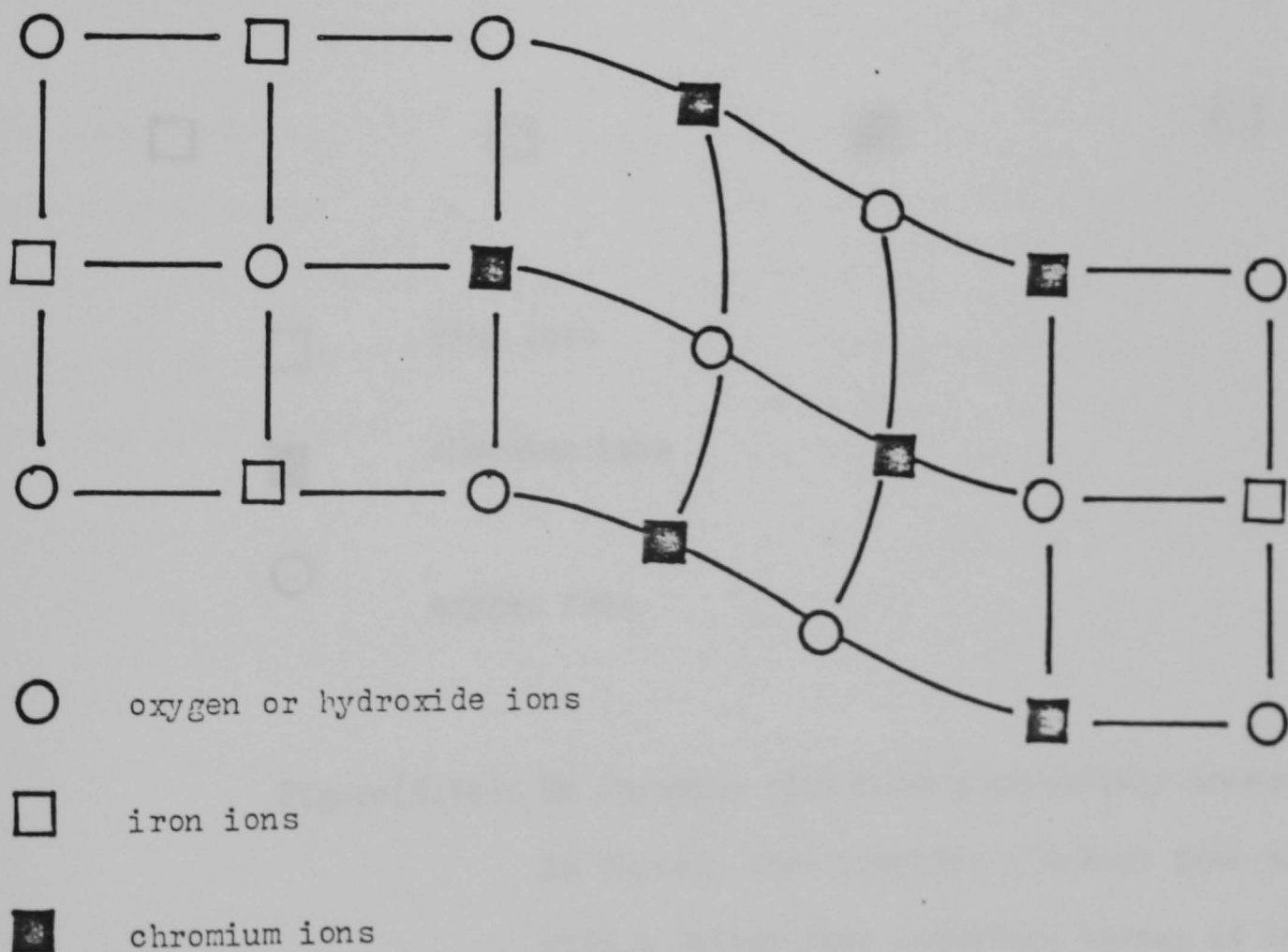
The incorporation of chromium into the lattice is shown schematically in fig. (6.1b). It can be seen that the local atomic environment appears ordered around most of the iron atoms, but disordered about the chromium. This view is supported by the chromium edge data obtained in the nitrite and chromate studies given earlier, since the chromium was found in a disordered environment while some order was still found in the local environment of the iron in the 16% atomic chromium alloys.

Finally, in chromium rich alloys a truly amorphous/glassy film may form, where both the iron and chromium atomic environments are disordered as shown in fig. (6.1c). In this film no defects or dislocations are present to aid diffusion of ions through the film. A perfect 'epitaxial' relationship exists between the oxide and the alloy since the bonding flexibility of the oxide allows perfect accommodation to be made between them. This will reduce any electronic defect states which may aid electron conduction and so the overall isolation of the alloy is enhanced and the film is seen to be a better passivator.

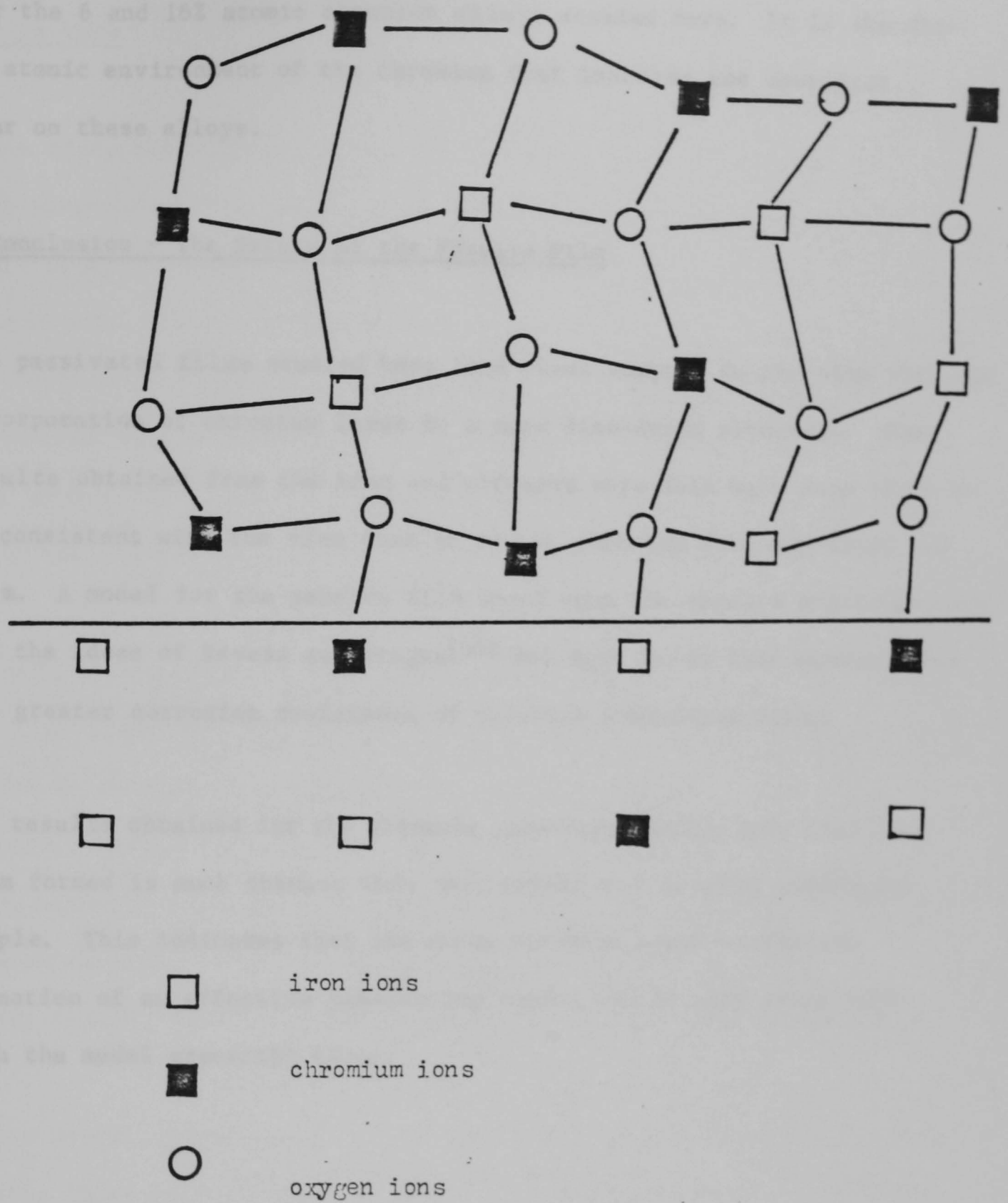
The above model is wholly compatible with an increase in corrosion resistance at 12% atomic chromium and the apparent similarity of the EXAFS



Figure(6.1a). The 'rigid' nature of bonding in an iron rich passive film leads to the formation of defects that aid ionic diffusion.



Figure(6.1b). The presence of chromium allows greater bonding flexibility and so the film can deform, thus avoiding any defects with their consequent deteriorative effect upon passivation.



Figure(6.1c). In chromium rich films a completely amorphous film is formed, that provides a defect free passivation layer with a defect free interface between it and the alloy.

data for the 6 and 16% atomic chromium alloys studied here. It is the disordered atomic environment of the chromium that improves the corrosion behaviour on these alloys.

6.4.1 Conclusion - The Nature of the Passive Film

The passivated films studied here lend clear support to the view that the incorporation of chromium leads to a more disordered structure. The results obtained from the iron and chromium edge data have been shown to be consistent with the view that it is the chromium that disorders the film. A model for the passive film based upon the results presented here and the ideas of Revesz and Kruger⁽⁴⁹⁾ has been given that accounts for the greater corrosion resistance of chromium containing films.

The results obtained for the chromate passivated films show that the film formed is much thinner than that formed on a nitrite passivated sample. This indicates that the extra chromium present aids the formation of an effective passivating layer, and is thus consistent with the model presented above.

6.5 Future Work

Since this study has not identified the precise structure of the passive film formed on iron-chromium alloys the following proposals for any future studies are made. Because of the ambiguous nature of the results of the comparison made here between the two EXAFS detection modes it is not possible to say what effect oxidation or dehydration has upon the films. To avoid these problems any future work should be directed towards using a fluorescence 'in situ' technique such as that used by Long et al⁽³¹⁾ thus ensuring that the sample remains in its passivating solution throughout the measurement.

A limitation of this work is that the passive films studied here were grown in thin alloy films that may not be representative of true bulk alloys. This problem can be avoided if bulk alloys were studied using the Reflection EXAFS method reported by Bosio⁽³⁰⁾. By ensuring that the X-ray beam is totally externally reflected, sampling depths of just 30Å could be obtained. If this were coupled with an 'in situ' fluorescence detection mode experiment, results representative of the 'real world' could be obtained.

Any results obtained from such a study must be analysed using more advanced methods than those used here and include the information available from the XANES data, since we have seen that the uncertainties and the resolution of this simple Fourier transform method of analysis prevent a precise film structure being presented. Finally, more model compounds such as $\gamma\text{-FeOOH}$ and $\gamma\text{-Fe}_2\text{O}_3$ and CrOOH should be studied to gain more information about the candidate film structures.

REFERENCES

1. F L McCracken, E Parsaglia, R S Stromberg and H L Steinberg
J.Res. (N.B.S.), 67A, 363 1963
2. J Kruger
J.Electrochem. Soc. 110, 654, 1963
3. N Sato and K Kudo
Electrochem. Acta. 16, 447, 1971
4. J C Riviere, AERE Report - R10436, 1982
5. M Seo, N Sato, J B L Lumsden and R W Staehle
Corros.Sci., 17, 209, 1979
6. C L Foley, J Kruger and C J Becholdt
J.Electrochem.Soc. 114, 994, 1967
7. M Cohen, in "Passivity of Metals": R P Frankenthal and J Kruger
eds. The Electrochemical Society, Princeton, 521, 1978
8. C D Stockbridge, P B Sewell and M Cohen
J.Electrochem.Soc. 108, 928, 1961
9. P B Sewell, C D Stockbridge and M Cohen
J.Electrochem.Soc. 108, 933, 1961
10. K J Vetter
Z.Electrochem. 62, 642, 1958
11. C L Foley, J Kruger and C J Bechtoldt
J. Electrochem Soc. 114, 994, 1967
12. T P Hoar and U R Evans
J.Chem.Soc. 2476, 1932
13. U R Evans, "The Corrosion and Oxidation of Metals", 1968, Edward Arnold
14. H Enge, "Introduction to Nuclear Physics", 459, 1978, Addison-Wesley
15. W E O'Grady
J. Electrochem.Soc. 127, 555, 1980
16. K Asami, K Hasimoto and S Shimodaira
Corros.Sci. 18, 151, 1978
17. P F King and H Uhlig
J.Phys.Che. 63, 2026, 1959
18. G Aronowitz and N Hackerman
J.Electrochem.Soc. 110, 633, 1963
19. R P Frankenthal
J.Electrochem.Soc. 114, 524, 1967
116, 580, 1969
116, 1646, 1969
20. A G Revesz and J Kruger, in "Passivity of Metals", R P Frankenthal and
J Kruger eds, The Electrochemical Society, Princeton, 137, 1978

21. S C Tjong, R W Hoffman and E B Yeager
J.Electrochem.Soc. 129, 1662, 1982
22. J E Halliday and R P Frankenthal
J.Electrochem.Soc. 119, 1190, 1972
23. K Asami, K Hasimoto and S Shimodaira
Corros.Sci. 16, 387, 1976
24. V Mitrovic-Scepanovic, B MacDougall and M J Graham
Corros.Sci. 24, 479, 1984
25. Th.Heumann and H S Panesar
J.Electrochem.Soc. 110, 629, 1963
26. C L McBee and J Kruger
Electrochim.Acta. 110, 633, 1972
27. G Okamoto
Corros.Sci. 13, 471, 1973
28. S M El-Mashri, R G Jones and A J Forty
Phil.Mag. 48, 665, 1983
29. I Davoli, L Palladino and S Stizza
Solid State Comms. 44, 1585, 1982
30. L Bosio, R Cortes and F Froment
3rd Int. EXAFS Conference, Stanford, 1984
31. G G Long, J Kruger, D R Black and M Kuriyama
J.Electroanal. Chem. 150, 603, 1983
32. G G Long, J Kruger, D R Black and M Kuriyama
J.Electrochem.Soc. 130, 240, 1983
33. J Kruger, G G Long, M Kuriyama and A I Goldman in, "Passivity of Metals and Semiconductors", M Froment, ed; Elsevier, Amsterdam, 1983
34. R Hoffman in, "Passivity of Metals and Semiconductors", M Froment, ed; Elsevier, Amsterdam, 1983
35. D E Sayers, E A Stern and F W Lytle
Phys.Rev.Lett. 27, 1204, 1971
36. C A Ashley and S Doniach
Phys.Rev. B11, 1279, 1975
37. P A Lee and J B Pendry
Phys.Rev. B11, 2795, 1975
38. P A Lee and G Beni
Phys.Rev. B11, 2795, 1977
39. B K Teo and P A Lee
J.Amer.Che.Soc. 101, 2815, 1979
40. D E Sayers and E A Stern
Phys.Rev.Lett. 27, 1204, 1971

41. D E Sayers, F W Lytle and E A Stern
J.Non.Cryst.Sol. 8-10, 401, 1972
42. P H Citrin, P Elsenberger and B M Kincaid
Phys.Rev.Lett. 36, 1346, 1976
43. J Stohr, L Johansson, I Lindau and P Panetta
Phys.Rev.B. 20, 664, 1979
44. S J Gurman
J.Met.Sci. 17, 1541, 1982
45. A J Forty, in "Proc. R. Inst. GB", 50, 1
47. T P Hoar
J.Electrochem.Soc. 117, 17C, 1970
48. J S L Leach
Surf.Sci. 53, 257, 1975
49. F P Fehlner, in "The Passivity of Metals", R P Frankenthal and J Kruger,
eds., The Electrochemical Society, Princeton, 181, 1978